UNIVERSITÄT SIEGEN

Yan Niu

Online Force Reconstruction for Structural Health Monitoring

Schriftenreihe der Arbeitsgruppe
für Technische Mechanik
im Institut für Mechanik und Regelungs-
technik - Mechatronik

Herausgeber: Claus-Peter Fritzen

Band 15

Impressum

Prof. Dr.-Ing. Claus-Peter Fritzen

Arbeitsgruppe für Technische Mechanik

Institut für Mechanik und Regelungstechnik - Mechatronik

Universität Siegen

57068 Siegen

ISSN 2191-5601

URN urn:nbn:de:hbz:467-14359

Zugl.: Siegen, Univ., Diss., 2019

Online Force Reconstruction for Structural Health Monitoring

genehmigte

DISSERTATION

zur Erlangung des Grades eines Doktors

der Ingenieurwissenschaften

vorgelegt von

Yan Niu, M.Sc.

geb. in Henan, V.R. China

eingereicht bei der Naturwissenschaftlich-Technischen Fakultät

der Universität Siegen

Siegen 2018

Referent: Prof. Dr.-Ing. Claus-Peter Fritzen

Korreferent: Prof. Dr.-Ing. Dirk Söffker

Tag der mündlichen Prüfung

26. Oktober 2018

Acknowledgements

The work which is presented in this thesis was carried out during my time as a doctoral student at the Institute of Mechanics and Control Engineering - Mechatronics in University of Siegen in Germany. During my doctoral study, I was also a member of the Multi-Modal Sensor Systems for Environmental Exploration (MOSES) Research School in North Rhine-Westphalia (NRW) in Germany. Before Joining the MOSES program, I graduated from the International Graduate Studies in Mechatronics Master Program in University of Siegen.

First of all, I would like to express my sincere gratitude to my supervisor Prof. Dr.-Ing. Claus-Peter Fritzen for offering me the valuable opportunity to be a member of his working group which is full of passion and joy, for his immerse knowledge and humor, and for his patient guidance and continuous motivation to my research work. It is really my pleasure to be guided by Prof. Dr.-Ing. Claus-Peter Fritzen to enter into the Structural Health Monitoring (SHM) society, and I would like to confirm that "Forschung macht Spaß!".

Besides my supervisor, I would also like to thank Prof. Dr.-Ing. Dirk Söffker for taking over the second reviewer responsibility, for his valuable comments to my work and for the encouragement to me. Furthermore, I would like to give my thanks to Prof. Dr.-Ing. Otmar Loffeld for his contribution to the MOSES Doctoral Program, for his illuminating questions during the anual spring and fall presentations in the MOSES program, and for his time and support to the implementation of doctorate. I would also like to take this opportunity to thank Prof. Dr.-Ing. Hubert Roth for his contribution to the International Graduate Studies in Mechatronics Master Program and for his time and support to the implementation of doctorate.

My doctoral study and my secondment in The Hong Kong Polytechnic University was financially supported by the MOSES program. I would like to thank the administration of the the MOSES program, Dr.-Ing. Holger Nies and Mrs. Silvia Niet-Wunram, for their support to my doctoral study and my secondment.

My sincere thanks go to Prof. Yi-Qing Ni from The Hong Kong Polytechnic University and his former group members Dr. Xiao-Wei Ye, Dr. Yang Chen, Dr. Shu-Qin Ye, Dr. You-Wu Wang, and Dr. Peng Zhang for their support to me during my secondment in The Hong Kong Polytechnic University. My thanks also go to Prof. Eliz-Mari Lourens from Delft University of Technology for the fruitful discussion on the topic of force reconstruction.

I would like to thank my former office colleague and friend Dr.-Ing. Miguel Angel Torres Arredondo for his continous motivation and for the creation of our office melody "confidence region" which was inspired from the exciting research work. It was really my

pleasure to have been working together with such a passionate fellow. I would like to thank my former working colleagues Dr.-Ing. Maksim Klinkov, M.Sc. Rannam Chaaban, and M.Sc. Daniel Ginsberg for the fruitful discussion on force reconstruction, robust observer and Kalman filter; to thank Dr.-Ing. Peter Krämer and Dr.-Ing. Dongsheng Li for the fruitful discussion on operational modal analysis (OMA); and to thank my former working colleagues Dr.-Ing. Martin Kübbeler, M.Sc. Henning Jung, and Dr.-Ing Philipp Hilgendorff for the time with Kicker and Jägermeister in lab Schellack. I would like to thank our secretary Mrs. Giesela Thomas for her warmhearted support and the tasty self-made cookies, and to thank our lab masters Mr. Gerhard Dietrich and Mr. Wolfgang Richter for their professional support to my experiments. My thanks also go to my former working colleagues Dr.-Ing Cheng Yang, Dr.-Ing Inka Müller, M.Sc. Erion Zenuni, Dr.-Ing. Rolf T. Schulte, Dr.-Ing. Kejia Xing, Dr.-Ing. Jochen Moll and Dr.-Ing. Philipp Köster for all the good memory in the institute.

Last but not the least, I would like to thank my parents and my wife for their love and their continuous support to me throughout my doctoral study.

Siegen, October 2018 Yan Niu

Contents

Nomenclature

Abbreviations

SS&IE_L	Simultaneous State and Input Estimator for Linear systems
SS&IE	Simultaneous State and Input Estimator
AKF	Augmented Kalman Filter
APS	Auto Power Spectrum
ARV	Vector AutoRegressive models
ARX	Auto-Regressive model with eXogenous input
CFT	Concrete-Filled-Tube
DAU	Data Acquisition Unit
DOF	Degrees of Freedom
DP	Damage Prognosis
EKF+RLSE	Extended Kalman Filter and a Recursive Least-Squares Estimator
EMA	Experimental Modal Analysis
EOC	Environmental and Operational Condition
FE	Finite Element
FEA	Finite Element Analysis
FFT	Fast Fourier Transform
FRF	Frequency Response Function
KF+RLSE	Kalman Filter and a Recursive Least-Squares Estimator
LHP	Left Half-Plane
LTR	Loop Transfer Recovery
MAC	Modal Assurance Criterion
MDOF	Multiple Degrees Of Freedom

OMA	Operational Modal Analysis
PI observer	Proportional-Integral observer
PSD	Power Spectral Density
RMSE	Root Mean Square Error
RTSF	Recursive Three-Step Filter
SDOF	Single Degree Of Freedom
SHM	Structural Health Monitoring
SSKF+LSE	Steady-State Kalman Filter and a Least-Squares Estimator
SVE	Singular Value Expansion
UIO	Unknown Input Observer
XPS	Cross Power Spectrum

Fixed symbols

$\boldsymbol{G}_{yy}(\omega)$	Auto power spectrum of the output $\boldsymbol{y}(t)$
$\boldsymbol{\varepsilon}_{arv,k}$	Uncorrelated zero-mean random vector in the AR model
$\boldsymbol{\eta}_k$	Increment of the unknown input $\boldsymbol{d}_k$
$\boldsymbol{\Upsilon}$	Input matrix of the process noise in continuous-time time-variant state-space model
$\boldsymbol{\Upsilon}_k$	Input matrix of the process noise in discrete-time time-variant state-space model
$\boldsymbol{\phi}_i^a$	Real mode shape vector for the i-th mode from FEA
$\boldsymbol{\phi}_i^e$	Real mode shape vector for the i-th mode from experiment
$\boldsymbol{\psi}_{arv,i}$	Eigenvector of $\boldsymbol{A}_{arv}$
$\boldsymbol{\psi}_{h,i}$	Complex mode shape vector for the i-th mode from AR(h)
$\boldsymbol{\psi}_i$	Real mode shape vector of the i-th mode
$\boldsymbol{\Lambda}_{arv}$	Diagonal matrix with $\lambda_{d,h,i}$ in the main diagonal
$\boldsymbol{\Phi}$	Mass normalized modal matrix

$\boldsymbol{\varphi}_{h,i}$	The i-th mode complex mode shape vector calculated from AR(h)
$\boldsymbol{\Psi}_{arv}$	Matrix with $\boldsymbol{\psi}_{arv,i}$ in the i-th column
$\boldsymbol{\xi}(t)$	State vector in the UIO
$\boldsymbol{A}(t)$	State transition matrix in continuous-time time-variant state-space model
$\boldsymbol{A}^{arv}$	State transition matrix in ARV state-space model
$\boldsymbol{A}_c$	State transition matrix for continuous-time state-space model
$\boldsymbol{A}_d$	State transition matrix for discrete-time state-space model
$\boldsymbol{A}_k$	State transition matrix in discrete-time time-variant state-space model
$\boldsymbol{A}_l^{arv}$	Coefficient matrix of the AR model
$\boldsymbol{b}$	Intercept vector in the AR model
$\boldsymbol{B}(t)$	Input matrix in continuous-time time-variant state-space model
$\boldsymbol{B}_k$	Input matrix in discrete-time time-variant state-space model
$\boldsymbol{B}_o$	Force input matrix
$\boldsymbol{C}(t)$	Output matrix of the process noise in continuous-time time-variant state-space model
$\boldsymbol{C}^{arv}$	Output matrix in ARV state-space model
$\boldsymbol{C}_a$	Output matrix for acceleration
$\boldsymbol{C}_c$	Output matrix for continuous-time state-space model
$\boldsymbol{C}_{ds}$	Output matrix for displacement (or strain)
$\boldsymbol{C}_d$	Output matrix for discrete-time state-space model
$\boldsymbol{C}_k$	Output matrix in discrete-time time-variant state-space model
$\boldsymbol{C}_m$	Modal damping matrix
$\boldsymbol{C}_n$	Damping matrix
$\boldsymbol{C}_v$	Output matrix for velocity

$\boldsymbol{d}(t)$	Input vector
$\boldsymbol{d}_k$	Input vector for discrete-time state-space model
$\boldsymbol{F}(\omega)$	Fourier transform of $\boldsymbol{f}(t)$
$\boldsymbol{F}(s)$	Laplace transform of $\boldsymbol{f}(t)$
$\boldsymbol{f}(t)$	Force input vector in nodal coordinates
$\boldsymbol{G}_c$	Input matrix for continuous-time state-space model
$\boldsymbol{G}_d$	Input matrix for discrete-time state-space model
$\boldsymbol{G}_{ff}(\omega)$	Auto power spectrum of the input force $\boldsymbol{f}(t)$
$\boldsymbol{H}(\omega)$	Frequency response function for the structure
$\boldsymbol{H}(s)$	Transfer function between $\boldsymbol{F}(s)$ and $\boldsymbol{Y}(s)$
$\boldsymbol{H}^*(\omega)$	Conjugate transpose of $\boldsymbol{H}(\omega)$
$\boldsymbol{H}_c$	Direct feedthrough for continuous-time state-space model
$\boldsymbol{H}_d$	Direct feedthrough for discrete-time state-space model
$\boldsymbol{H}_{nf}(s)$	Transfer function between $\boldsymbol{F}(s)$ and $\boldsymbol{Q}_n(s)$
$\boldsymbol{K}\,(t)$	Kalman gain in Kalman-Bucy filter
$\boldsymbol{K}_{c,ss}$	$\boldsymbol{K}\,(t)$ in steady-state
$\boldsymbol{K}_{d,ss}$	$\boldsymbol{K}_k$ in steady-state
$\boldsymbol{K}_k$	Kalman gain in Kalman filter
$\boldsymbol{K}_m$	Modal stiffness matrix
$\boldsymbol{K}_n$	Stiffness matrix
$\boldsymbol{L}_c$	Gain matrix in Luenberger observer
$\boldsymbol{M}_n$	Mass matrix
$\boldsymbol{P}^x\,(t)$	State estimate error covariance in Kalman-Bucy filter
$\boldsymbol{P}^x_{0/0}$	Initial value of $\boldsymbol{P}^x_{k/k}$
$\boldsymbol{P}^x_{c,ss}$	$\boldsymbol{P}^x\,(t)$ in steady-state

$\boldsymbol{P}^{x}_{k/k-1}$	Covariance of $\tilde{\boldsymbol{x}}_{k/k-1}$
$\boldsymbol{P}^{x}_{k/k}$	Covariance of $\tilde{\boldsymbol{x}}_{k/k}$
$\boldsymbol{P}^{d}_{k}$	Covariance of $\tilde{\boldsymbol{d}}_{k}$
$\boldsymbol{P}^{xd}_{k}$	Covariance of $\tilde{\boldsymbol{x}}_{k/k}$ and $\tilde{\boldsymbol{d}}_{k}$
$\boldsymbol{Q}_{k}$	Covariance of w_k
$\boldsymbol{Q}_{m}(s)$	Laplace transformation of $\boldsymbol{q}_{m}(t)$
$\boldsymbol{q}_{m}(t)$	Modal displacement vector
$\boldsymbol{Q}_{n}(s)$	Laplace transformation of $\boldsymbol{q}_{n}(t)$
$\boldsymbol{q}_{n}(t)$	Nodal displacement vector
$\boldsymbol{r}_{\phi}$	Residual vector of mode shape
$\boldsymbol{r}_{f}$	Residual vector of natural frequency
$\boldsymbol{R}_{k}$	Covariance of v_k
$\boldsymbol{u}\,(t)$	Control input in continuous-time state-space model
$\boldsymbol{u}\,(t)$	Known control input vector
$\boldsymbol{u}_{k}$	Control input in discrete-time state-space model
$\boldsymbol{v}\,(t)$	Measurement noise in continuous-time state-space model
$\boldsymbol{v}_{k}$	Measurement noise in discrete-time stochastic state-space model
$\boldsymbol{w}\,(t)$	Process noise in continuous-time state-space model
$\boldsymbol{W}^{\phi}$	Weighting matrix for $\boldsymbol{r}^{\phi}$ in model updating
$\boldsymbol{W}^{f}$	Weighting matrix for $\boldsymbol{r}^{f}$ in model updating
$\boldsymbol{w}_{k}$	Process noise in discrete-time stochastic state-space model
$\boldsymbol{w}^{arv}_{k}$	Input vector in ARV state-space model
$\boldsymbol{x}(t)$	State vector for continuous-time state-space model
$\boldsymbol{x}_{k}$	State vector for discrete-time state-space model
$\boldsymbol{x}^{arv}_{k}$	State vector in ARV state-space model

$\boldsymbol{Y}(\omega)$	Fourier transform of $\boldsymbol{y}(t)$
$\boldsymbol{Y}(s)$	Laplace transform of $\boldsymbol{y}(t)$
$\boldsymbol{y}(t)$	Output vector for continuous-time state-space model
$\boldsymbol{y}_k$	Output vector for discrete-time state-space model
$\delta(t)$	Dirac delta function
$\dot{\boldsymbol{x}}(t)$	First derivative of $\boldsymbol{x}(t)$
$\hat{\boldsymbol{d}}(t)$	Estimate of $\boldsymbol{d}(t)$
$\hat{\boldsymbol{d}}_k$	Estimate of $\boldsymbol{d}_k$
$\hat{\boldsymbol{x}}(t)$	Estimate of $\boldsymbol{x}(t)$
$\hat{\boldsymbol{x}}_{0/0}$	Initial value of $\hat{\boldsymbol{x}}_{k/k}$
$\hat{\boldsymbol{x}}_{k/k-1}$	The *a priori* state estimate
$\hat{\boldsymbol{x}}_{k/k}$	The *a posteriori* state estimate
$\hat{\boldsymbol{y}}(t)$	Estimate of $\boldsymbol{y}(t)$
λ	Regularization parameter in the objective function in model updating
$\lambda_{d,h,i}$	Discrete-time eigenvalue of $\boldsymbol{A}^{arv}$
$\lambda_{h,i}^{c}$	Continuous-time counterpart of $\lambda_{h,i}^{d}$
ϕ_i	Mode shape vector for the i-th mode
μ_i	The i-th singular value of $K(t,\tau)$
ω	Circular frequency
ω_i	Circular natural frequency for the i-th mode
$\overline{G}_{ff}(\omega)$	Average auto power spectrum of $\boldsymbol{f}(t)$
$\overline{G}_{yf}(\omega)$	Average cross power spectrum of $\boldsymbol{y}(t)$ and $\boldsymbol{f}(t)$
$\overline{G}_{yy}(\omega)$	Average auto power spectrum of $\boldsymbol{y}(t)$
$\phi_{q,i}$	The q-th element of $\boldsymbol{\psi}_i$
$\phi_{r,i}$	The r-th element of $\boldsymbol{\phi}_i$

$\tilde{\boldsymbol{d}}_k$	Estimate error of $\boldsymbol{d}_k$
$\tilde{\boldsymbol{x}}(t)$	Estimate error of $\boldsymbol{x}(t)$
$\tilde{\boldsymbol{x}}_{k/k-1}$	The *a priori* state estimate error
$\tilde{\boldsymbol{x}}_{k/k}$	The *a posteriori* state estimate error
$\triangle t$	Sampling interval
$\triangle \boldsymbol{\theta}$	Change of updating parameters in model updating
ζ_{diff}	Percentage damping ratio difference
$\zeta_{h,i}$	The i-th mode damping ratio calculated from AR(h)
ζ_i	Damping ratio for the i-th mode
$C_{yf}(\omega)$	Ordinary coherence function
d_{tol}	Tolerence value for ζ_{diff}
$f(t)$	Time-varying input force
f_{diff}	Percentage frequency difference
$f_{h,i}$	The i-th mode natural frequency calculated from AR(h)
f_i^a	Natural frequency for the i-th mode from FEA
f_i^e	Natural frequency for the i-th mode from experiment
$f_{perturb}(t)$	Reconstructed $f(t)$ using $y_{perturb}(t)$
f_{tol}	Tolerence value for f_{diff}
h	Order of AR model
$h(t)$	Impulse response function for the structure
$H_{nf\_qr}(\omega)$	$H_{nf\_qr}(s)$ in Fourier domain
$H_{nf\_qr}(s)$	The qr-th element of $\boldsymbol{H}_{nf}(s)$
J	Objective function in model updating
j	Imaginary unit
J_θ	Side constraint in the objective function in model updating

J_r	Measurement residual in the objective function in model updating
k	Nonnegtive integer
$K(t,\tau)$	Kernel
m	Number of elements in $\boldsymbol{d}(t)$
MAC_{tol}	Tolerence value for MAC
$mDOF$	Number of degrees of freedom in modal coordinates
n	Number of elements in $\boldsymbol{x}(t)$
$nDOF$	Number of degrees of freedom in nodal coordinates
p	Number of elements in $\boldsymbol{y}(t)$
p_a	Number of acceleration sensors
p_{ds}	Number of displacement (strain) sensors
p_v	Number of velocity sensors
r_i^{ϕ}	Residual of the real mode shape for the i-th mode
r_i^{f}	Residual of the natural frequency for the i-th mode
s	Laplace variable
$u_i(t)$	The i-th left singular function of $K(t,\tau)$
$v_i(\tau)$	The i-th right singular function of $K(t,\tau)$
$y(t)$	Structural response
$y_{perturb}(t)$	Perturbed $y(t)$
AR(h)	The h-th order AR model

Operators

$(\cdot)^*$	Conjugate operator
$(\cdot)^+$	Generalized inverse operator
$(\cdot)^T$	Transpose operator
$\|\cdot\|_2$	2-norm

$E[\cdot]$	Expectation operator
$Re(\cdot)$	Real part of a complex number

Sets

$\mathbb{C}^p$	$(p \times 1)$ complex vector
$\mathbb{R}^n$	$(n \times 1)$ real vector

Abstract

The knowledge of the external load acting on the structure under investigation is important for Structural Health Monitoring (SHM). The history of the external load can be used for updating the earlier lifetime prediction of the structure. An easy and direct way to get the external load information is to measure it directly using a certain type of force transducer. However, there are still many practical cases in which a direct measurement of the external load is physically or economically not feasible. For those cases, a possible solution is to reconstruct the external load using structural response measurements, e.g. displacement, strain, velocity, and acceleration. This process is defined as force reconstruction. It is a kind of inverse problem which often tends to be ill-posed, in the sense that the measurement noise and the modeling error can be amplified and can cause large deviations in the reconstructed force. Online force reconstruction is a research topic which studies how to realize force reconstruction in real-time. The thesis focuses on online force reconstruction.

The basic idea which is adopted in this thesis for online force reconstruction is to apply a real-time executable state and input estimation algorithm. The methodology for online force reconstruction consists of two stages, an offline stage and an online stage. In the offline stage, the modal parameters of the structure are identified, and a state-space model of the structure is constructed. If it is possible to apply an artificial force on the structure, the modal parameters of the structure can be identified using the Experimental Modal Analysis (EMA) technique. In case it is difficult or not possible to apply an artificial force on the structure, the modal parameters of the structure can be identified using the Operational Modal Analysis (OMA) technique. For this case, a model updating process is performed to get the correctly scaled mode shape vectors. In the online stage, a real-time executable state and input estimation algorithm is applied to provide an estimate of the force. The ill-posedness in the process of force reconstruction is relaxed by the convergence of the estimate error of the force. Together with the force, the structural responses at different positions can be reconstructed, too.

In this thesis, modifications to some of the available real-time executable state and input estimation algorithms are proposed, so that these algorithms are theoretically more suitable for online force reconstruction. These proposed algorithm modifications are as follows. The Unknown Input Observer (UIO) based Simultaneous State and Input Estimator (SS&IE) is modified to be suitable for linear systems. This modified SS&IE is named as SS&IE_L. To simplify the implementation of the Kalman Filter and a Recursive Least-Squares Estimator (KF+RLSE), the filter equations of the KF+RLSE at the steady-state are derived. The Kalman Filter with Unknown Inputs (KF-UI) is generalized to be compatible with the case that the process noise and the measurement noise

are correlated. The generalized KF-UI is named as G-KF-UI. The Steady-State Kalman Filter with a Least-Squares Estimator (SSKF+LSE) is modified to include the covariance matrix of the input and the covariance matrix of the measurement noise. This modified SSKF+LSE is named as MSSKF+LSE.

In the earlier research studies, some algorithms have already been proposed for online force reconstruction. All the available algorithms, including the proposed modified algorithms, are potential candidates for online force reconstruction. In case there is a practical need for online force reconstruction, it is reasonable to raise the question which algorithm to choose. In this thesis, a study on application-oriented algorithm selection is performed. The assumptions and the mathematical conditions in the algorithms are translated into practical requirements. A benchmark study is performed in which a laboratory structure is taken as the benchmark structure. The modal parameters of this benchmark structure is identified using the EMA technique. Two types of widely used sensors are installed on this benchmark structure, including strain gauge and accelerometer. Three different types of input forces are considered, including a quasi-static force, impact forces, and a wind load which is generated by an electric fan. In total eight different algorithms are tested. Based on the results from the benchmark study, an application oriented guidance for algorithm selection is extracted.

As an example of practical application, the presented methodology for online force reconstruction is applied for wind load reconstruction for the 600 meter tall Canton Tower. The field measurement data are recorded by the SHM system of the Canton Tower, including the data which were recorded during the Typhoon Nanmadol in 2011 and the Typhoon Kai-tak in 2012. The modal parameters of the Canton Tower during the Typhoon Nanmadol are identified by using an OMA technique. The available reduced-order Finite Element (FE) model of the Canton Tower is first modified to reflect the height adjustment of the Canton Tower, and then is updated according to the identified modal parameters. In consideration of the characteristics of the wind load and the sensor availability in the SHM system, the MSSKF+LSE algorithm is selected. The wind load on the Canton Tower during the Typhoon Kai-tak is reconstructed. The mean value of the wind load is calculated with the wind speed measurements and the aerodynamic force coefficients which are identified from a wind tunnel test. The dynamic part of the wind load is reconstructed by using the MSSKF+LSE algorithm and the acceleration measurements. To validate the reconstruction results, two acceleration channels are selected. The acceleration measurements from these two channels are not used in wind load reconstruction. The strategy for the validation is to compare the reconstructed acceleration for these two channels with the real acceleration measurements. The validation results show that the reconstructed wind load is acceptable.

Finally, a summary of this thesis is provided, and some open topics are described. These open topics can be considered in future study on online force reconstruction.

Keywords: online force reconstruction, state and input estimation, inverse problem, Experimental Modal Analysis (EMA), Operational Modal Analysis (OMA), Model updating, Structural Health Monitoring (SHM)

Kurzfassung

Für Structural Health Monitoring (SHM) ist die Kenntnis der externen Belastungen auf die zu untersuchende Struktur von großer Bedeutung. Der Kraftverlauf kann z.B. verwendet werden, um eine frühere Lebensdauervorhersage der Struktur zu aktualisieren. Der direkteste Weg diese Lasten zu bestimmen, ist die unmittelbare Messung mittels geeigneter Kraftsensoren. Für viele praktische Anwendungen ist eine direkte Kraftmessung allerdings physikalisch nicht möglich oder wirtschaftlich nicht sinnvoll. Eine mögliche Lösung ergibt sich in diesen Fällen durch die Rekonstruktion der Kräfte anhand der gemessenen Strukturantworten, wie z.B. Verschiebungen, Dehnungen, Geschwindigkeiten und Beschleunigungen. Dieser Prozess wird als Kraftrekonstruktion bezeichnet und zählt zu den inversen Problemen. Kraftrekonstruktion ist oftmals ein schlecht-gestelltes Problem. Kleine Störungen durch Messrauschen und Modellfehler können verstärkt werden, sodass große Abweichungen in der rekonstruierten Kraft auftreten. Online-Kraftrekonstruktion ist ein Forschungsgebiet, welches sich mit Methoden auseinandersetzt das schlecht-gestellte Problem zu lösen und somit eine Kraftrekonstruktion in Echtzeit zu ermöglichen. Der Fokus dieser Dissertation liegt auf der Online-Kraftrekonstruktion.

Die Grundidee dieser Arbeit zur Online-Kraftrekonstruktion besteht in der Anwendung von Zustands- und Eingangsschätzalgorithmen, welche echtzeitfähig sind. Die Methodologie zur Online-Kraftrekonstruktion besteht aus zwei Phasen, einer Offline-Phase und einer Online-Phase. In der Offline-Phase werden die modalen Parameter der Struktur identifiziert, und ein Zustandsraummodell (State-Space Model) der Struktur wird konstruiert. Für den Fall, dass es möglich ist, eine künstliche Kraft auf die Struktur anzuwenden, können die modalen Strukturparameter mit der experimentellen Modalanalyse identifiziert werden. Falls es allerdings schwierig oder nicht möglich ist, eine künstliche Kraft auf die Struktur anzuwenden, wird die operationelle Modalanalyse zur Bestimmung der modalen Strukturparameter herangezogen. Für diesen Fall muss ein Model-Updating-Verfahren angewendet werden, um die Skalierungsfaktoren der Vektoren für die Eigenschwingungsformen zu erhalten. In der Online-Phase, wird ein Zustands- und Eingangsschätzalgorithmus, welcher echtzeitfähig ist, angewendet, um die Kraft zu ermitteln. Das schlecht gestellte Problem im Prozess der Kraftrekonstruktion wird durch die Konvergenz des Schätzfehlers der Kraft gelöst. Zusammen mit der Kraft können die Strukturantworten an verschiedenen Positionen auch rekonstruiert werden.

In dieser Arbeit werden Modifikationen an einigen der bereits verfügbaren Zustands- und Eingangsschätzalgorithmen vorgeschlagen, so dass diese Algorithmen für die Online Kraftrekonstruktion theoretisch besser geeignet sind. Die vorgeschlagenen Modifikationen sind wie folgt: Der „Unknown Input Observer (UIO)“-basierte „Simultaneous State and Input Estimator (SS&IE)“ Algorithmus wird modifiziert, um für lineare Systeme geeignet

zu sein. Das modifizierte SS&IE wird als SS&IE_L bezeichnet. Um die Implementierung des „Kalman Filter and a Recursive Least-Squares Estimator (KF+RLSE)“ Algorithmus zu vereinfachen, werden die Filtergleichungen des KF+RLSE im Steady-State abgeleitet. Der „Kalman Filter with Unknown Inputs (KF-UI)“ wird verallgemeinert, um mit dem Fall, dass das Prozessrauschen und das Messrauschen korreliert sind, kompatibel zu sein. Das verallgemeinerte KF-UI wird als „Generalized KF-UI (G-KF-UI)“ bezeichnet. Das „Steady-State Kalman Filter with a Least-Squares Estimator (SSKF+LSE)“ wird so modifiziert, um eine Schätzung der Kovarianzmatrix des Eingangs und eine Schätzung der Kovarianzmatrix des Messrauschens zu berücksichtigen. Das modifiziert SSKF+LSE wird als MSSKF+LSE bezeichnet.

In früheren Forschungsstudien wurden bereits einige Algorithmen vorgeschlagen. Alle verfügbaren Algorithmen, einschließlich der vorgeschlagenen modifizierten Algorithmen, sind potentielle Kandidaten für die Online-Kraftrekonstruktion. Falls es einen praktischen Bedarf für eine Online-Kraftrekonstruktion gibt, ist es vernünftig, die Frage zu stellen, welcher Algorithmus zu wählen ist. In dieser Arbeit wird eine Untersuchung zur anwendungsorientierten Algorithmusauswahl durchgeführt. Die Annahmen und die mathematischen Bedingungen in den Algorithmen werden in praktische Anforderungen übersetzt. Eine Untersuchung ist durchgeführt, bei der eine Laborstruktur als Benchmark-Struktur herangezogen wird. Das modell dieser Benchmarkstruktur wird mit Hilfe der experimentellen Modalanalyse identifiziert. Zwei Arten von Sensoren sind auf dieser Benchmark-Struktur installiert, einschließlich DMS und Beschleunigungssensor. Drei verschiedene Belastungsarten werden berücksichtigt, einschließlich quasistatische Kräfte, Impulslasten, und einer von einem elektrischen Ventilator erzeugten Windlasten. Insgesamt werden acht verschiedene Algorithmen getestet. Basierend auf den Ergebnissen der Benchmark-Untersuchung wird eine anwendungsorientierte Empfehlung zur Algorithmusauswahl gegeben.

Als Beispiel für die praktische Anwendung wird die vorgestellte Methodologie zur Online-Kraftrekonstruktion zur Rekonstruktion der Windlast für den 600 Meter hohen Canton Tower verwendet. Die Feldmessdaten stammen aus dem SHM-System des Canton Towers, einschließlich der Daten, die während des Taifuns Nanmadol im Jahr 2011 und des Taifuns Kai-tak im Jahr 2012 aufgezeichnet wurden. Die modalen Parameter des Canton Towers während des Taifun Nanmadol werden mit Hilfe der operationellen Modalanalyse identifiziert. Das verfügbare Finite-Elemente-Modell des Canton Towers wird an die identifizierten modalen Parameter durch sogenanntes Model-Updating angepasst. Unter Berücksichtigung der Eigenschaften der Windlasten und der Sensorverfügbarkeit des SHM-Systems wird der MSSKF + LSE-Algorithmus ausgewählt. Die Windlasten auf den Canton Tower während des Taifun Kai-tak wird rekonstruiert. Der Mittelwert der Windlasten wird mit den Windgeschwindigkeitsmessungen und den aerodynamischen Koeffizienten berechnet. Die aerodynamischen Koeffizienten werden aus einem Windkanalversuch ermittelt.

Der dynamische Teil der Windlasten wird mit dem MSSKF + LSE-Algorithmus und der Beschleunigungsmessungen rekonstruiert. Zur Validierung der Rekonstruktionsergebnisse werden zwei Beschleunigungskanäle ausgewählt. Die Beschleunigungsmessungen von diesen beiden Kanälen werden bei der Rekonstruktion der Windlasten nicht verwendet. Die Strategie für die Validierung besteht darin, die rekonstruierten Beschleunigungen für diese zwei Kanäle mit den entsprechenden Beschleunigungsmessungen zu vergleichen. Die Validierungsergebnisse zeigen, dass die rekonstruierten Windlasten akzeptabel sind.

Abschließend wird eine Zusammenfassung dieser Dissertation gegeben, und einige offene Themen werden beschrieben. Diese offenen Themen können in zukünftigen Forschungen zur Online-Kraftrekonstruktion berücksichtigt werden.

Schlüsselwörter: Online-Kraftrekonstruktion, Zustands- und Eingangsschätzer, inverses Problem, Experimentelle Modalanalyse, Operationelle Modalanalyse, Model-Updating, Structural Health Monitoring (SHM)

1. Introduction

1.1. Introduction to Structural Health Monitoring (SHM)

"*Structural Health Monitoring (SHM) aims to give, at every moment during the life of a structure, a diagonosis of the 'state' of the constituent materials, of the different parts, and of the full assembly of these parts constituting the structure as a whole*" (Balageas, 2006). Farrar and Worden (2007) describes SHM as "*the process of implementing a damage identification strategy for aerospace, civil and mechanical engineering infrastructure*". According to the level of the information about the damage, four levels on the damage assesment scale are defined (Rytter, 1993).

- Level I: Damage detection. (Is there a damage?)
- Level II: Damage localization. (Where is the damage?)
- Level III: Damage quantification. (To what extent is the damage?)
- Level IV: Prognosis of remaining service life. (How much service life remains?)

The goal of SHM is to answer the question above in the parenthesis at each level. It is worth mentioning that some researchers also consider answering the question, "*what kind of damage is present*?", as an extra step between Level II and Level III (Sohn et al., 2004; Worden and Dulieu-Barton, 2004).

A possible classification of SHM methods is to divide them into local methods and global methods (Fritzen, 2006). Local methods inspect the structure in a relatively small area where it is known that the structure is highly loaded and it is likely that e.g. fatigue damage or cracks might occur. Local methods often work in high frequencies, e.g. ultrasonics waves, for diagnosis, so that small damages can be detected. Global methods uses the fact that the local damage has an influence on the global behavior of the structure. Global methods usually work with vibrations in the lower to the middle frequency range. Prognosis of remaining service life is the most sophisticated level in SHM. It requires the combination the global structural model with local damage models to predict the evolution of damage (Farrar et al., 2003; Inman et al., 2005; Dettmann and Söffker, 2011).

1.2. Motivation

Farrar and Lieven (2007) describes Damage Prognosis (DP) as the future of SHM, and states that *"DP attempts to forecast system performance by assessing the current damage state of the system (i.e. SHM), estimating the future loading environments for that*

system, and predicting through simulation and past experience the remaining useful life of the system". Here it is also worth mentioning usage monitoring which is the process of acquiring the information of operational loading on a structure. Figure 1.1 illustrates the relationship between usage monitoring, SHM, and DP in the form of a block diagram.

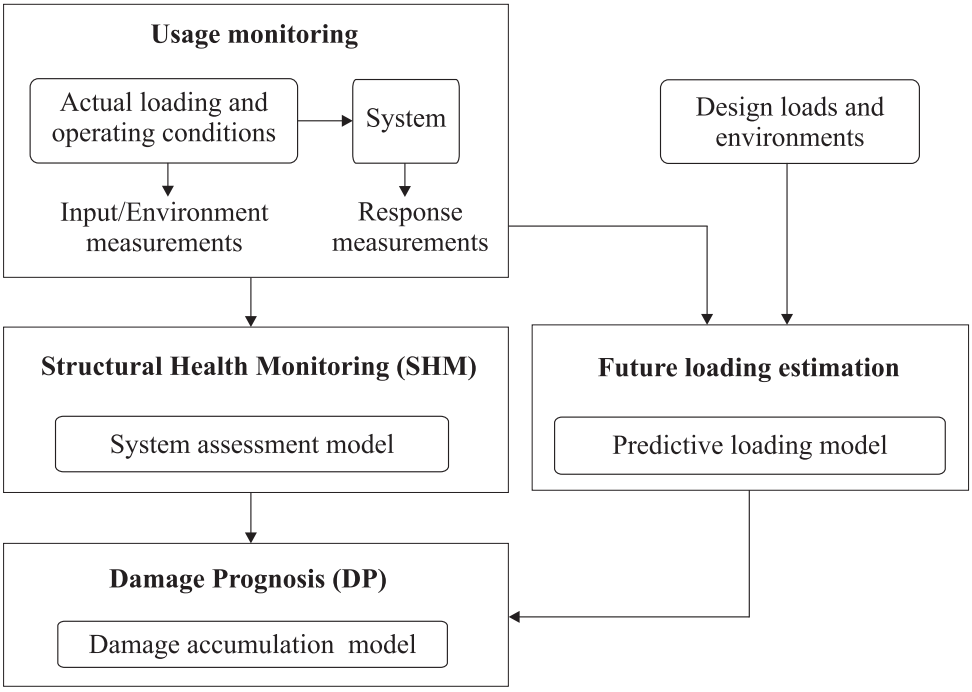

Figure 1.1. *The relationship between usage monitoring, Structural Health Monitoring (SHM) and Damage Prognosis (DP) (Farrar et al., 2005).*

The block diagram in figure 1.1 shows that SHM needs the load information from usage monitoring. In other words, the knowledge of the external load is important for SHM. An easy and direct way to get the information of the external load is to measure it directly using a certain type of force transducer. However, there are still many practical cases where a direct measurement is physically or economically not feasible. For example, it is still an engineering challenge to measure directly the traffic load, the rail-wheel contact force, and the wind load. For such practical cases, a possible solution is to reconstruct the force from the measured structural responses, e.g. displacement, strain, velocity, and acceleration. This process is defined as force reconstruction, and it often tends to be ill-posed. If the ill-posedness in force reconstruction can be relaxed, the structure itself actually becomes its own force sensor (Stevens, 1987).

1.3. Basic idea of online force reconstruction

Online force reconstruction is the research topic which studies how to realize force reconstruction in real-time. The basic idea which is adopted in this thesis for online force reconstruction is to apply a real-time executable state and input estimation algorithm.

This basic idea is described in the form of a block diagram in figure 1.2. Consider the structure under investigation as a system, the force which needs to be reconstructed as the input to the system, and the structural response as the output from the system. Given structural response measurements, the applied algorithm can provide an estimate of the input, i.e. the reconstructed force, in real-time. The ill-posedness in the force reconstruction process is relaxed through the convergence of the estimate error of the force, and the force reconstruction is realized in real-time. To apply this basic idea, the relationship between the force and the structural response is needed. In other words, a model of the structure is needed.

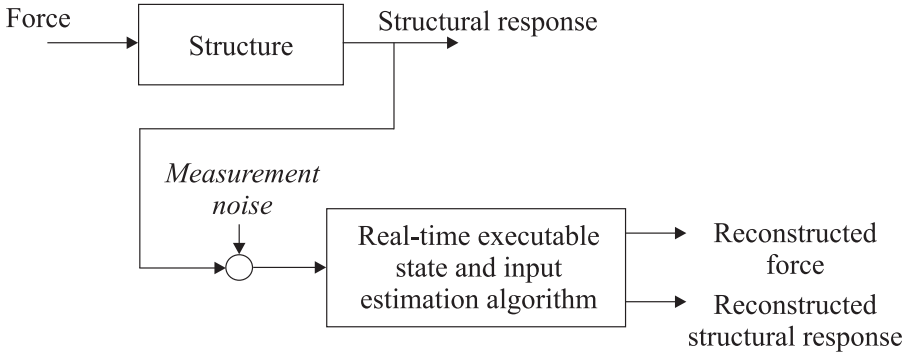

Figure 1.2. *Basic idea of online force reconstruction*

1.4. State of the art

Before the publication of this thesis, there are already available studies on online force reconstruction. According to the author's knowledge, these available studies can be grouped as follows.

- *Proportional-Integral observer (PI observer).* For example, Söffker (1999) estimated the contact forces of the nonlinear rail-wheel contact; and Krajcin and Söffker (2003) showed both simulation and experimental results for the contact force between the blade and the housing of a rotating machine.
- *Kalman Filter and a Recursive Least-Squres Estimator (KF+RLSE).* For example, Ma et al. (2003) estimated the input forces acting on a cantilever beam in a simulation study; Deng and Heh (2006) applied this method to reconstruct a distributed force in a numerical simulation; Chen and Lee (2008) studied the capability of this method for moving force estimation through several simulations; Wu et al. (2009) adopted this method in the identification of the soil force resulted from the soil-pile interaction in a shaking table test.
- *Extended Kalman Filter and a Recursive Least-Squares Estimator (EKF+RLSE).* For example, Ma and Ho (2004) proposed the EKF+RLSE method which is suitable

for nonlinear structural systems. The performance of this method is verified in numerical simulations for input force estimation of non-linear lumped-mass systems.

- *Augmented Kalman Filter (AKF).* Lourens et al. (2012b) proposed the AKF in the work for the estimation of impact force on an instrumented steel beam. The AKF augments the state vector with the input vector, and estimates the augmented state vector with the help of the state estimation function of the Kalman filter. In AKF, an estimate of the covariance matrix of the increment of the input is needed. Perisic et al. (2012) used the same method for the gearbox fatigue load estimation. Ji and Liang (2000) applied a method similar to the AKF, but without considering the direct feed-through in the output equation of the system model. A simulation study is performed for the estimation of forces on a rod. Berg and Miller (2010) adopts the same method in a simulation study for estimating the forces on a wind turbine blade.
- *Unknown Input Observer (UIO).* Ha and Trinh (2004) proposed a UIO design method for simultaneous state and input estimation for a class of non-linear systems. Klinkov and Fritzen (2006) named this UIO design method as SS&IE and adopted it for online force reconstruction. Furthermore, the SS&IE was also applied for wind load estimation on a 5MW wind energy plant (Klinkov and Fritzen, 2009; Fritzen et al., 2013).
- *Recursive Three-Step Filter (RTSF).* Gillijns and De Moor (2007) proposed an algorithm for unbiased minimum-variance input and state estimation for linear discrete-time systems with direct feed-through. Hsieh (2009) named this algorithm as RTSF. Lourens et al. (2012a) applied the RTSF for the estimation of the load on a laboratory suspended beam and the estimation of the load on a footbridge.
- *Steady-State Kalman Filter and a Least-Squares Estimator (SSKF+LSE).* Hwang et al. (2009a) proposed this algorithm and applied it in modal load estimation in a simulation study, and further tested this algorithm on a rectangular shaped concrete chimney in a wind tunnel test (Hwang et al., 2011).
- *Auto-Regressive model with eXogenous input (ARX)* . Müller et al. (2011) applied this algorithm for impact force estimation.
- *Bayesian regression with Gaussian processes.* Torres-Arredondo et al. (2011) adopted this algorithm to find the relationship between the impact force and the structural response, and applied it for impact force estimation.

1.5. Original contributions

This thesis focuses on online force reconstruction. Inspired by the available work on this topic, the basic idea in figure 1.2 is adopted in this thesis. The methodology for online

force reconstruction is presented in the form of block diagrams in chapter 3. The author's original contributions in this thesis are summarized blow.

- A modification to the SS&IE is proposed. The SS&IE was originally proposed for a class of non-linear systems. The structural model in the modal domain is linear. To make the SS&IE suitable for linear models, a modification to the SS&IE is proposed. This proposed modification is named as SS&IE_L, short for Simultaneous State and Input Estimation for Linear systems.
- The filter equations of the KF+RLSE in steady-state are derived. These derived filter equations can simplify the implementation of the KF+RLSE.
- The Kalman Filter with Unknown Inputs (KF-UI), which was proposed in Pan et al. (2011), is for the first time adopted for online force reconstruction. The filter equations of the KF-UI are proved to be equivalent with the filter equations of the RTSF. The necessary and sufficient conditions for the existence of the KF-UI are updated. Furthermore, the KF-UI is generalized to be compatible with the case that the process noise and the measurement noise are correlated.
- A modification to the SSKF+LSE is proposed. The SSKF+LSE was proposed in Hwang et al. (2009a). This algorithm assumes the input forces all have the same variance and are uncorrelated, and it assumes the measurement noises from the sensors all have the same variance. In practical applications, it might be not the case. In this thesis, a modified SSKF+LSE (MSSKF+LSE) is proposed, which suggests using the estimate of the covariance matrix of the forces and the estimate of the covariance matrix of the sensor measurement noise.
- An application-oriented guidance is proposed for algorithm selection for online force reconstruction. This proposed guidance is extracted based on a benchmark study, and it may assist the algorithm selection for a specific application.
- A wind load reconstruction study is performed using the SHM data from the 600 meter tall Canton Tower. The applied methodology and the reconstruction results are presented.

1.6. Organization of the thesis

Chapter 2 provides the theoretical foundations which are needed in this thesis for structural model construction, and the principle of the state estimation techniques, including the observer technique, Kalman filter, Unknown Input Observer (UIO), etc. To support the discussion in later chapters, the available real-time executable state and input estimation algorithms are briefly reviewed. Furthermore, the topic on the correlation of the process noise and the measurement noise is also covered.

Force reconstruction is the process to reconstruct the forces from structural response measurement. This process is a kind of inverse problem which often tends to be ill-posed. Online force reconstruction is the research topic which studies how to realize force reconstruction in real-time. Chapter 3 explains the ill-posedness in the force reconstruction process, and discusses the importance of the observability of the state and the importance of the convergence of the state estimate error and the force estimate error for the transformation from an ill-posed problem to a well-posed problem in online force reconstruction. The methodology for online force reconstruction is presented. Two different practical cases are considered, with one case having the possibility to apply an artificial excitation and the other case without such possibility. For each of these two practical cases, the methodology is described accordingly in the form of a block diagram. The presented methodology is capable of reconstructing both the force and the structural responses. Furthermore, the methodology for the reconstruction of distributed forces is also presented.

In consideration of the practical requirements in online force reconstructions, some modifications to some of the available algorithms are proposed. Chapter 4 provides the proposed modifications. Chapter 5 presents the results from a study on application-oriented algorithm selection. The assumptions and the mathematical conditions in the available algorithms are translated to practical requirements. A benchmark study is performed. A laboratory structure is taken as the benchmark structure, on which two types of widely used sensors are installed. Three different types of input forces are considered. In total eight different algorithms are tested. Based on the results from the benchmark study, a guidance for algorithm selection is extracted and presented.

In chapter 6, the presented methodology is applied to the 600 meter tall Canton Tower for wind load reconstruction. Field measurements from two different typhoon events are analyzed. The results from Operational Modal Analysis, model updating, and wind load reconstruction are presented.

Chapter 7 provides a summary of the contents in this thesis. Furthermore, some open topics are proposed. According to the author's understanding on the topic of online force reconstruction, these proposed open topics can be considered as an extension of the work in this thesis.

2. Theoretical foundations

The basic idea, which is adopted in this thesis for online force reconstruction, is to apply a real-time executable state and input estimation algorithm. This basic idea has been presented in the form of a block diagram in figure 1.2. It is worth mentioning that the applied algorithm needs the relationship between the force and the structural response. Thus, a reliable model of the structure is needed in order to successfully apply this basic idea. This chapter provides the theoretical foundations which are needed in this thesis, including structural model construction, observer, Kalman filter, Unknown Input Observer (UIO), and the available real-time executable state and input estimation algorithms. Furthermore, the topic on the correlation of the process noise and the measurement noise is also covered.

2.1. Structural model construction

A reliable model of the structure is important for a successful application of the basic idea in figure 1.2. This section provides the theoretical foundations which are needed in this thesis for structural model construction, including the transformation of the structural model from the nodal domain to the modal domain, the transformation of the structural model from the second-order form to the state-space from, Experimental Modal Analysis (EMA), Operational Modal Analysis (OMA), and the principle of model updating.

2.1.1. Second-order structural model

Assuming a structure is linear and with viscous damping, the forced motion of this structure can be represented by (Gawronski, 2004; De Silva, 2007)

$$\boldsymbol{M}_n\ddot{\boldsymbol{q}}_n(t) + \boldsymbol{C}_n\dot{\boldsymbol{q}}_n(t) + \boldsymbol{K}_n\boldsymbol{q}(t) = \boldsymbol{f}(t). \tag{2.1}$$

In equation (2.1), $\boldsymbol{q}_n(t) \in \mathbb{R}^{nDOF}$ denotes the displacement vector in the nodal coordinates, with $nDOF$ equal to the number of nodal Degrees Of Freedom (DOF); $\boldsymbol{f}(t) \in \mathbb{R}^{nDOF}$ is the force vector; $\boldsymbol{M}_n \in \mathbb{R}^{nDOF\times nDOF}$, $\boldsymbol{C}_n \in \mathbb{R}^{nDOF\times nDOF}$, and $\boldsymbol{K}_n \in \mathbb{R}^{nDOF\times nDOF}$ are the mass matrix, the damping matrix, and the stiffness matrix, respectively.

Denote $\boldsymbol{y}(t) \in \mathbb{R}^p$ as the output vector, where p represents the number of sensors. Introduce the matrix $\boldsymbol{C}_{ds} \in \mathbb{R}^{p_{ds}\times nDOF}$ which defines the positions of the displacement sensors (or the strain gauges), $\boldsymbol{C}_v \in \mathbb{R}^{p_v\times nDOF}$ defining the positions of the velocity sensors, and $\boldsymbol{C}_a \in \mathbb{R}^{p_a\times nDOF}$ defining the positions of the accelerometers. The value of p_{ds} is equal to the number of the displacement sensors (or the strain gauges), the value of p_v is equal

to the number of the velocity sensors, and the value of p_a is equal to the number of the acceleration sensors. The values of p , p_{ds} , p_v, and p_a fulfill the condition

$$p = p_{ds} + p_v + p_a. \tag{2.2}$$

Assume the damping matrix $\boldsymbol{C}_n$ can be expressed as

$$\boldsymbol{C}_n = \alpha \boldsymbol{M}_n + \beta \boldsymbol{K}_n, \tag{2.3}$$

where α is the constant of mass proportionality and β is the constant of stiffness proportionality. Equation (2.1) can be transformed to the canonical form (uncoupled modal equation)

$$\ddot{\boldsymbol{q}}_m(t) + \boldsymbol{C}_m \dot{\boldsymbol{q}}_m(t) + \boldsymbol{K}_m \boldsymbol{q}_m(t) = \boldsymbol{\Phi}^T \boldsymbol{f}(t), \tag{2.4}$$

with

$$\boldsymbol{q}_n(t) = \boldsymbol{\Phi} \boldsymbol{q}_m(t). \tag{2.5}$$

In equations (2.4) and (2.5), $\boldsymbol{q}_m(t) \in \mathbb{R}^{mDOF}$ represents the displacement vector in the modal coordinates, with the value of $mDOF$ fulfilling the condition $mDOF \leq nDOF$; and $\boldsymbol{\Phi} \in \mathbb{R}^{nDOF \times mDOF}$ is the modal matrix which is mass normalized so that the condition

$$\boldsymbol{\Phi}^T \boldsymbol{M}_n \boldsymbol{\Phi} = \boldsymbol{I}_{mDOF} \tag{2.6}$$

holds. The modal matrix $\boldsymbol{\Phi}$ has the form

$$\boldsymbol{\Phi} = \begin{bmatrix} \boldsymbol{\phi}_1 & \boldsymbol{\phi}_2 & \cdots & \boldsymbol{\phi}_{mDOF} \end{bmatrix}, \tag{2.7}$$

where $\boldsymbol{\phi}_i \in \mathbb{R}^{nDOF}$ represents the i -th column vector of $\boldsymbol{\Phi}$, with the value of i fulfilling the condition $1 \leq i \leq mDOF$. Matrix $\boldsymbol{C}_m$ represents the modal damping matrix and has the form

$$\boldsymbol{C}_m = \begin{bmatrix} 2\zeta_1\omega_1 & 0 & \cdots & 0 \\ 0 & 2\zeta_2\omega_2 & \cdots & 0 \\ \vdots & \vdots & \ddots & \vdots \\ 0 & 0 & \cdots & 2\zeta_{mDOF}\omega_{mDOF} \end{bmatrix}. \tag{2.8}$$

Matrix $\boldsymbol{K}_m$ denotes the modal stiffness matrix and has the form

$$\boldsymbol{K}_m = \begin{bmatrix} \omega_1^2 & 0 & \cdots & 0 \\ 0 & \omega_2^2 & \cdots & 0 \\ \vdots & \vdots & \ddots & \vdots \\ 0 & 0 & \cdots & \omega_{mDOF}^2 \end{bmatrix}. \tag{2.9}$$

In this thesis, $\boldsymbol{C}_m$ is named as modal damping matrix; and $\boldsymbol{K}_m$ is named as modal stiffness matrix. In equation (2.7), $\boldsymbol{\phi}_i$ represents the real mode shape vector. In equation (2.8), ζ_i denotes the damping ratio for the i-th mode. In equations (2.8) and (2.9), ω_i is the circular natural frequency for the i-th mode. The values for $\boldsymbol{\phi}_i$, ζ_i, and ω_i can be identified by using Experimental Modal Analysis (EMA) or Operational Modal Analysis (OMA). A brief review of the EMA and the OMA are provided in section 2.1.4 and section 2.1.5, respectively.

The force input vector $\boldsymbol{f}(t)$ in equations (2.1) and (2.4) can be represented by

$$\boldsymbol{f}(t) = \boldsymbol{B}_o \boldsymbol{d}(t), \tag{2.10}$$

where the i-th column of the matrix $\boldsymbol{B}_o \in \mathbb{R}^{nDOF \times m}$ describes the spatial distribution of the i-th force, and the i-th element of $\boldsymbol{d}(t) \in \mathbb{R}^m$ represents the weighting value of the spatial distribution of the i-th force in time.

2.1.2. Continuous-time state-space structural model

Define a state vector $\boldsymbol{x}(t) \in \mathbb{R}^n$

$$\boldsymbol{x}(t) = \begin{bmatrix} \boldsymbol{q}_m(t) \\ \dot{\boldsymbol{q}}_m(t) \end{bmatrix}. \tag{2.11}$$

The structural model which is described by equation (2.4) can be transformed to its state-space form

$$\dot{\boldsymbol{x}}(t) = \boldsymbol{A}_c \boldsymbol{x}(t) + \boldsymbol{G}_c \boldsymbol{d}(t) \tag{2.12}$$

and

$$\boldsymbol{y}(t) = \boldsymbol{C}_c \boldsymbol{x}(t) + \boldsymbol{H}_c \boldsymbol{d}(t), \tag{2.13}$$

where $\boldsymbol{A}_c$ represents the state transition matrix; $\boldsymbol{G}_c$ denotes the input matrix; $\boldsymbol{C}_c$ is the output matrix; $\boldsymbol{H}_c$ is the direct feed-through; and $\boldsymbol{y}(t) \in \mathbb{R}^p$ denotes the output vector;

The matrices $\boldsymbol{A}_c$, $\boldsymbol{G}_c$, $\boldsymbol{C}_c$, and $\boldsymbol{H}_c$ have the following forms (Gawronski, 2004),

$$\boldsymbol{A}_c = \begin{bmatrix} \boldsymbol{0}_{mDOF\times mDOF} & \boldsymbol{I}_{mDOF} \\ -\boldsymbol{K}_m & -\boldsymbol{C}_m \end{bmatrix}, \tag{2.14}$$

$$\boldsymbol{G}_c = \begin{bmatrix} \boldsymbol{0}_{mDOF\times m} \\ \boldsymbol{\Phi}^T\boldsymbol{B}_o \end{bmatrix}, \tag{2.15}$$

$$\boldsymbol{C}_c = \begin{bmatrix} \boldsymbol{C}_{ds}\boldsymbol{\Phi} & \boldsymbol{0}_{p_{ds}\times mDOF} \\ \boldsymbol{0}_{p_v\times mDOF} & \boldsymbol{C}_v\boldsymbol{\Phi} \\ -\boldsymbol{C}_a\boldsymbol{\Phi}\boldsymbol{K}_m & -\boldsymbol{C}_a\boldsymbol{\Phi}\boldsymbol{C}_m \end{bmatrix}, \tag{2.16}$$

and

$$\boldsymbol{H}_c = \begin{bmatrix} \boldsymbol{0}_{p_{ds}\times m} \\ \boldsymbol{0}_{p_v\times m} \\ \boldsymbol{C}_a\boldsymbol{\Phi}\boldsymbol{\Phi}^T\boldsymbol{B}_o \end{bmatrix}. \tag{2.17}$$

2.1.3. Discrete-time state-space structural model

The state-space model in equations (2.12) and (2.13) can be transformed into its discrete-time form

$$\boldsymbol{x}_{k+1} = \boldsymbol{A}_d\boldsymbol{x}_k + \boldsymbol{G}_d\boldsymbol{d}_k \tag{2.18}$$

and

$$\boldsymbol{y}_k = \boldsymbol{C}_d\boldsymbol{x}_k + \boldsymbol{H}_d\boldsymbol{d}_k, \tag{2.19}$$

where $\boldsymbol{x}_k$, $\boldsymbol{d}_k$, and $\boldsymbol{y}_k$ are the values of $\boldsymbol{x}(t)$, $\boldsymbol{d}(t)$, and $\boldsymbol{y}(t)$ at the time instant $t_k = k\triangle t$, respectively, with $\triangle t$ denoting the sampling interval. Matrices $\boldsymbol{A}_d$, $\boldsymbol{G}_d$, $\boldsymbol{C}_d$, and $\boldsymbol{H}_d$ are calculated with

$$\boldsymbol{A}_d = e^{\boldsymbol{A}_c\triangle t}, \tag{2.20}$$

$$\boldsymbol{G}_d = (\int_0^{\triangle t} e^{\boldsymbol{A}_c\eta}d\eta)\boldsymbol{G}_c, \tag{2.21}$$

$$\boldsymbol{C}_d = \boldsymbol{C}_c, \tag{2.22}$$

and

$$\boldsymbol{H}_d = \boldsymbol{H}_c. \tag{2.23}$$

2.1.4. Experimental Modal Analysis (EMA)

Experimental Modal Analysis (EMA) is a procedure of extracting the natural characteristics of a structure, i.e. natural frequencies, damping ratios, mode shapes, and modal participation factors, from the measured excitation and the measured structural responses (Avitabile, 2001). If the force $\boldsymbol{f}(t)$ and the response $\boldsymbol{y}(t)$ are both measurable, a dynamic model for the structure can be experimentally identified by using the EMA. This is a type of system identification problem which can be described by the block diagram in figure 2.1.

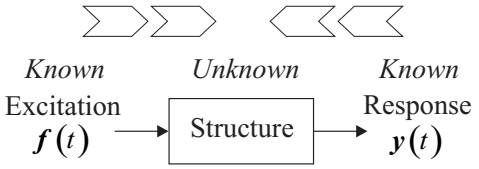

Figure 2.1. *System identification problem*

The block diagram in figure 2.1 can be mathematically represented by

$$\boldsymbol{Y}(s) = \boldsymbol{H}(s)\boldsymbol{F}(s), \tag{2.24}$$

where s denotes the Laplace variable; $\boldsymbol{F}(s)$ is the Laplace transform of $\boldsymbol{f}(t)$; $\boldsymbol{Y}(s)$ is the Laplace transform of $\boldsymbol{y}(t)$; and $\boldsymbol{H}(s)$ represents the transfer function of the structure.

If the condition

$$s = j\omega \tag{2.25}$$

holds, equation (2.24) can be expressed as

$$\boldsymbol{Y}(\omega) = \boldsymbol{H}(\omega)\boldsymbol{F}(\omega), \tag{2.26}$$

where ω denotes the circular frequency; $\boldsymbol{F}(\omega)$ is the Fourier transform of $\boldsymbol{f}(t)$; $\boldsymbol{Y}(\omega)$ is the Fourier transform of $\boldsymbol{y}(t)$; and $\boldsymbol{H}(\omega)$ represents the Frequency Response Function (FRF).

The standard steps of EMA are provided in the flowchart in figure 2.2 in which the FRF is the input to the modal parameter estimation algorithm. In order to remove the random noise and the nonlinearity, the FRF is actually calculated using the tri-spectrum averaging which is illustrated in figure 2.3.

In figure 2.3, FFT is the abbreviation of Fast Fourier Transform; APS is short for Auto Power Spectrum; and XPS denotes cross Power Spectrum. The Fourier transform assumes that the transform window captures the entire signal, or the measured data is periodic in the transform window. If it is not the case, a serious distortion will occur when the data is transformed to the frequency domain. This is called leakage. In order to minimize such distortion, windows which is also called weighting functions are often applied to

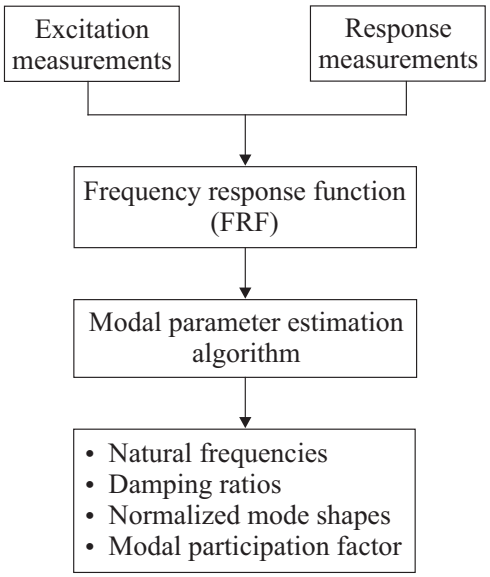

Figure 2.2. *Standard steps of EMA (De Silva, 2007)*

the data before performing FFT. In EMA, there are two commonly used types of input excitations: impact excitation and shaker excitation. Depending on the type of applied excitation signals, suitable windows need to be selected. For example, the force and exponential windows are often selected when an impact excitation is performed; and the Hanning window is usually considered when a random excitation is applied in a shaker testing. More details on the selection of windows may refer to e.g. Schwarz and Richardson (1999) and Avitabile (2001).

After calculating the average APS $\overline{G}_{yy}(\omega)$, the average APS $\overline{G}_{ff}(\omega)$, and the average XPS $\overline{G}_{yf}(\omega)$, an estimate of the FRF can be obtained.

In case that the extraneous noise and the randomly excited nonlinearity are added into the output, the FRF can be calculated by

$$H_1 = \frac{\overline{G}_{yf}(\omega)}{\overline{G}_{ff}(\omega)}. \tag{2.27}$$

It is proved that equation (2.27) provides the least-squares estimate of the FRF when the extraneous noise and randomly excited nonlinearities are modeled as Gaussian (Rocklin et al., 1985).

For the case that the noise is added to the input and the case that the noise is added to both the input and output, the corresponding estimates of the FRF can be found in Rocklin et al. (1985).

The degree of correlation of the response $\boldsymbol{y}(t)$ and the excitation $\boldsymbol{f}(t)$ is represented by the ordinary coherence function $C_{yf}(\omega)$ which can be calculated by

$$C_{yf}(\omega) = \frac{\left|\overline{G}_{yf}(\omega)\right|^2}{\overline{G}_{yy}(\omega)\overline{G}_{ff}(\omega)}, \tag{2.28}$$

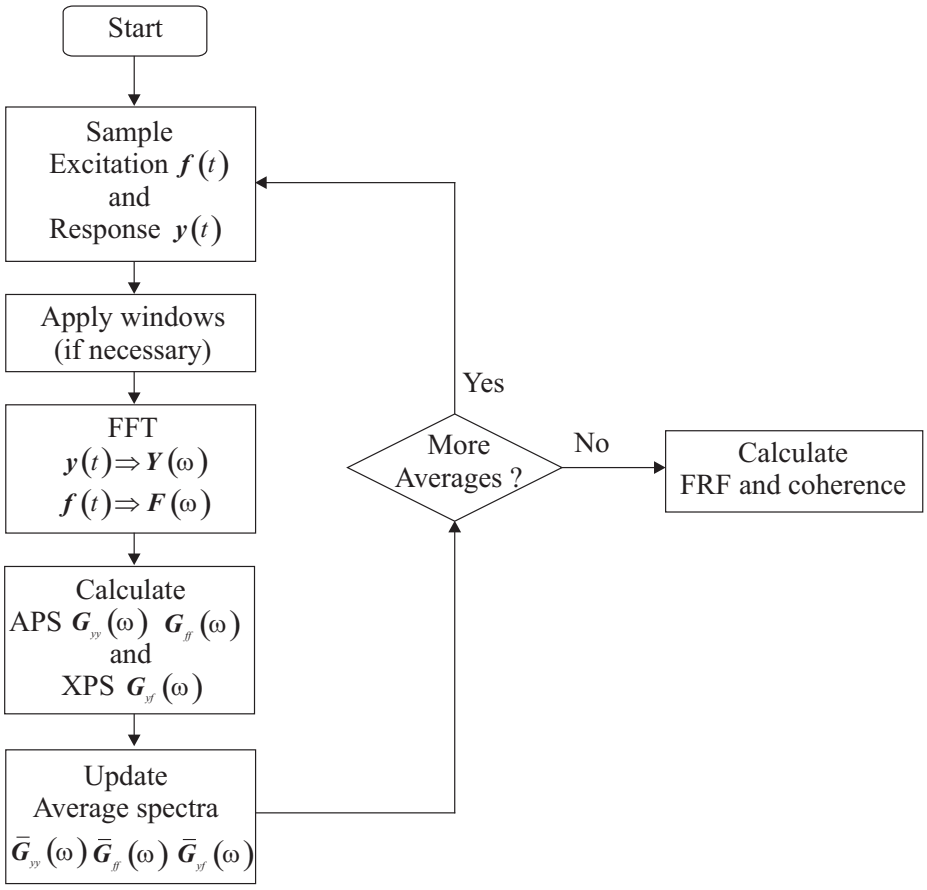

Figure 2.3. *Tri-spectrum averaging loop (Schwarz and Richardson, 1999)*

where the operator $|\cdot|$ denotes the Euclidean norm operator.

Assume that the zero initial condition holds for the structural model in section 2.1.1, the Laplace transform of equation (2.4) leads to

$$\boldsymbol{Q}_m(s) = \begin{bmatrix} \frac{1}{s^2+2\zeta_1\omega_1 s+\omega_1^2} & 0 & \cdots & 0 \\ 0 & \frac{1}{s^2+2\zeta_2\omega_2 s+\omega_2^2} & \cdots & 0 \\ \vdots & \vdots & \ddots & \vdots \\ 0 & 0 & \cdots & \frac{1}{s^2+2\zeta_{mDOF}\omega_{mDOF} s+\omega_{mDOF}^2} \end{bmatrix} \boldsymbol{\Phi}^T \boldsymbol{F}(s), \quad (2.29)$$

where $\boldsymbol{Q}_m(s)$ is the Laplace transform of $\boldsymbol{q}_m(t)$. Performing Laplace transform on equation (2.5) leads to

$$\boldsymbol{Q}_n(s) = \boldsymbol{\Phi}\boldsymbol{Q}_m(s), \quad (2.30)$$

where $\boldsymbol{Q}_n(s)$ is the Laplace transform of $\boldsymbol{q}_n(t)$. Substituting equation (2.29) into equation (2.30) leads to

$$\boldsymbol{Q}_n(s) = \boldsymbol{H}_{nf}(s)\boldsymbol{F}(s), \quad (2.31)$$

where $\boldsymbol{H}_{nf}(s)$ denotes the transfer function and has the form

$$\boldsymbol{H}_{nf}(s) = \boldsymbol{\Phi} \begin{bmatrix} \frac{1}{s^2+2\zeta_1\omega_1 s+\omega_1^2} & 0 & \cdots & 0 \\ 0 & \frac{1}{s^2+2\zeta_2\omega_2 s+\omega_2^2} & \cdots & 0 \\ \vdots & \vdots & \ddots & \vdots \\ 0 & 0 & \cdots & \frac{1}{s^2+2\zeta_{mDOF}\omega_{mDOF} s+\omega_{mDOF}^2} \end{bmatrix} \boldsymbol{\Phi}^T. \quad (2.32)$$

Denote the qr-th element of $\boldsymbol{H}_{nf}(s)$ as $H_{nf\_qr}(s)$ which defines the transfer characteristics between the force input in the r-th DOF in the nodal coordinates and the displacement of the q-th DOF in the nodal coordinates. The analytical expression of $H_{nf\_qr}(s)$ appears as

$$H_{nf\_qr}(s) = \sum_{i=1}^{mDOF} \frac{\phi_{q,i}\phi_{r,i}}{s^2 + 2\zeta_i\omega_i s + \omega_i^2}, \quad (2.33)$$

where $\phi_{q,i}$ denotes the q-th element of the real mode shape vector $\boldsymbol{\phi}_i$, and $\phi_{r,i}$ denotes the r-th element of the real mode shape vector $\boldsymbol{\phi}_i$. Detailed steps on the derivation of equation (2.33) can be found in e.g. De Silva (2007).

By substituting equation (2.25) into equation (2.33), the analytical expression of the FRF $H_{nf\_qr}(\omega)$ appears as

$$H_{nf\_qr}(\omega) = \sum_{i=1}^{mDOF} \frac{\phi_{q,i}\phi_{r,i}}{-\omega^2 + j2\zeta_i\omega_i\omega + \omega_i^2}. \quad (2.34)$$

In equation (2.34), the circular natural frequencies ω_i , the modal damping ratios ζ_i, and the elements in the real mode shape vectors $\boldsymbol{\phi}_i$ can be estimated by minimizing the squared error between the experimentally calculated FRF from the tri-spectrum averaging and the analytical expression of FRF in equation (2.34). This modal parameter estimation process is named as curve fitting (Schwarz and Richardson, 1999). There are many different curve fitting (or modal parameter estimation) algorithms. All these available algorithms can be grouped into the following four categories.

- Local SDOF.
- Local MDOF.
- Global.
- Multi-Reference (Poly-Reference).

SDOF denotes single degree of freedom; and MDOF represents multiple degrees of freedom. These four categories are organized in the order of increasing complexity. The SDOF methods can estimate the modal parameters of only one mode at a time, while the MDOF, Global and Multi-Reference (Poly-Reference) methods can estimate the modal

parameters of two or more modes at a time. The Local methods can be applied to only one FRF at a time, while the Global and Multi-Reference (Poly-Reference) methods are applicable to the entire set of FRFs at a time. Furthermore, the Multi-Reference (Poly-Reference) methods have the ability to identify very closely coupled modes (Schwarz and Richardson, 1999).

In this thesis, the PolyMAX method, which is shipped with LMS Test.Lab®, is applied for the EMA. The PolyMAX method is also called Poly-reference least-squares complex frequency-domain method, and it belongs to the Multi-Reference (Poly-Reference) category. More details on the PolyMAX algorithm can be found in e.g. Guillaume et al. (2003).

2.1.5. Operational Modal Analysis (OMA)

The EMA is an often-used tool in extracting modal parameters. However, it still has some limitations in some practical application cases.

- In EMA, an artificially applied force is usually needed to excite the structure and to measure the inputs. This is very difficult or not possible in field tests or for large-scale structures.
- The EMA is often performed in the lab environment which may differ from the real operational conditions of the structure.
- In EMA, it is often the component, not the complete system, to be tested. This requires the boundary conditions to be well concerned.

Operational Modal Analysis (OMA), which is also known as output-only modal analysis, is a group of modal parameter estimation methods, which use only structural reponse measurements that are recorded under operational rather than laboratory conditions.

Expressing equation (2.26) in the form of Power Spectra Density (PSD) leads to

$$\boldsymbol{G}_{yy}(\omega) = \boldsymbol{H}(\omega)\boldsymbol{G}_{ff}(\omega)\boldsymbol{H}^{*}(\omega), \tag{2.35}$$

where $\boldsymbol{G}_{ff}(\omega)$ denotes the cross power spectral density matrix of the excitation $\boldsymbol{f}(t)$; $\boldsymbol{G}_{yy}(\omega)$ is the cross power spectral density matrix of the response $\boldsymbol{y}(t)$; and $\boldsymbol{H}^{*}(\omega)$ represents the conjugate transpose of $\boldsymbol{H}(\omega)$. In OMA, the excitation is modelled as stochastic white noise, which indicates that $\boldsymbol{G}_{ff}(\omega)$ is assumed to be constant with respect to ω, and $\boldsymbol{G}_{yy}(\omega)$ contains all the information for estimating natural frequencies, damping ratios and mode shapes. Zhang et al. (2005) provides an overview on the OMA; Peeters et al. (2006) discuss the evolution and the applications of the OMA from an industry point of view; Reynders (2012) reviews and compares different OMA approaches in an extensive Monte Carlo simulation. Compared with EMA, OMA mainly has the following advantages (Zhang et al., 2005).

- In OMA, the artificial excitation is not needed.
- With OMA, the dynamic characteristics of the complete system, instead of the component, can be obtained under real boundary conditions and at much more representative working points.
- With OMA, the closely-spaced or repeated modes can be identified, which is very suitable for real world complex structures.

All these advantages above make OMA a good complement to EMA.

Kraemer and Fritzen (2010) proposed a Vector AutoRegressive models (ARV) method and applied it in the study of dynamic characteristics of offshore wind energy plants. In this thesis, this ARV method is adopted for OMA. To support the discussion in later chapters, a brief review of the ARV method is provided below.

The measurements $\boldsymbol{y}_k \in \mathbb{R}^p$ can be modeled by

$$\boldsymbol{y}_k = \boldsymbol{b}_{arv} + \sum_{l=1}^{h} \boldsymbol{A}_{arv,l} \boldsymbol{y}_{l-1} + \boldsymbol{\varepsilon}_{arv,k}, \tag{2.36}$$

where h is the order of this AR model; $\boldsymbol{A}_{arv,l} \in \mathbb{R}^{p \times p}$ are the coefficient matrices of the AR model, with the value of l fulfilling the condition $1 \leq l \leq h$; $\boldsymbol{b}_{arv} \in \mathbb{R}^p$ is an intercept vector; and $\boldsymbol{\varepsilon}_{arv,k} \in \mathbb{R}^p$ is assumed to be an uncorrelated zero-mean random vector, representing the residual between the real measurements and the AR model. Assuming $\boldsymbol{b}_{arv}$ is a zero vector, the h-th order AR model, named as AR(h), can be transformed to the state-space form

$$\boldsymbol{x}_{arv,k+1} = \boldsymbol{A}_{arv} \boldsymbol{x}_{arv,k} + \boldsymbol{w}_{arv,k} \tag{2.37}$$

and

$$\boldsymbol{y} = \boldsymbol{C}_{arv} \boldsymbol{x}_{arv,k}, \tag{2.38}$$

where $\boldsymbol{x}_{arv,k} \in \mathbb{R}^{ph}$, $\boldsymbol{A}_{arv} \in \mathbb{R}^{ph \times ph}$, $\boldsymbol{w}_{arv,k} \in \mathbb{R}^{ph}$, and $\boldsymbol{C}_{arv} \in \mathbb{R}^{p \times ph}$ are expressed by

$$\boldsymbol{x}_{arv,k} = \begin{bmatrix} \boldsymbol{y}_k \\ \boldsymbol{y}_{k-1} \\ \vdots \\ \boldsymbol{y}_{k-h+1} \end{bmatrix}, \tag{2.39}$$

$$\boldsymbol{A}_{arv} = \begin{bmatrix} \boldsymbol{A}_{arv,1} & \boldsymbol{A}_{arv,2} & \cdots & \boldsymbol{A}_{arv,(h-1)} & \boldsymbol{A}_{arv,h} \\ \boldsymbol{I}_p & \boldsymbol{0} & \cdots & \boldsymbol{0} & \mathbf{0} \\ \boldsymbol{0} & \boldsymbol{I}_p & \cdots & \boldsymbol{0} & \boldsymbol{0} \\ \vdots & \vdots & \ddots & \vdots & \vdots \\ \boldsymbol{0} & \mathbf{0} & \cdots & \boldsymbol{I}_p & \boldsymbol{0} \end{bmatrix}, \tag{2.40}$$

$$\boldsymbol{w}_{arv,k} = \begin{bmatrix} \boldsymbol{\varepsilon}_{arv,k+1} \\ \boldsymbol{0}_{p\times p} \\ \vdots \\ \boldsymbol{0}_{p\times p} \end{bmatrix}, \tag{2.41}$$

and

$$\boldsymbol{C}_{arv} = \begin{bmatrix} \boldsymbol{I}_p & \mathbf{0}_{p\times p} & \cdots & \boldsymbol{0}_{p\times p} \end{bmatrix}. \tag{2.42}$$

In equation (2.40), the coefficient matrices $\boldsymbol{A}_{arv,l}$ are estimated with the help of the ARFIT MATLAB® package which is presented in Schneider and Neumaier (2001) and Neumaier and Schneider (2001). The dynamic characteristics of the investigated structure can be extracted by solving

$$\boldsymbol{A}_{arv} = \boldsymbol{\Psi}_{arv}\boldsymbol{\Lambda}_{arv}\boldsymbol{\Psi}_{arv}^T, \tag{2.43}$$

where $\boldsymbol{\Lambda}_{arv} \in \mathbb{R}^{(ph)\times(ph)}$ is a diagonal matrix of the associated discrete-time eigenvalues $\lambda_{d,h,i}$, $i = 1, \cdots, hp$, and $\boldsymbol{\Psi}_{arv} \in \mathbb{R}^{(ph)\times(ph)}$ contains the corresponding eigenvectors $\boldsymbol{\psi}_{arv,i}$ in its i-th column. With

$$\lambda_{c,h,i} = \frac{ln(\lambda_{d,h,i})}{\triangle t}, \tag{2.44}$$

the discrete-time eigenvalue $\lambda_{d,h,i}$ can be transformed to its continuous-time counterpart $\lambda_{c,h,i}$. In equation (2.44), $\triangle t$ denotes the sampling interval. For the i-th mode of the h-th order AR model in equation (2.36), the natural frequency $f_{h,i}$, the damping ratio $\zeta_{h,i}$ and the complex mode shape vector $\boldsymbol{\psi}_{h,i} \in \mathbb{C}^p$ can be calculated with

$$\lambda_{c,h,i} = -\zeta_{h,i}\omega_{h,i} + j\omega_{h,i}\sqrt{1-\zeta_{h,i}^2}, \tag{2.45}$$

$$f_{h,i} = \frac{|\lambda_{c,h,i}|}{2\pi}, \tag{2.46}$$

$$\zeta_{h,i} = -\frac{Re(\lambda_{c,h,i})}{|\lambda_{c,h,i}|}, \tag{2.47}$$

and

$$\boldsymbol{\psi}_{h,i} = \begin{bmatrix} \mathbf{0}_{p\times p}, & \cdots, & \boldsymbol{0}_{p\times p}, & \boldsymbol{I}_p \end{bmatrix} \boldsymbol{\psi}_{arv,i}. \tag{2.48}$$

As aforementioned, the ARV method is a parametric method. An advantage of the parametric methods is that a so-called stabilization diagram can be constructed to objectively seperate the physical modes from the spurious ones which are caused by noise and numerical errors. To construct the stabilization diagram, three criteria are applied, including the percentage frequency difference f_{diff}, the percentage damping ratio difference ζ_{diff}, and the Modal Assurance Criterion (MAC) value between the modal properties from the AR(h) model and those from the AR($h-1$) model. f_{diff}, ζ_{diff}, and MAC are defined as

$$f_{diff} = \frac{|f_{h,q} - f_{h-1,r}|}{f_{h-1,r}} \leq f_{tol}, \tag{2.49}$$

$$\zeta_{diff} = \frac{|\zeta_{h,q} - \zeta_{h-1,r}|}{\zeta_{h-1,r}} \leq d_{tol}, \tag{2.50}$$

and

$$MAC = \frac{(\boldsymbol{\varphi}_{h,q}^T \boldsymbol{\varphi}_{h-1,r}^*)^2}{(\boldsymbol{\varphi}_{h,q}^T \boldsymbol{\varphi}_{h,q}^*)(\boldsymbol{\varphi}_{h-1,r}^T \boldsymbol{\varphi}_{h-1,r}^*)} \geq MAC_{tol}, \tag{2.51}$$

where $(\cdot)^T$ represents the transpose operator and $(\cdot)^*$ denotes the conjugate operator. In equations (2.49) through (2.51), the conditions $h \geq 2$, $1 \leq q \leq ph$, and $1 \leq r \leq p(h-1)$ hold.

The mode shape vectors which are identified from the EMA fulfills the orthogonality condition in equation (2.6). This means the model in equation (2.4) can be assembled using the EMA results. However, it is not the case for the OMA, because the identified mode shape vectors are not correctly scaled. This is due to the missing excitation information in OMA. Fortunately, a Finite Element (FE) model is often available for a complicated or large-scale structure. The scaled mode shape vectors, which fulfill the othogonality condition in equation (2.6), can be obtained from the updated FE model of the structure.

2.1.6. Model updating

Model updating is defined as the process of quantifying the discrepancy between the analytical prediction from the Finite Element Analysis (FEA) and the test results, and then adjusing certain parameters in the FE model to obtain a valid and reliable model which is capable of representing the dynamics of the real structure (Dascotte, 2007; Mottershead et al., 2011). The principle which is adopted in this thesis for model updating is described below.

For the i-th mode of a structure, define $f_{a,i}$ as the natural frequency from FEA, $f_{e,i}$ the experimentally identified natural frequency, $\boldsymbol{\phi}_{a,i}$ the mode shape vector from FEA, and $\boldsymbol{\phi}_{e,i}$ the experimentally identified mode shape vector. For the i-th mode, $r_{f,i}$ represents

the residual of the natural frequency, and $r_{\phi,i}$ denotes the residual of the mode shape. The value of $r_{f,i}$ can be calculated with

$$r_{f,i} = \frac{|f_{e,i} - f_{a,i}|}{f_{e,i}}. \tag{2.52}$$

The value of $r_{\phi,i}$ can be obtained with

$$r_{\phi,i} = 1 - \frac{(\boldsymbol{\phi}_{a,i}^T \boldsymbol{\phi}_{e,i}^*)^2}{(\boldsymbol{\phi}_{a,i}^T \boldsymbol{\phi}_{a,i}^*)(\boldsymbol{\phi}_{e,i}^T \boldsymbol{\phi}_{e,i}^*)}. \tag{2.53}$$

Define $\boldsymbol{r}_f$ as the residual vector of natural frequency, and $\boldsymbol{r}_\phi$ as and the residual vector of mode shape. The vector $\boldsymbol{r}_f$ can be assembled as

$$\boldsymbol{r}_f = \begin{bmatrix} r_{f,1}, & r_{f,2}, & \cdots, & r_{f,i}, & \cdots, & r_{f,mDOF} \end{bmatrix}^T. \tag{2.54}$$

The vector $\boldsymbol{r}_\phi$ has the form

$$\boldsymbol{r}_\phi = \begin{bmatrix} r_{\phi,1}, & r_{\phi,2}, & \cdots, & r_{\phi,i}, & \cdots, & r_{\phi,mDOF} \end{bmatrix}^T. \tag{2.55}$$

Introduce the objective function

$$J = J_r + \lambda^2 J_\theta, \tag{2.56}$$

where J_r and J_θ are calculated with

$$J_r = \begin{bmatrix} \boldsymbol{r}_f^T & \boldsymbol{r}_\phi^T \end{bmatrix} \begin{bmatrix} \boldsymbol{W}_f & \boldsymbol{0}_{mDOF \times mDOF} \\ \boldsymbol{0}_{mDOF \times mDOF} & \boldsymbol{W}_\phi \end{bmatrix} \begin{bmatrix} \boldsymbol{r}_f \\ \boldsymbol{r}_\phi \end{bmatrix} \tag{2.57}$$

and

$$J_\theta = \triangle\boldsymbol{\theta}^T \triangle\boldsymbol{\theta}. \tag{2.58}$$

In equation (2.56), J_r denotes the measurement residual; J_θ represents the side constraint; and λ is the regularization parameter. In equation (2.57), $\boldsymbol{W}_f \in \mathbb{R}^{mDOF \times mDOF}$ denotes the weighting matrix for $\boldsymbol{r}_f$, and $\boldsymbol{W}_\phi \in \mathbb{R}^{mDOF \times mDOF}$ represents the weighting matrix for $\boldsymbol{r}_\phi$. In equation (2.58), $\triangle\boldsymbol{\theta}$ represents the change of the updating parameters. The FE model is updated by minimizing the objective function J.

2.2. Observer

For state control design it is assumed that the system state is available for feedback. However, in many cases this assumption is rarely satisfied. Either the cost of sensors for

measuring the state may be prohibitive, or it is even not possible to physically measure the state. An approach which accounts for this issue is to design a system which can provide an estimate of the system state. When such designed system is in a deterministic setting, it is called an observer. In 1964, David G. Luenberger first proposed and developed the observer (also named as Luenberger observer) which can estimate the system state using the output measurements (Luenberger, 1964).

Consider a system which is described by

$$\dot{\boldsymbol{x}}(t) = \boldsymbol{A}_c x(t) + \boldsymbol{B}_c u(t) \tag{2.59}$$

and

$$\boldsymbol{y}(t) = \boldsymbol{C}_c x(t), \tag{2.60}$$

where $\boldsymbol{x}(t) \in \mathbb{R}^n$ denotes the system state; $\boldsymbol{u}(t) \in \mathbb{R}^r$ represents the known control input vector; $\boldsymbol{y}(t) \in \mathbb{R}^p$ is the output; and $\boldsymbol{A}_c$, $\boldsymbol{B}_c$, and $\boldsymbol{C}_c$ are the system matrices with appropriate dimensions.

The observer is described by

$$\dot{\hat{\boldsymbol{x}}}(t) = \boldsymbol{A}_c \hat{\boldsymbol{x}}(t) + \boldsymbol{B}_c \boldsymbol{u}(t) + \boldsymbol{L}_c (\boldsymbol{y}(t) - \boldsymbol{C}_c \hat{\boldsymbol{x}}(t)) \tag{2.61}$$

and

$$\hat{\boldsymbol{y}}(t) = \boldsymbol{C}_c \hat{\boldsymbol{x}}(t), \tag{2.62}$$

where $\hat{\boldsymbol{x}}(t) \in \mathbb{R}^n$ denotes the estimate of the system state $\boldsymbol{x}(t)$, $\hat{\boldsymbol{y}}(t) \in \mathbb{R}^p$ represents the estimate of the system output $\boldsymbol{y}(t)$, and $\boldsymbol{L}_c \in \mathbb{R}^{n \times p}$ is the gain matrix which needs to be designed.

The operation of the observer can be illustrated by the block diagram in figure 2.4. It can be seen that the inaccessible system state within the dynamic system becomes accessible with the help of the observer.

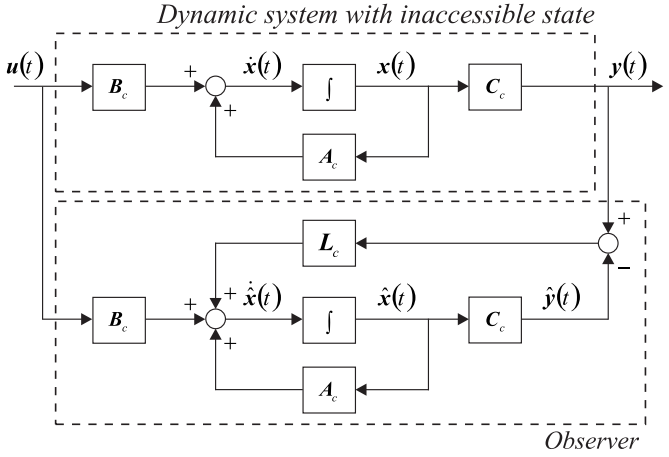

Figure 2.4. *Description of the observer in the form of a block diagram (Luenberger, 1964)*

Define the state estimate error $\tilde{\boldsymbol{x}}(t) \in \mathbb{R}^n$

$$\tilde{\boldsymbol{x}}(t) = \boldsymbol{x}(t) - \hat{\boldsymbol{x}}(t). \tag{2.63}$$

The dynamics of $\tilde{\boldsymbol{x}}(t)$ can be described by

$$\dot{\tilde{\boldsymbol{x}}}(t) = (\boldsymbol{A}_c - \boldsymbol{L}_c\boldsymbol{C}_c)\,\tilde{\boldsymbol{x}}(t). \tag{2.64}$$

If a gain matrix $\boldsymbol{L}_c$ exists so that the eigenvalues of the matrix $(\boldsymbol{A}_c - \boldsymbol{L}_c\boldsymbol{C}_c)$ are all on the Left Half-Plane (LHP), $\tilde{\boldsymbol{x}}(t)$ will decay to zero independant of the initial condition of $\hat{\boldsymbol{x}}(t)$. The observer can be designed to have arbitrary dynamics if and only if the system in equations (2.59) and (2.60) is observable. More details on the derivation of equation (2.64) and the observer design can be found in e.g. Luenberger (1971) and Franklin et al. (2006).

2.3. Unknown Input Observer (UIO)

Yang and Wilde (1988) proposed a direct design procedure for a type of full-order observer for linear systems with unknown inputs. Darouach et al. (1994) showed that the design for this type of full-order observer can be reduced to the Luenberger observer design. Darouach (2009) further generalized his earlier work by considering the unknown inputs appearing in both state equation and output equation. This type of full-order observer is called Unknown Input Observer (UIO). The UIO is also named as robust observer (O'Reilly, 1983).

Consider the system

$$\dot{\boldsymbol{x}}(t) = \boldsymbol{A}_c\boldsymbol{x}(t) + \boldsymbol{B}_c\boldsymbol{u}(t) + \boldsymbol{G}_c\boldsymbol{d}(t) \tag{2.65}$$

and

$$\boldsymbol{y}(t) = \boldsymbol{C}_c\boldsymbol{x}(t) + \boldsymbol{H}_c\boldsymbol{d}(t), \tag{2.66}$$

where $\boldsymbol{x}(t) \in \mathbb{R}^n$ denotes the state; $\boldsymbol{u}(t) \in \mathbb{R}^r$ represents the (known) control input; $\boldsymbol{d}(t) \in \mathbb{R}^m$ is the disturbance (unknown input); $\boldsymbol{y}(t) \in \mathbb{R}^p$ is the output; and $\boldsymbol{A}_c$, $\boldsymbol{B}_c$, $\boldsymbol{G}_c$, $\boldsymbol{C}_c$, and $\boldsymbol{H}_c$ are the system matrices with appropriate dimensions.

The UIO has the form

$$\dot{\boldsymbol{\xi}}(t) = \boldsymbol{N}_{uio}\boldsymbol{\xi}(t) + \boldsymbol{L}_{uio}\boldsymbol{y}(t) + \boldsymbol{H}_{uio}\boldsymbol{d}(t) \tag{2.67}$$

and

$$\hat{\boldsymbol{x}}(t) = \boldsymbol{\xi}(t) + \boldsymbol{Q}_{uio}\boldsymbol{y}(t), \tag{2.68}$$

where $\boldsymbol{\xi}(t) \in \mathbb{R}^n$ denotes the state vector in the UIO; $\hat{\boldsymbol{x}}(t) \in \mathbb{R}^n$ is the estimate of $\boldsymbol{x}(t)$; and $\boldsymbol{N}_{uio}$, $\boldsymbol{L}_{uio}$, and $\boldsymbol{Q}_{uio}$ are the matrices which need to be determined. The UIO can be

described by the block diagram in figure 2.5.

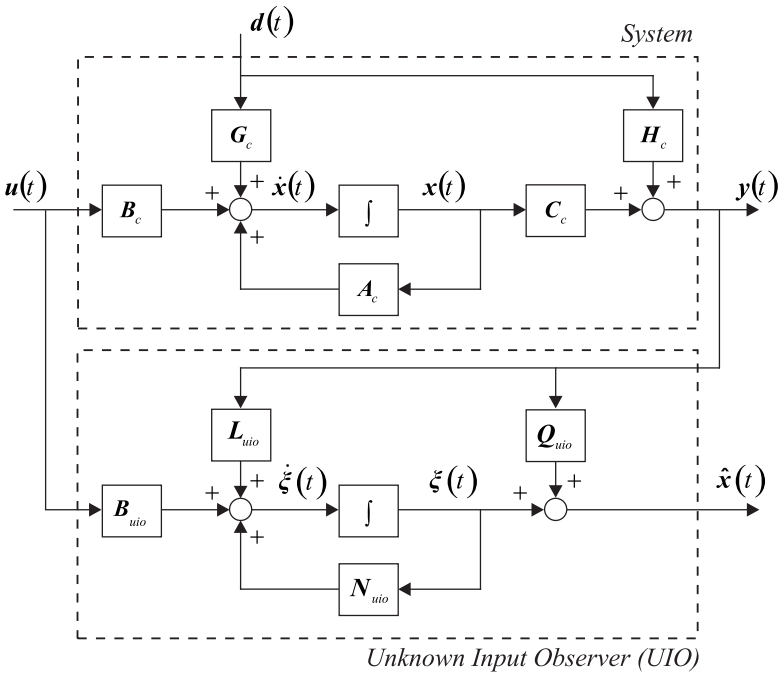

Figure 2.5. *Description of the UIO in the form of a block diagram (O'Reilly, 1983)*

Define matrix $\boldsymbol{P}_{uio}$ as

$$\boldsymbol{P}_{uio} = \boldsymbol{I} - \boldsymbol{Q}_{uio}\boldsymbol{C}_c. \tag{2.69}$$

The full-order UIO in equations (2.67) and (2.68) will estimate (asymptotically) $\boldsymbol{x}(t)$ if all the following conditions hold.

(1) The eigenvalues of matrix $\boldsymbol{N}_{uio}$ are all on the LHP.

(2) Condition $\boldsymbol{P}_{uio}\boldsymbol{A}_c - \boldsymbol{N}_{uio}\boldsymbol{P}_{uio} - \boldsymbol{L}_{uio}\boldsymbol{C}_c = \boldsymbol{0}$ holds.

(3) Condition $\boldsymbol{P}_{uio}\boldsymbol{G}_c + \boldsymbol{N}_{uio}\boldsymbol{Q}_{uio}\boldsymbol{H}_c - \boldsymbol{L}_{uio}\boldsymbol{H}_c = \boldsymbol{0}$ holds.

(4) Condition $\boldsymbol{Q}_{uio}\boldsymbol{H}_c = \boldsymbol{0}$ holds.

(5) Condition $\boldsymbol{H}_{uio} = \boldsymbol{P}_{uio}\boldsymbol{B}_c$ holds

Introduce the matrices

$$\boldsymbol{\Sigma}_{uio} = \begin{bmatrix} \boldsymbol{C}_c\boldsymbol{G}_c & \boldsymbol{H}_c \\ \boldsymbol{H}_c & \boldsymbol{0} \end{bmatrix}, \tag{2.70}$$

$$\boldsymbol{\Theta}_{uio} = \begin{bmatrix} -\boldsymbol{G}_c & \boldsymbol{0} \end{bmatrix}, \tag{2.71}$$

$$\boldsymbol{A}_{uio} = \boldsymbol{A}_c + \boldsymbol{\Theta}_{uio}\boldsymbol{\Sigma}_{uio}^{+} \begin{bmatrix} \boldsymbol{C}_c\boldsymbol{A}_c \\ \boldsymbol{C}_c \end{bmatrix}, \tag{2.72}$$

and

$$\boldsymbol{C} = \left(\boldsymbol{I} - \boldsymbol{\Sigma}_{uio}\boldsymbol{\Sigma}_{uio}^{+}\right)\begin{bmatrix}\boldsymbol{C}_c\boldsymbol{A}_c \\ \boldsymbol{C}_c\end{bmatrix}, \tag{2.73}$$

where $\boldsymbol{\Sigma}_{uio}^{+}$ denotes the left inverse of $\boldsymbol{\Sigma}_{uio}$. Define the state estimate error $\tilde{\boldsymbol{x}}(t)$ as

$$\tilde{\boldsymbol{x}}(t) = \boldsymbol{x}(t) - \hat{\boldsymbol{x}}(t). \tag{2.74}$$

The dynamics of $\tilde{\boldsymbol{x}}(t)$ can be described by

$$\dot{\tilde{\boldsymbol{x}}}(t) = \left(\boldsymbol{A}_{uio} - \boldsymbol{Z}_{uio}\boldsymbol{C}_{uio}\right)\tilde{\boldsymbol{x}}(t). \tag{2.75}$$

If a gain matrix $\boldsymbol{Z}_{uio}$ exists so that the eigenvalues of the matrix $(\boldsymbol{A}_{uio} - \boldsymbol{Z}_{uio}\boldsymbol{C}_{uio})$ are all on the LHP, $\tilde{\boldsymbol{x}}(t)$ will decay to zero independent of the initial condition of $\hat{\boldsymbol{x}}(t)$. More details on the derivation of equation (2.75) and the UIO design can be found in Darouach (2009).

2.4. Kalman filter

Kalman (1960) published a recursive solution to estimate the system state. The recursive nature of this solution makes it very practical for implementation. Together with the advances of digital computing, this recursive solution was extensively studied and found itself in many applications, e.g. navigation (Maybeck, 1979; Brown and Hwang, 1997). This recursive solution is named as Kalman filter.

Consider the disrete-time time-variant stochastic system

$$\boldsymbol{x}_{k+1} = \boldsymbol{A}_k\boldsymbol{x}_k + \boldsymbol{B}_k\boldsymbol{u}_k + \boldsymbol{\Upsilon}_k\boldsymbol{w}_k \tag{2.76}$$

and

$$\boldsymbol{y}_k = \boldsymbol{C}_k\boldsymbol{x}_k + \boldsymbol{v}_k, \tag{2.77}$$

where $\boldsymbol{x}_k \in \mathbb{R}^n$ denotes the state; $\boldsymbol{u}_k \in \mathbb{R}^r$ is the control (known) input; $\boldsymbol{y}_k \in \mathbb{R}^p$ is the output; $\boldsymbol{w}_k \in \mathbb{R}^m$ is the process noise; $\boldsymbol{v}_k \in \mathbb{R}^p$ is the measurement noise; and $\boldsymbol{A}_k$, $\boldsymbol{B}_k$, $\boldsymbol{\Upsilon}_k$, and $\boldsymbol{C}_k$ are matrices with appropriate dimensions.

Assume $\boldsymbol{w}_k$ and $\boldsymbol{v}_k$ are zero-mean Gaussian white-noise processes, which means the conditions

$$E\left[\boldsymbol{w}_k\boldsymbol{w}_j^T\right] = \begin{cases}\boldsymbol{0} & k \neq j \\ \boldsymbol{Q}_k & k = j\end{cases} \tag{2.78}$$

and

$$E\left[\boldsymbol{v}_k\boldsymbol{v}_j^T\right] = \begin{cases} \boldsymbol{0} & k \neq j \\ \boldsymbol{R}_k & k = j \end{cases} \tag{2.79}$$

hold. In equations (2.78) and (2.79), $E[\cdot]$ represents the expectation operator, $\boldsymbol{Q}_k$ denotes the covariance matrix of the process noise $\boldsymbol{w}_k$, and $\boldsymbol{R}_k$ is the covariance matrix of the measurement noise $\boldsymbol{v}_k$. $\boldsymbol{w}_k$ and $\boldsymbol{v}_k$ are assumed mutually uncorrelated.

Define $\hat{\boldsymbol{x}}_{k|k-1} \in \mathbb{R}^n$ as the *a priori* state estimate at the step k using the information of the process priori to the step k; $\hat{\boldsymbol{x}}_{k|k} \in \mathbb{R}^n$ as the *a posteriori* state estimate at the step k using the measurement $\boldsymbol{y}_k$; $\tilde{\boldsymbol{x}}_{k|k-1} \in \mathbb{R}^n$ as the *a priori* state estimate error; $\tilde{\boldsymbol{x}}_{k|k} \in \mathbb{R}^n$ as the *a posteriori* state estimate error; $\boldsymbol{P}^x_{k|k-1}$ the covariance of $\tilde{\boldsymbol{x}}_{k|k-1}$; and $\boldsymbol{P}^x_{k|k}$ the covariance of $\tilde{\boldsymbol{x}}_{k|k}$. The definition for $\tilde{\boldsymbol{x}}_{k|k-1}$, $\tilde{\boldsymbol{x}}_{k|k}$, $\boldsymbol{P}^x_{k|k-1}$ and $\boldsymbol{P}^x_{k|k}$ are given as

$$\tilde{\boldsymbol{x}}_{k|k-1} = \boldsymbol{x}_k - \hat{\boldsymbol{x}}_{k|k-1}, \tag{2.80}$$

$$\tilde{\boldsymbol{x}}_{k|k} = \boldsymbol{x}_k - \hat{\boldsymbol{x}}_{k|k}, \tag{2.81}$$

$$\boldsymbol{P}^x_{k|k-1} = E\left[\tilde{\boldsymbol{x}}_{k|k-1}\tilde{\boldsymbol{x}}^T_{k|k-1}\right], \tag{2.82}$$

and

$$\boldsymbol{P} = E\left[\tilde{\boldsymbol{x}}_{k|k}\tilde{\boldsymbol{x}}^T_{k|k}\right]. \tag{2.83}$$

The discrete-time Kalman filter is comprised by

$$\hat{\boldsymbol{x}}_{k|k-1} = \boldsymbol{A}_{k-1}\hat{\boldsymbol{x}}_{k-1|k-1} + \boldsymbol{B}_{k-1}\boldsymbol{u}_{k-1}, \tag{2.84}$$

$$\boldsymbol{P}^x_{k|k-1} = \boldsymbol{A}_{k-1}\boldsymbol{P}^x_{k-1|k-1}\boldsymbol{A}^T_{k-1} + \boldsymbol{\Upsilon}_{k-1}\boldsymbol{Q}_{k-1}\boldsymbol{\Upsilon}^T_{k-1}, \tag{2.85}$$

$$\boldsymbol{K}_k = \boldsymbol{P}^x_{k|k-1}\boldsymbol{C}^T_k\left(\boldsymbol{C}_k\boldsymbol{P}^x_{k|k-1}\boldsymbol{C}^T_k + \boldsymbol{R}_k\right)^{-1}, \tag{2.86}$$

$$\hat{\boldsymbol{x}}_{k|k} = \hat{\boldsymbol{x}}_{k|k-1} + \boldsymbol{K}_k\left(\boldsymbol{y}_k - \boldsymbol{C}_k\hat{\boldsymbol{x}}_{k|k-1}\right), \tag{2.87}$$

and

$$\boldsymbol{P}^x_{k|k} = \left(\boldsymbol{I} - \boldsymbol{K}_k\boldsymbol{C}_k\right)\boldsymbol{P}^x_{k|k-1}, \tag{2.88}$$

where the matrix $\boldsymbol{K}_k \in \mathbb{R}^{n\times p}$ denotes the Kalman gain.

The operation of the discrete-time Kalman filter is illustrated in figure 2.6. If an initial conditon $\hat{\boldsymbol{x}}_0$ and $\boldsymbol{P}^x_0$ are given to the time update stage, $\boldsymbol{P}^x_{0|0} = \boldsymbol{P}^x_0$ and $\hat{\boldsymbol{x}}_{0|0} = \hat{\boldsymbol{x}}_0$, the time update stage project the state estimate and the error covariance forward to get the *a priori* estimates, while the measurement update stage correct the state estimate and the error covariance using the measurement to yield the *a posteriori* estimates. In such a predictor-corrector form operates the discrete-time Kalman filter.

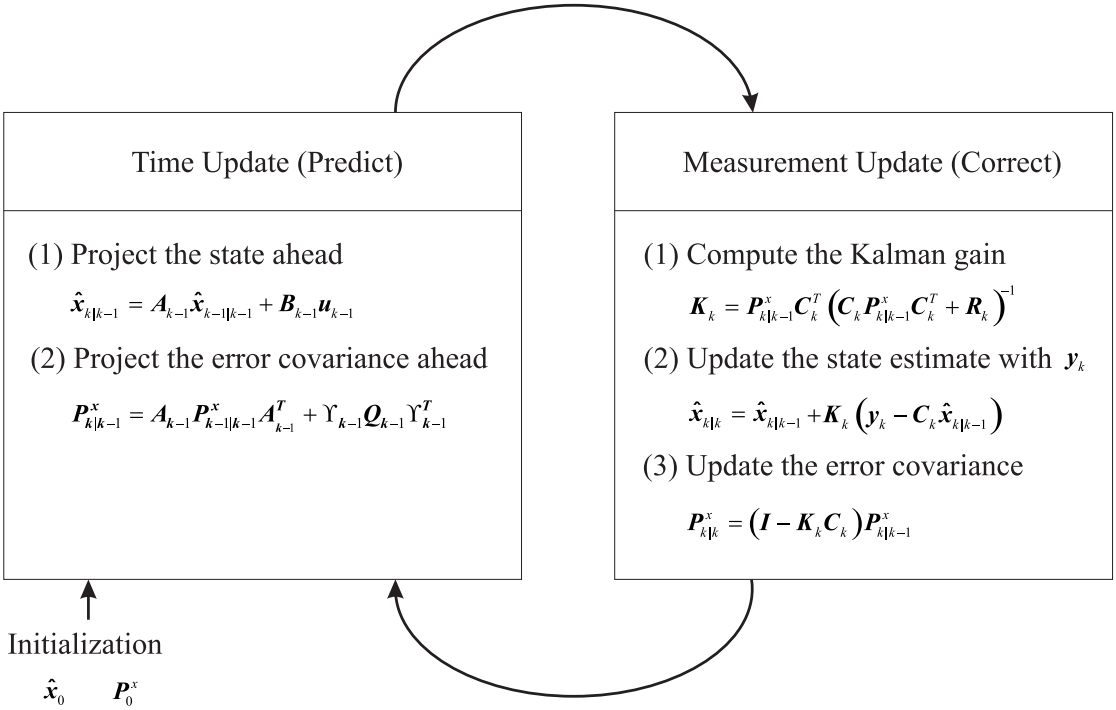

Figure 2.6. *Operation of the discrete-time Kalman filter (Welch and Bishop, 2006)*

Substituting equations (2.88) and (2.86) into equation (2.85) leads to the Riccati recursion

$$\boldsymbol{P}^x_{k+1|k} = \boldsymbol{A}_k\boldsymbol{P}^x_{k|k-1}\boldsymbol{A}^T_k - \boldsymbol{A}_k\boldsymbol{P}^x_{k|k-1}\boldsymbol{C}^T_k\left(\boldsymbol{C}_k\boldsymbol{P}^x_{k|k-1}\boldsymbol{C}^T_k + \boldsymbol{R}_k\right)^{-1}\boldsymbol{C}_k\boldsymbol{P}^x_{k|k-1}\boldsymbol{A}^T_k + \boldsymbol{\Upsilon}_k\boldsymbol{Q}_k\boldsymbol{\Upsilon}^T_k. \tag{2.89}$$

If $\boldsymbol{A}_k$, $\boldsymbol{B}_k$, $\boldsymbol{\Upsilon}_k$, $\boldsymbol{C}_k$, $\boldsymbol{Q}_k$ and $\boldsymbol{R}_k$ are constant matrices, the system in equations (2.76) and (2.77) will be discrete-time time-invariant with stationary noise, and the Riccati recursion in equation (2.89) will reach a steady-state and appears as the discrete-time algebraic Riccati equation

$$\boldsymbol{P}^x_{d,ss} = \boldsymbol{A}_d\boldsymbol{P}^x_{d,ss}\boldsymbol{A}^T_k - \boldsymbol{A}_d\boldsymbol{P}^x_{d,ss}\boldsymbol{C}^T_d\left(\boldsymbol{C}_d\boldsymbol{P}^x_{d,ss}\boldsymbol{C}^T_d + \boldsymbol{R}_d\right)^{-1}\boldsymbol{C}_d\boldsymbol{P}^x_{d,ss}\boldsymbol{A}^T_d + \boldsymbol{\Upsilon}_d\boldsymbol{Q}_d\boldsymbol{\Upsilon}^T_d, \tag{2.90}$$

where $\boldsymbol{P}^x_{d,ss}$ is the steady-state value of $\boldsymbol{P}^x_{k|k-1}$, and $\boldsymbol{A}_d$, $\boldsymbol{\Upsilon}_d$, $\boldsymbol{C}_d$, $\boldsymbol{Q}_d$ and $\boldsymbol{R}_d$ are the constant versions of $\boldsymbol{A}_k$, $\boldsymbol{\Upsilon}_k$, $\boldsymbol{C}_k$, $\boldsymbol{Q}_k$ and $\boldsymbol{R}_k$. By solving equation (2.90), $\boldsymbol{P}^x_{d,ss}$ can be determined.

Introduce $\boldsymbol{K}_{d,ss}$ as the steady-state of $\boldsymbol{K}_k$. Then $\boldsymbol{K}_{d,ss}$ can be calculated with

$$\boldsymbol{K}_{d,ss} = \boldsymbol{P}^x_{d,ss}\boldsymbol{C}^T_d\left(\boldsymbol{C}_d\boldsymbol{P}^x_{d,ss}\boldsymbol{C}^T_d + \boldsymbol{R}_d\right)^{-1}. \tag{2.91}$$

The matrix $\boldsymbol{K}_{d,ss}$ is also named as the steady-state Kalman gain. Such a constant Kalman gain can significantly simplify the implementation and reduce the computational load.

With $\boldsymbol{K}_{d,ss}$, the dynamics of $\tilde{\boldsymbol{x}}_{k|k}$ can be derived as

$$\tilde{\boldsymbol{x}}_{k+1|k+1} = \left(\boldsymbol{A}_d - \boldsymbol{K}_{d,ss}\boldsymbol{C}_d\boldsymbol{A}_d\right)\tilde{\boldsymbol{x}}_{k|k} + \left(\boldsymbol{\Upsilon}_k - \boldsymbol{K}_{d,ss}\boldsymbol{C}_d\boldsymbol{\Upsilon}_k\right)\boldsymbol{w}_k - \boldsymbol{K}_{d,ss}\boldsymbol{v}_{k+1}. \tag{2.92}$$

2.5. Kalman-Bucy filter

Kalman and Bucy (1961) presented a continuous-time counterpart to the discrete-time Kalman filter. This type of filter is named as Kalman-Bucy filter.

Consider the continuous-time time-variant stochastic model

$$\dot{\boldsymbol{x}}(t) = \boldsymbol{A}(t)\,\boldsymbol{x}(t) + \boldsymbol{B}(t)\,\boldsymbol{u}(t) + \boldsymbol{\Upsilon}(t)\,\boldsymbol{w}(t) \tag{2.93}$$

and

$$\boldsymbol{y}(t) = \boldsymbol{C}(t)\,\boldsymbol{x}(t) + \boldsymbol{v}(t)\,, \tag{2.94}$$

where $\boldsymbol{x}(t) \in \mathbb{R}^n$ represents the state; $\boldsymbol{u}(t) \in \mathbb{R}^r$ denotes the control (known) input; $\boldsymbol{y}(t) \in \mathbb{R}^p$ is the output; and $\boldsymbol{A}(t)$, $\boldsymbol{B}(t)$, $\boldsymbol{\Upsilon}(t)$ and $\boldsymbol{C}(t)$ are the system matrices with appropriate dimensions; $\boldsymbol{w}(t) \in \mathbb{R}^m$ and $\boldsymbol{v}(t) \in \mathbb{R}^p$ are zero-mean Gaussian white-noise processes, which indicates that the conditions

$$E\left[\boldsymbol{w}(t)\,\boldsymbol{w}^T(\tau)\right] = \boldsymbol{Q}(t)\,\delta(t-\tau) \tag{2.95}$$

and

$$E\left[\boldsymbol{v}(t)\,\boldsymbol{v}^T(\tau)\right] = \boldsymbol{R}(t)\,\delta(t-\tau) \tag{2.96}$$

hold. In equations (2.95) and (2.96), $\delta(t)$ represents the Dirac delta function. $\boldsymbol{w}(t)$ and $\boldsymbol{v}(t)$ are assumed uncorrelated, which means the condition

$$E\left[\boldsymbol{w}(t)\,\boldsymbol{v}^T(t)\right] = 0 \tag{2.97}$$

holds.

The Kalman-Bucy filter is comprised by

$$\boldsymbol{K}(t) = \boldsymbol{P}^x(t)\,\boldsymbol{C}(t)\,\boldsymbol{R}^{-1}(t)\,, \tag{2.98}$$

$$\dot{\boldsymbol{P}}^x(t) = \boldsymbol{A}(t)\,\boldsymbol{P}^x(t) + \boldsymbol{P}^x(t)\,\boldsymbol{A}^T(t) - \boldsymbol{P}^x(t)\,\boldsymbol{C}^T(t)\,\boldsymbol{R}^{-1}(t)\,\boldsymbol{C}(t)\,\boldsymbol{P}^x(t) + \boldsymbol{\Upsilon}(t)\,\boldsymbol{Q}(t)\,\boldsymbol{\Upsilon}^T(t)\,, \tag{2.99}$$

and

$$\dot{\hat{\boldsymbol{x}}}(t) = \boldsymbol{A}(t)\,\hat{\boldsymbol{x}}(t) + \boldsymbol{B}(t)\,\boldsymbol{u}(t) + \boldsymbol{K}(t)\left(\boldsymbol{y}(t) - \boldsymbol{C}(t)\,\hat{\boldsymbol{x}}(t)\right), \tag{2.100}$$

where $\boldsymbol{K}(t) \in \mathbb{R}^{n\times p}$ represents the Kalman gain; $\hat{\boldsymbol{x}}(t) \in \mathbb{R}^n$ denotes the estimate of the state; and $\boldsymbol{P}^x(t) \in \mathbb{R}^{n\times n}$ is the estimate error covariance .

If the matrices $\boldsymbol{A}(t)$, $\boldsymbol{B}(t)$, $\boldsymbol{\Upsilon}(t)$, $\boldsymbol{C}(t)$, $\boldsymbol{Q}(t)$ and $\boldsymbol{R}(t)$ are constant, the system which is described by equations (2.93) through (2.97) will be time-invariant with stationary

zero-mean white noise, and can be represented by

$$\dot{\boldsymbol{x}}(t) = \boldsymbol{A}_c \boldsymbol{x}(t) + \boldsymbol{B}_c \boldsymbol{u}(t) + \boldsymbol{\Upsilon}_c \boldsymbol{w}(t), \tag{2.101}$$

$$\boldsymbol{y}(t) = \boldsymbol{C}_c \boldsymbol{x}(t) + \boldsymbol{v}(t), \tag{2.102}$$

$$E\left[\boldsymbol{w}(t)\,\boldsymbol{w}^T(\tau)\right] = \boldsymbol{Q}_c \delta(t-\tau), \tag{2.103}$$

and

$$E\left[\boldsymbol{v}(t)\,\boldsymbol{v}^T(\tau)\right] = \boldsymbol{R}_c \delta(t-\tau), \tag{2.104}$$

where $\boldsymbol{A}_c$, $\boldsymbol{B}_c$, $\boldsymbol{\Upsilon}_c$, $\boldsymbol{C}_c$, $\boldsymbol{Q}_c$ and $\boldsymbol{R}_c$ are the constant values of $\boldsymbol{A}(t)$, $\boldsymbol{B}(t)$, $\boldsymbol{\Upsilon}(t)$, $\boldsymbol{C}(t)$, $\boldsymbol{Q}(t)$ and $\boldsymbol{R}(t)$, respectively. In this case, equation (2.99) will reach a steady-state and appears as the continuous-time algebraic Riccati equation

$$\boldsymbol{0} = \boldsymbol{A}_c \boldsymbol{P}^x_{c,ss} + \boldsymbol{P}^x_{c,ss} \boldsymbol{A}_c - \boldsymbol{P}^x_{c,ss} \boldsymbol{C}_c \boldsymbol{R}_c^{-1} \boldsymbol{C} \boldsymbol{P}^x_{c,ss} + \boldsymbol{\Upsilon}_c \boldsymbol{Q}_c \boldsymbol{\Upsilon}_c, \tag{2.105}$$

where $\boldsymbol{P}^x_{c,ss}$ is the steady-state value of $\boldsymbol{P}^x(t)$. Equation (2.100) appears as

$$\dot{\hat{\boldsymbol{x}}}(t) = \boldsymbol{A}_c \hat{\boldsymbol{x}}(t) + \boldsymbol{B}_c \boldsymbol{u}(t) + \boldsymbol{K}_{c,ss}\left(\boldsymbol{y}(t) - \boldsymbol{C}_c \hat{\boldsymbol{x}}(t)\right), \tag{2.106}$$

where $\boldsymbol{K}_{c,ss}$ denotes the steady-state continuous-time Kalman gain. By solving equation (2.105), $\boldsymbol{P}^x_{c,ss}$ can be determined. The steady-state Kalman gain can be calculated with

$$\boldsymbol{K}_{c,ss} = \boldsymbol{P}^x_{c,ss} \boldsymbol{C}_c \boldsymbol{R}_c^{-1}. \tag{2.107}$$

In the steady-state, the Kalman-Bucy filter operates like a Luenberger observer, but with an optimal feedback gain. Define the state estimate error $\tilde{\boldsymbol{x}}(t)$ as in equation (2.63), then the dynamics of $\tilde{\boldsymbol{x}}(t)$ can be described by

$$\dot{\tilde{\boldsymbol{x}}}(t) = \left(\boldsymbol{A}_c - \boldsymbol{K}_{c,ss} \boldsymbol{C}_c\right) \tilde{\boldsymbol{x}}(t) + \boldsymbol{\Upsilon}_c \boldsymbol{w}(t) - \boldsymbol{K}_{c,ss} \boldsymbol{v}(t). \tag{2.108}$$

2.6. Real-time executable state and input estimation algorithms

In this section, the available state and input estimation algorithms are briefly reviewed. These algorithms are all real-time executable, which indicates that an online operation of these algorithms is possible. Figure 2.7 describes the principle of real-time state and input estimation in the form of a block diagram.

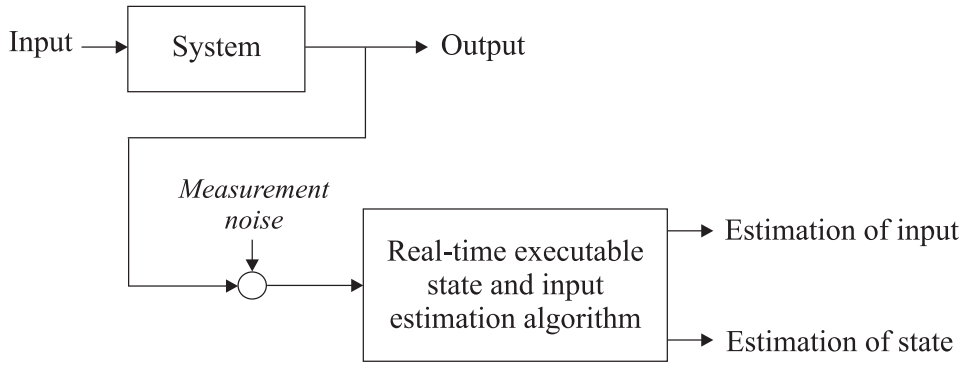

Figure 2.7. *Principle of real-time state and input estimation*

2.6.1. Proportional-Integral observer (PI observer)

Söffker et al. (1995) presented a design method for Proportional-Integral observer (PI observer). In this paper, it is stated that without exact knowledge about the dynamic behavior of the unknown input, a very general approach is possible by assuming the unknown input as piece-wise constant.

Consider the nonlinear system which is described by

$$\dot{\boldsymbol{x}}(t) = \boldsymbol{A}_c \boldsymbol{x}(t) + \boldsymbol{B}_c \boldsymbol{u}(t) + \boldsymbol{N}_c \boldsymbol{d}(t) \tag{2.109}$$

and

$$\boldsymbol{y}(t) = \boldsymbol{C}_c \boldsymbol{x}(t), \tag{2.110}$$

where $\boldsymbol{x}(t) \in \mathbb{R}^n$ represents the state; $\boldsymbol{u}(t) \in \mathbb{R}^r$ denotes the (known) control input; $\boldsymbol{d}(t) \in \mathbb{R}^m$ is the disturbance (unknown input); $\boldsymbol{y}(t) \in \mathbb{R}^p$ is the output; and $\boldsymbol{A}_c$, $\boldsymbol{B}_c$, $\boldsymbol{N}_c$ and $\boldsymbol{C}_c$ are the system matrices with appropriate dimensions.

The PI observer has the form

$$\begin{bmatrix} \dot{\hat{\boldsymbol{x}}}(t) \\ \dot{\hat{\boldsymbol{d}}}(t) \end{bmatrix} = \begin{bmatrix} \boldsymbol{A}_c - \boldsymbol{L}_{pio,1}\boldsymbol{C}_c & \boldsymbol{N}_c \\ -\boldsymbol{L}_{pio,2} & \boldsymbol{0} \end{bmatrix} \begin{bmatrix} \hat{\boldsymbol{x}}(t) \\ \hat{\boldsymbol{d}}(t) \end{bmatrix} + \begin{bmatrix} \boldsymbol{B}_c \\ \boldsymbol{0} \end{bmatrix} \boldsymbol{u}(t) + \begin{bmatrix} \boldsymbol{L}_{pio,1} \\ \boldsymbol{L}_{pio,2} \end{bmatrix} \boldsymbol{y}(t) \tag{2.111}$$

and

$$\hat{\boldsymbol{y}}(t) = \boldsymbol{C}_c \hat{\boldsymbol{x}}(t), \tag{2.112}$$

where $\hat{\boldsymbol{x}}(t)$ represents the estimate of $\boldsymbol{x}(t)$; $\hat{\boldsymbol{d}}(t)$ denotes the estimate of $\boldsymbol{d}(t)$; $\hat{\boldsymbol{y}}(t)$ is the estimate of $\mathbf{y}(t)$; and $\boldsymbol{L}_{pio,1}$ and $\boldsymbol{L}_{pio,2}$ are the matrices which need to be determined.

Figure 2.8 describes the PI observer in the form of a block diagram. Compared with the Luenberger observer, the PI observer uses not only the proportional but also the integral information of the difference between the measured output $\boldsymbol{y}(t)$ and the reconstructed output $\hat{\boldsymbol{y}}(t)$, so that both the current and the past information can be used to correct the state estimate.

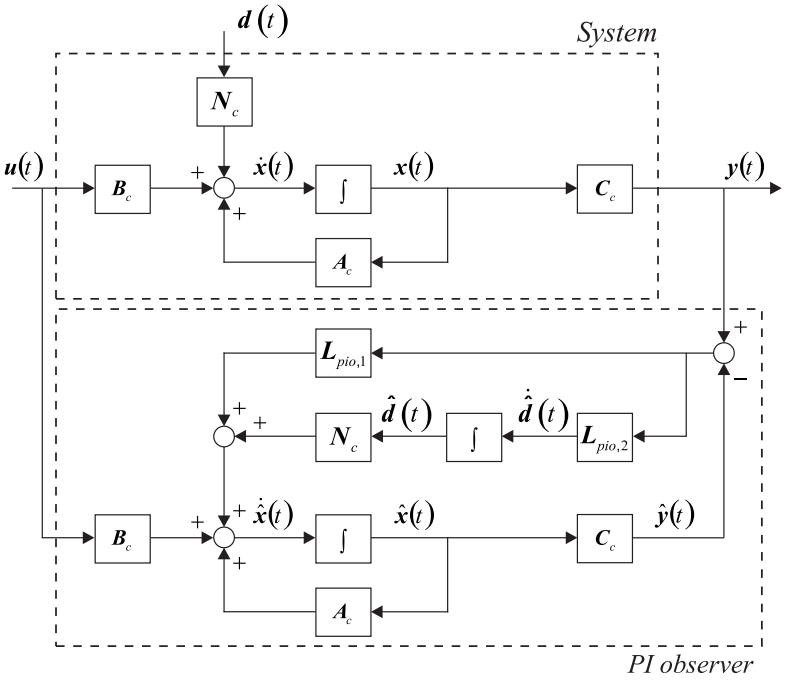

Figure 2.8. *Description of the PI observer in the form of a block diagram (Söffker et al., 1995)*

Define the state estimate error $\tilde{\boldsymbol{x}}(t)$ and the input estimate error $\tilde{\boldsymbol{d}}(t)$ as

$$\tilde{\boldsymbol{x}}(t) = \boldsymbol{x}(t) - \hat{\boldsymbol{x}}(t) \tag{2.113}$$

and

$$\tilde{\boldsymbol{d}}(t) = \boldsymbol{d}(t) - \hat{\boldsymbol{d}}(t). \tag{2.114}$$

The dynamics of the estimate error can be described by

$$\begin{bmatrix} \dot{\tilde{\boldsymbol{x}}}(t) \\ \dot{\tilde{\boldsymbol{d}}}(t) \end{bmatrix} = [\boldsymbol{A}_{pio} - \boldsymbol{L}_{pio}\boldsymbol{C}_{pio}] \begin{bmatrix} \tilde{\boldsymbol{x}}(t) \\ \tilde{\boldsymbol{d}}(t) \end{bmatrix} + \begin{bmatrix} \boldsymbol{0} \\ \boldsymbol{I} \end{bmatrix} \dot{\boldsymbol{d}}(t), \tag{2.115}$$

where $\boldsymbol{A}_{pio}$, $\boldsymbol{C}_{pio}$ and $\boldsymbol{L}_{pio}$ are calculated with

$$\boldsymbol{A}_{pio} = \begin{bmatrix} \boldsymbol{A}_c & \boldsymbol{N}_c \\ \boldsymbol{0} & \boldsymbol{0} \end{bmatrix}, \tag{2.116}$$

$$\boldsymbol{C}_{pio} = \begin{bmatrix} \boldsymbol{C}_c & \boldsymbol{0} \end{bmatrix}, \tag{2.117}$$

and

$$\boldsymbol{L}_{pio} = \begin{bmatrix} \boldsymbol{L}_{pio,1} \\ \boldsymbol{L}_{pio,2} \end{bmatrix}. \tag{2.118}$$

In equation (2.115), $\dot{\boldsymbol{d}}(t)$ acts as the error input.

Assume that the unknown input $\boldsymbol{d}(t)$ is bounded, a high-gain PI observer exists such that the state estimate error $\widetilde{\boldsymbol{x}}(t)$ goes to zero for any initial states $\boldsymbol{x}(0)$, $\hat{\boldsymbol{x}}(0)$, and $\hat{\boldsymbol{d}}(0)$, if the following sufficient conditions are fulfilled.

(1) Matrix pair ($\boldsymbol{A}_{pio}$, $\boldsymbol{C}_{pio}$) is observable.

(2) The condition $rank\left(\begin{bmatrix} \boldsymbol{A}_c & \boldsymbol{N}_c \\ \boldsymbol{C}_c & \boldsymbol{0} \end{bmatrix}\right) = n + m$ holds.

(3) The condition $\boldsymbol{C}_c\boldsymbol{A}_c^i\boldsymbol{N}_c = \boldsymbol{0}$ $(i = 0, 1, 2, \cdots, k-2)$ holds, where k is the observability index of the matrix pair ($\boldsymbol{A}_c$, $\boldsymbol{C}_c$).

In this thesis, the gain matrix $\boldsymbol{L}_{pio}$ is calculated using the Loop Transfer Recovery (LTR) design method which is suggested in Krajcin and Söffker (2005). The main steps for calculating $\boldsymbol{L}_{pio}$ are provided below.

Introduce the matrices

$$\boldsymbol{N}_{pio} = \begin{bmatrix} \boldsymbol{0}_{n\times m} \\ \boldsymbol{I}_{m\times m} \end{bmatrix}, \tag{2.119}$$

$$\boldsymbol{Q}_{pio} = \boldsymbol{I}_{(n+m)\times(n+m)} + q\boldsymbol{N}_{pio}\boldsymbol{N}_{pio}^T, \tag{2.120}$$

and

$$\boldsymbol{R}_{pio} = \boldsymbol{I}_{m\times m}. \tag{2.121}$$

By solving the continous-time algebraic Riccati equation

$$\boldsymbol{A}_{pio}\boldsymbol{P} + \boldsymbol{P}\boldsymbol{A}_{pio}^T + \boldsymbol{Q}_{pio} - \boldsymbol{P}\boldsymbol{C}_{pio}^T\boldsymbol{R}_{pio}^{-1}\boldsymbol{C}_{pio}\boldsymbol{P} = \boldsymbol{0}, \tag{2.122}$$

a solution of the matrix $\boldsymbol{P}$ can be obtained, and the gain matrix $\boldsymbol{L}_{pio}$ is determined with

$$\boldsymbol{L}_{pio} = \boldsymbol{P}\boldsymbol{C}_{pio}^T\boldsymbol{R}_{pio}^{-1}. \tag{2.123}$$

In Equation (2.120), q denotes the LTR design parameter. For fast changing input where $\dot{\boldsymbol{d}}(t)$ is large, the value of q needs to be set very large in order to get satisfactory results.

2.6.2. Simultaneous State and Input Estimator (SS&IE)

Ha and Trinh (2004) proposed a UIO design which can realize simultaneous state and input estimation for a class of nonlinear systems. Klinkov and Fritzen (2006) named this

method as Simultaneous State and Input Estimator (SS&IE), and adopted it for online force reconstruction.

Consider the system which is described by

$$\dot{\boldsymbol{x}}(t) = \boldsymbol{A}_c \boldsymbol{x}(t) + \boldsymbol{G}_c \boldsymbol{d}(t) + f\left(\left(\boldsymbol{x}(t), \boldsymbol{u}(t)\right), \boldsymbol{y}(t)\right) \tag{2.124}$$

and

$$\boldsymbol{y}(t) = \boldsymbol{C}_c \boldsymbol{x}(t) + \boldsymbol{H}_c \boldsymbol{d}(t), \tag{2.125}$$

where $\boldsymbol{x}(t) \in \mathbb{R}^n$ represents the state; $\boldsymbol{d}(t) \in \mathbb{R}^m$ denotes the unknown input; $\boldsymbol{y}(t) \in \mathbb{R}^p$ is the output; and $\boldsymbol{A}_c$, $\boldsymbol{G}_c$, $\boldsymbol{C}_c$ and $\boldsymbol{H}_c$ are the system matrices with appropriate dimensions. In equation (2.124), $f\left(\left(\boldsymbol{x}(t), \boldsymbol{u}(t)\right), \boldsymbol{y}(t)\right)$ is a nonlinear vector and is expressed by

$$f\left(\left(\boldsymbol{x}(t), \boldsymbol{u}(t)\right), \boldsymbol{y}(t)\right) = f_L\left(\left(\boldsymbol{x}(t), \boldsymbol{u}(t)\right), \boldsymbol{y}(t)\right) + \boldsymbol{W}_{ssie} f_U\left(\left(\boldsymbol{x}(t), \boldsymbol{u}(t)\right), \boldsymbol{y}(t)\right), \tag{2.126}$$

where $f_L\left(\left(\boldsymbol{x}(t), \boldsymbol{u}(t)\right), \boldsymbol{y}(t)\right) \in \mathbb{R}^n$ and $f_U\left(\left(\boldsymbol{x}(t), \boldsymbol{u}(t)\right), \boldsymbol{y}(t)\right) \in \mathbb{R}^n$ are, respectively, the nonlinear term satisfying Lipschitz condition and the unknown nonlinear term; and $\boldsymbol{W}_{ssie} \in \mathbb{R}^{n \times d}$ is a constant matrix with full column rank.

Introduce an augmented state vector $\boldsymbol{x}_{aug}(t)$ as

$$\boldsymbol{x}_{aug}(t) = \begin{bmatrix} \boldsymbol{x}(t) \\ \\ \boldsymbol{d}(t) \end{bmatrix}. \tag{2.127}$$

The nonlinear term $f_L\left(\left(\boldsymbol{x}(t), \boldsymbol{u}(t)\right), \boldsymbol{y}(t)\right)$ is assumed to be Lipschitz in $\boldsymbol{x}_{aug}(t)$ with a Lipschitz constant γ, and fulfills the condition

$$\left\| f_L\left(\boldsymbol{x}_{aug}(t), \boldsymbol{y}(t)\right) - f_L\left(\hat{\boldsymbol{x}}_{aug}(t), \boldsymbol{y}(t)\right) \right\| \leq \gamma \left\| \boldsymbol{x}_{aug}(t) - \hat{\boldsymbol{x}}_{aug}(t) \right\|, \tag{2.128}$$

where $\hat{\boldsymbol{x}}_{aug}(t)$ is the estimate of $\boldsymbol{x}_{aug}(t)$; γ is a positive real scalar; and $\|\cdot\|$ denotes the Euclidean norm. The matrix $[\boldsymbol{D_c}, \boldsymbol{C}_c \boldsymbol{W}_{ssie}]$ is assumed to have full column rank, which indicates the condition $y \geq m + d$ holds.

Introduce the matrices

$$\boldsymbol{E}_{ssie} = \begin{bmatrix} \boldsymbol{I}_n & \boldsymbol{0}_{n \times m} \end{bmatrix}, \tag{2.129}$$

$$\boldsymbol{M}_{ssie} = \begin{bmatrix} \boldsymbol{A}_c & \boldsymbol{G}_c \end{bmatrix}, \tag{2.130}$$

and

$$\boldsymbol{H}_{ssie} = \begin{bmatrix} \boldsymbol{C}_c & \boldsymbol{H}_c \end{bmatrix}. \tag{2.131}$$

The system which is described by equations (2.124) and (2.125) can be transformed to

$$\boldsymbol{E}_{ssie}\dot{\boldsymbol{x}}_{aug}(t) = \boldsymbol{M}_{ssie}\boldsymbol{x}_{aug}(t) + f_L(\boldsymbol{x}_{aug}(t), \boldsymbol{y}(t)) + \boldsymbol{W}_{ssie}f_U(\boldsymbol{x}_{aug}(t), \boldsymbol{y}(t)) \quad (2.132)$$

and

$$\boldsymbol{y}(t) = \boldsymbol{H}_{ssie}\boldsymbol{x}_{aug}(t). \quad (2.133)$$

The SS&IE is described by

$$\dot{\boldsymbol{\xi}}_{aug}(t) = \boldsymbol{N}_{ssie}\boldsymbol{\xi}_{aug}(t) + \boldsymbol{L}_{ssie}\boldsymbol{y}(t) + \boldsymbol{T}_{ssie}\boldsymbol{f}_L(\hat{\boldsymbol{x}}_{aug}(t), \boldsymbol{y}(t)) \quad (2.134)$$

and

$$\hat{\boldsymbol{x}}_{aug}(t) = \boldsymbol{\xi}_{aug}(t) + \boldsymbol{Q}_{ssie}\boldsymbol{y}(t), \quad (2.135)$$

where $\boldsymbol{N}_{ssie}$, $\boldsymbol{L}_{ssie}$, $\boldsymbol{T}_{ssie}$ and $\boldsymbol{Q}_{ssie}$ are the matrices which need to be designed. Figure 2.9 describes the SS&IE in the form of a block diagram.

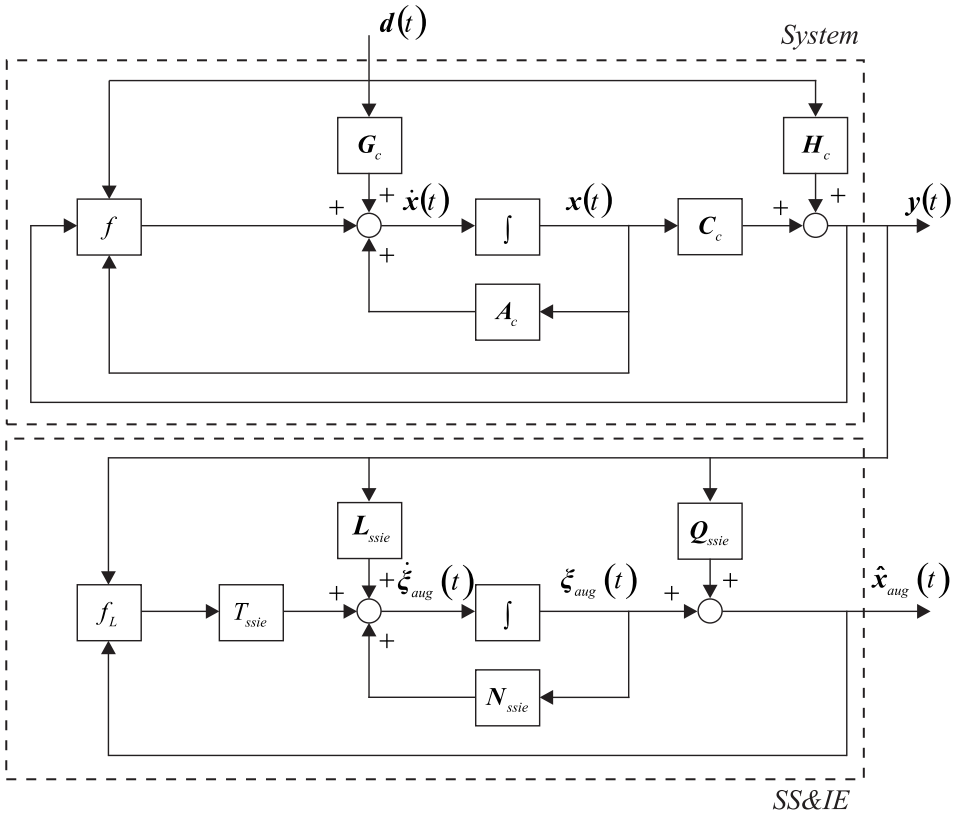

Figure 2.9. *Description of the SS&IE in the form of a block diagram (Ha and Trinh, 2004)*

Introduce the notations

$$\boldsymbol{S}_{ssie} = \begin{bmatrix} \boldsymbol{E}_{ssie} & \boldsymbol{W}_{ssie} \\ \boldsymbol{H}_{ssie} & \boldsymbol{0} \end{bmatrix}, \quad (2.136)$$

$$\boldsymbol{J}_{ssie} = \begin{bmatrix} \boldsymbol{I}_{n+m} & \boldsymbol{0} \end{bmatrix} \boldsymbol{S}_{ssie}^{+} \begin{bmatrix} \boldsymbol{I}_n \\ \boldsymbol{0} \end{bmatrix}, \tag{2.137}$$

$$\boldsymbol{\Phi}_{ssie} = \boldsymbol{J}_{ssie} \boldsymbol{M}_{ssie}, \tag{2.138}$$

$$\boldsymbol{G}_{ssie} = \left(\boldsymbol{I}_{n+p} - \boldsymbol{S}_{ssie} \boldsymbol{S}_{ssie}^{+}\right) \begin{bmatrix} \boldsymbol{I}_n \\ \boldsymbol{0} \end{bmatrix}, \tag{2.139}$$

$$\boldsymbol{\Psi}_{ssie} = \boldsymbol{G}_{ssie} \boldsymbol{M}_{ssie}, \tag{2.140}$$

$$\boldsymbol{V}_{ssie} = \begin{bmatrix} \boldsymbol{I}_{n+m} & \boldsymbol{0} \end{bmatrix} \boldsymbol{S}_{ssie}^{+} \begin{bmatrix} \boldsymbol{0} \\ \boldsymbol{I}_p \end{bmatrix}, \tag{2.141}$$

and

$$\boldsymbol{K}_{ssie} = \left(\boldsymbol{I}_{n+p} - \boldsymbol{S}_{ssie} \boldsymbol{S}_{ssie}^{+}\right) \begin{bmatrix} \boldsymbol{0} \\ \boldsymbol{I}_p \end{bmatrix}, \tag{2.142}$$

where $\boldsymbol{S}_{ssie}^{+}$ denotes the left inverse of $\boldsymbol{S}_{ssie}$.

The vector $\hat{\boldsymbol{x}}_{aug}(t)$ will asymptotically approach $\boldsymbol{x}_{aug}(t)$, if there exist matrices $\boldsymbol{P}_{ssie} = \boldsymbol{P}_{ssie}^{+} > \boldsymbol{0}$, $\boldsymbol{X}_{ssie}$, $\boldsymbol{Y}_{ssie}$, and positive scalars δ_1 and δ_2, so that the following Linear Matrix Inequality (LMI)

$$\begin{bmatrix} \boldsymbol{\Phi}_{ssie}^{T} \boldsymbol{P}_{ssie} + \boldsymbol{\Psi}_{ssie} \boldsymbol{Y}_{ssie}^{T} - \boldsymbol{H}_{ssie}^{T} \boldsymbol{X}_{ssie}^{T} & \boldsymbol{P}_{ssie} \boldsymbol{J}_{ssie} & \boldsymbol{Y}_{ssie} \boldsymbol{G}_{ssie} \\ + \boldsymbol{P}_{ssie} \boldsymbol{\Phi}_{ssie} + \boldsymbol{Y}_{ssie} \boldsymbol{\Psi}_{ssie} - \boldsymbol{X}_{ssie} \boldsymbol{H}_{ssie} & & \\ + \gamma^2 (\delta_1 + \delta_2) \boldsymbol{I} & & \\ \boldsymbol{J}_{ssie}^{T} \boldsymbol{P}_{ssie} & -\delta_1 \boldsymbol{I} & 0 \\ \mathbf{G}_{ssie}^{T} \boldsymbol{Y}_{ssie}^{T} & 0 & -\delta_1 \boldsymbol{I} \end{bmatrix} < \boldsymbol{0} \tag{2.143}$$

is satisfied. The LMI above can be solved in a computationally efficient manner using e.g., MATLAB LMI Control Toolbox.

Introduce the matrices $\boldsymbol{Z}_{ssie}$ and $\boldsymbol{F}_{ssie}$ as

$$\boldsymbol{Z}_{ssie} = \boldsymbol{P}_{ssie}^{-1} \boldsymbol{Y}_{ssie} \tag{2.144}$$

and

$$\boldsymbol{F}_{ssie} = \boldsymbol{P}_{ssie}^{-1} \boldsymbol{Y}_{ssie}. \tag{2.145}$$

The matrices $\boldsymbol{N}_{ssie}$, $\boldsymbol{L}_{ssie}$, $\boldsymbol{T}_{ssie}$ and $\boldsymbol{Q}_{ssie}$ can be determined respectively with

$$\boldsymbol{N}_{ssie} = \boldsymbol{\Phi}_{ssie} + \boldsymbol{Z}_{ssie}\boldsymbol{\Psi}_{ssie} - \boldsymbol{F}_{ssie}\boldsymbol{H}_{ssie}, \tag{2.146}$$

$$\boldsymbol{L}_{ssie} = \boldsymbol{F}_{ssie} + \boldsymbol{N}_{ssie}\boldsymbol{Q}_{ssie}, \tag{2.147}$$

$$\boldsymbol{T}_{ssie} = \boldsymbol{J}_{ssie} + \boldsymbol{Z}_{ssie}\boldsymbol{G}_{ssie}, \tag{2.148}$$

and

$$\boldsymbol{Q}_{ssie} = \boldsymbol{V}_{ssie} + \boldsymbol{Z}_{ssie}\boldsymbol{K}_{ssie}. \tag{2.149}$$

When $f\left(\left(\boldsymbol{x}\left(t\right), \boldsymbol{u}\left(t\right)\right), \boldsymbol{y}\left(t\right)\right)$ includes only $f_U\left(\left(\boldsymbol{x}\left(t\right), \boldsymbol{u}\left(t\right)\right), \boldsymbol{y}\left(t\right)\right)$, $\hat{\boldsymbol{x}}_{aug}\left(t\right)$ will asymptotically approach $\boldsymbol{x}_{aug}\left(t\right)$, if there exist matrices $\boldsymbol{Z}_{ssie}$ and $\boldsymbol{F}_{ssie}$ so that the eigenvalues of the matrix $\boldsymbol{N}_{ssie}$ are all on the LHP.

2.6.3. Kalman Filter and a Recursive Least-Squares Estimator (KF+RLSE)

Tuan et al. (1996) presented a state and input estimation algorithm to solve two-dimensional inverse heat conduction problems. This algorithm is named as Kalman Filter and a Recursive Least-Squares Estimator (KF+RLSE).

Consider the discrete-time time-invariant system which is described by

$$\boldsymbol{x}_{k+1} = \boldsymbol{A}_d\boldsymbol{x}_k + \boldsymbol{G}_d\boldsymbol{d}_k + \boldsymbol{w}_k \tag{2.150}$$

and

$$\boldsymbol{y}_k = \boldsymbol{C}_d\boldsymbol{x}_k + \boldsymbol{v}_k, \tag{2.151}$$

where $\boldsymbol{x}_k \in \mathbb{R}^n$ represents the state; $\boldsymbol{d}_k \in \mathbb{R}^m$ denotes the unknown input; $\boldsymbol{y}_k \in \mathbb{R}^p$ is the output; and $\boldsymbol{A}_d$, $\boldsymbol{G}_d$ and $\boldsymbol{C}_d$ are the system matrices with appropriate dimensions; $\boldsymbol{w}_k \in \mathbb{R}^n$ is the process noise; $\boldsymbol{v}_k \in \mathbb{R}^p$ is the measurement noise. $\boldsymbol{w}_k$ and $\boldsymbol{v}_k$ are assumed as stationary zero-mean Gaussian white-noise processes, with covariance matrices $\boldsymbol{Q}_d$ and $\boldsymbol{R}_d$, respectively.

The KF+RLSE algorithm consists of the following two part, a Kalman filter part which includes

$$\hat{\boldsymbol{x}}_{k|k-1} = \boldsymbol{A}_d\hat{\boldsymbol{x}}_{k-1|k-1}, \tag{2.152}$$

$$\boldsymbol{P}^x_{k|k-1} = \boldsymbol{A}_d\boldsymbol{P}^x_{k-1|k-1}\boldsymbol{A}_d^T + \boldsymbol{Q}_d, \tag{2.153}$$

$$\boldsymbol{S}_k = \boldsymbol{C}_d\boldsymbol{P}_{k|k-1}\boldsymbol{C}_d^T + \boldsymbol{R}_d, \tag{2.154}$$

$$\boldsymbol{K}_k = \boldsymbol{P}_{k|k-1}\boldsymbol{C}_d^T\boldsymbol{S}_k^{-1}, \tag{2.155}$$

$$\boldsymbol{P}^x_{k|k} = \left(\boldsymbol{I} - \boldsymbol{K}_k\boldsymbol{C}_d\right)\boldsymbol{P}^x_{k|k-1}, \tag{2.156}$$

$$\tilde{\boldsymbol{y}}_k = \boldsymbol{y}_k - \boldsymbol{C}_d \hat{\boldsymbol{x}}_{k|k-1}, \tag{2.157}$$

and

$$\hat{\boldsymbol{x}}_{k|k} = \hat{\boldsymbol{x}}_{k|k-1} + \boldsymbol{K}_k \tilde{\boldsymbol{y}}_k. \tag{2.158}$$

and a recursive least-squares estimator which includes

$$\boldsymbol{B}_k = \boldsymbol{C}_d \left(\boldsymbol{A}_d \boldsymbol{M}_{k-1} + \boldsymbol{I} \right) \boldsymbol{G}_d, \tag{2.159}$$

$$\boldsymbol{M}_k = \left(\boldsymbol{I} - \boldsymbol{K}_k \boldsymbol{C}_d \right) \left(\boldsymbol{A}_d \boldsymbol{M}_{k-1} + \boldsymbol{I} \right), \tag{2.160}$$

$$\boldsymbol{K}_k^d = \gamma^{-1} \boldsymbol{P}_{k-1}^d \boldsymbol{B}_k^T \left(\boldsymbol{B}_k \gamma^{-1} \boldsymbol{P}_{k-1}^d \boldsymbol{B}_k^T + \boldsymbol{S}_k \right)^{-1}, \tag{2.161}$$

$$\boldsymbol{P}_k^d = \left(\boldsymbol{I} - \boldsymbol{K}_k^d \boldsymbol{B}_k \right) \gamma^{-1} \boldsymbol{P}_{k-1}^d, \tag{2.162}$$

and

$$\hat{\boldsymbol{d}}_k = \hat{\boldsymbol{d}}_{k-1} + \boldsymbol{K}_k^d \left(\tilde{\boldsymbol{y}}_k - \boldsymbol{B}_k \hat{\boldsymbol{d}}_{k-1} \right). \tag{2.163}$$

In equations (2.152) through (2.163), $\hat{\boldsymbol{x}}_{k|k-1}$ denotes the *a priori* state estimate; $\hat{\boldsymbol{x}}_{k|k-1}$ is the *a posteriori* sate estimate; $\hat{\boldsymbol{d}}_k$ is the estimate of $\boldsymbol{d}_k$; $\boldsymbol{P}_{k|k-1}^x$ represents the estimate error covariance of $\hat{\boldsymbol{x}}_{k|k-1}$; $\boldsymbol{P}_{k|k}^x$ is the estimate error covariance of $\hat{\boldsymbol{x}}_{k|k}$; $\boldsymbol{P}_k^d$ is the estimate error covariance of $\boldsymbol{d}_k$; $\boldsymbol{B}_k$ and $\boldsymbol{M}_k$ denote sensitivity matrices; $\boldsymbol{S}_k$, $\boldsymbol{K}_k$ and $\boldsymbol{K}_k^d$ are gain matrices; and $\gamma (0 < \gamma < 1)$ is a forgetting factor which prevents $\boldsymbol{K}_k^d$ from shrinking to zero and to compromise between the fast adaptive capability and the loss of estimate accuracy. A necessary condition for the existence of the KF+RLSE algorithm is that the matrix pair ($\boldsymbol{A}_k$, $\boldsymbol{C}_k$) should be observable.

2.6.4. Recursive Three-Step Filter (RTSF)

Gillijns and De Moor (2007) proposed an unbiased minimum-variance input and state estimation algorithm for linear discrete-time systems with direction feedthrough. This algorithm is named as Recursive Three-Step Filter (RTSF) (Hsieh, 2010).

Consider the linear discrete-time time-variant system which is described by

$$\boldsymbol{x}_{k+1} = \boldsymbol{A}_k \boldsymbol{x}_k + \boldsymbol{G}_k \boldsymbol{d}_k + \boldsymbol{w}_k \tag{2.164}$$

and

$$\boldsymbol{y}_k = \boldsymbol{C}_k \boldsymbol{x}_k + \boldsymbol{H}_k \boldsymbol{d}_k + \boldsymbol{v}_k. \tag{2.165}$$

where $\boldsymbol{x}_k \in \mathbb{R}^n$ represents the state; $\boldsymbol{d}_k \in \mathbb{R}^m$ denotes the unknown input; $\boldsymbol{y}_k \in \mathbb{R}^p$ is the output; and $\boldsymbol{A}_k$, $\boldsymbol{G}_k$, $\boldsymbol{C}_k$ and $\boldsymbol{H}_k$ are system matrices with appropriate dimensions; $\boldsymbol{w}_k \in \mathbb{R}^n$ and $\boldsymbol{v}_k \in \mathbb{R}^p$ represent the process noise and the measurement noise, respectively. It is assumed that $\boldsymbol{w}_k$ and $\boldsymbol{v}_k$ are stationary, mutually uncorrelated, zero-mean and white,

with known covariance matrices

$$\boldsymbol{Q}_k = E\left[\boldsymbol{w}_k \boldsymbol{w}_k^T\right] \tag{2.166}$$

and

$$\boldsymbol{R}_k = E\left[\boldsymbol{v}_k \boldsymbol{v}_k^T\right]. \tag{2.167}$$

Introduce the *a priori* state estimate $\hat{\boldsymbol{x}}_{k|k-1}$, the *a posteriori* state estimate $\hat{\boldsymbol{x}}_{k|k}$ and the input estimate $\hat{\boldsymbol{d}}_k$. The a priori state estimate error $\tilde{\boldsymbol{x}}_{k|k-1}$, the *a posteriori* state estimate error $\tilde{\boldsymbol{x}}_{k|k}$, the input estimate error $\tilde{\boldsymbol{d}}_k$, and their covariances are defined by

$$\tilde{\boldsymbol{x}}_{k|k-1} = \boldsymbol{x}_k - \hat{\boldsymbol{x}}_{k|k-1}, \tag{2.168}$$

$$\tilde{\boldsymbol{x}}_{k|k} = \boldsymbol{x}_k - \hat{\boldsymbol{x}}_{k|k}, \tag{2.169}$$

$$\tilde{\boldsymbol{d}}_k = \boldsymbol{d}_k - \hat{\boldsymbol{d}}_k, \tag{2.170}$$

$$\boldsymbol{P}^x_{k|k-1} = E\left[\tilde{\boldsymbol{x}}_{k|k-1} \tilde{\boldsymbol{x}}^T_{k|k-1}\right], \tag{2.171}$$

$$\boldsymbol{P}^x_{k|k} = E\left[\tilde{\boldsymbol{x}}_{k|k} \tilde{\boldsymbol{x}}^T_{k|k}\right], \tag{2.172}$$

$$\boldsymbol{P}^d_k = E\left[\tilde{\boldsymbol{d}}_k \tilde{\boldsymbol{d}}^T_k\right], \tag{2.173}$$

and

$$\boldsymbol{P}^{xd}_k = E\left[\tilde{\boldsymbol{x}}_{k|k} \tilde{\boldsymbol{d}}^T_k\right]. \tag{2.174}$$

Assume the estimate of the initial state, $\hat{\boldsymbol{x}}_{0|0}$, is unbiased with known covariance $\boldsymbol{P}^x_{0|0}$. The filter equations of the RTSF consist of three steps:

- Estimation of unknown input, which includes

$$\tilde{\boldsymbol{R}}_{rtsf,k} = \boldsymbol{C}_k \boldsymbol{P}^x_{k|k-1} \boldsymbol{C}^T_k + \boldsymbol{R}_k, \tag{2.175}$$

$$\boldsymbol{M}_{rtsf,k} = \left(\boldsymbol{H}^T_k \tilde{\boldsymbol{R}}^{-1}_{rtsf,k} \boldsymbol{H}_k\right)^{-1} \boldsymbol{H}^T_k \tilde{\boldsymbol{R}}^{-1}_k, \tag{2.176}$$

$$\hat{\boldsymbol{d}}_k = \boldsymbol{M}_{rtsf,k}\left(\boldsymbol{y}_k - \boldsymbol{C}_k \hat{\boldsymbol{x}}_{k|k-1}\right), \tag{2.177}$$

  and

$$\boldsymbol{P}^d_k = \left(\boldsymbol{H}^T_k \tilde{\boldsymbol{R}}^{-1}_{rtsf,k} \boldsymbol{H}_k\right)^{-1}. \tag{2.178}$$

- Measurement update, which includes

$$\boldsymbol{K}_{rtsf,k} = \boldsymbol{P}^x_{k|k-1} \boldsymbol{C}^T_k \tilde{\boldsymbol{R}}^{-1}_{rtsf,k}, \tag{2.179}$$

$$\hat{\boldsymbol{x}}_{k|k} = \hat{\boldsymbol{x}}_{k|k-1} + \boldsymbol{K}_{rtsf,k}\left(\boldsymbol{y}_k - \boldsymbol{C}_k \hat{\boldsymbol{x}}_{k|k-1} - \boldsymbol{H}_k \hat{\boldsymbol{d}}_k\right), \tag{2.180}$$

$$\boldsymbol{P}_{k|k}^{x} = \boldsymbol{P}_{k|k-1}^{x} - \boldsymbol{K}_{rtsf,k}\left(\tilde{\boldsymbol{R}}_{rtsf,k} - \boldsymbol{H}_k \boldsymbol{P}_k^d \boldsymbol{H}_k^T\right) \boldsymbol{K}_{rtsf,k}^T, \tag{2.181}$$

and

$$\boldsymbol{P}_k^{xd} = \left(\boldsymbol{P}_k^{dx}\right)^T = -\boldsymbol{K}_{rtsf,k}\boldsymbol{H}_k\boldsymbol{P}_k^d. \tag{2.182}$$

- Time update, which includes

$$\hat{\boldsymbol{x}}_{k+1|k} = \boldsymbol{A}_k\hat{\boldsymbol{x}}_{k|k} + \boldsymbol{G}_k\hat{\boldsymbol{d}}_k \tag{2.183}$$

and

$$\boldsymbol{P}_{k+1|k}^{x} = \begin{bmatrix} \boldsymbol{A}_k & \boldsymbol{G}_k \end{bmatrix} \begin{bmatrix} \boldsymbol{P}_{k|k}^{x} & \boldsymbol{P}_k^{xd} \\ \boldsymbol{P}_k^{dx} & \boldsymbol{P}_k^{d} \end{bmatrix} \begin{bmatrix} \boldsymbol{A}_k^T \\ \boldsymbol{G}_k^T \end{bmatrix} + \boldsymbol{Q}_k. \tag{2.184}$$

The existence of the RTSF requires that the following necessary and sufficient conditions should be fulfilled.

(1) The unbiased estimate of the initial state is available;

(2) Matrix pair ($\boldsymbol{A}_k$, $\boldsymbol{C}_k$) is observable;

(3) Matrix $\boldsymbol{H}_k$ has full column rank.

2.6.5. Kalman Filter with Unknown Inputs (KF-UI)

Pan et al. (2011) proposed a Kalman Filter with Unknown Inputs (KF-UI) algorithm by using the weighted least-squares estimation method.

Consider the same system which is described by equations (2.164) and (2.165) and the same definitions which are introduced in equations (2.168) through (2.174).

The KF-UI algorithm consists of the following three steps:

- Step 1: Compute the time update for estimated states, which includes

$$\hat{\boldsymbol{x}}_{k|k-1} = \boldsymbol{A}_{k-1}\hat{\boldsymbol{x}}_{k-1|k-1} + \boldsymbol{G}_{k-1}\hat{\boldsymbol{d}}_{k-1}. \tag{2.185}$$

- Step 2: Calculate the gain matrices $\boldsymbol{K}_{kfui,k}$ and $\boldsymbol{S}_{kfui,k}$, which includes

$$\boldsymbol{K}_{kfui,k} = \boldsymbol{P}_{k|k-1}^{x}\boldsymbol{C}_k^T\left[\boldsymbol{R}_k + \boldsymbol{C}_k\boldsymbol{P}_{k|k-1}^{x}\boldsymbol{C}_k^T\right]^{-1} \tag{2.186}$$

and

$$\boldsymbol{S}_{kfui,k} = \left[\boldsymbol{H}_k^T\boldsymbol{R}_k^{-1}(\boldsymbol{I} - \boldsymbol{C}_k\boldsymbol{K}_{kfui,k})\boldsymbol{H}_k\right]^{-1}. \tag{2.187}$$

In equation (2.186), $\boldsymbol{P}_{k|k-1}^{x}$ is determined by

$$\boldsymbol{P}_{k|k-1}^{x} = \boldsymbol{A}_{k-1}\boldsymbol{P}_{k-1|k-1}^{x}\boldsymbol{A}_{k-1}^T + \boldsymbol{G}_{k-1}\boldsymbol{H}_{k-1}^T\boldsymbol{R}_{k-1}^{-1}\boldsymbol{C}_{k-1}\boldsymbol{A}_{k-1}^T$$

$$+ \boldsymbol{A}_{k-1}\boldsymbol{C}_{k-1}^{T}\boldsymbol{R}_{k-1}^{-1}\boldsymbol{H}_{k-1}\boldsymbol{G}_{k-1}^{T} + \boldsymbol{G}_{k-1}\boldsymbol{S}_{kfui,k-1}\boldsymbol{G}_{k-1}^{T} + \boldsymbol{Q}_{k-1}, \tag{2.188}$$

where $\boldsymbol{P}_{k-1|k-1}^{x}$ is calculated with

$$\boldsymbol{P}_{k-1|k-1}^{x} = (\boldsymbol{I}+\boldsymbol{K}_{kfui,k-1}\boldsymbol{H}_{k-1}\boldsymbol{S}_{kfui,k-1}\boldsymbol{H}_{k-1}^{T}\boldsymbol{R}_{k-1}^{-1}\boldsymbol{C}_{k-1})(\boldsymbol{I}-\boldsymbol{K}_{kfui,k-1}\boldsymbol{C}_{k})\boldsymbol{P}_{k-1|k-2}^{x}. \tag{2.189}$$

- Step 3: Compute the input estimate $\hat{\boldsymbol{d}}_k$ and the *a posteriori* state estimate $\hat{\boldsymbol{x}}_{k|k}$, which includes

$$\hat{\boldsymbol{d}}_k = \boldsymbol{S}_{kfui,k}\boldsymbol{H}_k^{T}\boldsymbol{R}_k^{-1}(\boldsymbol{I}_p - \boldsymbol{C}_k\boldsymbol{K}_{kfui,k})(\boldsymbol{y}_k - \boldsymbol{C}_k\hat{\boldsymbol{x}}_{k|k-1}) \tag{2.190}$$

and

$$\hat{\boldsymbol{x}}_{k|k} = \hat{\boldsymbol{x}}_{k|k-1} + \boldsymbol{K}_{kfui,k}\left[\boldsymbol{y}_k - \boldsymbol{C}_k\hat{\boldsymbol{x}}_{k|k-1} - \boldsymbol{H}_k\hat{\boldsymbol{d}}_k\right]. \tag{2.191}$$

The existence of the KF-UI requires that the following necessary and sufficient conditions should be fulfilled.

(1) Condition $p > m$ holds.

(2) Matrix $\left[\begin{array}{cccc} \boldsymbol{C}_1^T, & \boldsymbol{A}_1^T\boldsymbol{C}_2^T, & \cdots, & \boldsymbol{A}_1^T\boldsymbol{A}_2^T\cdots\boldsymbol{A}_{k-1}^T\boldsymbol{C}_k^T \end{array}\right]^T$ has full column rank.

(3) Matrix $\left[\boldsymbol{H}_i - \boldsymbol{C}_i\boldsymbol{A}_i^{-1}\boldsymbol{G}_i\right]$ has full column rank, $(i = 1, 2, \ldots, k-1)$.

(4) Matrix $\boldsymbol{H}_k$ has full column rank.

2.6.6. Augmented Kalman Filter (AKF)

Lourens et al. (2012b) proposed an Augmented Kalman Filter (AKF) method for the estimation of impact force on an instrumented steel beam. The main steps of the AKF are provided below.

Consider the linear discrete-time system which is described by

$$\boldsymbol{x}_{k+1} = \boldsymbol{A}_d\boldsymbol{x}_k + \boldsymbol{G}_d\boldsymbol{d}_k + \boldsymbol{w}_k \tag{2.192}$$

and

$$\boldsymbol{y}_k = \boldsymbol{C}_d\boldsymbol{x}_k + \boldsymbol{H}_d\boldsymbol{d}_k + \boldsymbol{v}_k, \tag{2.193}$$

where $\boldsymbol{x}_k \in \mathbb{R}^n$ represents the state; $\boldsymbol{d}_k \in \mathbb{R}^m$ denotes the unknown input; $\boldsymbol{y}_k \in \mathbb{R}^p$ is the output; $\boldsymbol{A}_d$, $\boldsymbol{G}_d$, $\boldsymbol{C}_d$ and $\boldsymbol{H}_d$ are system matrices with appropriate dimensions; $\boldsymbol{w}_k \in \mathbb{R}^n$ and $\boldsymbol{v}_k \in \mathbb{R}^p$ represent the process noise and the measurement noise, respectively. It is assumed that $\boldsymbol{w}_k$ and $\boldsymbol{v}_k$ are stationary, mutually uncorrelated, zero-mean and white, with known covariance matrices

$$\boldsymbol{Q}_d = E\left[\boldsymbol{w}_k\boldsymbol{w}_k^T\right] \tag{2.194}$$

and

$$\boldsymbol{R}_d = E\left[\boldsymbol{v}_k \boldsymbol{v}_k^T\right]. \tag{2.195}$$

Assume the dynamics of the input $\boldsymbol{d}_k$ can be described by

$$\boldsymbol{d}_{k+1} = \boldsymbol{d}_k + \boldsymbol{\eta}_k, \tag{2.196}$$

where $\boldsymbol{\eta}_k \in \mathbb{R}^m$ represents the increment of the unknown input $\boldsymbol{d}_k$. $\boldsymbol{\eta}_k$ is assumed to be a stationary zero-mean stochastic process which is uncorrelated with $\boldsymbol{w}_k$ and has the covariance matrix

$$\boldsymbol{Q}_d^{input} = E[\boldsymbol{\eta}_k \boldsymbol{\eta}_k^T]. \tag{2.197}$$

Introduce an augmented state $\boldsymbol{x}_{aug,k}$ as

$$\boldsymbol{x}_{aug,k} = \begin{bmatrix} \boldsymbol{x}_k \\ \\ \boldsymbol{d}_k \end{bmatrix}. \tag{2.198}$$

The system which is described by equaitons (2.192) and (2.193) can be transformed to

$$\boldsymbol{x}_{aug,k+1} = \boldsymbol{A}_{akf} \boldsymbol{x}_{aug,k} + \boldsymbol{w}_{aug,k} \tag{2.199}$$

and

$$\boldsymbol{y}_k = \boldsymbol{C}_{akf} \boldsymbol{x}_{aug,k} + \boldsymbol{v}_k, \tag{2.200}$$

where $\boldsymbol{A}_{akf}$ and $\boldsymbol{C}_{akf}$ are defined as

$$\boldsymbol{A}_{akf} = \begin{bmatrix} \boldsymbol{A}_d & \boldsymbol{G}_d \\ \\ \boldsymbol{0} & \boldsymbol{I} \end{bmatrix} \tag{2.201}$$

and

$$\boldsymbol{C}_{akf} = \begin{bmatrix} \boldsymbol{C}_d & \boldsymbol{H}_d \end{bmatrix}, \tag{2.202}$$

and $\boldsymbol{w}_{aug,k} \in \mathbb{R}^{n+m}$ denotes the augmented process noise.

By applying the Kalman filter, which has been reviewed in section 2.4, to the system which is described by equation (2.199) and equation (2.200), the estimates of the state and the unknown input can be obtained.

The existence of the AKF requires that the matrix pair $(\boldsymbol{A}_{akf}, \boldsymbol{C}_{akf})$ should be observable.

2.6.7. Steady-State Kalman Filter and a Least-Squares Estimator

Hwang et al. (2009a) proposed a procedure for input estimation based on Kalman filter

scheme. This procedure includes a Steady-State Kalman Filter and a Least-Squares Estimator (SSKF+LSE). To support the discussion in later chapters, a brief review of the SSKF+LSE is provided below.

Consider the system which is described by

$$\dot{\boldsymbol{x}}(t) = \boldsymbol{A}_c \boldsymbol{x}(t) + \boldsymbol{G}_c \boldsymbol{d}(t) \tag{2.203}$$

and

$$\boldsymbol{y}(t) = \boldsymbol{C}_c \boldsymbol{x}(t) + \boldsymbol{H}_c \boldsymbol{d}(t) + \boldsymbol{v}(t), \tag{2.204}$$

where $\boldsymbol{x}(t) \in \mathbb{R}^n$ represents the state; $\boldsymbol{d}(t) \in \mathbb{R}^m$ denotes the unknown input; $\boldsymbol{y}(t) \in \mathbb{R}^p$ is the output; $\boldsymbol{v}(t) \in \mathbb{R}^p$ is the measurement noise and the noise from higher modes which are not considered in the structural model; and $\boldsymbol{A}_c$, $\boldsymbol{G}_c$, $\boldsymbol{C}_c$, and $\boldsymbol{H}_c$ are the system matrices with appropriate dimensions. Vectors $\boldsymbol{d}(t)$ and $\boldsymbol{v}(t)$ are assumed to be mutually uncorrelated and white stationary processes, with the covariance matrices $\boldsymbol{Q}_{input}$ and $\boldsymbol{Q}_{meas}$, respectively.

The state update is described by

$$\dot{\hat{\boldsymbol{x}}}(t) = \boldsymbol{A}_c \hat{\boldsymbol{x}}(t) + \boldsymbol{K}_{sskf+lse}\left(\boldsymbol{y}(t) - \boldsymbol{C}_c \hat{\boldsymbol{x}}(t)\right) \tag{2.205}$$

and the input estimate is calculated by

$$\hat{\boldsymbol{d}}(t) = \boldsymbol{G}_c^{+} \boldsymbol{K}_{sskf+lse}\left(\boldsymbol{y}(t) - \boldsymbol{C}_c \hat{x}(t)\right), \tag{2.206}$$

where $\hat{\boldsymbol{x}}(t) \in \mathbb{R}^n$ represents the state estimate; $\hat{\boldsymbol{d}}(t) \in \mathbb{R}^m$ denotes the input estimate; $\boldsymbol{G}_c^{+}$ is the generalized inverse of $\boldsymbol{G}_c$ and is calculated by

$$\boldsymbol{G}_c^{+} = \left(\boldsymbol{G}_c^T \boldsymbol{G}_c\right)^{-1} \boldsymbol{G}_c^T; \tag{2.207}$$

and $\boldsymbol{K}_{sskf+lse}$ is the gain matrix and is determined by

$$\boldsymbol{K}_{sskf+lse} = \left(\boldsymbol{G}_c \boldsymbol{Q}_{input} \boldsymbol{H}_c^T + \boldsymbol{P} \boldsymbol{C}_c^T\right)\left(\boldsymbol{H}_c \boldsymbol{Q}_{input} \boldsymbol{H}_c^T + \boldsymbol{Q}_{meas}\right)^{-1}, \tag{2.208}$$

where the matrix $\boldsymbol{P}$ is determined by solving the algebraic Ricatti equation

$$\begin{aligned} \boldsymbol{A}_c \boldsymbol{P} + \boldsymbol{P} \boldsymbol{A}_c^T - \left(\mathrm{G}_c \boldsymbol{Q}_{input} \boldsymbol{H}_c^T + \boldsymbol{P} \boldsymbol{C}_c^T\right)\left(\boldsymbol{H}_c \boldsymbol{Q}_{input} \boldsymbol{H}_c^T + \boldsymbol{Q}_{meas}\right)^{-1}\left(\boldsymbol{C}_c \boldsymbol{P} + \boldsymbol{H}_c \mathrm{Q}_{input} \boldsymbol{G}_c^T\right) \\ + \boldsymbol{G}_c \boldsymbol{Q}_{input} \boldsymbol{G}_c^T = \boldsymbol{0}. \end{aligned} \tag{2.209}$$

In Hwang et al. (2009b), the values of the covariance matrices $\boldsymbol{Q}_{input}$ and $\boldsymbol{Q}_{meas}$ are

considered to be unknown, and are set as

$$\boldsymbol{Q}_{input} = \boldsymbol{I}_m \tag{2.210}$$

and

$$\boldsymbol{Q}_{meas} = \gamma \boldsymbol{I}_p. \tag{2.211}$$

By adjusting the value of γ, the values of $\boldsymbol{P}$ and $\boldsymbol{K}_{sskf+lse}$ are determined by solving equations (2.209) and (2.208).

Define the state estimate error $\tilde{\boldsymbol{x}}(t)$ as in equation (2.212),

$$\tilde{\boldsymbol{x}}(t) = \boldsymbol{x}(t) - \hat{\boldsymbol{x}}(t). \tag{2.212}$$

The dynamics of $\tilde{\boldsymbol{x}}(t)$ can be described by

$$\dot{\tilde{\boldsymbol{x}}}(t) = (\boldsymbol{A}_c - \boldsymbol{K}_{sskf+lse}\boldsymbol{C}_c)\,\tilde{\boldsymbol{x}}(t) + (\boldsymbol{G}_c - \boldsymbol{K}_{sskf+lse}\boldsymbol{H}_c)\,\boldsymbol{d}(t) - \boldsymbol{K}_{sskf+lse}\boldsymbol{v}(t). \tag{2.213}$$

The existence of the SSKF+LSE indicates that the following necessary conditions are fulfilled.

(1) Matrix $\boldsymbol{G}_c$ has full column rank.

(2) Matrix pair ($\boldsymbol{A}_c$, $\boldsymbol{C}_c$) is observable.

2.7. Correlation of the process noise and the measurement noise

Assume the structure under investigation can be modeled in the form of a continuous-time state-space model as in equations (2.12) and (2.13). If the process noise (or the modeling error) and the measurement noise are considered, the state-space structural model appear as

$$\dot{\boldsymbol{x}}(t) = \boldsymbol{A}_c\boldsymbol{x}(t) + \boldsymbol{G}_c\boldsymbol{d}(t) + \boldsymbol{w}(t) \tag{2.214}$$

and

$$\boldsymbol{y}(t) = \boldsymbol{C}_c\boldsymbol{x}(t) + \boldsymbol{H}_c\boldsymbol{d}(t) + \boldsymbol{v}(t), \tag{2.215}$$

where the vectors $\boldsymbol{x}(t)$, $\boldsymbol{d}(t)$ and $\boldsymbol{y}(t)$ and the matrices $\boldsymbol{A}_c$, $\boldsymbol{G}_c$, $\boldsymbol{C}_c$ and $\boldsymbol{H}_c$ are defined the same as in section (2.1.2); $\boldsymbol{w}(t) \in \mathbb{R}^n$ denotes the process noise with the form

$$\boldsymbol{w}(t) = \begin{bmatrix} \boldsymbol{0}_{mDOF\times 1} \\ \boldsymbol{w}_{model}(t) \end{bmatrix}, \tag{2.216}$$

where $\boldsymbol{w}_{model}(t) \in \mathbb{R}^m$ denotes the modeling error, and $\boldsymbol{v}(t) \in \mathbb{R}^p$ represents the process noise with the form

$$\boldsymbol{v}(t) = \begin{bmatrix} \boldsymbol{v}_{ds}(t) \\ \boldsymbol{v}_v(t) \\ \boldsymbol{v}_a(t) \end{bmatrix}, \tag{2.217}$$

with $\boldsymbol{v}_{ds}(t) \in \mathbb{R}^{p\_ds}$, $\boldsymbol{v}_v(t) \in \mathbb{R}^{p\_v}$ and $\boldsymbol{v}_a(t) \in \mathbb{R}^{p\_a}$ representing respectively the noise in the displacement (or strain) measurement, the velocity measurement, and the acceleration measurement, respectively. The $\boldsymbol{v}_a(t)$ can be expressed as

$$\boldsymbol{v}_a(t) = \boldsymbol{v}_{a,sensor}(t) + \boldsymbol{v}_{a,model}(t), \tag{2.218}$$

where $\boldsymbol{v}_{a,sensor}(t)$ represents the noise from the sensor, and $\boldsymbol{v}_{a,model}(t)$ denotes the noise from the modeling error. With equations (2.14) through (2.17), $\boldsymbol{v}_{a,model}(t)$ can be determined with

$$\boldsymbol{v}_{a,model}(t) = [\boldsymbol{C}_a \boldsymbol{\Phi} \boldsymbol{w}_{model}(t)]. \tag{2.219}$$

In equation (2.219), the linear relationship between $\boldsymbol{v}_{a,model}(t)$ and $\boldsymbol{w}_{model}(t)$ actually indicates that $\boldsymbol{w}_{model}(t)$ and $\boldsymbol{v}_{a,model}(t)$ are correlated. The covariance matrix of the process noise $\boldsymbol{w}(t)$ can be calculated with

$$E\left[\boldsymbol{w}(t)\,\boldsymbol{w}(t)^T\right] = \begin{bmatrix} \mathbf{0}_{mDOF\times mDOF} & \boldsymbol{0}_{mDOF\times m} \\ \boldsymbol{0}_{m\times mDOF} & E\left[\boldsymbol{w}_{model}(t)\,\boldsymbol{w}_{model}(t)^T\right] \end{bmatrix} \tag{2.220}$$

and the covariance matrices of the measurement noise $\boldsymbol{v}(t)$ can be calculated with

$$\begin{aligned} E\left[\boldsymbol{v}(t)\,\boldsymbol{v}(t)^T\right] &= \begin{bmatrix} E\left[\boldsymbol{v}_{ds}(t)\,\boldsymbol{v}_{ds}(t)^T\right] & \boldsymbol{0}_{p_{ds}\times p_v} & \boldsymbol{0}_{p_{ds}\times p_a} \\ \boldsymbol{0}_{p_v\times p_{ds}} & E\left[\boldsymbol{v}_v(t)\,\boldsymbol{v}_v(t)^T\right] & \boldsymbol{0}_{p_v\times p_a} \\ \boldsymbol{0}_{p_a\times p_{ds}} & \mathbf{0}_{p_a\times p_v} & E\left[\boldsymbol{v}_a(t)\,\boldsymbol{v}_a(t)^T\right] \end{bmatrix} \\ &+ \begin{bmatrix} \boldsymbol{0}_{p_{ds}\times p_{ds}} & \boldsymbol{0}_{p_{ds}\times p_v} & \mathbf{0}_{p_{ds}\times p_a} \\ \boldsymbol{0}_{p_v\times p_{ds}} & \boldsymbol{0}_{p_v\times p_v} & \mathbf{0}_{p_v\times p_a} \\ \boldsymbol{0}_{p_a\times p_{ds}} & \boldsymbol{0}_{p_a\times p_v} & \boldsymbol{C}_a\boldsymbol{\Phi}E\left[\boldsymbol{w}_{model}(t)\,\boldsymbol{w}_{model}(t)^T\right]\boldsymbol{\Phi}^T\boldsymbol{C}_a^T \end{bmatrix}. \end{aligned} \tag{2.221}$$

Assume $\boldsymbol{w}_{model}(t)$ is uncorrelated with $\boldsymbol{v}_{ds}(t)$, $\boldsymbol{v}_v(t)$ and $\boldsymbol{v}_{a,sensor}(t)$. The crosscorrelation

of $\boldsymbol{w}(t)$ and $\boldsymbol{v}(t)$ can be calculated with

$$E\left[\boldsymbol{w}(t)\,\boldsymbol{v}(t)^T\right] = \begin{bmatrix} \boldsymbol{0}_{mDOF\times p_{ds}} & \boldsymbol{0}_{mDOF\times p_v} & \boldsymbol{0}_{mDOF\times p_a} \\ \boldsymbol{0}_{mDOF\times p_{ds}} & \boldsymbol{0}_{mDOF\times p_v} & E\left[\boldsymbol{w}_{model}(t)\,\boldsymbol{w}_{model}(t)^T\right]\boldsymbol{\Phi}^T\boldsymbol{C}_a^T \end{bmatrix}. \tag{2.222}$$

With equation (2.222) it can be concluded that the process noise $\boldsymbol{w}(t)$ and the measurement noise $\boldsymbol{v}(t)$ are correlated if acceleration responses are considered in the output equation of the state-space structural model.

The structural model which is described by equations (2.214) and (2.215) can be transformed to its discrete-time counterpart as

$$\boldsymbol{x}_{k+1} = \boldsymbol{A}_d\boldsymbol{x}_k + \boldsymbol{G}_d\boldsymbol{d}_k + \boldsymbol{w}_k \tag{2.223}$$

and

$$\boldsymbol{y}_k = \boldsymbol{C}_d\boldsymbol{x}_k + \boldsymbol{H}_d\boldsymbol{d}_k + \boldsymbol{v}_k, \tag{2.224}$$

where $\boldsymbol{A}_d$, $\boldsymbol{G}_d$, $\boldsymbol{C}_d$, and $\boldsymbol{H}_d$ represent the system matrices; the process noise $\boldsymbol{w}_k$ is determined by

$$\boldsymbol{w}_k = \int_{k\triangle t}^{(k+1)\triangle t} e^{\boldsymbol{A}_c\triangle t}\boldsymbol{w}(t)\,dt \tag{2.225}$$

and the measurement noise $\boldsymbol{v}_k$ is determined by

$$\boldsymbol{v}_k = \frac{1}{\triangle t}\int_{(k-1)\triangle t}^{k\triangle t} \boldsymbol{v}(t)\,dt. \tag{2.226}$$

The covariance matrix of $\boldsymbol{w}_k$ is calculated with

$$E\left[\boldsymbol{w}_k\boldsymbol{w}_k^T\right] = \int_{k\triangle t}^{(k+1)\triangle t}\int_{k\triangle t}^{(k+1)\triangle t} \left(e^{\boldsymbol{A}_c\triangle t}\right) E\left[\boldsymbol{w}(\xi)\,\boldsymbol{w}(\eta)^T\right]\left(e^{\boldsymbol{A}_c\triangle t}\right)^T d\xi d\eta \tag{2.227}$$

and the covariance matrix of $\boldsymbol{v}_k$ is calculated with

$$E\left[\boldsymbol{v}_k\boldsymbol{v}_k^T\right] = \frac{1}{(\triangle t)^2}\int_{(k-1)\triangle t}^{k\triangle t}\int_{(k-1)\triangle t}^{k\triangle t} E\left[\boldsymbol{v}(t)\,\boldsymbol{v}(t)^T\right] d\xi d\eta. \tag{2.228}$$

For the discrete-time model, the cross-correlation of the process noise and the measurement noise is calculated with (Brown and Hwang, 1997)

$$\boldsymbol{S}_k = E\left[\boldsymbol{w}_{k-1}\boldsymbol{v}_k^T\right]. \tag{2.229}$$

Substituting equation (2.225) and equation (2.226) into the right side of equation (2.229)

leads to

$$\boldsymbol{S}_k = \frac{e^{\boldsymbol{A}_c \triangle t}}{\triangle t} \int_{(k-1)\triangle t}^{k\triangle t} \int_{(k-1)\triangle t}^{k\triangle t} E\left[\boldsymbol{w}\left(\xi\right) \boldsymbol{v}\left(\eta\right)^T\right] d\xi d\eta. \tag{2.230}$$

It can be proved that if the matrix $\boldsymbol{C}_a$ in equation (2.222)is a non-zero matrix, $\mathbf{S}_k$ will be a non-zero matrix. As introduced in section (2.1.1), $\boldsymbol{C}_a$ defines the positions of the acceleration sensors. This means that if acceleration responses are considered in the output equation of the state-space structural model, the process noise and the measurement noise will be correlated.

3. Problem formulation and methodology

Force reconstruction is the process to reconstruct the forces from structural response measurements. This process is a kind of inverse problem which often tends to be ill-posed. Online force reconstruction is the research topic which studies how to realize force reconstruction in real-time. Thus, online force reconstruction needs to solve the following two problems.

(1) How to relax the ill-posedness in the process of force reconstruction?

(2) How to realize force reconstruction in real-time?

In section 3.1, force reconstruction is classified as a kind of inverse problem. The ill-posed nature in the force reconstruction process is described in section 3.2. Section 3.3 discusses the observability of the state and the convergence of the estimate error of the force.

The basic idea which is adopted in this thesis for online force reconstruction has been introduced in section 1.3. It is clearly stated that the structural model is needed in the design of the real-time executable state and input estimation algorithm. In this thesis, the methodology for online force reconstruction is composed of an offline stage and an online stage. In the offline stage, the structural model is identified. In the online stage, a simultaneous reconstruction of the external force and the structural response is realized.

In practice, it is often one of the following two cases:

- Case I: It is possible to apply an artificial excitation force on the investigated structure.
- Case II: It is difficult or not possible to apply an artificial excitation force on the investigated structure.

In this chapter, the methodology for each of the above two practical cases is presented in the form of block diagram in section 3.4 and section 3.5. Furthermore, the method which is applied in this thesis for the reconstruction of a distributed force with unknown spatial distribution is explained in section 3.6.

3.1. Force reconstruction is a kind of inverse problem

"*We call two problems inverses of one another if the formulation of each involves all or part of the solution of the other. Often, for historical reasons, one of the two problems have been studied extensively for some time, while the other is newer and not so well*

understood. In such cases, the former is called the direct problem, while the later is called the inverse problem." (Keller, 1976).

Consider a linear problem which can be formulated in the following very general form (Hansen, 1998),

$$\int_{\Omega} \text{input} \times \text{system}\, d\Omega = \text{output}. \tag{3.1}$$

The direct problem is to compute the output, with known input and mathematical description of the system. Figure 3.1 describes the direct problem in the form of a block diagram. The inverse problem is to determine either the input or the system which gives rise to the (noisy) measurements of the output. There are two kinds of inverse problem. One is to determine the unknown input, as described in figure 3.2a. The other one is to identify a model for the unknwon system, as described in figure 3.2b.

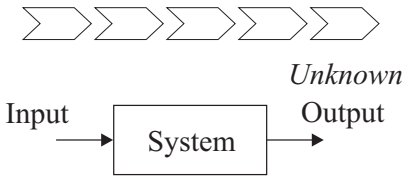

Figure 3.1. *Description of the direct problem in the form of a block diagram*

Consider a structure which is assumed as linear and is at rest at time $t = 0$. If an arbitrary force $f(t)$ is applied on this structure at time $t = 0$, the response of this structure to the arbitrary force $f(t)$ can be expressed using the Duhamel integral (Clough and Penzien, 2003)

$$y(t) = \int_0^t f(\tau)\, h(t-\tau)\, d\tau, \tag{3.2}$$

where $y(t)$ denotes the structural response, $f(\tau)$ is the value of the force $f(t)$ at time $t = \tau$, and $h(t-\tau)$ represents the impulse response function of the structure with a unit impulse applied at time $t = \tau$. The impulse response function $h(t)$ is actually a mathematical description of the structure. Force reconstruction is the process to determine the force $f(t)$, given the known structural model $h(t)$ and the measurements of the structural response $y(t)$. This process can be described by the block diagram in figure 3.3. By comparing figure 3.3 with figure 3.2a, it can be concluded that force reconstruction belongs to the inverse problem in figure 3.2a.

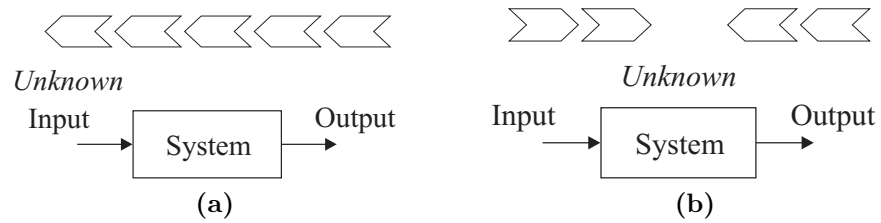

Figure 3.2. *Description of the two kinds inverse problems in the form of block diagrams*

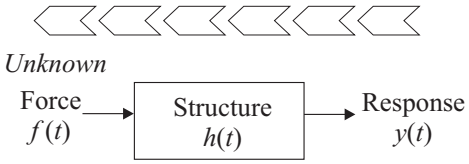

Figure 3.3. *Description of the force reconstruction process in the form of a block diagram*

3.2. Ill-posed nature in force reconstruction

The concept of well-posedness dates back to Hadamard (1902). Hadamard (1923) proposed the following three postulates.

(1) Existence of a solution.

(2) Uniqueness of the solution.

(3) Continuous dependence of the solution on the data.

If a problem satisfies the three postulates above, it is called well-posed. Otherwise, the problem is said to be ill-posed. According to this definition, there are the following three types of ill-posedness (Kress, 1989).

(a) Nonexistence of a solution, i.e. the problem is not solvable.

(b) Nonuniqueness of the solution, i.e. there are more than one solution.

(c) Instability of the solution, i.e. the solution does not depends continuously on the data.

A linear Fredholm integral equation of the first kind can be written in the form

$$\int_{I_\tau} K(t,\tau) f(\tau) d\tau = y(t), \; t \in I_t, \tag{3.3}$$

where $K(t,\tau)$ is called the kernel. If the norm

$$\|K(t,\tau)\|_2 = \left(\int_{I_t} \int_{I_\tau} K(t,\tau)^2 d\tau dt \right)^{1/2} \tag{3.4}$$

exists, the kernel $K(t,\tau)$ is said to be square integrable and can be expressed in the form of a Singular Value Expansion (SVE) as

$$K(t,\tau) = \sum_{i=1}^{\infty} \mu_i u_i(t) v_i(\tau), \; t \in I_t, \; \tau \in I_\tau, \tag{3.5}$$

where μ_i represents the i-th singular value of the kernel $K(t,\tau)$, $u_i(t)$ denotes the i-th left singular function of $K(t,\tau)$, and $v_i(\tau)$ is the i-th right singular function of the kernel

$K(t,\tau)$ (Hansen, 1988). The singular values have the property $\mu_1 \geq \mu_2 \geq \mu_3 \cdots \geq 0$. The singular functions $u_i(t)$ and $v_i(\tau)$ are orthonormal.

The Duhamel integral in equation (3.2) can be formulated into the form of the linear Fredholm integral equation of the first kind in equation (3.3). Assume the structural response $y(t)$ is known, and the impulse response function $h(t-\tau)$ in equation (3.2) is square integrable. Then there is a solution of the force $f(\tau)$ to the Duhamel integral in equation (3.2), if and only if the condition

$$\sum_{i=1}^{\infty} \left(\frac{\int_{I_t} y(t)\, u_i(t)\, dt}{\mu_i} \right)^2 < \infty \tag{3.6}$$

holds. In this case the solution of $f(\tau)$ is given by

$$f(\tau) = \sum_{i=1}^{\infty} \left(\frac{\int_{I_t} y(t)\, u_i(t)\, dt}{\mu_i} \right) v_i(\tau). \tag{3.7}$$

The above statement can be proved with the help of the Picard criterion (or the Picard condition) in e.g. Kress (1989) and Engl et al. (1996).

In practice, the structural response $y(t)$ is measured by sensors, which indicates that the measured $y(t)$ will be contaminated by unavoidable measurement noise. Besides this, if a structure is modeled in its modal form which includes only limited number of modes, it leads to a difference between the modeled structural response and the measured structural response. Assume the structural response $y(t)$ is perturbed as

$$y_{perturb}(t) = y(t) + \delta u_n(t), \tag{3.8}$$

where $y_{perturb}(t)$ denotes the perturbed $y(t)$, and δ, together with the left singular function $u_n(t)$, forms a small perturbation $\delta u_n(t)$. Introduce $f_{perturb}(t)$ as the reconstructed $f(t)$. With equation (3.7) and equation (3.8), the following relationship can be obtained,

$$\frac{\| f_{perturb}(t) - f(t) \|_2}{\| y_{perturb}(t) - y(t) \|_2} = \frac{1}{\mu_n}. \tag{3.9}$$

As the singular value μ_n tends to zero, the left side of equation (3.9) can be extremely large. This means that a small perturbation in the measured structural response can cause a very large deviation in the reconstructed force. If $y_{perturb}(t)$ is inserted into equation (3.7), the value of $f_{perturb}(t)$ can be arbitrarily large. In this case, the reconstructed force does not depend continuously on the measured structural response, or the reconstructed force is lack of stability. This contradicts with the Hadamard's postulates of well-posedness, and demonstrates the ill-posed nature in force reconstruction.

Thus, one main task in force reconstruction study is to find a stable approximate solution of this ill-posed problem, so that the reconstructed force depends on the measured structural response continuously, or a small perturbation in the measured structural response causes a small deviation in the reconstructed force.

3.3. From ill-posedness to well-posedness in online force reconstruction

The basic idea which is adopted in this thesis for online force reconstruction is to apply a real-time executable state and input estimation algorithm. Figure 1.2 describes this basic idea in the form of a block diagram. Consider the structure under investigation as a system, the force which needs to be reconstructed as the input to the system, and the structural response as the output from the system. Given structural response measurements, the applied algorithm can provide an estimate of the force in real-time. The ill-posedness in the force reconstruction process is relaxed through the convergence of the estimate error of the force. To apply this basic idea, the system, i.e. the structural model, should be observable. Section 3.3.1 gives the definition of observability and the mathematical test for determining observability. In section 3.3.2 the convergence of the estimate error of the force is discussed.

3.3.1. Observability

The concept of observability was introduced in Kalman (1959). It is the ability to deduce information about all the modes of the system by monitoring only the sensed outputs (Franklin et al., 2006). When applying the basic idea in figure 1.2 for online force reconstruction, the observability should be checked first.

Consider the continuous-time state-space structural model which is described by equation (2.12) and equation (2.13). The mathematical test for determining the observability is that the matrix

$$\boldsymbol{O}_{bc} = \begin{bmatrix} \boldsymbol{C}_c \\ \boldsymbol{C}_c\boldsymbol{A}_c \\ \boldsymbol{C}_c\boldsymbol{A}_c^2 \\ \vdots \\ \boldsymbol{C}_c\boldsymbol{A}_c^{n-1} \end{bmatrix} \tag{3.10}$$

must have independent columns. In other words, the condition $rank\,(\boldsymbol{O}_{bc}) = n$ should hold, where n represents the dimension of the state vector. The matrix $\boldsymbol{O}_{bc}$ is called

the observability matrix. For the case that the state-space structural model is in its discrete-time form, the observability matrix appears in the form

$$\boldsymbol{O}_{bd} = \begin{bmatrix} \boldsymbol{C}_d \\ \boldsymbol{C}_d\boldsymbol{A}_d \\ \boldsymbol{C}_d\boldsymbol{A}_d^2 \\ \vdots \\ \boldsymbol{C}_d\boldsymbol{A}_d^{n-1} \end{bmatrix}. \tag{3.11}$$

The mathematical test for determining the observability is that the condition $rank\,(\boldsymbol{O}_{bd}) = n$ should hold.

3.3.2. Stability and convergence

In section 3.2, the ill-posed nature in force reconstruction has been discussed. It is concluded that one main task in force reconstruction study is to find a stable solution of this ill-posed problem, so that reconstructed force depends on the measured structural response continuously. As it is described in figure 1.2, the basic idea which is adopted in this thesis for online force reconstruction is to apply a real-time executable state and input estimation algorithm. If the input estimation can provide an estimate of the force which converges to the true value of the force, the ill-posedness in force reconstruction is relaxed.

In case the state-space structural model is deterministic, i.e. in the form of equations (2.12) and (2.13), the estimate error of the force should converge to zero.

In case the state-space structural model includes stochastic information, e.g. the modeling errors and the measurement noise, the covariance matrix of the estimate error of the force should converge.

The requirements on stability and convergence can be fulfilled by proper structural model construction, proper sensor selection, and proper sensor placement.

3.4. Methodology for online force reconstruction with structural modal parameters identified by experimental modal analysis

For practical cases where it is possible to apply an artificial force on the structure, the methodology for online force reconstruction is presented in figure 3.4. This methodology is composed of two stages, an offline stage and an online stage.

In the offline stage, Experimental Modal Analysis (EMA) is applied to identify the modal parameters of the structure, including natural frequencies, damping ratios, mode shape vectors, and modal participation factors. With the identified modal parameters, a state-space structural model in the modal coordinates can be constructed. The principle of the EMA has been briefly reviewed in section 2.1.4. The steps for constructing the state-space structural model in the modal coordinates have been provided in section 2.1.1 through section 2.1.3. It is noted here that the mode shape vectors which are identified from the EMA do not correspond to the columns of the modal matrix $\boldsymbol{\Phi}$ but the columns of the matrix $\boldsymbol{M}_n^{1/2}\boldsymbol{\Phi}$.

In the online stage, a suitable real-time executable state and input estimation algorithm is applied to reconstruct the force. Furthermore, this methodology is also capable of reconstructing the structural responses at selected positions.

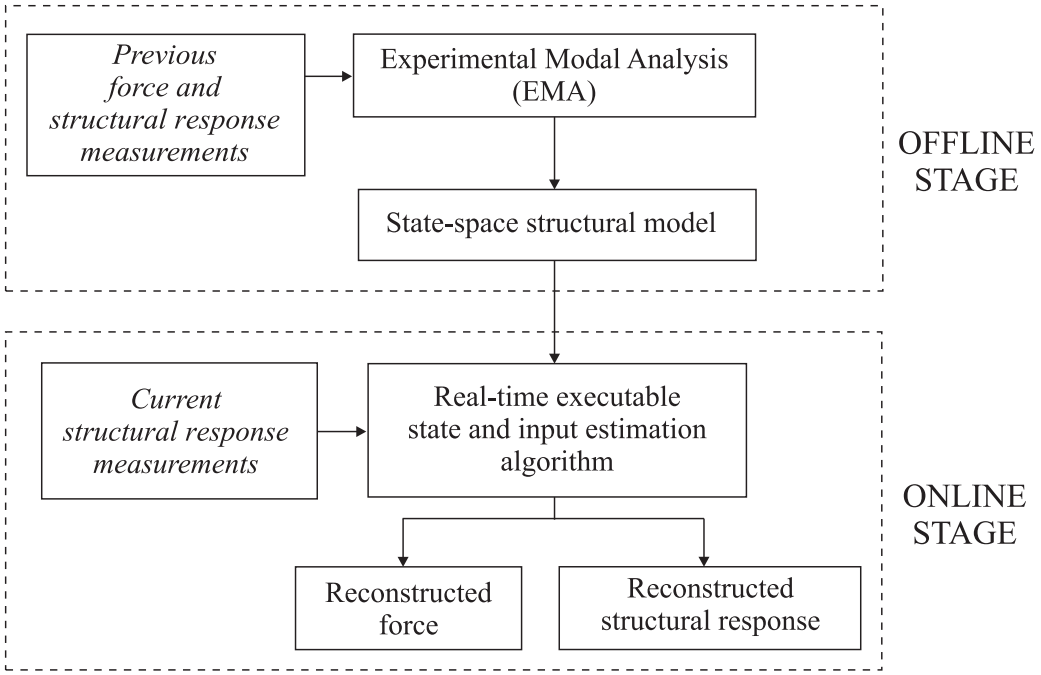

Figure 3.4. *Block diagram of the methodology for online force reconstruction with structural modal parameters identified by experimental modal analysis*

3.5. Methodology for online force reconstruction with structural modal parameters identified by operational modal analysis

For practical cases where it is difficult or not possible to apply an artificial force on the structure, the methodology for online force reconstruction is presented in figure 3.5. This methodology is composed of two stages, an offline stage and an online stage.

In the offline stage, Operational Modal Analysis (OMA) is applied to identify the modal parameters of the structure, including natural frequencies, damping ratios, and mode shape vectors. The principle of OMA has been briefly reviewed in section 2.1.5. Each of the identified mode shape vectors is proportional to one of the columns of the modal matrix $\boldsymbol{\Phi}$. However, the scaling factor for the identified mode shape vector is missing. According to equation (2.6), the columns of $\boldsymbol{\Phi}$ are mass normalized. This indicates that if the mass matrix of the structural model is available, it is still possible to correctly scale the identified mode shapes. In practice, an FE model of the structure under investigation is often available. The mass matrix of the FE model usually reflects the mass distribution of the structure with good accuracy. In this methodology, the FE model of the structure is updated according to the modal parameters which are identified from the OMA. The mode shape vectors which are calculated from the FE model are already correctly scaled, and usually have high spatial resolution than the mode shape vectors which are identified from the OMA. With the natural frequencies and the damping ratios which are identified from the OMA and the mode shape vectors which are calculated from the FE model, the state-space structural model in the modal coordinates can be constructed by following the steps which have been provided in section 2.1.1 through section 2.1.5.

In the online stage, a suitable real-time executable state and input estimation algorithm is applied to reconstruct the force. Furthermore, this methodology is also capable of reconstructing the structural responses at selected positions.

3.6. Methodology for the reconstruction of a distributed force with unknown spatial distribution

A distributed force is characterized by

$$f(x,t) = \sum_{i=1}^{m} B_{o_i}(x)\, d_i(t)\,, \tag{3.12}$$

where $B_{o_i}(x)$ represents the i-th spatial distribution, and $d_i(t)$ denotes the weighting value of $B_{o_i}(x)$ in time. If m is equal to one, it means that the spatial distribution of

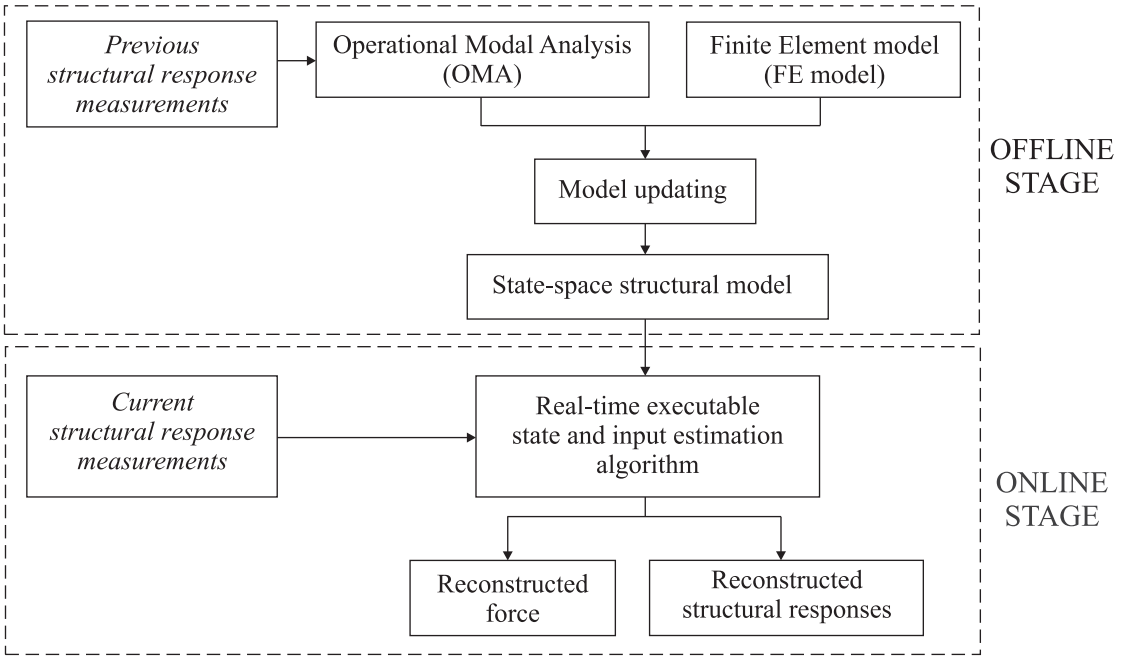

Figure 3.5. *Block diagram of the methodology for online force reconstruction with structural modal parameters identified by operational modal analysis*

the force does not change, and only the weighting value changes with time. If m is larger than one, the distributed force $f(x,t)$ is a combination of several distributed forces, and the weighting values $d_i(t)$ all change with time. If $B_{o_i}(x)$ is described by Dirac's delta function, $B_{o_i}(x)$ describes the spatial distribution of a concentrated force. If the spatial distribution function $B_{o_i}(x)$ is known, $d_i(t)$ can be estimated in real-time by using the basic idea in figure 1.2. Then the distributed force $f(x,t)$ can be reconstructed with equation (3.12) online. In case the spatial distribution of the force $f(x,t)$ is unknown, a suitable mathematical description for $B_{o_i}(x)$ needs to be defined first. Then $d_i(t)$ can be estimated in real-time by by using the basic idea in figure 1.2, and the distributed force $f(x,t)$ can be reconstructed with equation (3.12) online. For this case, the selection of the mathematical description for the spatial distribution $B_{o_i}(x)$ will have an effect on the reconstruction results.

In practice, structures are usually complicated and a FE model of the structure is often available. Thus it is of more interest to consider the equivalent forces on the nodes of the FE model of the structure. In this case, equation (3.12) can be expressed in the form of equation (2.10).

If the spatial distribution of the force is known in advance, the online reconstruction of the distributed force can be realized through a real-time estimation of the weighting value of the spatial distribution of the force. However, there are still many cases where the spatial distribution of the force is not known in advance. This thesis focuses on the cases where the force is distributed on the structure. In practice, a FE model of the structure is often available, and it is usually of more interest to consider the distributed force in

the form of equivalent nodal loading. According to section 2.1.1, when the second-order structural model is transformed from the nodal coordinates to the modal coordinates, the force $\boldsymbol{f}(t)$ is transformed to the modal force $\boldsymbol{f}_m(t)$ as

$$\boldsymbol{f}_m(t) = \boldsymbol{\Phi}^T \boldsymbol{f}(t). \tag{3.13}$$

Substituting equation (2.10) into equation (3.13) leads to

$$\boldsymbol{f}_m(t) = \boldsymbol{\Phi}^T \boldsymbol{B}_o \boldsymbol{d}(t), \tag{3.14}$$

where $\boldsymbol{\Phi} \in \mathbb{R}^{nDOF \times mDOF}$ represents the modal matrix, and the j-th column of the matrix $\boldsymbol{B}_o \in \mathbb{R}^{nDOF \times m}$ describes the spatial distribution of the j-th force. The j-th element of $\boldsymbol{d}(t) \in \mathbb{R}^m$ is the weighting value of the spatial distribution of the j-th force. Here, $nDOF$ represents the number of nodal Degrees of Freedom (DOF), $mDOF$ denotes the number of modes which are considered in the model, and the value of $nDOF$ and the value of $mDOF$ fulfill the condition $mDOF \leq nDOF$. m denotes the number of input forces, and the value of j is in the range $0 \leq j \leq m$. If the elements in the i-th row of the matrix $\boldsymbol{\Phi}^T \boldsymbol{B}_o$ are all zero, there is no excitation to the the i-th mode of the structure. The value of i is in the range $0 \leq i \leq mDOF$. Thus, the columns of $\boldsymbol{\Phi}$ actually works as a kind of filter. Only when the inner product of the i-th row of $\boldsymbol{\Phi}^T$ and the j-th column of the $\boldsymbol{B}_o$ is not zero, or the j-th column of the $\boldsymbol{B}_o$ has a projection on the i-th row of $\boldsymbol{\Phi}^T$, the j-th force has effect on the i-th mode of the structure.

For cases where the spatial distribution of the external force is unknown, the method which is applied in this thesis is to set

$$\boldsymbol{B}_o = \boldsymbol{M}_n \boldsymbol{\Phi}, \tag{3.15}$$

where $\boldsymbol{M}_n \in \mathbb{R}^{nDOF \times nDOF}$ denotes the mass matrix of the structural model. If the condition $mDOF = nDOF$ holds, which means the number of modes is equal to the number of DOF in the nodal coordinates, $\boldsymbol{B}_o$ will be a square matrix with full rank. Then any spatial distribution vectors with $nDOF$ elements can be expressed by a linear combination of the columns of $\boldsymbol{B}_o$. In most practical cases, the condition $mDOF < nDOF$ holds, which means only limited modes are considered in the structural model. In these cases, the distributed force can only be spatially partly reconstructed.

4. Proposed algorithm modifications

In chapter 3, the methodology for online force reconstruction has been presented. This methodology is composed of two stages, an offline stage and an online stage. In the offline stage, a state-space structural model is constructed. In the online stage, a real-time executable state and input estimation algorithm is applied to provide an estimate of the force. The available state and input estimation algorithms have been reviewed in section 2.6. In this chapter, modifications to some of the available algorithms are proposed, so that these algorithms are theoretically more suitable for online force reconstruction. In section 4.1, the SS&IE is modified so that it is suitable for linear structural models. In section 4.2, the filter equations of the KF+RLSE in steady-state are presented. These presented filter equations can simplify the implementation of the KF+RLSE. According to the discussion in section 2.7, the usage of accelerometers means the process noise and the measurement noise are correlated. To be compatible with such correlation, a generalized KF-UI (G-KF-UI) is proposed in section 4.3. In section 4.4, the SSKF+LSE is modified to consider an estimate of the covariance matrix of the force and an estimate of the covariance matrix of the measurement noise.

4.1. Simultaneous State and Input Estimator for Linear systems (SS&IE_L)

The SS&IE, which has been reviewed in section 2.6.2, was originally proposed for a class of nonlinear systems. In the SS&IE, it is assumed that there is a known nonlinear term which fulfills a Lipschitz condition and an unknown nonlinear term. As introduced in section 2.1.1 through section 2.1.3, the structural model in the modal coordinates is linear. Based on the work in Ha and Trinh (2004), the SS&IE is modified to be suitable for linear systems. In this thesis, this modified SS&IE is named as SS&IE_L which is short for Simultaneous State and Input Estimator for Linear systems.

Consider the structural model which is described by equations (2.12) and (2.13). Introduce the augmented state $\boldsymbol{x}_{aug}(t)$ as in equation (2.127). With the matrix definition in equations (2.129) through (2.131), the structural model which is described by equations (2.12) and (2.13) can be transformed into

$$\boldsymbol{E}_{ssie}\dot{\boldsymbol{x}}_{aug}(t) = \boldsymbol{M}_{ssie}\boldsymbol{x}_{aug}(t) \tag{4.1}$$

and

$$\boldsymbol{y}(t) = \boldsymbol{H}_{ssie}\boldsymbol{x}_{aug}(t). \tag{4.2}$$

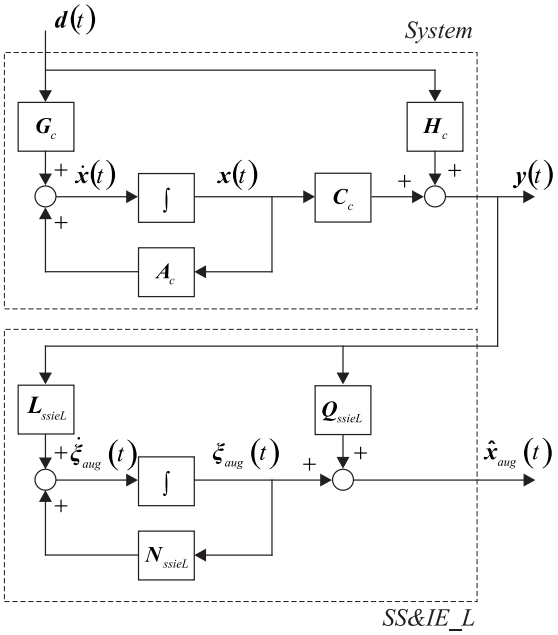

Figure 4.1. *Description of the SS&IE_L in the form of a block diagram*

The UIO is described by

$$\dot{\boldsymbol{\xi}}_{aug}(t) = \boldsymbol{N}_{ssieL}\boldsymbol{\xi}_{aug}(t) + \boldsymbol{L}_{ssieL}\boldsymbol{y}(t) \tag{4.3}$$

and

$$\hat{\boldsymbol{x}}_{aug}(t) = \boldsymbol{\xi}_{aug}(t) + \boldsymbol{Q}_{ssieL}\boldsymbol{y}(t), \tag{4.4}$$

where $\hat{\boldsymbol{x}}_{aug}(t)$ represents the estimate of $\boldsymbol{x}_{aug}(t)$, and $\boldsymbol{N}_{ssieL}$, $\boldsymbol{L}_{ssieL}$ and $\boldsymbol{Q}_{ssieL}$ are the matrices which need to be designed. Figure 4.1 describes the SS&IE_L in the form of a block diagram.

Introduce the notations

$$\boldsymbol{S}_{ssieL} = \begin{bmatrix} \boldsymbol{E}_{ssie} \\ \boldsymbol{H}_{ssie} \end{bmatrix}, \tag{4.5}$$

$$\boldsymbol{J}_{ssieL} = \boldsymbol{I}_{n+m}\boldsymbol{S}^{+}_{ssieL}\begin{bmatrix} \boldsymbol{I}_n \\ \boldsymbol{0} \end{bmatrix}, \tag{4.6}$$

$$\boldsymbol{\Phi}_{ssieL} = \boldsymbol{J}_{ssieL}\boldsymbol{M}_{ssie}, \tag{4.7}$$

$$\boldsymbol{G}_{ssieL} = \left(\boldsymbol{I}_{n+p} - \boldsymbol{S}_{ssieL}\boldsymbol{S}^{+}_{ssieL}\right)\begin{bmatrix} \boldsymbol{I}_n \\ \boldsymbol{0} \end{bmatrix}, \tag{4.8}$$

$$\boldsymbol{\Psi}_{ssieL} = \boldsymbol{G}\boldsymbol{M}_{ssie}, \tag{4.9}$$

$$\boldsymbol{V}_{ssieN} = \boldsymbol{I}_{n+m}\boldsymbol{S}^{+}_{ssieN}\begin{bmatrix} \boldsymbol{0} \\ \boldsymbol{I}_m \end{bmatrix}, \tag{4.10}$$

and

$$\boldsymbol{K}_{ssieL} = \left(\boldsymbol{I}_{n+p} - \boldsymbol{S}_{ssieN}\boldsymbol{S}^{+}_{ssieN}\right)\begin{bmatrix} \boldsymbol{0} \\ \boldsymbol{I}_p \end{bmatrix}, \tag{4.11}$$

where $\boldsymbol{S}^{+}_{ssieL}$ represents the left inverse of $\boldsymbol{S}_{ssieL}$. Define $\tilde{\boldsymbol{x}}_{aug}(t)$ as

$$\tilde{\boldsymbol{x}}_{aug}(t) = \boldsymbol{x}_{aug}(t) - \hat{\boldsymbol{x}}_{aug}(t). \tag{4.12}$$

The dynamics of $\tilde{\boldsymbol{x}}_{aug}(t)$ can be described by

$$\dot{\tilde{\boldsymbol{x}}}_{aug}(t) = \boldsymbol{N}_{ssieL}\tilde{\boldsymbol{x}}_{aug}(t), \tag{4.13}$$

where $\boldsymbol{N}_{ssieL}$ is determined by equation (4.14),

$$\boldsymbol{N}_{ssieL} = \boldsymbol{\Phi}_{ssieL} - \begin{bmatrix} \boldsymbol{Z}_{ssieL} & \boldsymbol{F}_{ssieL} \end{bmatrix}\begin{bmatrix} -\boldsymbol{\Psi}_{ssieL} \\ \boldsymbol{H}_{ssie} \end{bmatrix}. \tag{4.14}$$

If the eigenvalues of $\boldsymbol{N}_{ssieL}$ all have negative real part, $\tilde{\boldsymbol{x}}_{aug}(t)$ will asymptotically converge to zero. In equation (4.14) matrices $\boldsymbol{\Phi}_{ssieL}$, $\boldsymbol{\Psi}_{ssieL}$, and $\boldsymbol{H}_{ssie}$ are all known. If solutions for matrices $\boldsymbol{Z}_{ssieL}$ and $\boldsymbol{F}_{ssieL}$ exist, matrices $\boldsymbol{Q}_{ssieL}$ and $\boldsymbol{L}_{ssieL}$ can be calculated with

$$\boldsymbol{Q}_{ssieL} = \boldsymbol{V}_{ssieL} + \boldsymbol{Z}_{ssieL}\boldsymbol{K}_{ssieL} \tag{4.15}$$

and

$$\boldsymbol{L}_{ssieL} = \boldsymbol{F}_{ssieL} + \boldsymbol{N}_{ssieL}\boldsymbol{Q}_{ssieL}. \tag{4.16}$$

In equations (4.15) and (4.16), the matrices $\boldsymbol{Z}_{ssieL}$ and $\boldsymbol{F}_{ssieL}$ can be obtained a pole-placement method in which the eigenvalues of the matrix $\boldsymbol{N}_{ssieL}$ are all set with negative real part. An introduction to the pole-placement method can be found in e.g. Franklin et al. (2006).

The existence of the SS&IE_L requires that the following sufficient conditions should be fulfilled.

(1) The eigenvalues of matrix $\boldsymbol{N}_{ssieL}$ should be all with negative real part.

(2) The direct feed-through $\boldsymbol{H}_c$ should have full column rank.

(3) The matrix pair $(\boldsymbol{\Phi}_{ssieL}, \begin{bmatrix} -\boldsymbol{\Psi}_{ssieL} \\ \boldsymbol{H}_{ssie} \end{bmatrix})$ should be observable.

The derivation of the SS&IE_L is provided in appendix A.

4.2. Steady-state of KF+RLSE

The KF+RLSE algorithm has been reviewed in section 2.6.3. Assume the KF+RLSE can reach a steady-state. Introduce $\boldsymbol{K}^x_{ss,kf+rlse}$ as the steady-state of $\boldsymbol{K}_k$ and $\boldsymbol{K}^d_{ss,kf+rlse}$ as the steady-state of $\boldsymbol{K}^d_k$. Then the steady-state of KF+RLSE can be represented by

$$\begin{bmatrix} \hat{\boldsymbol{x}}_{k|k} \\ \hat{\boldsymbol{d}}_k \end{bmatrix} = \boldsymbol{A}_{ss,kf+rlse} \begin{bmatrix} \hat{\boldsymbol{x}}_{k-1|k-1} \\ \hat{\boldsymbol{d}}_{k-1} \end{bmatrix} + \boldsymbol{L}_{ss,kf+rlse} \boldsymbol{y}_k, \tag{4.17}$$

where the matrices $\boldsymbol{A}_{ss,kf+rlse}$ and $\boldsymbol{L}_{ss,kf+rlse}$ have the form

$$\boldsymbol{A}_{ss,kf+rlse} = \begin{bmatrix} \boldsymbol{A}_d - \boldsymbol{K}^x_{ss,kf+rlse} \boldsymbol{C}_d \boldsymbol{A}_d & \boldsymbol{0}_{n\times m} \\ -\boldsymbol{K}^d_{ss,kf+rlse} \boldsymbol{C}_d \boldsymbol{A}_d & \boldsymbol{I}_m - \boldsymbol{K}^d_{ss,kf+rlse} \end{bmatrix} \tag{4.18}$$

and

$$\boldsymbol{L}_{ss,kf+rlse} = \begin{bmatrix} \boldsymbol{K}^x_{ss,kf+rlse} \\ \boldsymbol{K}^d_{ss,kf+rlse} \end{bmatrix}. \tag{4.19}$$

The steady-state form in equation (4.17) can simplify the implementation the KF+RLSE and can reduce the computational load.

4.3. Generalized Kalman filter with unknown inputs (G-KF-UI)

Pan et al. (2011) proposed a Kalman Filter with Unknown Inputs (KF-UI) algorithm. A brief review of the the KF-UI has been provided in section 2.6.5. In the derivation of the KF-UI, it is assumed that the process noise and the measurement noise are uncorrelated. According to the discussion in section 2.7, the usage of accelerometers means the process noise and the measurement noise will be correlated. To be compatible with such correlation, a generalized KF-UI (G-KF-UI) is proposed in this section. In section 4.3.1, the difference and the relationship between the KF-UI and the Recusive Three-Step Filter

(RTSF) are discussed. Based on the discussion in section 4.3.1, some modifications to the KF-UI are proposed in section 4.3.2. The filter equations of the G-KF-UI are presented in section 4.3.3. In section 4.3.4, the steady-state of the G-KF-UI is discussed, and the G-KF-UI in steady-state is presented.

4.3.1. Difference and relationship between the KF-UI and the RTSF

The KF-UI and the RTSF have been reviewed in section 2.6.5 and section 2.6.4, respectively. The difference between the KF-UI and the RTSF can be summarized as below.

- The KF-UI and the RTSF have different filter equations.
- The KF-UI and the RTSF have different necessary and sufficient conditions.
- The RTSF assumes the unbiased estimate of the initial state is available, while the KF-UI do not have such assumption on the initial state estimate.

Both the KF-UI and the RTSF are derived based on the same system model, and both algorithms can provide the unbiased estimate of the state and the unbiased estimate of the input. In this thesis, the filter equations of the KF-UI are proved to be equivalent to those of the RTSF. The proof is provided in appendix B. If the direct feed-through matrix $\boldsymbol{H}_k$ is set as zero matrix, the filter equations of both algorithms end up with the same form as the discrete-time Kalman filter.

4.3.2. Proposed modifications to the KF-UI

Equation (2.188) can be transformed to

$$\boldsymbol{P}^x_{k+1|k} = \begin{bmatrix} \boldsymbol{A}_k & \boldsymbol{G}_k \end{bmatrix} \begin{bmatrix} \boldsymbol{P}^x_{k|k} & \boldsymbol{C}_k^T \boldsymbol{R}_k^{-1} \boldsymbol{H}_k \\ \boldsymbol{H}_k^T \boldsymbol{R}_k^{-1} \boldsymbol{C}_k & \boldsymbol{S}_{kfui,k} \end{bmatrix} \begin{bmatrix} \boldsymbol{A}_k^T \\ \boldsymbol{G}_k^T \end{bmatrix} + \boldsymbol{Q}_k. \tag{4.20}$$

By comparing equation (4.20) with equation (2.184), it is noticed that these two equations have similar form but with different element matrices, e.g. the element matrix $\boldsymbol{C}_k^T \boldsymbol{R}_k^{-1} \boldsymbol{H}_k$ in equation (4.20) is not equivalent with the covariance matrix $\boldsymbol{P}_k^{xd}$ in the RTSF. According to the proof in appendix B, the filter equations of the KF-UI are equivalent to those of the RTSF. This leads to a contradiction. So it is concluded that the derivations in the appendix in Pan et al. (2009) are correct, and there is a typing error in the filter equations of the KF-UI in the context in Pan et al. (2009).

Based on the above discussion, a modification to the KF-UI is proposed. Equation (2.188)

is modified to the form

$$\boldsymbol{P}^{x}_{k|k-1} = \begin{bmatrix} \boldsymbol{A}_{k-1} & \boldsymbol{G}_{k-1} \end{bmatrix} \begin{bmatrix} \boldsymbol{P}^{x}_{k-1|k-1} & -\boldsymbol{K}_{kfui,k-1}\boldsymbol{H}_{k-1}\boldsymbol{S}_{kfui,k-1} \\ -\boldsymbol{S}^{T}_{kfui,k-1}\boldsymbol{H}^{T}_{k-1}\boldsymbol{K}^{T}_{kfui,k-1} & \boldsymbol{S}_{kfui,k-1} \end{bmatrix} \begin{bmatrix} \boldsymbol{A}^{T}_{k-1} \\ \boldsymbol{G}^{T}_{k-1} \end{bmatrix} \tag{4.21}$$

Furthermore, the necessary and sufficient conditions for the existence of the KF-UI are updated and provided below.

(1) Condition $p \geqslant m + n/2$ should be fulfilled.

(2) Matrix $\begin{bmatrix} \boldsymbol{C}^{T}_{1}, & \boldsymbol{A}^{T}_{1}\boldsymbol{C}^{T}_{2}, & \cdots, & \boldsymbol{A}^{T}_{1}\boldsymbol{A}^{T}_{2}\cdots\boldsymbol{A}^{T}_{k-1}\boldsymbol{C}^{T}_{k} \end{bmatrix}^{T}$ should have full column rank.

(3) Matrix $\left[\boldsymbol{H}_i - \boldsymbol{C}_i\boldsymbol{A}_i^{-1}\boldsymbol{G}_i\right]$ should have full column rank, with $i = 1, 2, \ldots, k-1$.

(4) Matrix $\boldsymbol{H}_k$ should have full column rank.

It is noted here that the change from $p > m$ to $p \geqslant m+n/2$ actually gives a more accurate constraint for the sensor number.

4.3.3. Generalized form of the KF-UI

In the derivation of the KF-UI, it is assumed that the process noise and the measurement noise are not correlated. For the existence of the KF-UI, one of the necessary and sufficient conditions is that the direct feed-through $\boldsymbol{H}_k$ should have full column rank. With equation (2.17) and equation (2.23), it can be concluded that a direct feed-through $\boldsymbol{H}_k$ with full column rank means acceleration responses are considered in the output equation of the state-space structural model. According to the discussion in section (2.7), if acceleration responses are considered in the output equation of the state-space structural model, the process noise and the measurement noise will be correlated. This is contradicted with the assumption which is made in the derivation of the KF-UI. Figure 4.2 describes such contradiction. In this section, a generalized KF-UI is presented which is compatible with the correlation of the process noise and the measurement noise.

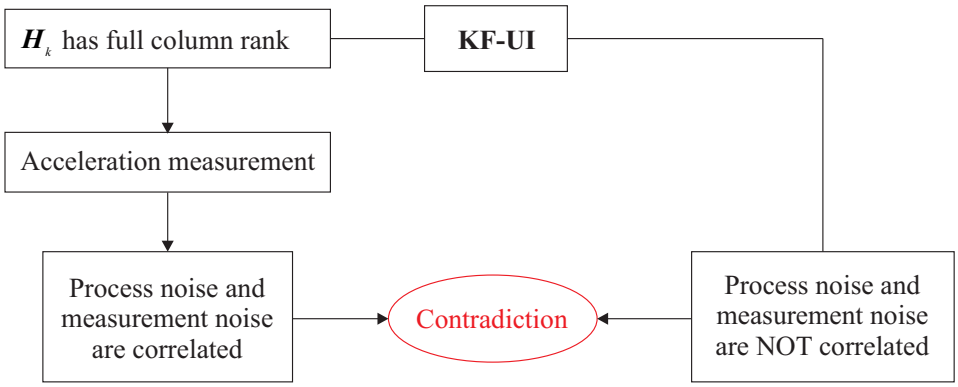

Figure 4.2. *Noticed contradiction*

Consider the system which is represented by

$$\boldsymbol{x}_{k+1} = \boldsymbol{A}_k\boldsymbol{x}_k + \boldsymbol{B}_k\boldsymbol{u}_k + \boldsymbol{G}_k\boldsymbol{d}_k + \boldsymbol{w}_k \tag{4.22}$$

and

$$\boldsymbol{y}_k = \boldsymbol{C}_k\boldsymbol{x}_k + \boldsymbol{D}_k\boldsymbol{u}_k + \boldsymbol{H}_k\boldsymbol{d}_k + \boldsymbol{v}_k, \tag{4.23}$$

where $\boldsymbol{x}_k \in \mathbb{R}^n$ represents the state; $\boldsymbol{u}_k \in \mathbb{R}^r$ denotes the (known) control input; $\boldsymbol{d}_k \in \mathbb{R}^m$ is the unknown input; $\boldsymbol{y}_k \in \mathbb{R}^p$ is the output; $\boldsymbol{A}_k$, $\boldsymbol{B}_k$, $\boldsymbol{G}_k$, $\boldsymbol{C}_k$, $\boldsymbol{D}_k$ and $\boldsymbol{H}_k$ are systems matrices with appropriate dimensions; $\boldsymbol{w}_k \in \mathbb{R}^n$ and $\boldsymbol{v}_k \in \mathbb{R}^p$ represent the process noise and the measurement noise, respectively. It is assumed that $\boldsymbol{w}_k$ and $\boldsymbol{v}_k$ are stationary, zero-mean and white, with known covariance matrices

$$\boldsymbol{Q}_k = E\left[\boldsymbol{w}_k\boldsymbol{w}_k^T\right] \tag{4.24}$$

and

$$\boldsymbol{R}_k = E\left[\boldsymbol{v}_k\boldsymbol{v}_k^T\right]. \tag{4.25}$$

The cross-correlation of the process noise and the measurement noise is determined as in equation (2.229).

The generalized KF-UI (G-KF-UI) consists of equation (4.26) through equation (4.35).

- Time update, which includes

$$\hat{\boldsymbol{x}}_{k|k-1} = \boldsymbol{A}_{k-1}\hat{\boldsymbol{x}}_{k-1|k-1} + \boldsymbol{B}_{k-1}\boldsymbol{u}_{k-1} + \boldsymbol{G}_{k-1}\hat{\boldsymbol{d}}_{k-1} \tag{4.26}$$

and

$$\boldsymbol{P}^x_{k|k-1} = \begin{bmatrix} \boldsymbol{A}_{k-1} & \boldsymbol{G}_{k-1} \end{bmatrix} \begin{bmatrix} \boldsymbol{P}^x_{k-1|k-1} & \boldsymbol{P}^{xd}_{k-1} \\ \boldsymbol{P}^{dx}_{k-1} & \boldsymbol{P}^{d}_{k-1} \end{bmatrix} \begin{bmatrix} \boldsymbol{A}^T_{k-1} \\ \boldsymbol{G}^T_{k-1} \end{bmatrix} + \boldsymbol{Q}_{k-1}. \tag{4.27}$$

- Estimation of unknown input, which includes

$$\tilde{\boldsymbol{R}}_{gkfui,k} = \boldsymbol{C}_k \boldsymbol{P}^x_{k|k-1} \boldsymbol{C}_k^T + \boldsymbol{R}_k + \boldsymbol{C}_k \boldsymbol{S}_k + \boldsymbol{S}_k^T \boldsymbol{C}_k^T, \tag{4.28}$$

$$\boldsymbol{M}_{gkfui,k} = \left(\boldsymbol{H}_k^T \tilde{\boldsymbol{R}}^{-1}_{gkfui,k} \boldsymbol{H}_k \right)^{-1} \boldsymbol{H}_k^T \tilde{\boldsymbol{R}}^{-1}_{gkfui,k}, \tag{4.29}$$

$$\hat{\boldsymbol{d}}_k = \boldsymbol{M}_{gkfui,k} \left(\boldsymbol{y}_k - \boldsymbol{C}_k \hat{\boldsymbol{x}}_{k|k-1} \right), \tag{4.30}$$

and

$$\boldsymbol{P}^d_k = \left(\boldsymbol{H}_k^T \tilde{\boldsymbol{R}}^{-1}_{gkfui,k} \boldsymbol{H}_k \right)^{-1}. \tag{4.31}$$

- Measurement update, which includes

$$\boldsymbol{K}_{gkfui,k} = \left(\boldsymbol{P}^x_{k|k-1} \boldsymbol{C}_k^T + \boldsymbol{S}_k \right) \tilde{\boldsymbol{R}}^{-1}_{gkfui,k}, \tag{4.32}$$

$$\hat{\boldsymbol{x}}_{k|k} = \hat{\boldsymbol{x}}_{k|k-1} + \boldsymbol{K}_{gkfui,k} \left(\boldsymbol{y}_k - \boldsymbol{C}_k \hat{\boldsymbol{x}}_{k|k-1} - \boldsymbol{D}_k \boldsymbol{u}_k - \boldsymbol{H}_k \hat{\boldsymbol{d}}_k \right), \tag{4.33}$$

$$\boldsymbol{P}^x_{k|k} = \boldsymbol{P}^x_{k|k-1} - \boldsymbol{K}_{gkfui,k} \left(\tilde{\boldsymbol{R}}_{gkfui,k} - \boldsymbol{H}_k \boldsymbol{P}^d_k \boldsymbol{H}_k^T \right) \boldsymbol{K}^T_{gkfui,k}, \tag{4.34}$$

and

$$\boldsymbol{P}^{xd}_k = \left(\boldsymbol{P}^{dx}_k \right)^T = -\boldsymbol{K}_{gkfui,k} \boldsymbol{H}_k \boldsymbol{P}^d_k. \tag{4.35}$$

In equation (4.28), $\boldsymbol{S}_k$ denotes the cross-correlation of the process noise and the measurement noise. Given the initial conditions $\hat{\boldsymbol{x}}_0$, $\hat{\boldsymbol{d}}_0$, $\boldsymbol{P}^x_0$, $\boldsymbol{P}^d_0$, and $\boldsymbol{P}^{xd}_0$, the unbiased estimate of the state and the unbiased estimate of the input can be determined with the G-KF-UI.

The existence of the G-KF-UI requires that the following necessary and sufficient conditions should be fulfilled.

(1) Condition $p \geqslant m + n/2$ should hold.

(2) Matrix $\left[\begin{array}{cccc} \boldsymbol{C}_1^T, & \boldsymbol{A}_1^T \boldsymbol{C}_2^T, & \cdots, & \boldsymbol{A}_1^T \boldsymbol{A}_2^T \cdots \boldsymbol{A}_{k-1}^T \boldsymbol{C}_k^T \end{array} \right]^T$ should have full column rank.

(3) Matrix $\left[\boldsymbol{H}_i - \boldsymbol{C}_i \boldsymbol{A}_i^{-1} \boldsymbol{G}_i \right]$ should have full column rank, with $i = 1, 2, \ldots, k-1$.

(4) Matrix $\boldsymbol{H}_k$ should have full column rank.

4.3.4. Steady-state of G-KF-UI

In case the parameters of the structural model are constant, the state-space structural model is a time-invariant system. Assume the process noise and the measurement noise are stationary, and the G-KF-UI can reach steady-state. Introduce $\boldsymbol{A}_d$, $\boldsymbol{B}_d$, $\boldsymbol{G}_d$, $\boldsymbol{C}_d$, $\boldsymbol{D}_d$, $\boldsymbol{H}_d$, $\boldsymbol{Q}_d$, $\boldsymbol{R}_d$, and $\boldsymbol{S}_d$ as the values of $\boldsymbol{A}_k$, $\boldsymbol{B}_k$, $\boldsymbol{G}_k$, $\boldsymbol{C}_k$, $\boldsymbol{D}_k$, $\boldsymbol{H}_k$, $\boldsymbol{Q}_k$, $\boldsymbol{R}_k$, and $\boldsymbol{S}_k$ in steady-state, respectively. Denote $\boldsymbol{M}$ as the value of $\boldsymbol{M}_{gkfui,k}$ in steady-state, and $\boldsymbol{K}_{ss,gkfui}$ as the value of $\boldsymbol{K}_{gkfui,k}$ in steady-state. Then the G-KF-UI in steady-state can

be represented by

$$\begin{bmatrix} \hat{\boldsymbol{x}}_{k|k} \\ \hat{\boldsymbol{d}}_k \end{bmatrix} = \boldsymbol{A}_{ss,gkfui} \begin{bmatrix} \hat{\boldsymbol{x}}_{k-1|k-1} \\ \hat{\boldsymbol{d}}_{k-1} \end{bmatrix} + \boldsymbol{L}_{ss,gkfui}\boldsymbol{y}_k + \boldsymbol{D}_{ss,gkfui}\boldsymbol{u}_k + \boldsymbol{B}_{ss,gkfui}\boldsymbol{u}_{k-1}, \quad (4.36)$$

where matrices $\boldsymbol{A}_{ss,gkfui}$, $\boldsymbol{L}_{ss,gkfui}$, $\boldsymbol{D}_{ss,gkfui}$, and $\boldsymbol{B}_{ss,gkfui}$ are expressed by

$$\boldsymbol{A}_{ss,gkfui} = \begin{bmatrix} \boldsymbol{A}_{ss,gkfui}(1,1) & \boldsymbol{A}_{ss,gkfui}(1,2) \\ \boldsymbol{A}_{ss,gkfui}(2,1) & \boldsymbol{A}_{ss,gkfui}(2,2) \end{bmatrix}, \quad (4.37)$$

with

$$\boldsymbol{A}_{ss,gkfui}(1,1) = \left(\boldsymbol{I} - \boldsymbol{K}_{ss,gkfui}\boldsymbol{C}_d + \boldsymbol{K}_{ss,gkfui}\boldsymbol{H}_d\boldsymbol{M}_{ss,gkfui}\boldsymbol{C}_d\right)\boldsymbol{A}_d, \quad (4.38)$$

$$\boldsymbol{A}_{ss,gkfui}(1,2) = \left(\boldsymbol{I} - \boldsymbol{K}_{ss,gkfui}\boldsymbol{C}_d + \boldsymbol{K}_{ss,gkfui}\boldsymbol{H}_d\boldsymbol{M}_{ss,gkfui}\boldsymbol{C}_d\right)\boldsymbol{G}_d, \quad (4.39)$$

$$\boldsymbol{A}_{ss,gkfui}(2,1) = -\boldsymbol{M}_{ss,gkfui}\boldsymbol{C}_d\boldsymbol{A}_d, \quad (4.40)$$

$$\boldsymbol{A}_{ss,gkfui}(2,2) = -\boldsymbol{M}_{ss,gkfui}\boldsymbol{C}_d\boldsymbol{G}_d, \quad (4.41)$$

$$\boldsymbol{L}_{ss,gkfui} = \begin{bmatrix} \boldsymbol{K}_{ss,gkfui} - \boldsymbol{K}_{ss,gkfui}\boldsymbol{H}_d\boldsymbol{M}_{ss,gkfui} \\ \boldsymbol{M}_{ss,gkfui} \end{bmatrix}, \quad (4.42)$$

$$\boldsymbol{D}_{ss,gkfui} = \begin{bmatrix} -\boldsymbol{K}_{ss,gkfui}\boldsymbol{D}_d \\ \boldsymbol{0}_{m\times r} \end{bmatrix}, \quad (4.43)$$

and

$$\boldsymbol{B}_{ss,gkfui} = \begin{bmatrix} \left(\boldsymbol{I} - \boldsymbol{K}_{ss,gkfui}\boldsymbol{C}_d + \boldsymbol{K}_{ss,gkfui}\boldsymbol{H}_d\boldsymbol{M}_{ss,gkfui}\boldsymbol{C}_d\right)\boldsymbol{B}_d \\ -\boldsymbol{M}_{ss,gkfui}\boldsymbol{B}_d \end{bmatrix}. \quad (4.44)$$

The steady-state form of the G-KF-UI can simplify the implementation and reduce the computational load. If the matrices $\boldsymbol{B}_d$ and $\boldsymbol{D}_d$ are set as zero matrices, equation (4.36) represents the KF-UI in steady-state.

4.4. Modified Steady-State Kalman Filter and a Least-Squares Estimator

A brief review of the SSKF+LSE method has been provided in section 2.6.7. In the algebraic Riccati equation in equation (2.209), the input covariance matrix $\boldsymbol{Q}_{input}$ and the

measurement noise covariance matrix $\boldsymbol{Q}_{meas}$ work as two weighting matrices. The values of $\boldsymbol{Q}_{input}$ and $\boldsymbol{Q}_{meas}$ affect the calculated $\boldsymbol{P}$. In equation (2.208), the value of $\boldsymbol{P}$ affects the gain matrix $\boldsymbol{K}_{sskf+lse}$. Thus, it can be concluded that the values of $\boldsymbol{Q}_{input}$ and $\boldsymbol{Q}_{meas}$ affect the calculated gain matrix $\boldsymbol{K}_{sskf+lse}$ and subsequently the reconstruction results.

The SSKF+LSE considers the covariance matrices $\boldsymbol{Q}_{input}$ and $\boldsymbol{Q}_{meas}$ to be unknown, and sets $\boldsymbol{Q}_{input}$ as an identity matrix $\boldsymbol{I}_m$ and $\boldsymbol{Q}_{meas}$ as $\gamma \boldsymbol{I}_p$, where γ is a tuning parameter. The matrix $\boldsymbol{P}$ and the gain matrix $\boldsymbol{K}_{sskf+lse}$ are determined by adjusting the value of γ. As the covariance matrix of the input force, $\boldsymbol{Q}_{input}$ actually includes the information on the intensity difference and the correlation of different input forces. Each of the diagonal elements of $\boldsymbol{Q}_1$ is the variance of each input force, and the off-diagonal elements of $\boldsymbol{Q}_{input}$ reflect the correlation of different forces. If the covariance matrix $\boldsymbol{Q}_{input}$ is set as an identity matrix, it indicates that the input forces all have the same variance and are uncorrelated. In some practical applications, it might be not the case. Thus, it is proposed to consider an estimate of the covariance matrix $\boldsymbol{Q}_{input}$ which provides the information on the difference of the intensity of the input forces and the correlation of the input forces, and to consider an estimate of the covariance matrix $\boldsymbol{Q}_{meas}$ which includes the information on the difference of the measurement noise from different types of sensors. To differentiate with the SSKF+LSE, this proposed modification is named as MSSKF+LSE.

The necessary conditions of for the existence of the MSSKF+LSE are the same as those of the SSKF+LSE. The improvement which can be brought by this proposed modification will be demonstrated by test results in section 5.2.9.

5. Study on application-oriented algorithm selection

The methodology which is adopted in this thesis for online force reconstruction has been presented in chapter 3. According to figure 3.4 and figure 3.5, a real-time executable state and input estimation algorithm is needed in the online stage of the methodology. In section 2.6, a brief review of the available real-time executable state and input estimation algorithms have been provided. To be theoretically suitable for online force reconstruction, some algorithm modifications are proposed in chapter 4. Given a practical need for online force reconstruction, it is reasonable to raise the following questions.

(i) Which algorithms are suitable for the reconstruction of the force?

(ii) If the structure under investigation has already been instrumented with some sensors for some other monitoring purposes, can the force be reconstructed with the available sensors?

This chapter intends to contribute some ideas in answering the questions above.

Each of the available algorithms has some assumptions and requires some mathematical conditions to be fulfilled. The discussion in section 5.1 focuses on the translation of these assumptions and mathematical conditions into practical requirements for the application of these algorithms. In section 5.2, a benchmark study is performed. A laboratory two-story structure is taken as the benchmark structure on which two types of widely used sensors are installed, including strain gauge and accelerometer. Three different types of input forces are considered, including quasi-static force, impact force, and wind load generated by an electric fan. The methodology in figure 3.4 is applied. In the offline stage of the adopted methodology, the structural model of the benchmark structure is identified with the help of the Experimental Modal Analysis (EMA) technique. In the online stage of the adopted methodology, in total eight different algorithms are tested. The goal of this benchmark study is to find the suitable algorithms for the reconstruction of the considered force types with considered sensor types. Based on the results from the benchmark study, a guidance for algorithm selection is is extracted and presented in section 5.3.

5.1. From mathematics to practical requirements

The methodology in chapter 3 shows that a real-time executable state and input estimation algorithm is needed for the reconstruction of the force and the reconstruction of the structural response. The available real-time executable state and input estimation algorithms have been reviewed in section 2.6, and some algorithm modifications have been

proposed in chapter 4. In these algorithms, there are some mathematical assumptions, e.g. on the input, on the initial state estimate, on the direct feed-through, etc. Furthermore, the existence of those algorithms requires that some mathematical conditions should be fulfilled. These mathematical conditions often appear in the form of necessary conditions, or sufficient conditions, or necessary and sufficient conditions. What do these mathematical assumptions and conditions actually mean for the practical application of those algoirthms? The discussion in this section tries to translate these mathematical assumptions and conditions into practical requirements.

5.1.1. Assumption on inputs

The basic idea which is adopted in this thesis for online force reconstruction has been illustrated by the block diagram in figure 1.2. The input estimate in the algorithm corresponds to the force estimate. Therefore, the assumption on the inputs is actually the assumption on the input forces.

In the PI observer design method which is proposed by Söffker et al. (1995), the inputs are assumed to be piece-wise constant. In combination with the high-gain approach in Söffker et al. (1995), this allows the reconstruction of dynamical effects under certain conditions.

In the AKF method which is proposed by Lourens et al. (2012b), the inputs are assumed to be stationary zero-mean stochastic processes, with a known covariance matrix of the increment of the inputs. When the AKF is applied for online force reconstruction, this assumption indicates that the input forces should have zero-mean, and an estimate of the covariance matrix of the increment of the input forces should be available.

In the SSKF+LSE method which is proposed by Hwang et al. (2009a), the co-variance is the input is set as an identity matrix. Such a setting assumes that different inputs have the same variance and are uncorrelated. When this method is applied for online force reconstruction, the input forces are assumed to have the same variance and are uncorrelated with each other. In practice, it might not always be the case. In consideration of this, a modification to this algorithm is proposed in section 4.4, where it is suggested to take the covariance of the inputs into account.

5.1.2. Assumption on initial state estimate

According to the definition in equation (2.11), the elements of the state vector $\boldsymbol{x}(t)$ in the continuous-time state-space structural model are composed of the modal displacement vector $\boldsymbol{q}_m(t)$ and the first derivative of $\boldsymbol{q}_m(t)$. According to equation (2.5), the nodal displacement vector $\boldsymbol{q}_n(t)$ can be expressed as the product of the modal matrix $\boldsymbol{\Phi}$ and the modal displacement vector $\boldsymbol{q}_m(t)$. Thus the state vector $\boldsymbol{x}(t)$ can be expressed by the nodal displacement vector $\boldsymbol{q}_n(t)$ and its first derivative. In some algorithms, the initial

state estimate is assumed to be unbiased. When these algorithms are applied for online force reconstruction, such an assumption actually means that an unbiased estimate of the initial displacement of the structure should be available. The structural displacement can be measured by displacement sensors, or can be derived from strain measurements. If there is no available displacement sensors or strain gauges on the structure, it is often difficult to get an unbiased initial state estimate, and the application of those algorithms is dependent on the practical applications. If the structure has no bending deformation in the initial condition, the unbiased initial state estimates can be set as zero. If the structure does have a bending deformation in the initial condition, the unbiased initial state estimates can not be set as zero. A biased initial state estimate might cause a biased estimate of the force.

5.1.3. Assumption on direct feed-through

In the continuous-time state-space structural model which is represented by equation (2.12) and equation (2.13), the direct feed-through $\boldsymbol{H}_c$ has the form in equation (2.17). The form of $\boldsymbol{H}_c$ shows that the input forces are directly related with the structural response by $\boldsymbol{C}_a\boldsymbol{\Phi}\boldsymbol{\Phi}^T\boldsymbol{B}_o$ in which $\boldsymbol{C}_a$ defines the positions of acceleration sensors; $\boldsymbol{\Phi}$ represents the mass normalized modal matrix; and $\boldsymbol{B}_o$ describes the spatial distribution of the input forces. Both $\boldsymbol{\Phi}$ and $\boldsymbol{B}_o$ are non-zero matrices. If the direct feed-through is assumed to be a non-zero matrix, it means that $\boldsymbol{C}_a$ is a non-zero matrix and the rank condition requirement for the direct feed-through is also the rank condition requirement for $\boldsymbol{C}_a\boldsymbol{\Phi}\boldsymbol{\Phi}^T\boldsymbol{B}_o$. When $\boldsymbol{\Phi}$ and $\boldsymbol{B}_o$ are known, the rank conditions for the direct feed-through can be transformed to some mathematical conditions for $\boldsymbol{C}_a$. The fulfillment of the mathematical conditions for $\boldsymbol{C}_a$ actually sets constraints for the number of acceleration sensors and their positions. For example, if the direct feed-through is assumed with full column rank, the row number of $\boldsymbol{C}_a$ should be larger than or equal to the column number of $\boldsymbol{B}_o$. This means that the number of acceleration sensors should be larger than or equal to the number of input forces. The fulfillment of the full column rank condition sets constraints for the positions of the acceleration sensors.

5.1.4. Mathematical conditions on system matrices

The existence of the available algorithms requires that some mathematical conditions should be fulfilled. These mathematical conditions come from the derivation of the state estimation and the input estimation, e.g. by fulfilling the observability condition and the stability condition, and are often in the form of necessary conditions, or sufficient conditions, or necessary and sufficient conditions. The fulfillment of such mathematical conditions actually sets some practical constraints in the selection of sensor type, sensor number, and sensor position.

5.2. Benchmark study

According to the methodology in chapter 3, a real-time executable state and input estimation algorithm is needed. There are already some available real-time executable state and input estimation algorithms. A brief review of those algorithms have been provided in section 2.6. Furthermore, some modifications to some of these algorithms have been proposed in chapter 4. Then it is reasonable to raise the question which algorithm to choose. In this section, a benchmark study is performed. A laboratory two-story structure is taken as the benchmark structure. For measuring the structural responses, two types of widely used sensors, strain gauge and accelerometer, are instrumented on this structure. Three different types of forces are considered, including a quasi-static force, impact forces, and wind load which is generated by an electric fan. In total eight different real-time executed state and input estimation algorithms are tested. This benchmark study intends to find the answers to the following questions.

(a) Can the three types of considered forces be reconstructed?

(b) Which algorithms are suitable for the reconstruction of the three types of forces?

(c) In case several algorithms are suitable, which algorithm needs less sensors?

An introduction to the benchmark structure is given in section 5.2.1. Considering that it is possible to apply an artificial excitation force on the laboratory two-story structure, the methodology in figure 3.4 is adopted in this benchmark study. The modal parameters of the benchmark structure are identified using the EMA technique. The identified natural frequencies, damping ratios, and mode shapes are presented in section 5.2.2. The position and the time history of each of the three different types of forces are provided in section 5.2.3. The obtained reconstruction results from using eight different algorithms are presented in section 5.2.4 through section 5.2.9, where the reconstructed forces are compared with the measured (or true) forces in the form of a direct comparison in time history plot and in the form of calculated Root Mean Square Error (RMSE).

5.2.1. Introduction to the benchmark structure

In this benchmark study, a laboratory two-story structure is taken as the benchmark structure. Figure 5.1 shows this benchmark structure and the connection of the test instruments. This benchmark structure consists of one upper mass block, one lower mass block, and one base. The upper block, the lower block, and the base are all made of aluminum, and are connected by four steel bars. The base is fixed. Table 5.1 lists the related parameters for the benchmark structure.

For measuring the structural response, two strain gauges and two accelerometers are instrumented on the laboratory two-story structure. The two acceleromters are PCB model

M353B15, with the sensitivity as 10mV/g and the frequency range from 1 Hz to 10 kHz. These two accelerometers are connected with a Kistler type 5134A coupler for power supply and signal conditioning. The two strain gauges are of the type HBM 1-LY11-0.6/120. In order to eliminate the temperature effect, half-bridge configuration is applied. These two strain gauges are connected with a PICAS amplifier from PEEKEL Instruments. The Kistler coupler and the PICAS amplifier are connected with a dSPACE DS1104 R&D controller board where the real-time executable state and input algorithms are implemented for the online reconstruction of the external force. The sampling frequency is 1000 Hz.

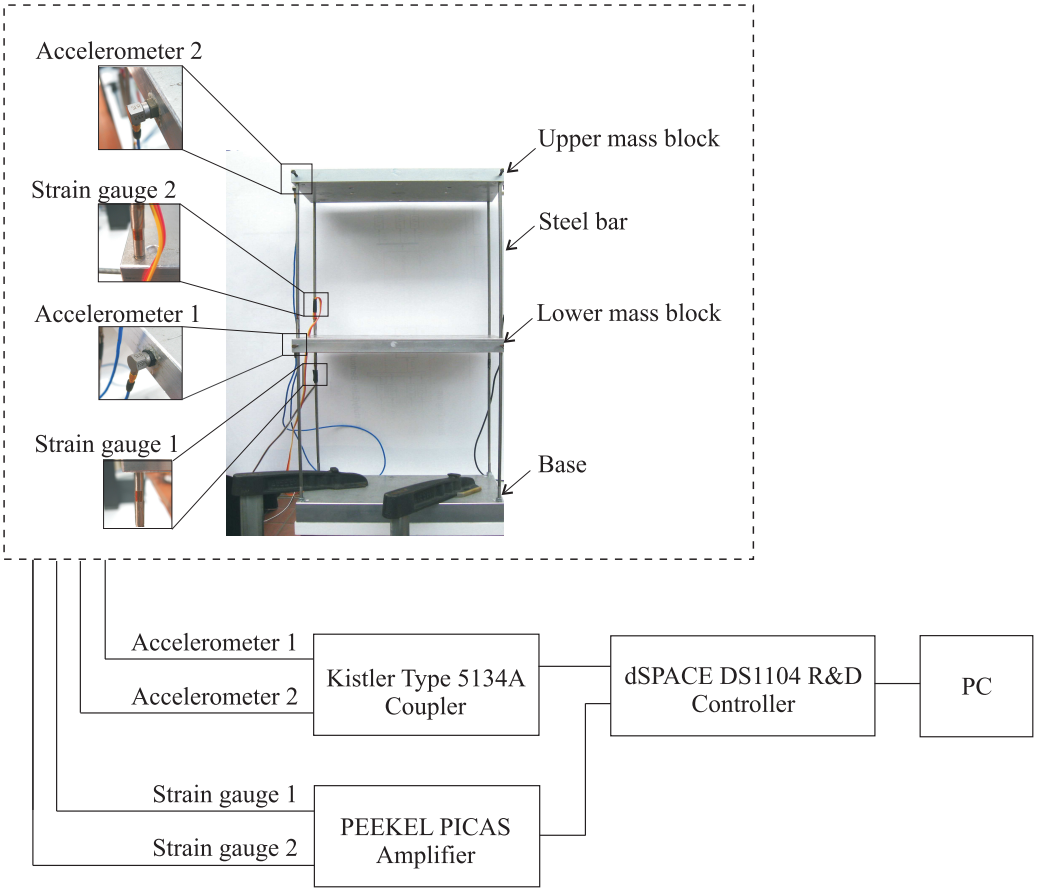

Figure 5.1. *Benchmark structure and the connection of the test instruments*

Table 5.1. *Parameters for the laboratory two-story structure*

Name	Value	Unit
Mass of the upper mass block	1.95	kg
Mass of the lower mass block	1.95	kg
Diameter of the steel bar	0.00396	m
Young's modulus of the steel bar	210	GPa
Length of the steel bar between the upper mass block and the lower mass block	0.232	m
Length of steel bar between the lower mass block and the base	0.232	m

5.2.2. Structural model construction for the benchmark structure

On the benchmark structure in figure 5.1, it is possible to apply an artificial excitation force. This case belongs to Case I in chapter 3. According to the methodology in figure 3.4, the structural model of the benchmark structure can be constructed with the help of the EMA technique. The principle of the EMA technique has been reviewed in section 2.1.4.

In this benchmark study, a Kistler type 9722A impulse hammer is used to apply the excitation force on the benchmark structure. The applied force is measured by a quartz sensor which is instrumented on the impulse hammer. The structural response is measured by two accelerometers. Figure 5.2 shows the position where the excitation force is applied and the positions of the two accelerometers. The excitation force is applied in the x-z plane. This will activate the vibration modes of the benchmark structure in the x-z plane. The measured force and the measured structural response are recorded and processed by the LMS Test.Lab®. The modal parameters of the benchmark structure are identified using the PolyMAX algorithm which is shipped together with the LMS Test.Lab®. The PolyMAX algorithm is capable of estimating modal parameters of two or more modes at one time (Peeters et al., 2004). Table 5.2 lists the identified natural frequencies and damping ratios of the first two modes of the benchmark structure in the x-z plane. The identified mode shapes of these two modes are scaled and plotted in figure 5.3.

Following the steps in section 2.1.1, a second-order structural model in the modal coordinates is constructed for the benchmark structure. This model includes the two modes in table 5.2, and it assumes that the damping matrix is a linear combination of the mass matrix and the stiffness matrix. The modal displacement vector is of order two. Two input forces are considered, with one force being applied on the lower mass block and the other one on the upper mass block. This means the input vector has two elements. In this benchmark study, the matrix $\boldsymbol{B}_o$ in equation (2.10) is set as

$$\boldsymbol{B}_o = \begin{bmatrix} 1 & 0 \\ 0 & 1 \end{bmatrix}. \tag{5.1}$$

Define the state vector which includes the modal displacement vector and the modal velocity vector. Thus the state vector is of order four. Following the steps in section 2.1.2, the second-order structural model is transformed to a state-space form, and the state transition matrix $\boldsymbol{A}_c$ and the input matrix $\boldsymbol{G}_c$ are assembled. The output matrix $\boldsymbol{C}_c$ and the direct feed-through $\boldsymbol{H}_c$ are in the output equation of the state-space structural model, and are related with the sensor type, sensor number, sensor position. These two matrices will be determined specifically for each real-time executable state and input estimation algorithm.

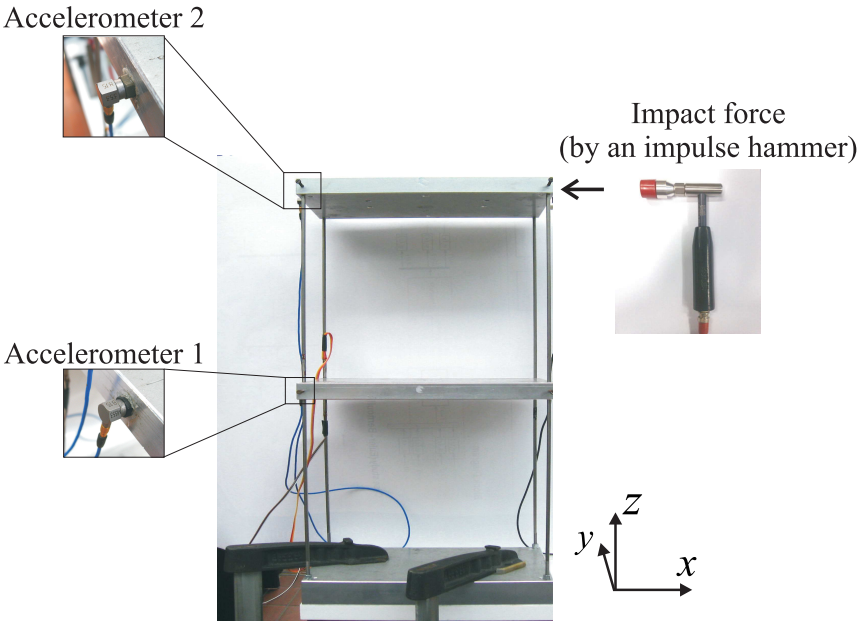

Figure 5.2. *Positions of excitation force and accelerometers for EMA*

Table 5.2. *Identified natural frequencies and damping ratios of the first two modes of the benchmark structure in the x-z plane*

Mode	Natural frequency (Hz)	Damping ratio (-)
1	5.911	0.0017
2	15.983	0.0009

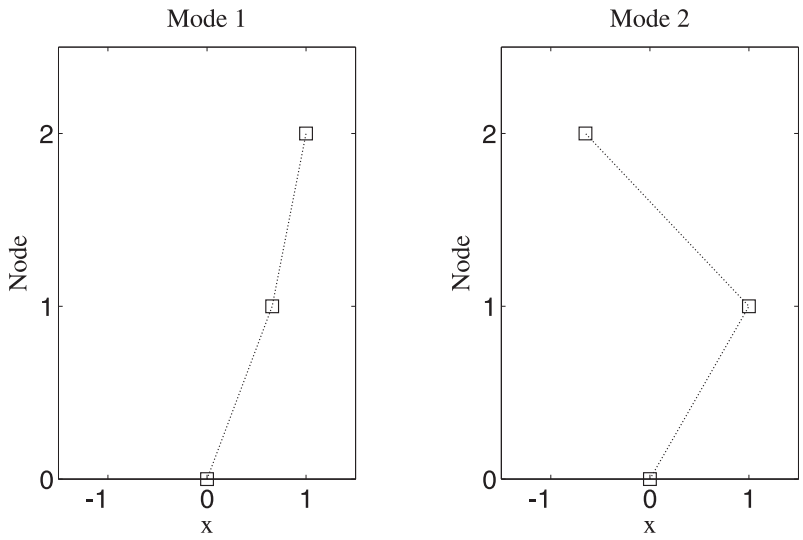

(a) *1st mode in the x-z plane* **(b)** *2nd mode in the x-z plane*

Figure 5.3. *Scaled mode shapes of the first two modes in the x-z plane*

5.2.3. Considered forces

In this benchmark study, the following three different types of forces are considered.

(1) Quasi-static force.

(2) Impact force.

(3) Wind load which is generated by an electric fan.

The quasi-static force is applied on the upper mass block of the benchmark structure, and is measured by a force transducer, a HBM S9M load cell. Figure 5.4 shows the position where the force transducer is installed. The force transducer is instrumented on the upper mass block. The quasi-static force is applied by hand directly on the force transducer which not only transmits the force but also measures the force. This type of force transducer is based on strain measurements and can transform strain measurements into force information. Figure 5.5 provides the time history of the applied quasi-static force. When the quasi-static force is applied on the upper mass block, no force is applied on the lower mass block in the x direction.

The impact force is applied on the lower mass block by using a Kistler type 9722A impulse hammer. Figure 5.6 shows the position where the impact force is applied. The applied impact force is measured by a quartz sensor which is instrumented on the impulse hammer. The time history of measured impact force is plotted in Figure 5.7, where a zoom-in of the time window from 11.9 seconds to 12.1 seconds is provided. In the zoom-in, the first peak is the impact that is intended to be applied, while the second peak and the third peak are caused by the interaction between the impulse hammer and the lower block. When the impact force is applied on the lower mass block, no force is applied on the upper mass block in the x direction.

The wind load is generated by an electric fan. To collect the generated wind load, an aluminum plate is applied. The aluminum plate is connected with the upper mass block through a force transducer which is an HBM S9M load cell. Figure 5.8 shows how the aluminum plate, the force transducer, and the upper mass block are connected. The force transducer works not only as an adapter for connecting the aluminum plate and the upper block but also as a sensor for measuring the wind load which is applied on the upper mass block. Figure 5.9 provides the time history of the measured wind load, including a zoom-in of the time window from 80.5 seconds to 81.0 seconds. When the wind load is applied on the upper mass block, no force is applied on the lower mass block in the x direction.

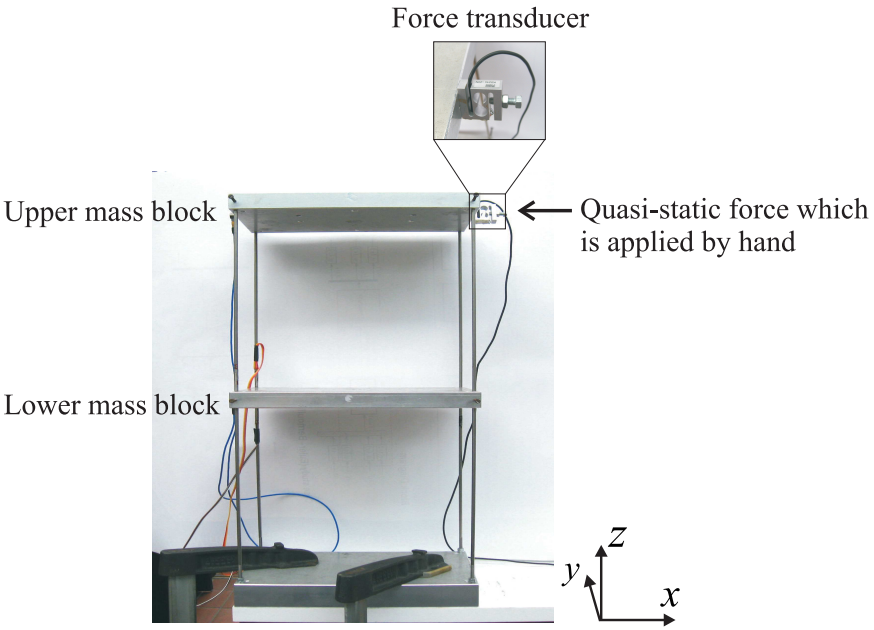

Figure 5.4. *Position of the applied quasi-static force*

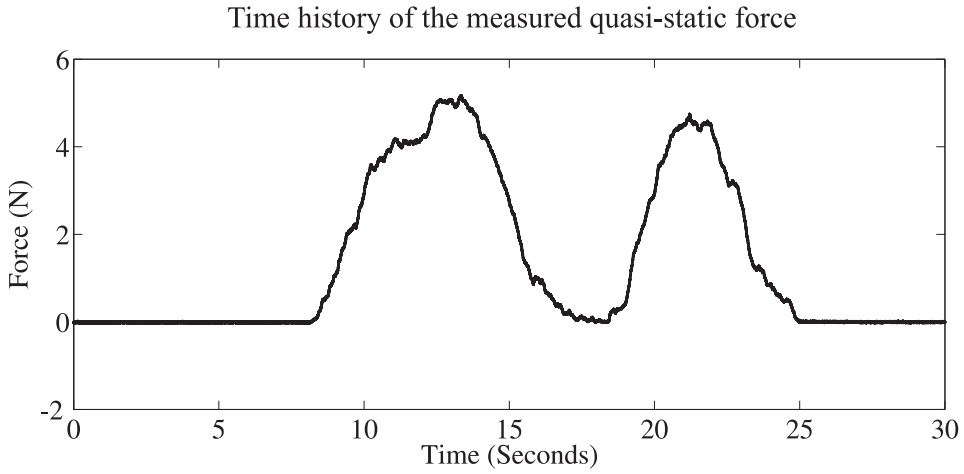

Figure 5.5. *Time history of measured quasi-static force*

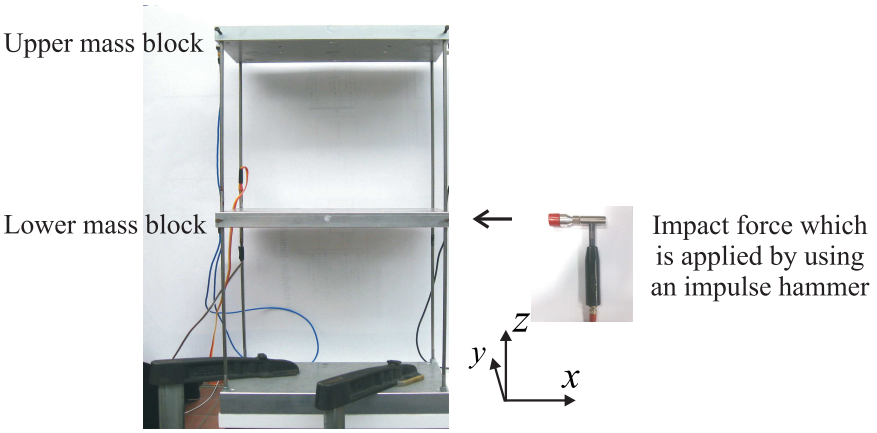

Figure 5.6. *Position of the applied impact force*

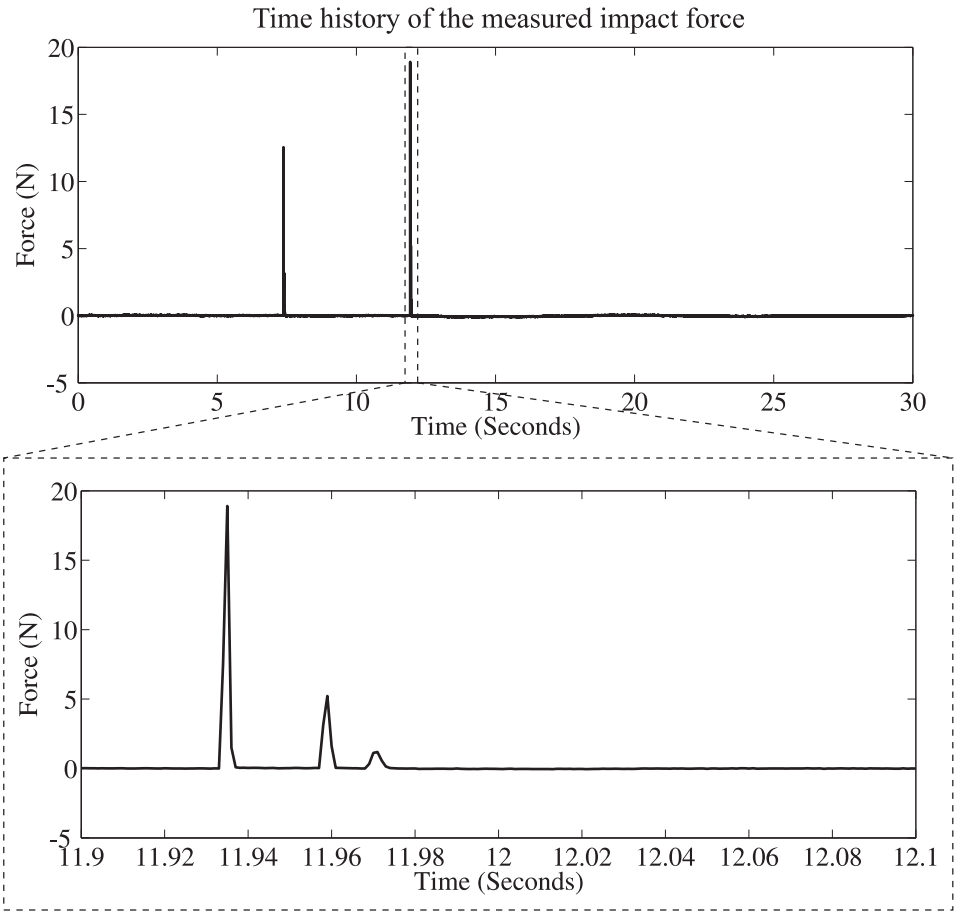

Figure 5.7. *Time history of measured impact force*

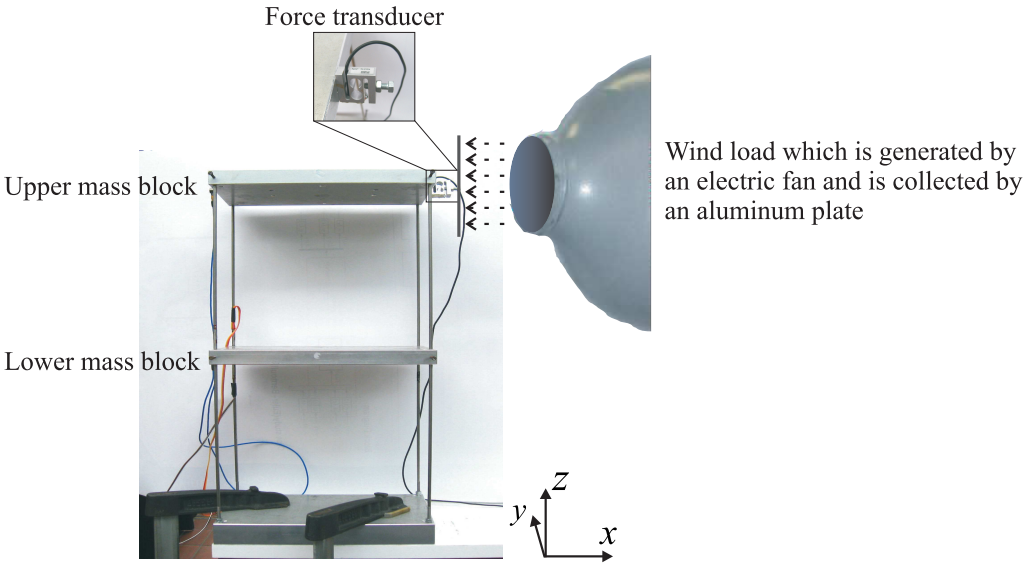

Figure 5.8. *Position of the applied wind load*

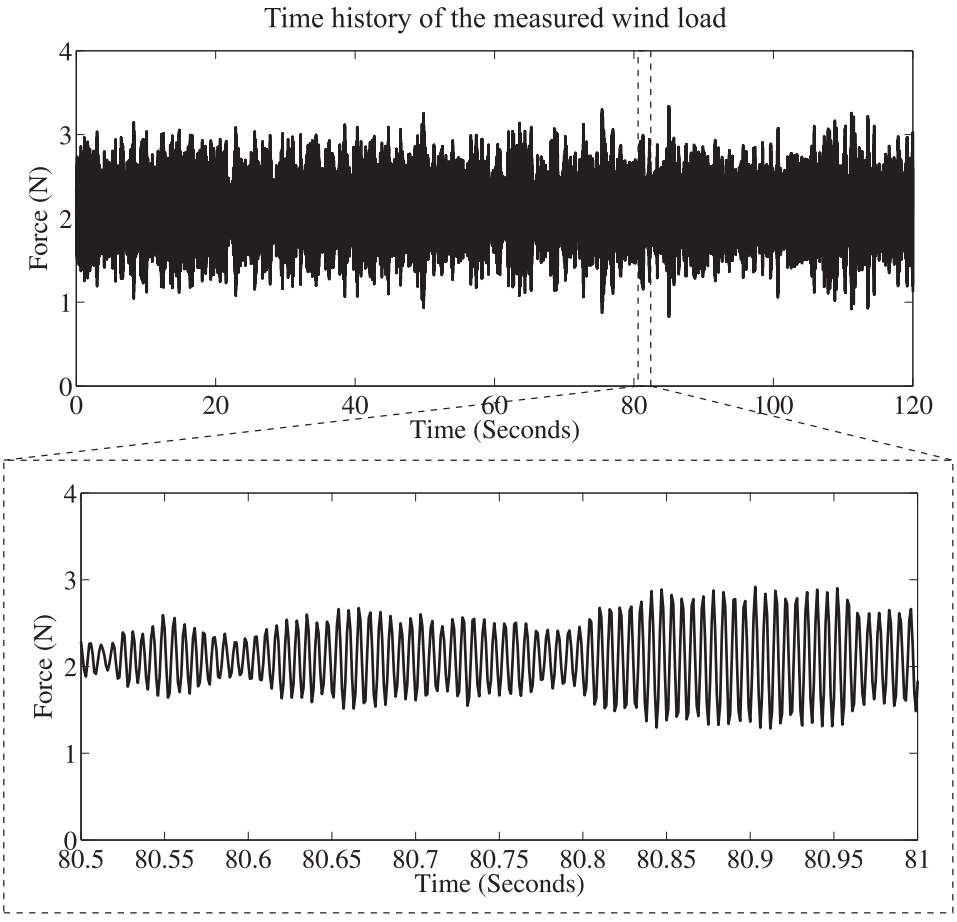

Figure 5.9. *Time history of measured wind load*

5.2.4. Test using PI observer

Söffker et al. (1995) proposed a design method for the Proportional-Integral observer (PI-observer). This design method was adopted for force reconstruction, e.g. reconstruction of contact forces of the nonlinear rail-wheel contact (Söffker, 1999), and reconstruction of the contact forces on a one side clamped elastic beam and on a all side clamped elastic plate (Krajcin and Söffker, 2005), etc. A short review of this PI observer design has been provided in section 2.6.1.

Within this benchmark study, the PI observer design that was proposed in Söffker et al. (1995) is applied for reconstructing the three different types of forces which have been introduced in section 5.2.3. In Söffker et al. (1995), it is stated that without exact knowledge about the dynamic behavior of the unknown input, a very general approach is possible by assuming the unknown input as piece-wise constant. Furthermore, this paper provides the sufficient conditions for the existence of a high-gain PI observer for any initial conditions of the state and the input, under the assumption that the unknown input is bounded. When this PI observer design is adopted for online force reconstruction, it assumes that the input forces are quasi-static and are bounded. An unbiased initial estimate of the state is not needed. As in equation (2.110), the direct feed-through is not considered in the output equation of the system model. According to equation (2.17), this indicates that the acceleration response of the benchmark structure is not considered in the output equation of the state-space model of the benchmark structure. Inspired by the work in Krajcin and Söffker (2005), the gain matrix $\boldsymbol{L}_{pio}$ in the PI observer design is calculated with the Loop Transfer Recovery (LTR) design method. . The main steps for calculating $\boldsymbol{L}_{pio}$ have been provided in section 2.6.1. In this benchmark study, the MATLAB function *care* is applied to solve the continuous-time algebraic Riccati equation in equation (2.122). This indicates that the following two sufficient conditions need to be fulfilled (Arnold and Laub, 1984).

(1) Matrix pair ($\boldsymbol{A}_{pio}$, $\boldsymbol{C}_{pio}$) is observable.

(2) Condition $\begin{bmatrix} \boldsymbol{Q}_{pio} & \boldsymbol{0} \\ \mathbf{0} & \boldsymbol{R}_{pio} \end{bmatrix} > \boldsymbol{0}$ holds.

The definitions for matrices $\boldsymbol{A}_{pio}$, $\boldsymbol{C}_{pio}$, $\boldsymbol{Q}_{pio}$, and $\boldsymbol{R}_{pio}$ have been provided in section 2.6.1. After checking the fulfillment of the above two sufficient conditions, the sensors in table 5.3 are selected. Table 5.4 provides the dimension of the state, the input, and the output of the state-space model of the benchmark structure.

Table 5.3. *Selected sensors in test using PI observer*

Sensor type	Selected sensors
Only strain gauge	Strain gauge 1
	Strain gauge 2

Table 5.4. *Dimension of the state, the input, and the output of the state-space model of the benchmark structure in test using PI observer*

Name	Symbol	Dimension
State	$\boldsymbol{x}(t)$	4×1
Input	$\boldsymbol{d}(t)$	2×1
Output	$\boldsymbol{y}(t)$	2×1

The dynamics of the estimate error is described by equation (2.115) in which the first derivative of the unknown input appears as the input to the dynamics equation of the estimate error. When this PI observer design is applied for online force reconstruction, the first derivative of the input force will be an input to the estimate error. If the force is constant, the first derivative of the force will be zero, and the estimate error will converge to zero. If the force is not constant, the first derivative of the force will be non-zero. In this case, the estimate error still may converge, but to a non-zero value. For forces with fast dynamics, the LTR design parameter q needs to be set very large to in order to achieve a satisfactory result. However, the value of the LTR design parameter q can not be arbitrarily large due to the amplification effects from the measurement noise and the model uncertainty (Krajcin and Söffker, 2005). This indicates that this PI observer design may have some limitation on the reconstruction of forces with fast dynamics. In this benchmark study, three different settings are considered for the LTR design parameter q. Table 5.5 lists the values of these settings. The reconstruction results are plotted in figure 5.10 through figure 5.12. The values of the RMSE between the reconstructed forces and the measured (or true) forces are calculated and are plotted in form of bar plot in figure 5.13 through figure 5.15.

The reconstruction results show that the PI observer design which was proposed in Söffker et al. (1995) is suitable for the reconstruction of the quasi-static force, but not suitable for the reconstruction of the impact force. Furthermore, it is suitable for the reconstruction of the static part of the wind load, but not the dynamic part.

Table 5.5. *Settings for the LTR design parameter q in test using PI observer*

Case	Parameter	Setting	Unit
Case 1	q	1×10^{18}	$(-)$
Case 2	q	1×10^{17}	$(-)$
Case 3	q	1×10^{15}	$(-)$

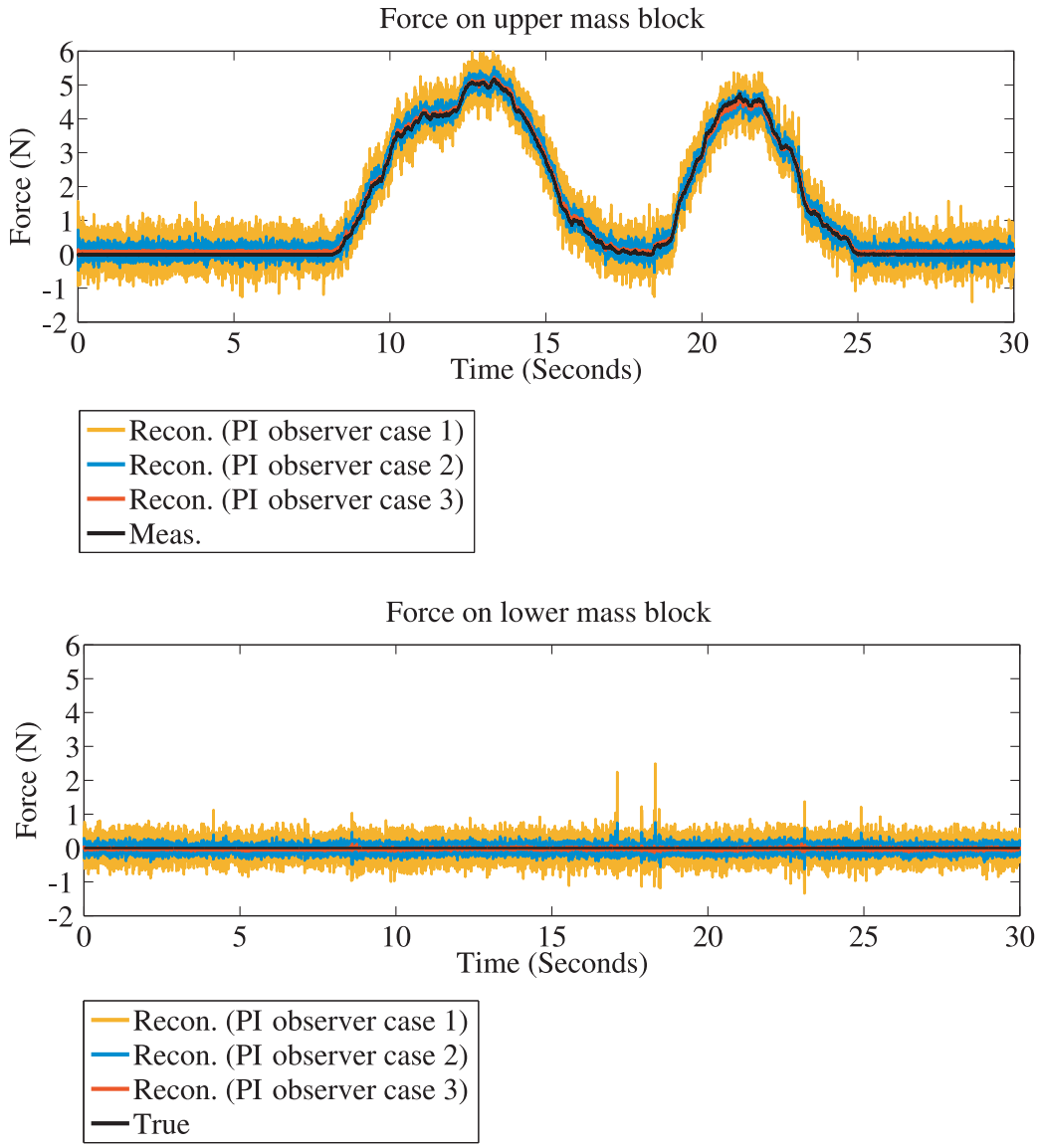

Figure 5.10. *Reconstruction results for the quasi-static force in test using PI observer (with two strain gauges)*

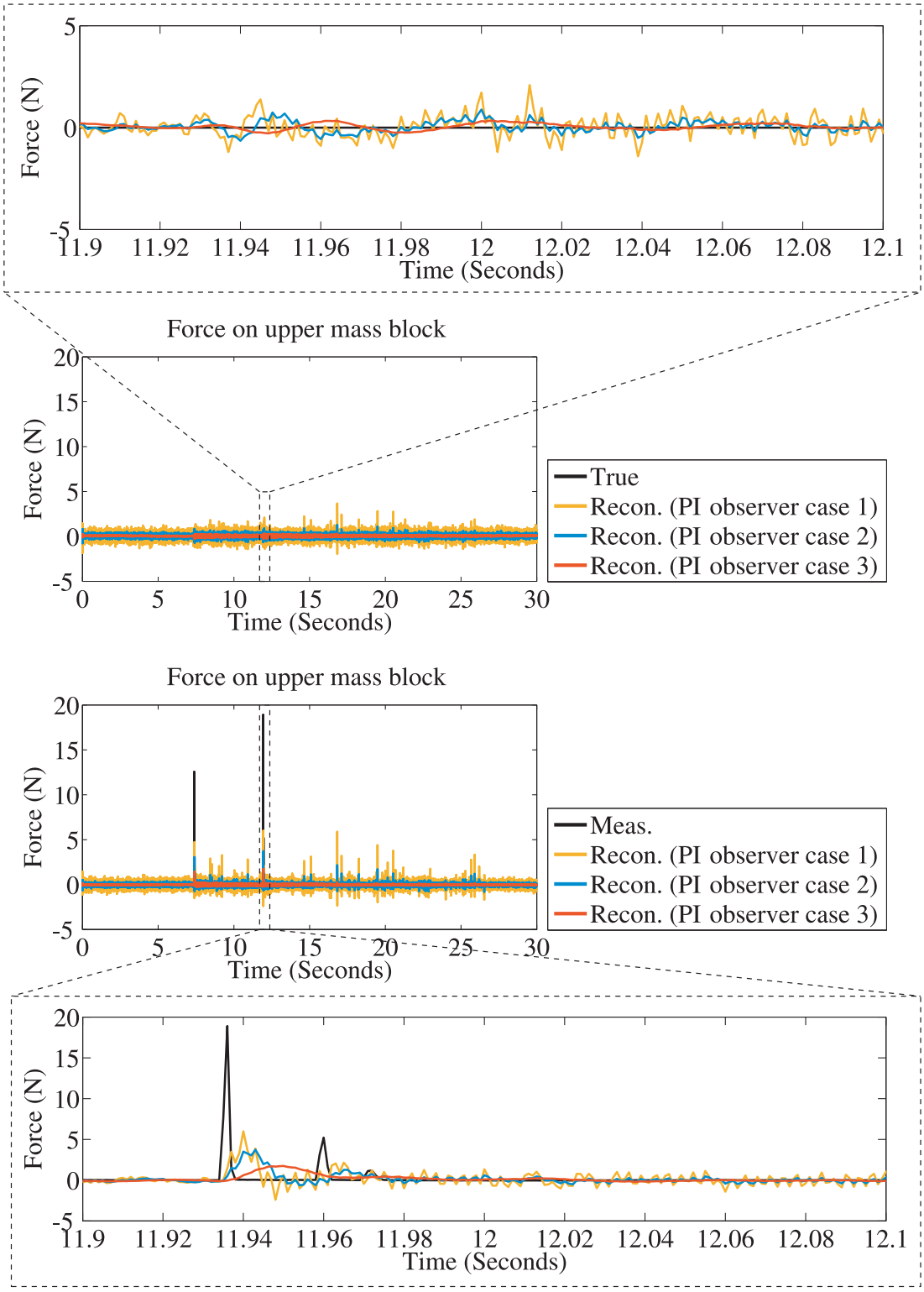

Figure 5.11. *Reconstruction results for the impact force in test using PI observer (with two strain gauges)*

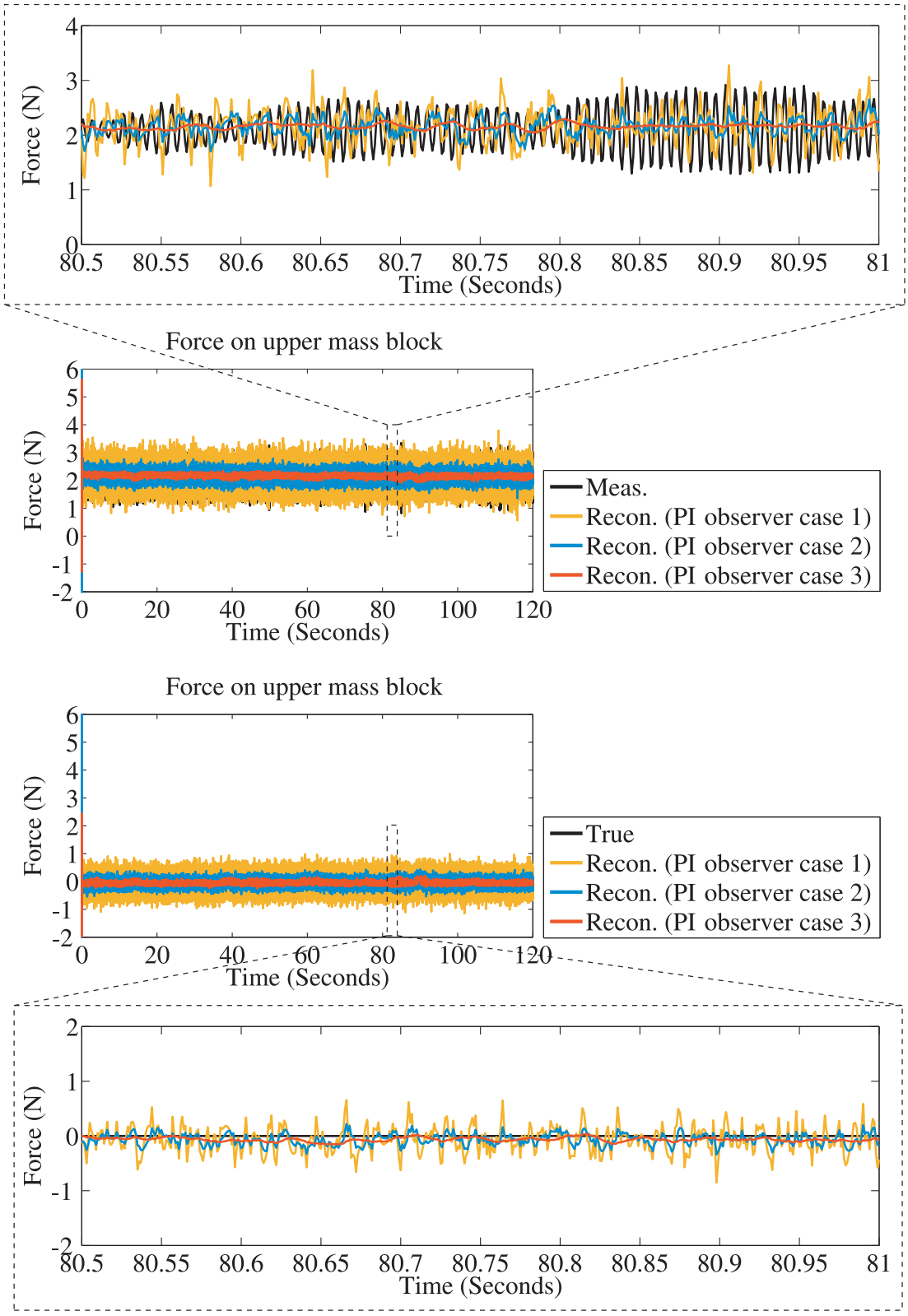

Figure 5.12. *Reconstruction results for the wind load in test using PI observer (with two strain gauges)*

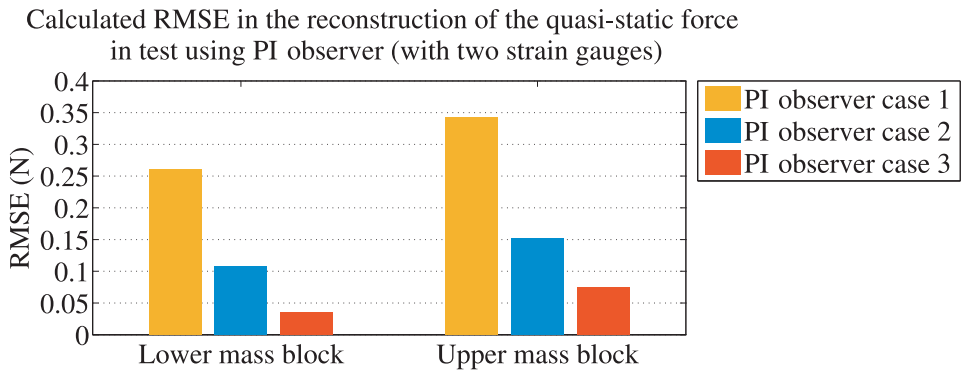

Figure 5.13. *Calculated RMSE in the reconstruction of the quasi-static force in test using PI observer (with two strain gauges)*

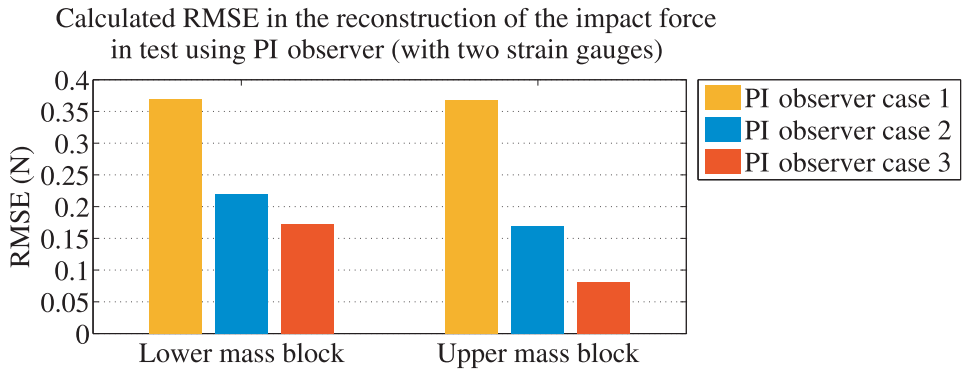

Figure 5.14. *Calculated RMSE in the reconstruction of the impact force in test using PI observer (with two strain gauges)*

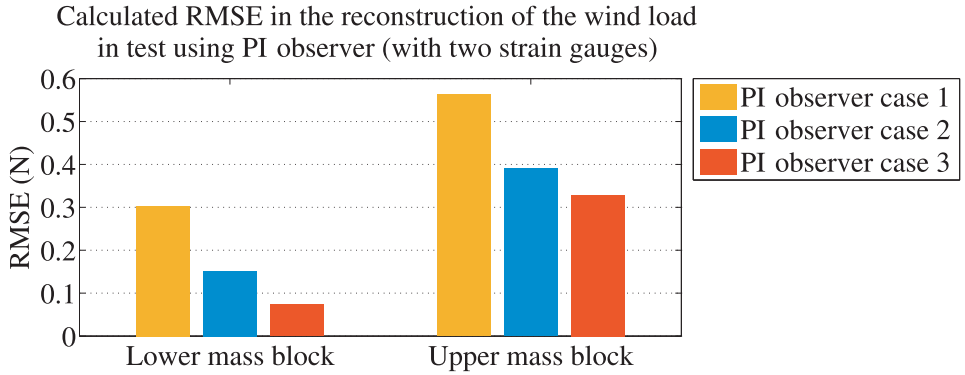

Figure 5.15. *Calculated RMSE in the reconstruction of the wind load in test using PI observer (with two strain gauges)*

5.2.5. Test using KF+RLSE

The Kalman Filter and a Recursive Least-Squares Estimator (KF+RLSE) is proposed in Tuan et al. (1996) for solving online two-dimensional inverse heat conduction problems. This algorithm was later adopted for force reconstruction by several researchers. For example, Ma et al. (2003) used this method to estimate the input forces acting on a

cantilever beam; Chen and Lee (2008) applied this method for moving force estimation through several simulations; and Wu et al. (2009) adopted this method in the identification of the soil force resulted from the soil-pile interaction in a shaking table test, etc. A short review of the KF+RLSE algorithm has been provided in section 2.6.3.

Within this benchmark study, the KF+RLSE algorithm is applied for reconstructing the three different types of forces which have been introduced in section 5.2.3. This algorithm does not need *a priori* information on the dynamics of the inputs, and does not require that the initial state estimate has to be unbiased. The direct feed-through is not considered in the output equation of system model. According to equation (2.17), this indicates that acceleration response of the benchmark structure is not considered in the output equation of the state-space model of the benchmark structure. The necessary condition for the existence of the KF+RLSE has been provided in section 2.6.3. After checking the fulfillment of this necessary condition, the sensors in table 5.6 are selected. Table 5.7 lists the dimension of the state, the input, and the output of the state-space model of the benchmark structure. Table 5.8 provides the parameter settings which are applied in this study. The stability of this method is achieved through the convergence of the covariance matrix of the state estimate error and the convergence of the covariance of the force estimate error. The reconstruction results are plotted in figure 5.16 through figure 5.18. The values of the RMSE between the reconstructed forces and the measured (or true) forces are calculated and are plotted in form of bar plot in figure 5.19 through figure 5.21. The reconstruction results show that the KF+RLSE method is suitable for the reconstruction of the quasi-static force, but not suitable for the reconstruction of the impact force. Furthermore, it is suitable for the reconstruction of the static part of the wind load, but not the dynamic part.

Table 5.6. *Selected sensors in test using KF+RLSE*

Sensor type	Selected sensors
Only strain gauge	Strain gauge 1
	Strain gauge 2

Table 5.7. *Dimension of the state, the input, and the output of the state-space model of the benchmark structure in test using KF+RLSE*

Name	Symbol	Dimension
State	$\boldsymbol{x}(t)$	4×1
Input	$\boldsymbol{d}(t)$	2×1
Output	$\boldsymbol{y}(t)$	2×1

Table 5.8. *Parameter settings in test using KF+RLSE*

Parameter	Setting	Unit
$\boldsymbol{Q}_d$	$1 \times 10^{-10}\boldsymbol{I}_4$	$\begin{bmatrix} (\mathrm{m^2/s^2}) & (\mathrm{m^2/s^2}) & (\mathrm{m^2/s^3}) & (\mathrm{m^2/s^3}) \\ (\mathrm{m^2/s^2}) & (\mathrm{m^2/s^2}) & (\mathrm{m^2/s^3}) & (\mathrm{m^2/s^3}) \\ (\mathrm{m^2/s^3}) & (\mathrm{m^2/s^3}) & (\mathrm{m^2/s^4}) & (\mathrm{m^2/s^4}) \\ (\mathrm{m^2/s^3}) & (\mathrm{m^2/s^3}) & (\mathrm{m^2/s^4}) & (\mathrm{m^2/s^4}) \end{bmatrix}$
$\boldsymbol{R}_d$	$1.5 \times 10^{-13}\boldsymbol{I}_2$	$\begin{bmatrix} (-) & (-) \\ (-) & (-) \end{bmatrix}$
γ	1×10^{-1}	$(-)$
$\hat{\boldsymbol{x}}_{0\|0}$	$\begin{bmatrix} 0 & 0 & 0 & 0 \end{bmatrix}^T$	$\begin{bmatrix} (\mathrm{m}) & (\mathrm{m}) & (\mathrm{m/s}) & (\mathrm{m/s}) \end{bmatrix}^T$
$\hat{\boldsymbol{d}}_0$	$\begin{bmatrix} 0 & 0 \end{bmatrix}^T$	$\begin{bmatrix} (\mathrm{N}) & (\mathrm{N}) \end{bmatrix}^T$
$\boldsymbol{P}^x_{0\|0}$	$1 \times 10^{-4}\boldsymbol{I}_4$	$\begin{bmatrix} (\mathrm{m^2}) & (\mathrm{m^2}) & (\mathrm{m^2/s}) & (\mathrm{m^2/s}) \\ (\mathrm{m^2}) & (\mathrm{m^2}) & (\mathrm{m^2/s}) & (\mathrm{m^2/s}) \\ (\mathrm{m^2/s}) & (\mathrm{m^2/s}) & (\mathrm{m^2/s^2}) & (\mathrm{m^2/s^2}) \\ (\mathrm{m^2/s}) & (\mathrm{m^2/s}) & (\mathrm{m^2/s^2}) & (\mathrm{m^2/s^2}) \end{bmatrix}$
$\boldsymbol{P}^d_0$	$1 \times 10^{-4}\boldsymbol{I}_2$	$\begin{bmatrix} (\mathrm{N^2}) & (\mathrm{N^2}) \\ (\mathrm{N^2}) & (\mathrm{N^2}) \end{bmatrix}$
$\boldsymbol{M}_0$	$1 \times 10^{-4}\boldsymbol{I}_4$	$\begin{bmatrix} (-) & (-) & (-) & (-) \\ (-) & (-) & (-) & (-) \\ (-) & (-) & (-) & (-) \\ (-) & (-) & (-) & (-) \end{bmatrix}$

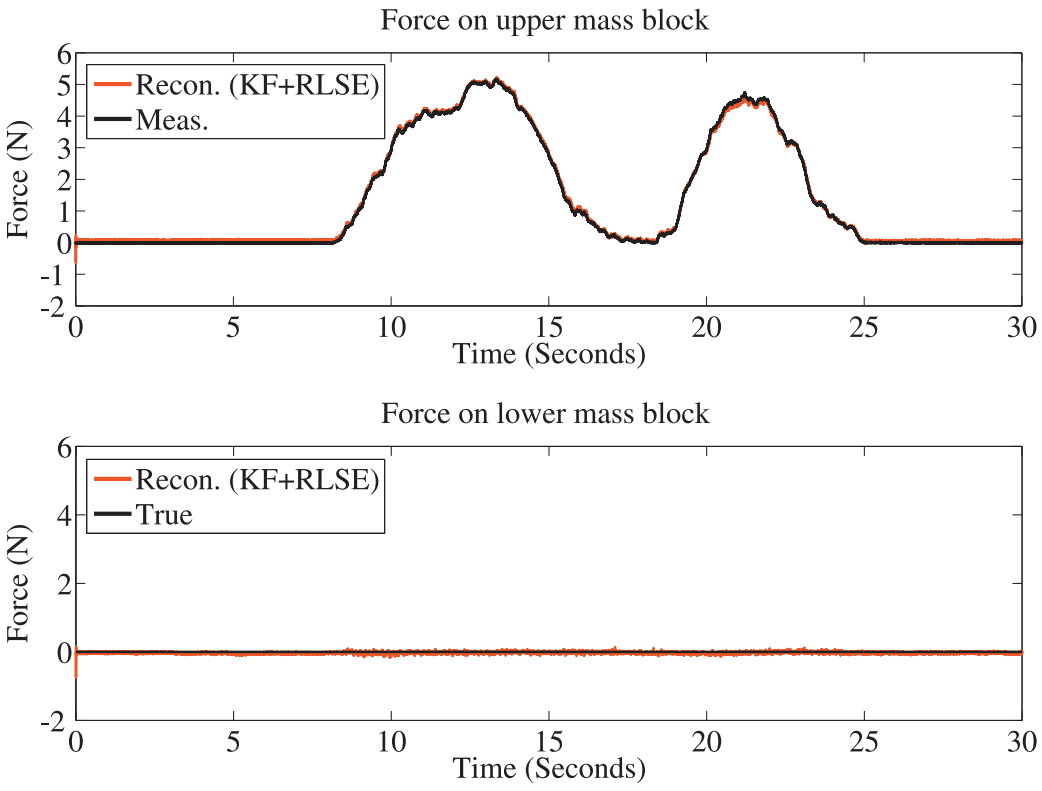

Figure 5.16. *Reconstruction results for the quasi-static force in test using KF+RLSE (with two strain gauges)*

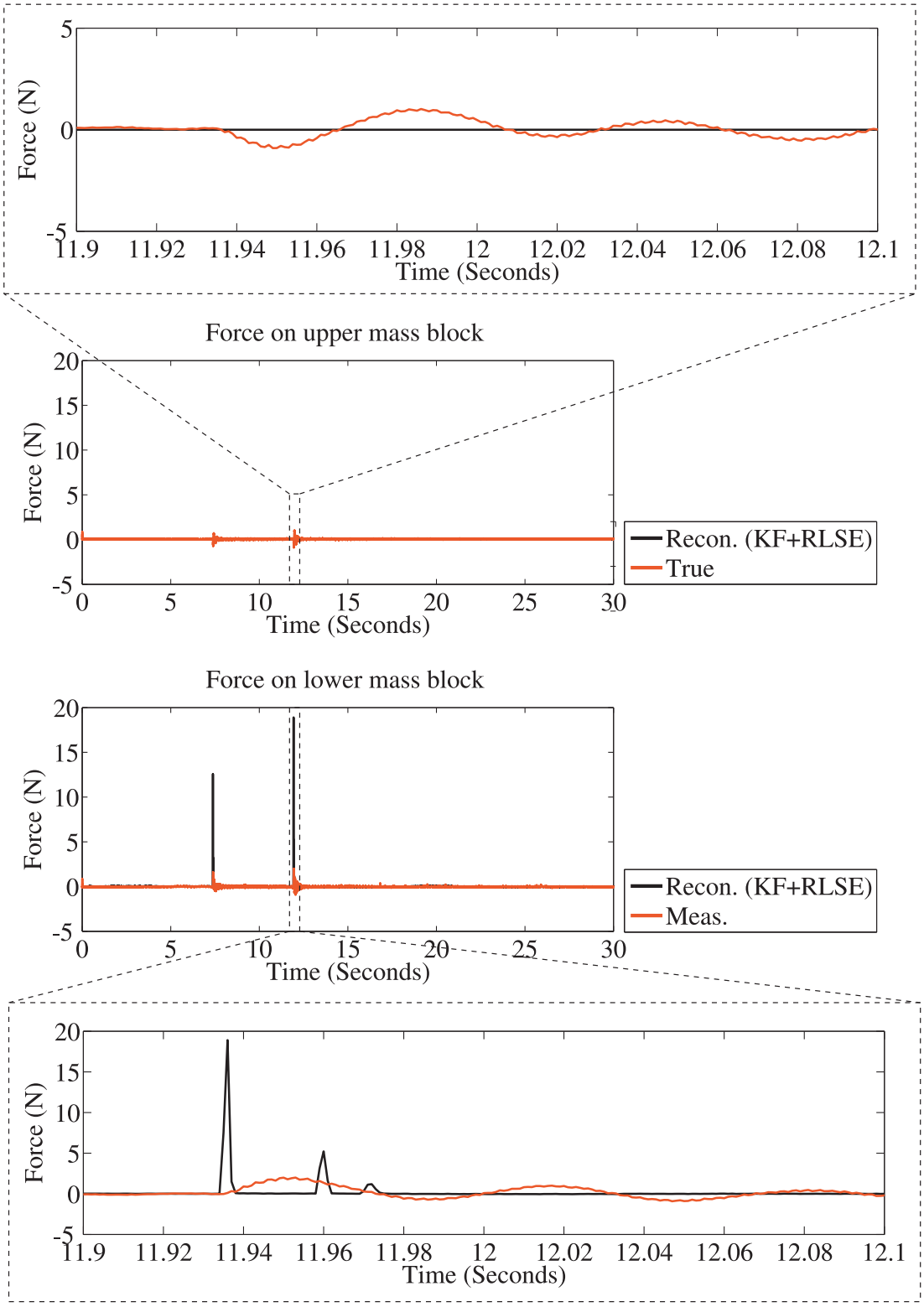

Figure 5.17. *Reconstruction results for the impact force in test using KF+RLSE (with two strain gauges)*

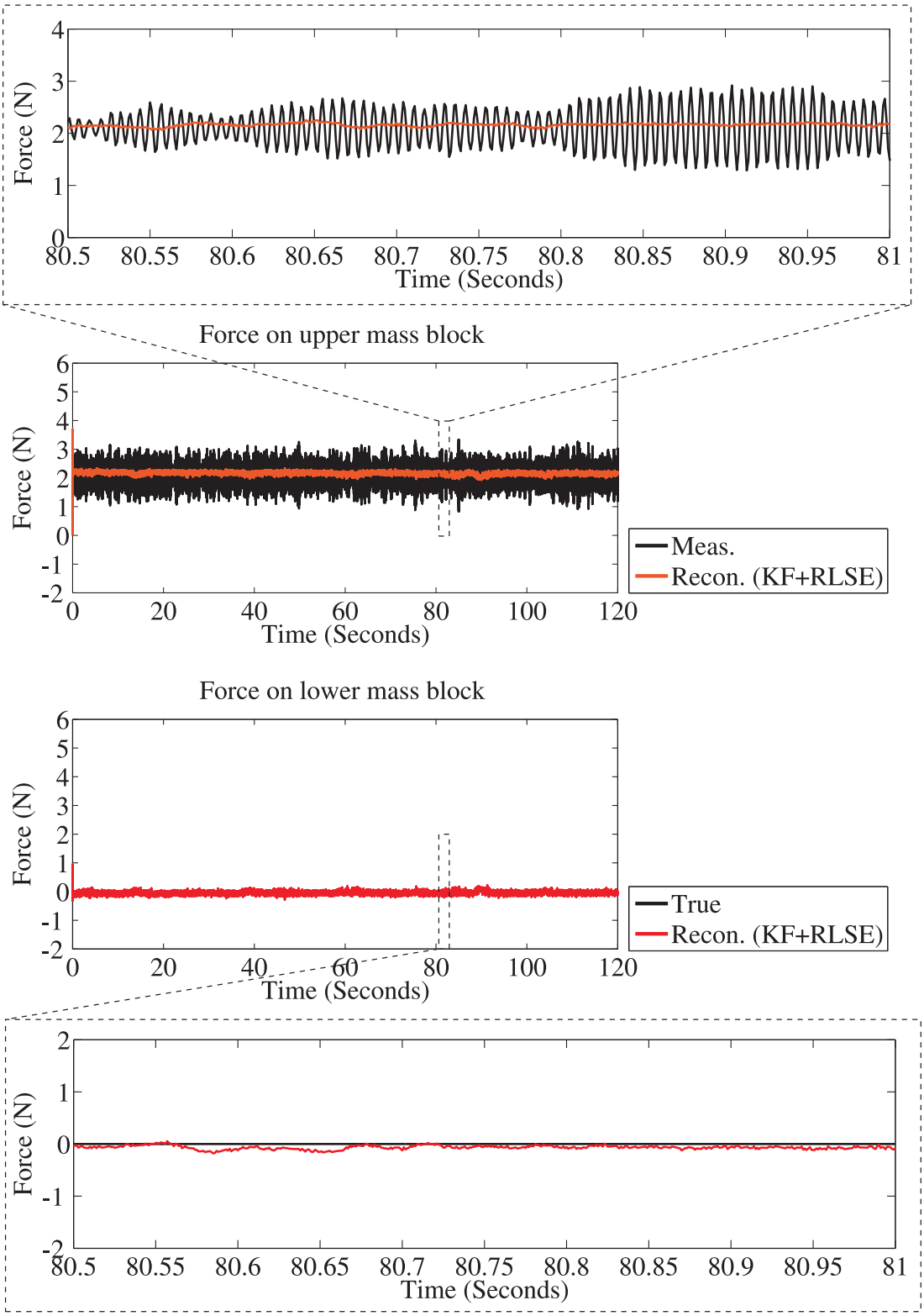

Figure 5.18. *Reconstruction results for the wind load in test using KF+RLSE (with two strain gauges)*

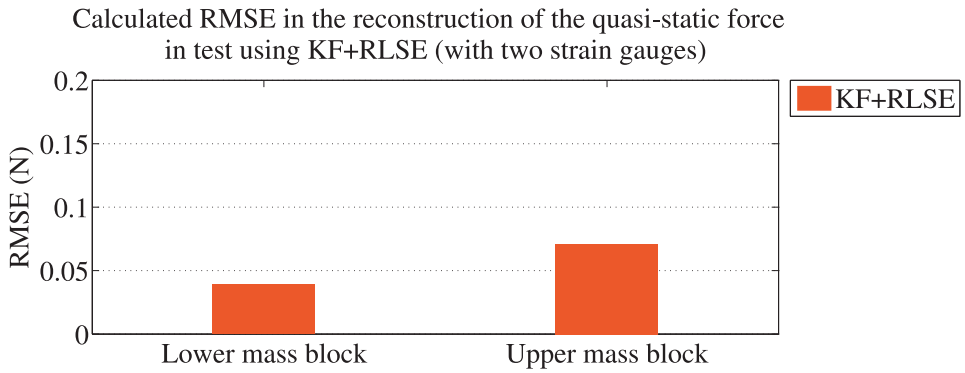

Figure 5.19. *Calculated RMSE in the reconstruction of the quasi-static force in test using KF+RLSE (with two strain gauges)*

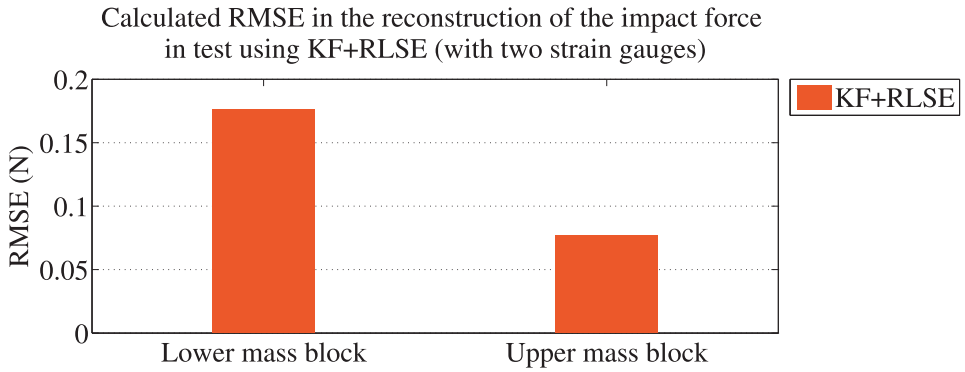

Figure 5.20. *Calculated RMSE in the reconstruction of the impact force in test using KF+RLSE (with two strain gauges)*

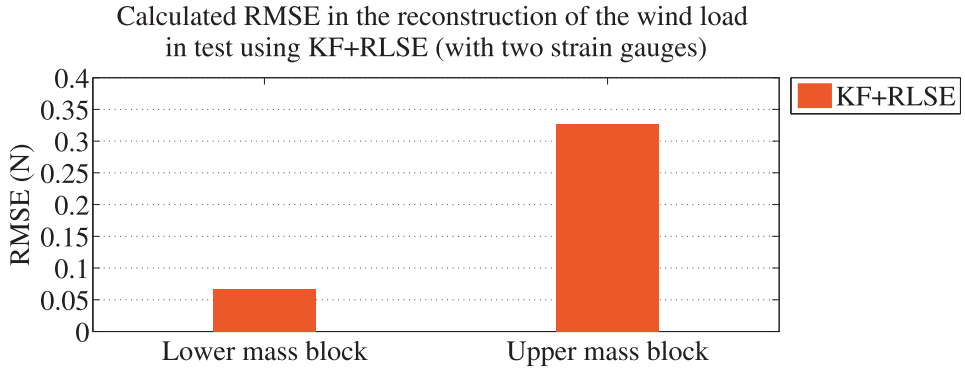

Figure 5.21. *Calculated RMSE in the reconstruction of the wind load in test using KF+RLSE (with two strain gauges)*

5.2.6. Test using SS&IE_L

Ha and Trinh (2004) proposed a UIO based method which can realize simultaneous state and input estimation for a class of nonlinear systems. Klinkov and Fritzen (2006) named this method as SS&IE and adopted it for online force reconstruction. The SS&IE was applied in a study for the reconstruction of the wind load on a 5 MW wind energy plant (Klinkov and Fritzen, 2009; Fritzen et al., 2013). In this thesis, this method is

named as SS&IE_N which is short for Simultaneous State and Input Estimation for a class of Nonlinear systems. A short review of the SS&IE_N algorithm has been provided in section 2.6.2. In the SS&IE_N, a Linear Matrix Inequality (LMI) needs to be solved. Ha and Trinh (2004) suggested to use MATLAB LMI Control Toolbox as a computationally efficient manner to solve the LMI. However, it is noticed that the solution of the LMI may have convergence problem, when the number of the inputs is larger than two. In many practical cases, a structure can be assumed to be linear. Motivated by this practical assumption, a modification to the SS&IE_N is proposed in section 4.1, so that the modified algorithm is suitable for linear systems. In this thesis, this modified algorithm is named as SS&IE_L which is short for Simultaneous State and Input Estimation for Linear systems. Some preliminary results from a simulation study on online force reconstruction using the SS&IE_L has been presented in Niu et al. (2010).

Within this benchmark study, the SS&IE_L is applied for reconstructing the three different types of forces which have been introduced in section 5.2.3. The SS&IE_L do not need *a priori* information on the dynamics of the input forces, and does not require that the initial estimate of the state has to be unbiased. The direct feed-through is considered in the output equation of the system model. The necessary and sufficient conditions for the existence of the SS&IE_L have been provided in section 4.1. The SS&IE_L requires that the direct feed-through should have full column rank. According to equation (2.17), this indicates that acceleration sensors should be applied and the number of acceleration sensors should be equal to or larger than the number of input forces. After checking the fulfillment of those necessary and sufficient conditions, the sensors in table 5.9 are selected. Table 5.10 lists the dimension of the state, the input, and the output of the state-space model of the benchmark structure. To filter out the low frequency drift in the acceleration measurements, a second-order Butterworth filter is applied, with the cutoff frequency being set at 0.5 Hz. The matrices $\boldsymbol{Z}_{ssieL}$ and $\boldsymbol{F}_{ssieL}$ in equation (4.14) are calculated with the help of the MATLAB function *place*. The eigenvalues of matrix $\boldsymbol{N}_{ssieL}$ are all placed on the LHP of the s-plane at -1. The stability of this method is achieved by the convergence of $\tilde{\boldsymbol{x}}_{aug}(t)$ which is the estimate error of the augmented state $\boldsymbol{x}_{aug}(t)$. The reconstruction results are plotted in figure 5.22 through figure 5.24. The values of the RMSE between the reconstructed forces and the measured (or true) forces are calculated and are plotted in form of bar plot in figure 5.25 through figure 5.27. The reconstruction results show that the SS&IE_L is suitable for the reconstruction of the quasi-static force, the impace force and the wind load.

Table 5.9. *Selected sensors in test using SS&IE_L*

Sensor type	Selected sensors
Strain gauge & accelerometer	Strain gauge 1
	Strain gauge 2
	Accelerometer 1
	Accelerometer 2

Table 5.10. *Dimension of the state, the input, and the output of the state-space model of the benchmark structure in test using SS&IE_L*

Name	Symbol	Dimension
State	$\boldsymbol{x}(t)$	4×1
Input	$\boldsymbol{d}(t)$	2×1
Output	$\boldsymbol{y}(t)$	4×1

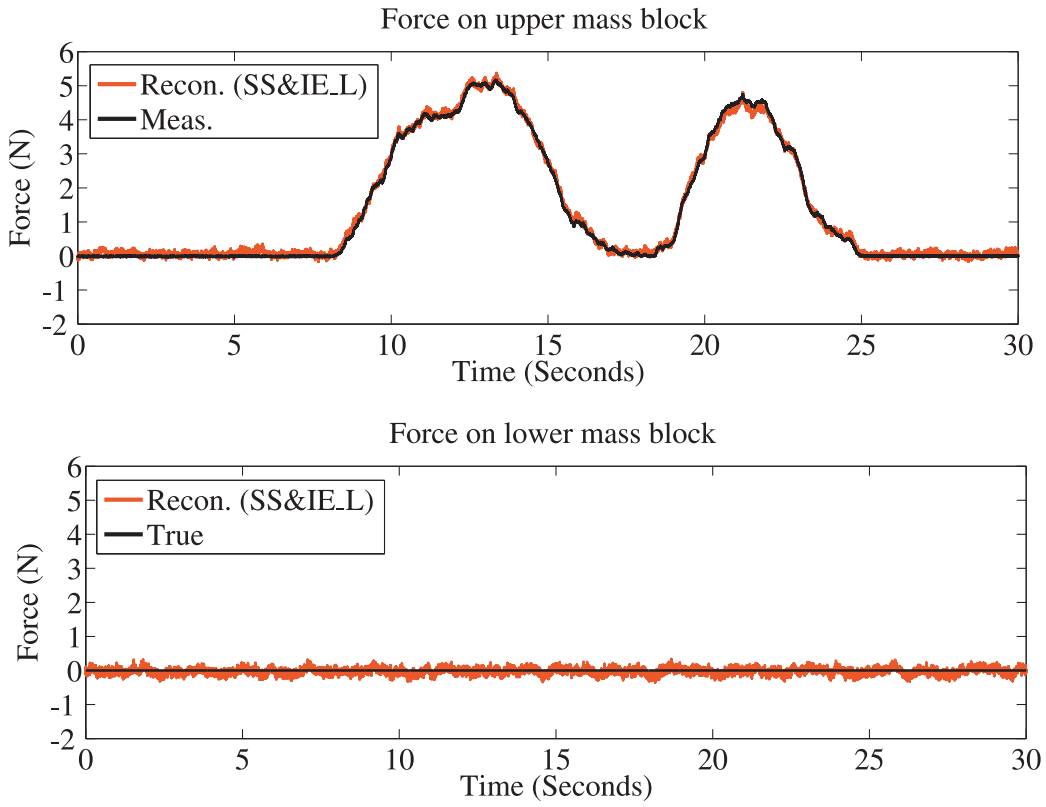

Figure 5.22. *Reconstruction results for the quasi-static force in test using SS&IE_L (with two strain gauges and two accelerometers)*

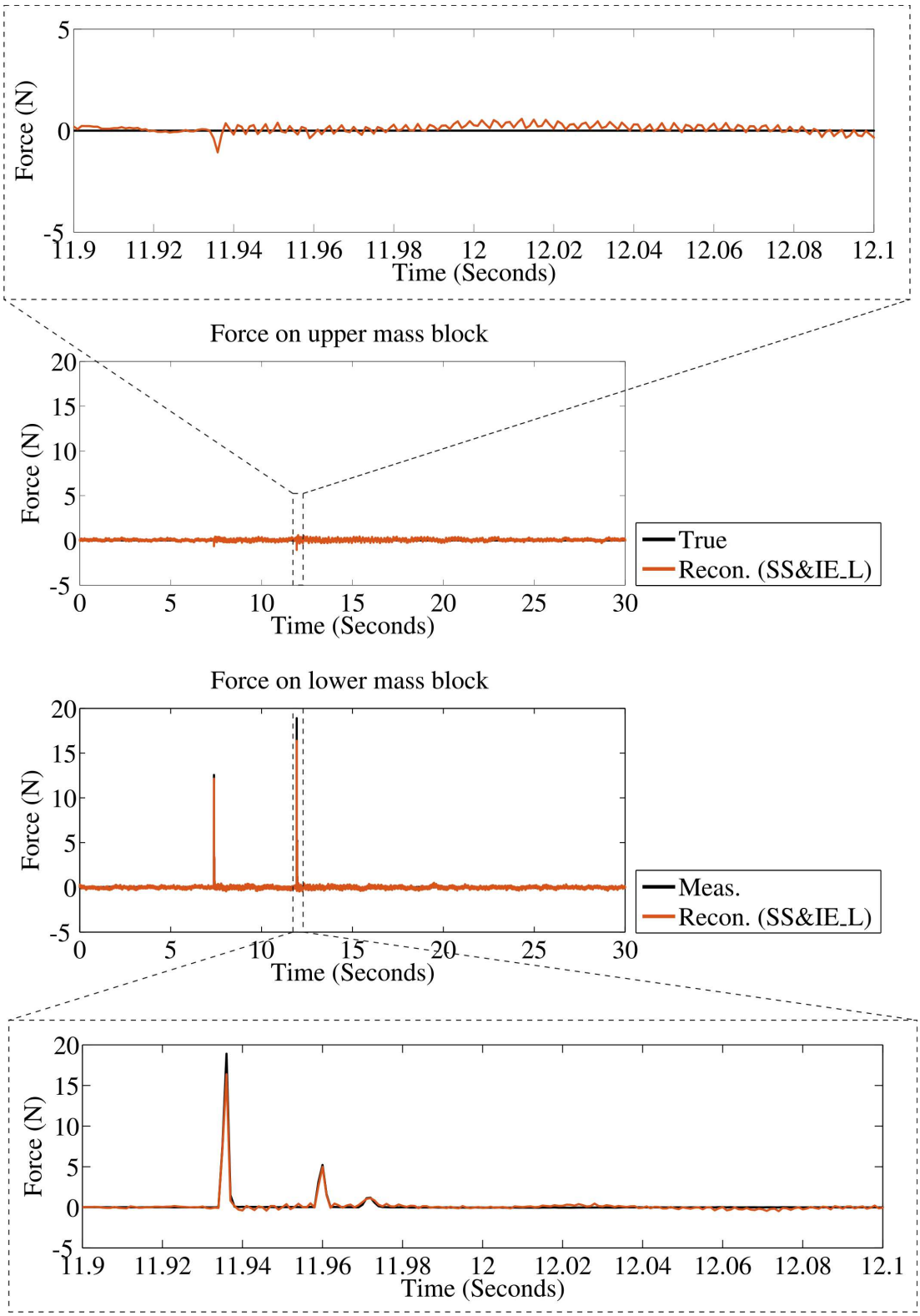

Figure 5.23. *Reconstruction results for the impact force in test using SS&IE_L (with both strain gauges and accelerometers)*

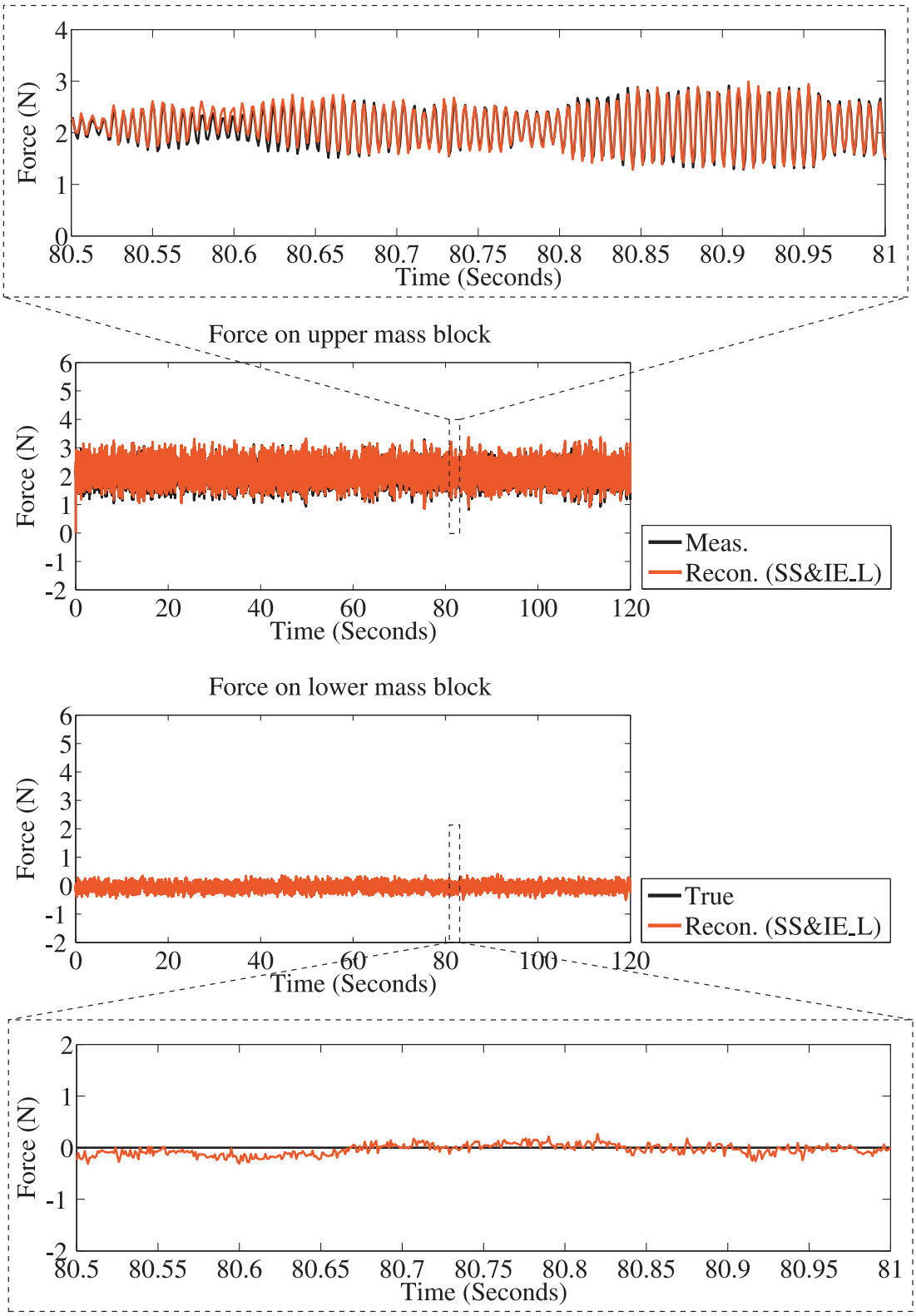

Figure 5.24. *Reconstruction results for the wind load in test using SS&IE_L (with both strain gauges and accelerometers)*

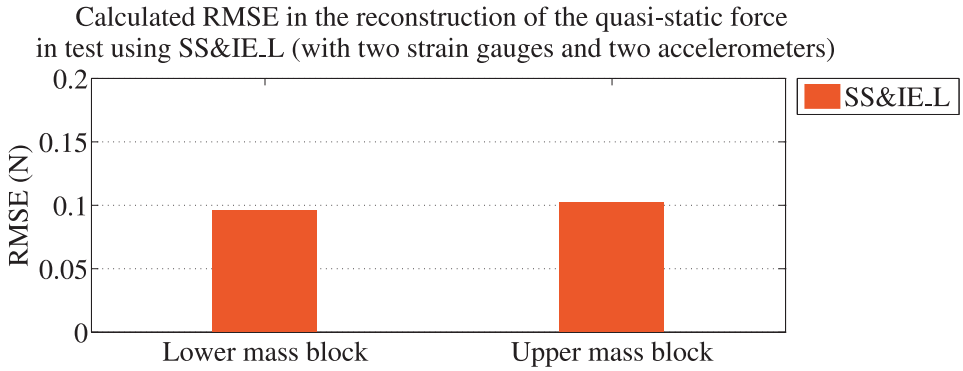

Figure 5.25. *Calculated RMSE in the reconstruction of the quasi-static force in test using SS&IE_L (with two strain gauges and two accelerometers)*

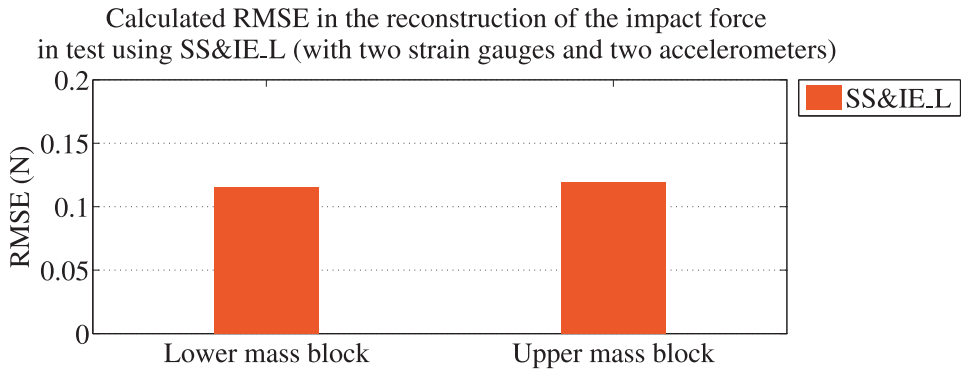

Figure 5.26. *Calculated RMSE in the reconstruction of the impact force in test using SS&IE_L (with two strain gauges and two accelerometers)*

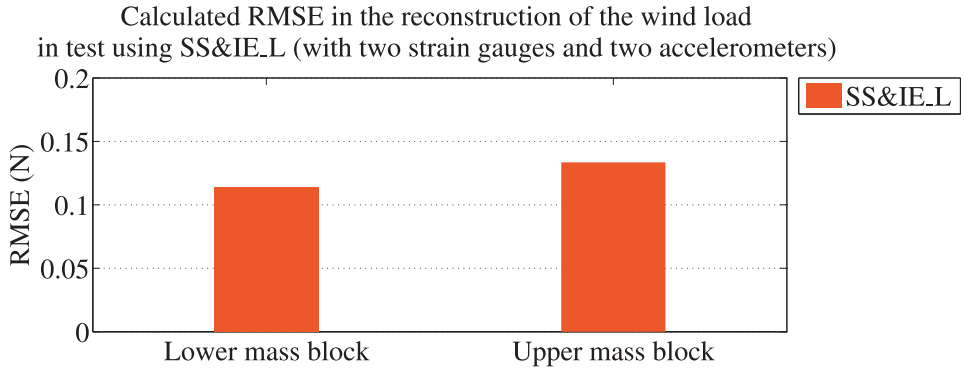

Figure 5.27. *Calculated RMSE in the reconstruction of the wind load in test using SS&IE_L (with two strain gauges and two accelerometers)*

5.2.7. Test using AKF

Lourens et al. (2012b) proposed the Augmented Kalman Filter (AKF) and applied this method for the estimation of an impact force which was applied on a laboratory steel beam. A brief review of the the AKF has been provided in section 2.6.6. In this method, the state vector is augmented with the input vector, and the augmented state vector is

estimated with the help of the Kalman filter. The direct feed-through is considered in the output equation of the system model. Perisic et al. (2012) applied the same method as the AKF for gearbox fatigue load estimation for condition monitoring of wind turbines. In some previous studies, a method which is similar to the AKF has already been used for force reconstruction, e.g. in Ji and Liang (2000) and Berg and Miller (2010). In these two studies, the state vector is augmented with the input vector, and the augmented state vector is estimated with the help of the Kalman filter, too. The difference between this method and the AKF is that this method does not consider the direct feed-through in the system model while the AKF does consider the direct feed-through.

In this benchmark study, the AKF is applied for reconstructing the three different types of forces which have been introduced in section 5.2.3. The AKF assumes the matrix $\boldsymbol{Q}_d^{input}$, which is the covariance matrix of the increment of the inputs, is known. It does not require that the initial estimate of the state has to be unbiased. The direct feed-through is considered in the output equation of the system model. This makes it possible to use acceleration sensors. As stated above, the AKF needs the information of $\boldsymbol{Q}_d^{input}$, the covariance matrix of the increment of the inputs. However, such information is not always available in practice. In order to check the influence of $\boldsymbol{Q}_d^{input}$ on the reconstruction results, two different settings for $\boldsymbol{Q}_d^{input}$ are considered for each of the three different types of forces, with one being calculated based on the measured (or true) forces and the other one being set as an identity matrix. Table 5.11 lists the settings for $\boldsymbol{Q}_d^{input}$. The common parameter settings are provided in table 5.12.

Table 5.11. *Settings for $\boldsymbol{Q}_d^{input}$ in test using AKF*

Case No.	Force Type	Parameter	Setting	Unit
1	Quasi-static	$\boldsymbol{Q}_d^{input}$	$\begin{bmatrix} 1\times10^{-10} & 0 \\ 0 & 1.029\times10^{-4} \end{bmatrix}$	$\begin{bmatrix} (\mathrm{N}^2) & (\mathrm{N}^2) \\ (\mathrm{N}^2) & (\mathrm{N}^2) \end{bmatrix}$
2	Quasi-static	$\boldsymbol{Q}_d^{input}$	$\boldsymbol{I}_2$	$\begin{bmatrix} (\mathrm{N}^2) & (\mathrm{N}^2) \\ (\mathrm{N}^2) & (\mathrm{N}^2) \end{bmatrix}$
3	Impact	$\boldsymbol{Q}_d^{input}$	$\begin{bmatrix} 2.64\times10^{-2} & 0 \\ 0 & 1\times10^{-10} \end{bmatrix}$	$\begin{bmatrix} (\mathrm{N}^2) & (\mathrm{N}^2) \\ (\mathrm{N}^2) & (\mathrm{N}^2) \end{bmatrix}$
4	Impact	$\boldsymbol{Q}_d^{input}$	$\boldsymbol{I}_2$	$\begin{bmatrix} (\mathrm{N}^2) & (\mathrm{N}^2) \\ (\mathrm{N}^2) & (\mathrm{N}^2) \end{bmatrix}$
5	Wind load	$\boldsymbol{Q}_d^{input}$	$\begin{bmatrix} 1\times10^{-10} & 0 \\ 0 & 9.44\times10^{-2} \end{bmatrix}$	$\begin{bmatrix} (\mathrm{N}^2) & (\mathrm{N}^2) \\ (\mathrm{N}^2) & (\mathrm{N}^2) \end{bmatrix}$
6	Wind load	$\boldsymbol{Q}_d^{input}$	$\boldsymbol{I}_2$	$\begin{bmatrix} (\mathrm{N}^2) & (\mathrm{N}^2) \\ (\mathrm{N}^2) & (\mathrm{N}^2) \end{bmatrix}$

Table 5.12. *Common parameter settings in test using AKF*

Parameter	Setting	Unit
$\hat{\boldsymbol{x}}_{0\|0}$	$\begin{bmatrix} 0 & 0 & 0 & 0 \end{bmatrix}^T$	$\begin{bmatrix} (\mathrm{m}) & (\mathrm{m}) & (\mathrm{m/s}) & (\mathrm{m/s}) \end{bmatrix}^T$
$\hat{\boldsymbol{d}}_{0\|0}$	$\begin{bmatrix} 0 & 0 \end{bmatrix}^T$	$\begin{bmatrix} (\mathrm{N}) & (\mathrm{N}) \end{bmatrix}^T$
$\boldsymbol{Q}_d$	$1 \times 10^{-10} \boldsymbol{I}_4$	$\begin{bmatrix} (\mathrm{m^2/s^2}) & (\mathrm{m^2/s^2}) & (\mathrm{m^2/s^3}) & (\mathrm{m^2/s^3}) \\ (\mathrm{m^2/s^2}) & (\mathrm{m^2/s^2}) & (\mathrm{m^2/s^3}) & (\mathrm{m^2/s^3}) \\ (\mathrm{m^2/s^3}) & (\mathrm{m^2/s^3}) & (\mathrm{m^2/s^4}) & (\mathrm{m^2/s^4}) \\ (\mathrm{m^2/s^3}) & (\mathrm{m^2/s^3}) & (\mathrm{m^2/s^4}) & (\mathrm{m^2/s^4}) \end{bmatrix}$

Results from using only strain gauges

The necessary condition for the existence of the AKF has been provided in section 2.6.6. After checking the fulfillment of the necessary condition, the sensor in table 5.13 are selected. Table 5.14 lists the dimension of the state, the input, and the output of the state-space model of the benchmark structure. The setting for the covariance matrix of the measurement noise is provided in table 5.15. The stability of this method is achieved through the convergence of the covariance matrix of the estimate error of the augmented state $\boldsymbol{x}_{aug,k}$. The reconstruction results are plotted in figure 5.28 through figure 5.30. The values of the RMSE between the reconstructed forces and the measured (or true) forces are calculated and are plotted in form of bar plot in figure 5.31 through figure 5.33.

The reconstruction results show that the AKF with only strain gauge is suitable for the reconstruction of the quasi-static force, but not suitable for the reconstruction of the impact force. It is suitable for the reconstruction of the static part of the wind load, but not the dynamic part. Furthermore, with a correct setting for the matrix $\boldsymbol{Q}_d^{input}$, the AKF can provide better reconstruction results for the mass block where actually no force is applied in the x direction.

Table 5.13. *Selected sensors in test using AKF with only strain gauges*

Sensor type	Selected sensors
Only strain gauge	Strain gauge 1
	Strain gauge 2

Table 5.14. *Dimension of the state, the input, and the output of the state-space model of the benchmark structure in test using AKF (with two strain gauges)*

Name	Symbol	Dimension
State	$\boldsymbol{x}(t)$	4×1
Input	$\boldsymbol{d}(t)$	2×1
Output	$\boldsymbol{y}(t)$	2×1

Table 5.15. *Setting for the covariance matrix of the measurement noise in test using AKF (with two strain gauges)*

Parameter	Setting	Unit
$\boldsymbol{R}_d$	$\begin{bmatrix} 1.5\times10^{-13} & 0 \\ 0 & 1.5\times10^{-13} \end{bmatrix}$	$\begin{bmatrix} (-) & (-) \\ (-) & (-) \end{bmatrix}$

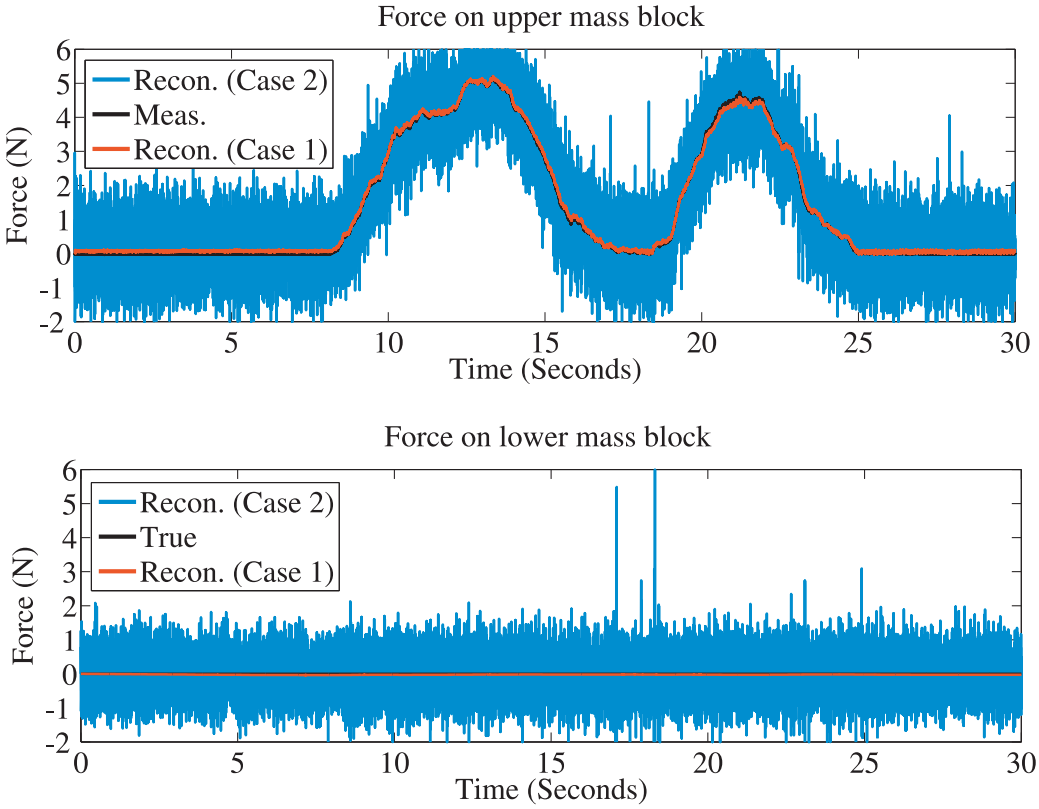

Figure 5.28. *Reconstruction results for the quasi-static force in test using AKF (with two strain gauges)*

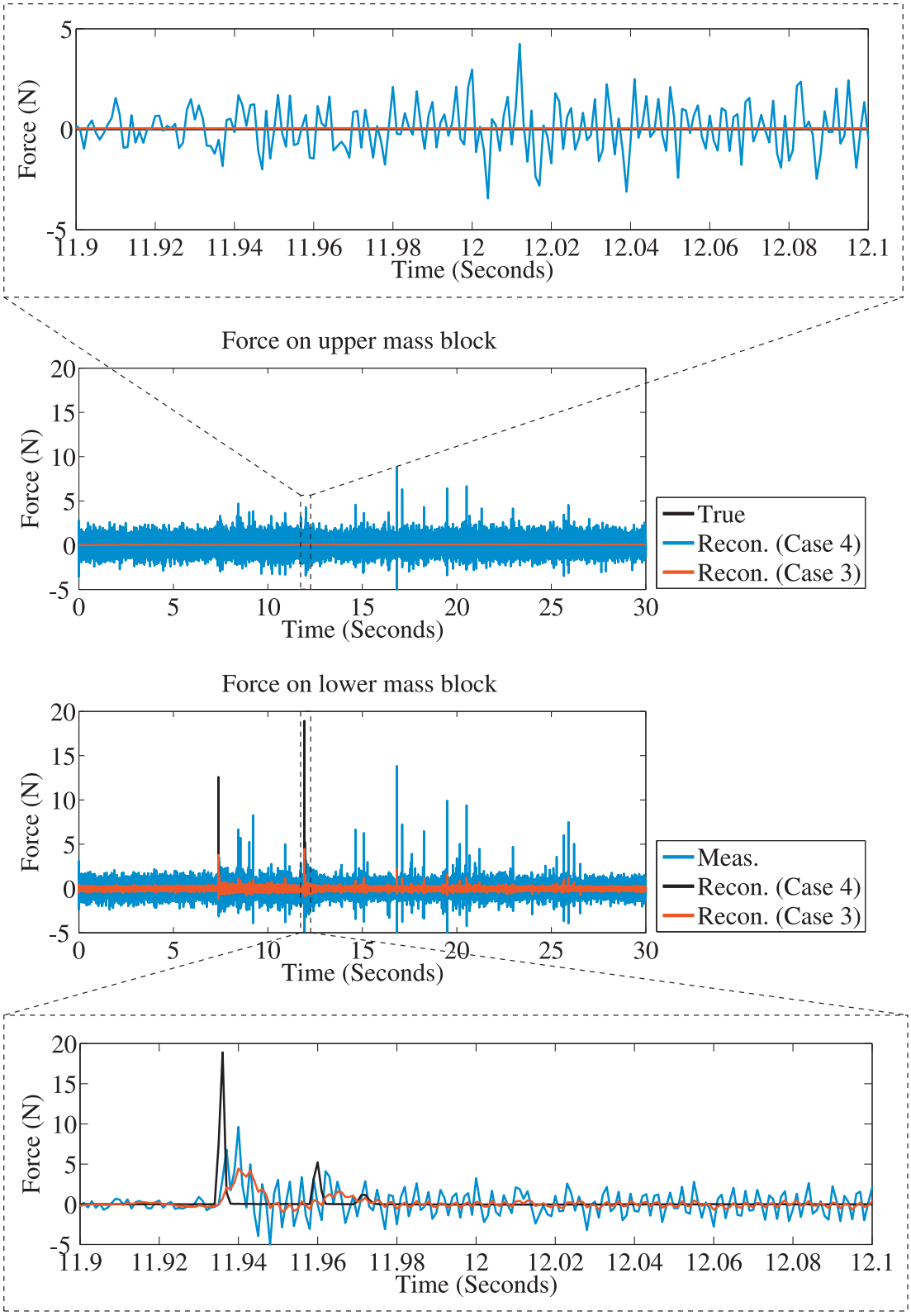

Figure 5.29. *Reconstruction results for the impact force in test using AKF (with two strain gauges)*

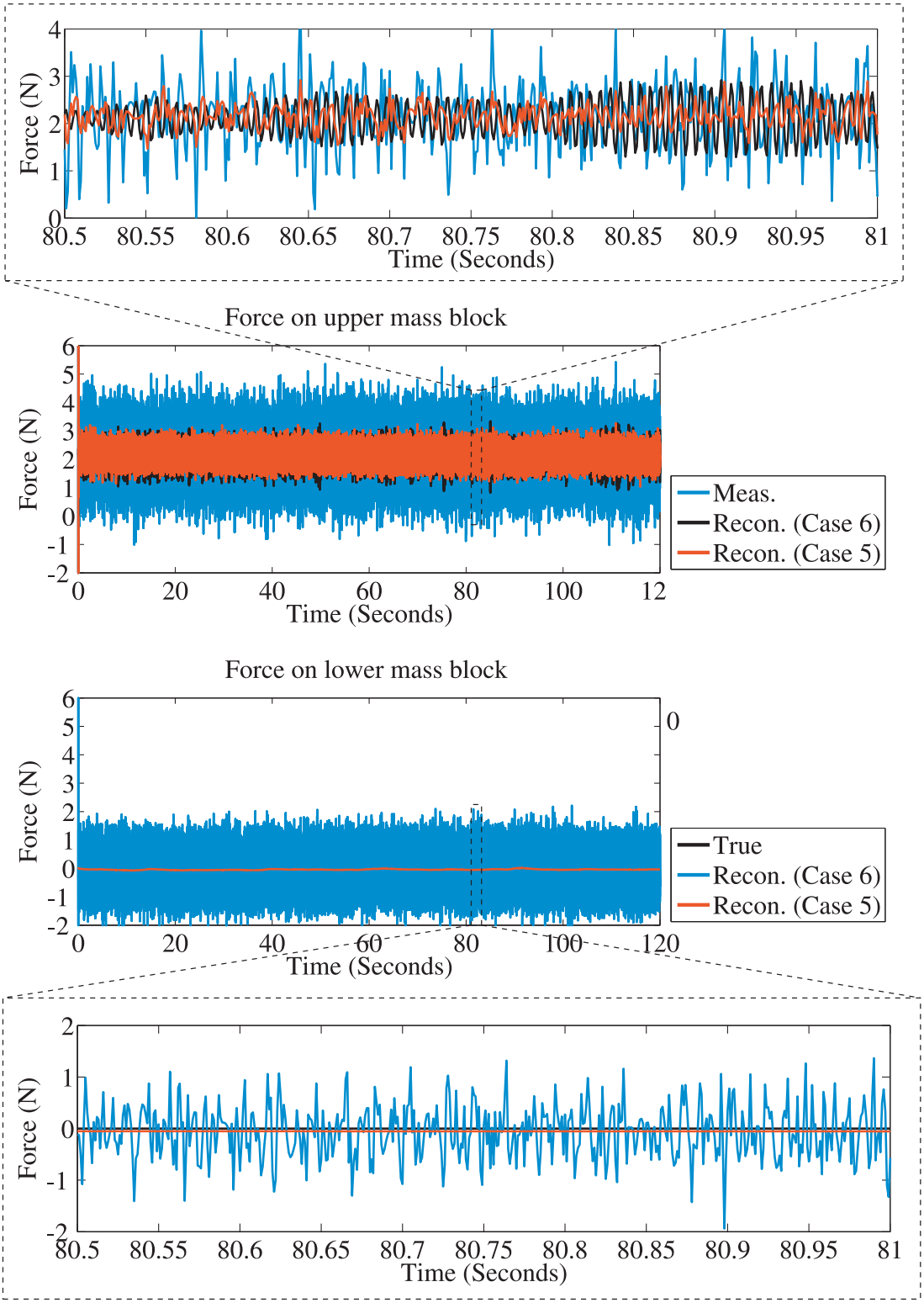

Figure 5.30. *Reconstruction results for the wind load in test using AKF (with two strain gauges)*

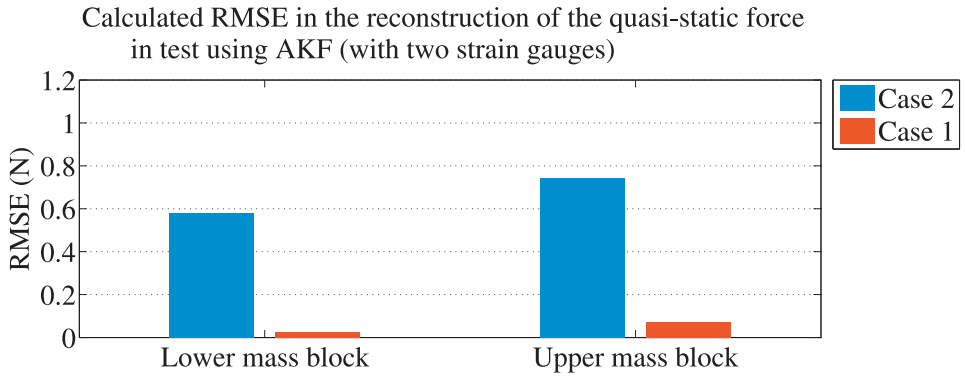

Figure 5.31. *Calculated RMSE in the reconstruction of the quasi-static force in test using AKF (with two strain gauges)*

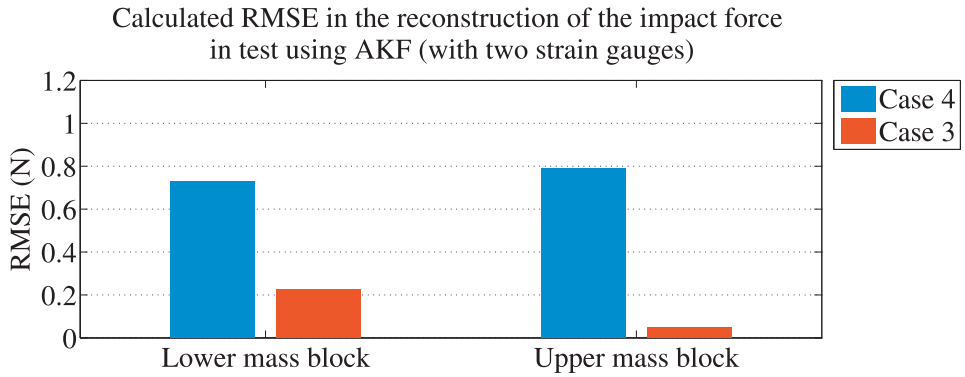

Figure 5.32. *Calculated RMSE in the reconstruction of the impact force in test using AKF (with two strain gauges)*

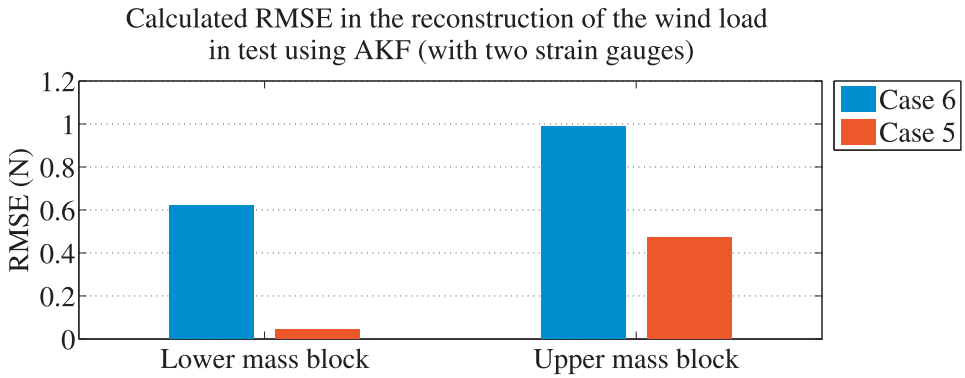

Figure 5.33. *Calculated RMSE in the reconstruction of the wind load in test using AKF (with two strain gauges)*

Results from using both strain gauges and accelerometers

The necessary condition for the existence of the AKF has been provided in section 2.6.6. After checking the fulfillment of the necessary condition, the sensor in table 5.16 are selected. Table 5.17 lists the dimension of the state, the input, and the output of the state-space model of the benchmark structure. To filter out the low frequency drift in the acceleration measurements, a second-order Butterworth filter is applied, with the cutoff frequency being set at 0.5 Hz. The setting for the matrix $\boldsymbol{R}_d$, which is the covariance matrix of the measurement noise, is provided in table 5.18. The unit of the matrix $\boldsymbol{R}_d$ is provided in table 5.19. The stability of this method is achieved through the convergence of the covariance matrix of the estimate error of the augmented state $\boldsymbol{x}_{aug,k}$. The reconstruction results are plotted in figure 5.34 through figure 5.36. The values of the RMSE between the reconstructed forces and the measured (or true) forces are calculated and are plotted in form of bar plot in figure 5.37 through figure 5.39.

The reconstruction results show that the AKF with both strain gauges and accelerometers is suitable for the reconstruction of the quasi-static force, the impact force, and the wind load. Furthermore, with a correct setting for the matrix $\boldsymbol{Q}_d^{input}$, the AKF can provide better reconstruction results for the mass block where actually no force is applied in the x direction.

Table 5.16. *Selected sensors in test using AKF with both strain gauges and accelerometers*

Sensor type	Selected sensors
Strain gauge & accelerometer	Strain gauge 1
	Strain gauge 2
	Accelerometer 1
	Accelerometer 2

Table 5.17. *Dimension of the state, the input, and the output of the state-space model of the benchmark structure in test using AKF (with two strain gauges and two accelerometers)*

Name	Symbol	Dimension
State	$\boldsymbol{x}(t)$	4×1
Input	$\boldsymbol{d}(t)$	2×1
Output	$\boldsymbol{y}(t)$	4×1

Table 5.18. *Setting for the covariance matrix of the measurement noise in test using AKF (with two strain gauges and two accelerometers)*

Parameter	Setting			
$\boldsymbol{R}_d$	1.5×10^{-13}	0	0	0
	0	1.5×10^{-13}	0	0
	0	0	3×10^{-3}	0
	0	0	0	3×10^{-3}

Table 5.19. *Unit of the covariance matrix of the measurement noise in test using AKF (with two strain gauges and two accelerometers)*

Parameter	Unit			
$\boldsymbol{R}_d$	$(-)$	$(-)$	$(\mathrm{m/s^2})$	$(\mathrm{m/s^2})$
	$(-)$	$(-)$	$(\mathrm{m/s^2})$	$(\mathrm{m/s^2})$
	$(\mathrm{m/s^2})$	$(\mathrm{m/s^2})$	$(\mathrm{m^2/s^4})$	$(\mathrm{m^2/s^4})$
	$(\mathrm{m/s^2})$	$(\mathrm{m/s^2})$	$(\mathrm{m^2/s^4})$	$(\mathrm{m^2/s^4})$

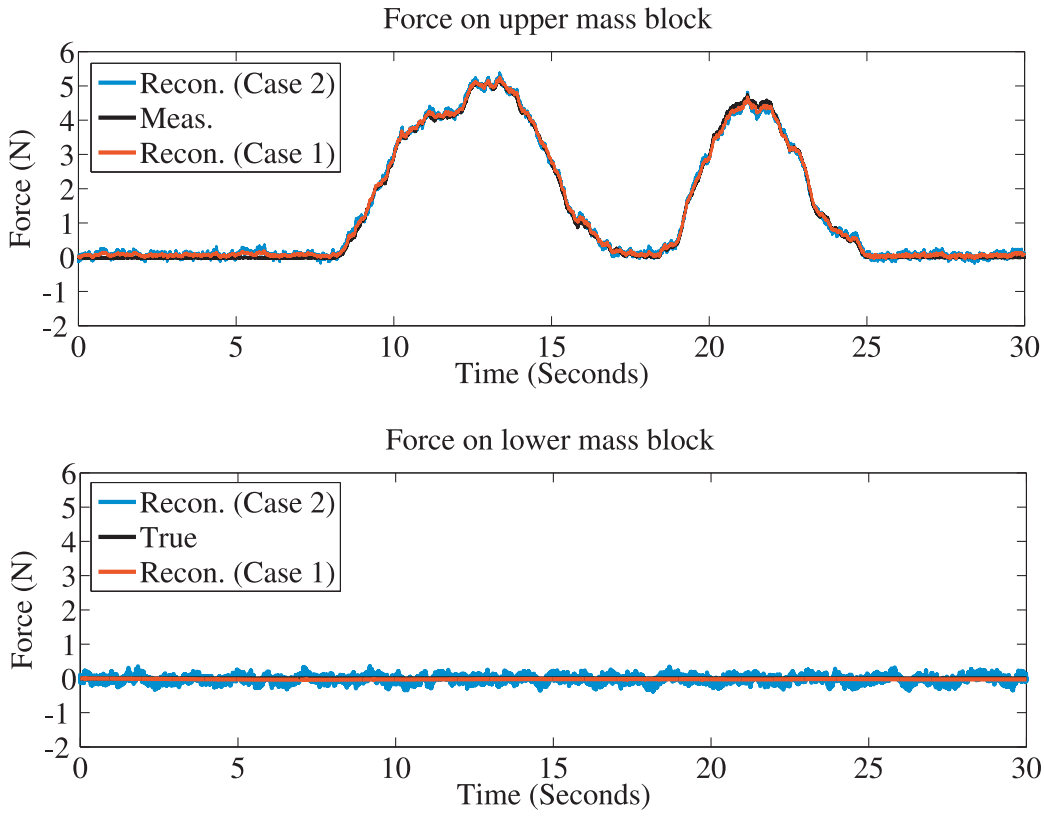

Figure 5.34. *Reconstruction results for the quasi-static force in test using AKF (with two strain gauges and two accelerometers)*

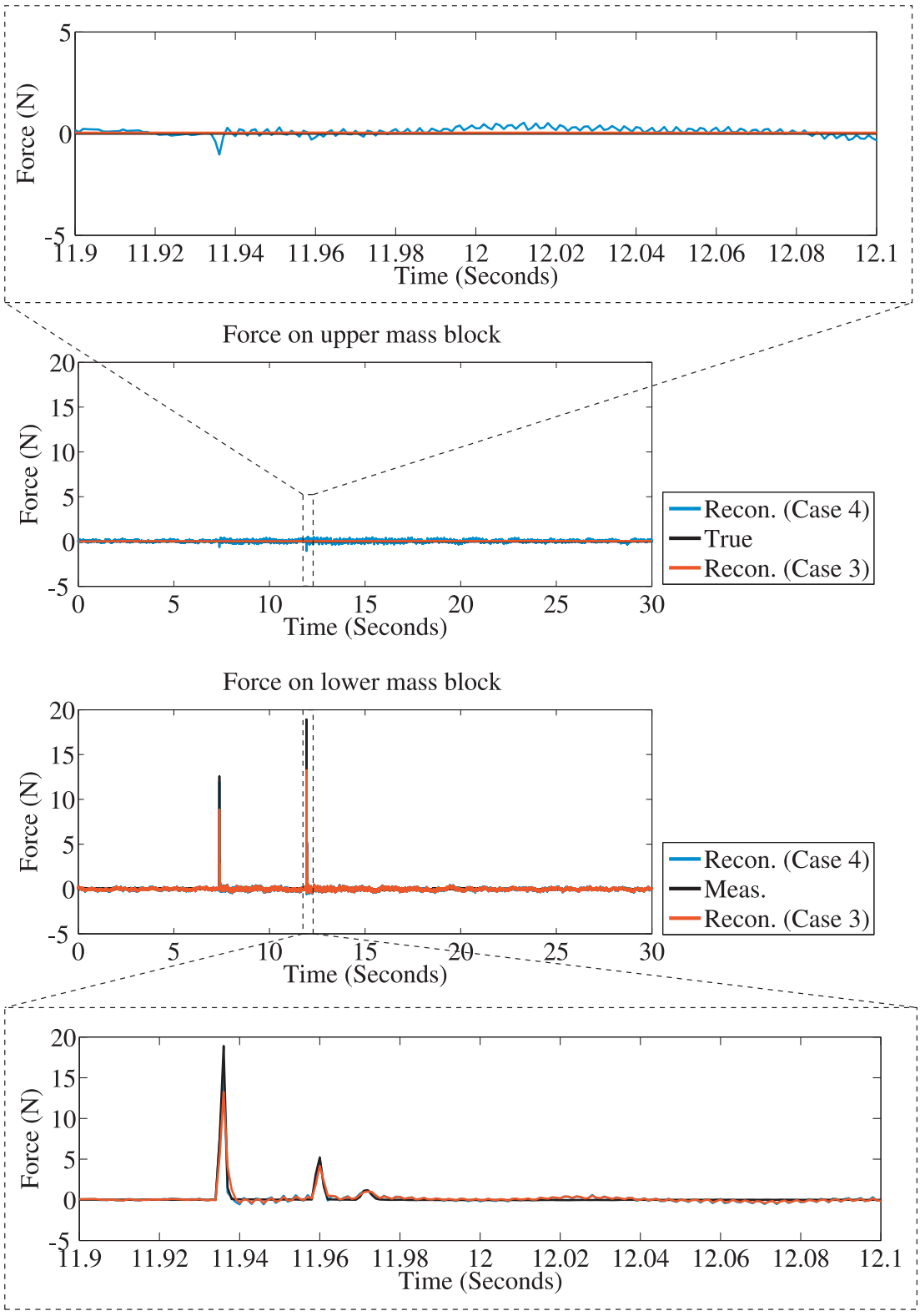

Figure 5.35. *Reconstruction results for the impact force in test using AKF (with both strain gauges and accelerometers)*

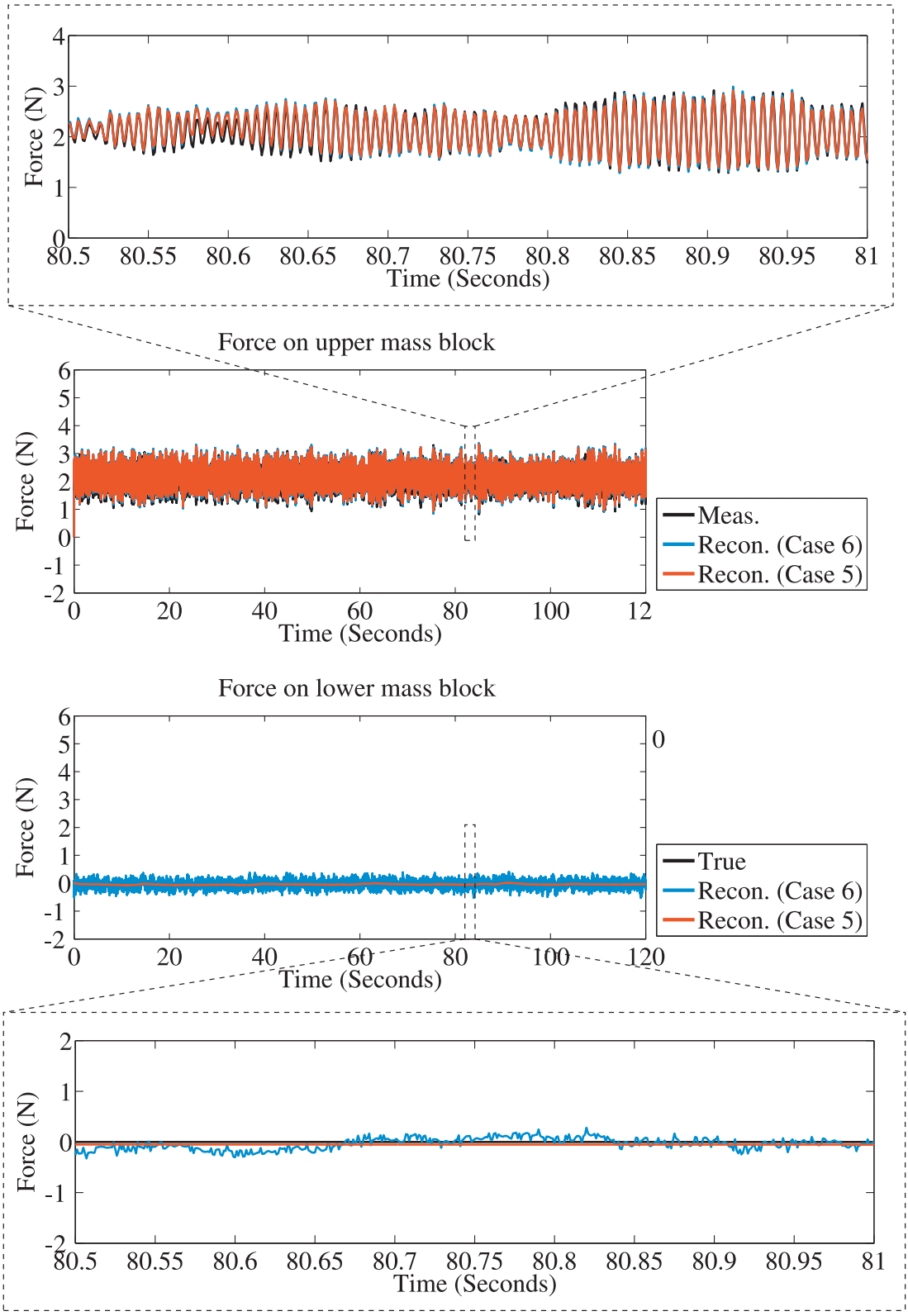

Figure 5.36. *Reconstruction results for the wind load in test using AKF (with two strain gauges and two accelerometers)*

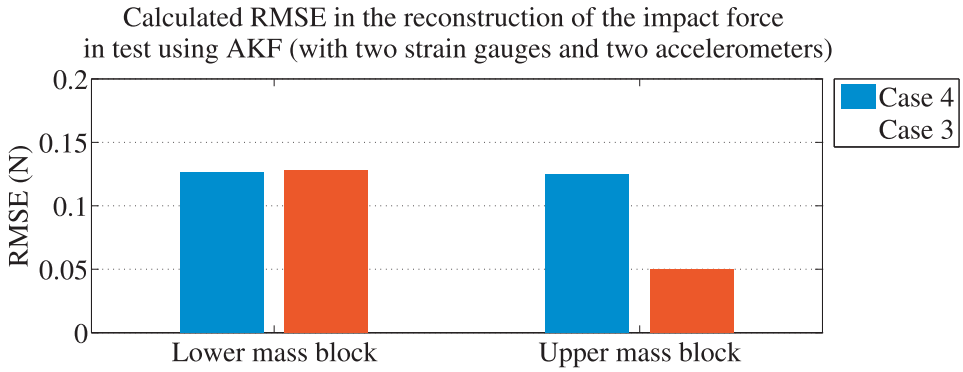

Figure 5.37. *Calculated RMSE in the reconstruction of the quasi-static force in test using AKF (with two strain gauges and two accelerometers)*

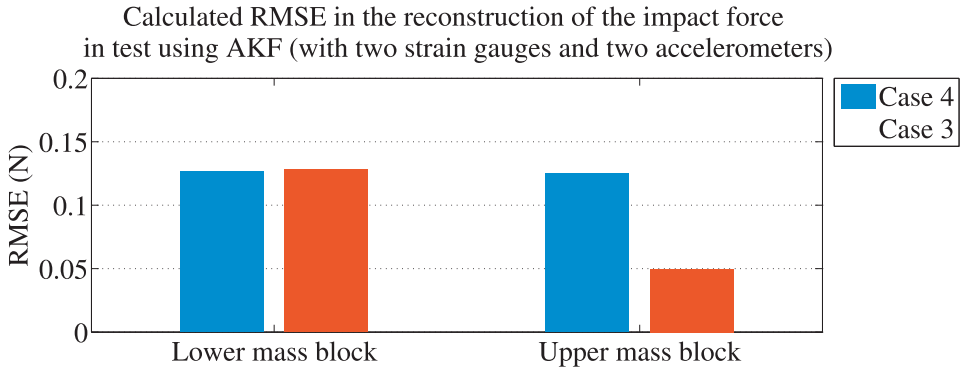

Figure 5.38. *Calculated RMSE in the reconstruction of the impact force in test using AKF (with two strain gauges and two accelerometers)*

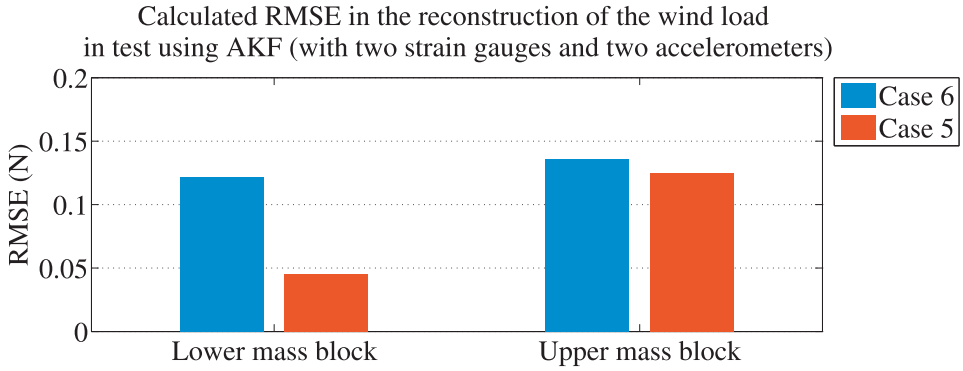

Figure 5.39. *Calculated RMSE in the reconstruction of the wind load in test using AKF (with two strain gauges and two accelerometers)*

5.2.8. Test using KF-UI and G-KF-UI

Pan et al. (2011) presented a Kalman Filter with Unknown Inputs (KF-UI) approach for joint input and state estimation for discrete-time stochastic systems with direct feed-through. This approach is derived with the weighted least-squares estimation method, and the state estimate and the input estimate are proven optimal in the minimum-variance

and unbiased sense. Niu et al. (2011) noticed the input estimation capability of the KF-UI approach and adopted it for online force reconstruction. A brief review of the the KF-UI has been provided in section 2.6.5, where it is listed that the existence of the KF-UI requires that the direct feed-through should have full column rank. According to equation (2.17) and equation (2.23), this requirement actually means that acceleration response should be considered in the output equation of the state-space structural model. According to the discussion in section 2.7, the consideration of acceleration in the output equation indicates that the process noise and the measurement noise are correlated. However, In the derivation of the KF-UI approach, the process noise and the measurement noise are assumed to be uncorrelated. To make the KF-UI theoretically suitable for online force reconstruction, Niu and Fritzen (2012) presented a generalized KF-UI which is compatible with the correlation of the process noise and the measurement noise. This generalized KF-UI is abbreviated as G-KF-UI. The filter equations of the G-KF-UI have been provided in section 4.3.3.

In this benchmark study, both the KF-UI and the G-KF-UI are applied for reconstructing the three different types of forces which have been introduced in section 5.2.3. A brief review of the KF-UI has been provided in section 2.6.5. Furthermore, some modifications to the KF-UI have been proposed in section 4.3.2. The filter equations of the G-KF-UI have been presented in section 4.3.3. Both the KF-UI and the G-KF-UI do not need *a priori* information on the dynamics of the input, and do not an unbiased initial state estimate. Section 4.3.2 presentsthe necessary and sufficient conditions for the existence of the KF-UI. These mathematical conditions are applicable to the G-KF-UI, too. Both methods require that the direct feed-through should have full column rank. According to equation (2.17), this indicates that acceleration sensors should be applied and the number of acceleration sensors should be equal to or larger than the number of input forces. After checking the fulfillment of those necessary and sufficient conditions, the sensors in table 5.20 are selected. Table 5.21 lists the dimension of the state, the input, and the output of the state-space model of the benchmark structure. To filter out the low frequency drift in the acceleration measurements, a second-order Butterworth filter is applied, with the cutoff frequency being set at 0.5 Hz.

Table 5.20. *Selected sensors in test using KF-UI and G-KF-UI*

Sensor type	Selected sensors
Strain gauge & accelerometer	Strain gauge 1
	Strain gauge 2
	Accelerometer 1
	Accelerometer 2

Table 5.21. *Dimension of the state, the input, and the output of the state-space model of the benchmark structure in test using KF-UI and G-KF-UI*

Name	Symbol	Dimension
State	$\boldsymbol{x}(t)$	4×1
Input	$\boldsymbol{d}(t)$	2×1
Output	$\boldsymbol{y}(t)$	4×1

Table 5.22. *Parameter settings in test using KF-UI and G-KF-UI*

Parameter	Setting
$\hat{\boldsymbol{x}}_{0\|0}$	$\begin{bmatrix} 0 & 0 & 0 & 0 \end{bmatrix}^T$
$\hat{\boldsymbol{d}}_0$	$\begin{bmatrix} 0 & 0 \end{bmatrix}^T$
$\boldsymbol{P}^x_{0\|0}$	$1 \times 10^{-4}\boldsymbol{I}_4$
$\boldsymbol{P}^d_0$	$1 \times 10^{-2}\boldsymbol{I}_2$
$\boldsymbol{P}^{xd}_0$	$\begin{bmatrix} 0 & 0 & 0 & 0 \\ 0 & 0 & 0 & 0 \end{bmatrix}^T$
$\boldsymbol{P}^{dx}_0$	$\begin{bmatrix} 0 & 0 & 0 & 0 \\ 0 & 0 & 0 & 0 \end{bmatrix}$
$\boldsymbol{Q}_d$	$1 \times 10^{-10}\boldsymbol{I}_4$
$\boldsymbol{R}_d$	$\begin{bmatrix} 1.5\times10^{-13} & 0 & 0 & 0 \\ 0 & 1.5\times10^{-13} & 0 & 0 \\ 0 & 0 & 3\times10^{-3} & 0 \\ 0 & 0 & 0 & 3\times10^{-3} \end{bmatrix}$
$\boldsymbol{S}_d$	$\begin{bmatrix} 0 & 0 & 0 & 0 \\ 0 & 0 & 0 & 0 \\ 0 & 0 & 3.1681\times10^{-10} & 4.8094\times10^{-10} \\ 0 & 0 & 1.0435\times10^{-10} & -6.7825\times10^{-11} \end{bmatrix}$

Table 5.23. *Parameter unit in test using KF-UI and G-KF-UI*

Parameter	Unit
$\hat{\boldsymbol{x}}_{0\|0}$	$\begin{bmatrix} (\mathrm{m}) & (\mathrm{m}) & (\mathrm{m/s}) & (\mathrm{m/s}) \end{bmatrix}^T$
$\hat{\boldsymbol{d}}_0$	$\begin{bmatrix} (\mathrm{N}) & (\mathrm{N}) \end{bmatrix}^T$
$\boldsymbol{P}^x_{0\|0}$	$\begin{bmatrix} (\mathrm{m^2}) & (\mathrm{m^2}) & (\mathrm{m^2/s}) & (\mathrm{m^2/s}) \\ (\mathrm{m^2}) & (\mathrm{m^2}) & (\mathrm{m^2/s}) & (\mathrm{m^2/s}) \\ (\mathrm{m^2/s}) & (\mathrm{m^2/s}) & (\mathrm{m^2/s^2}) & (\mathrm{m^2/s^2}) \\ (\mathrm{m^2/s}) & (\mathrm{m^2/s}) & (\mathrm{m^2/s^2}) & (\mathrm{m^2/s^2}) \end{bmatrix}$
$\boldsymbol{P}^d_0$	$\begin{bmatrix} (\mathrm{N^2}) & (\mathrm{N^2}) \\ (\mathrm{N^2}) & (\mathrm{N^2}) \end{bmatrix}$
$\boldsymbol{P}^{xd}_0$	$\begin{bmatrix} (\mathrm{Nm}) & (\mathrm{Nm}) & (\mathrm{Nm/s}) & (\mathrm{Nm/s}) \\ (\mathrm{Nm}) & (\mathrm{Nm}) & (\mathrm{Nm/s}) & (\mathrm{Nm/s}) \end{bmatrix}^T$
$\boldsymbol{P}^{dx}_0$	$\begin{bmatrix} (\mathrm{Nm}) & (\mathrm{Nm}) & (\mathrm{Nm/s}) & (\mathrm{Nm/s}) \\ (\mathrm{Nm}) & (\mathrm{Nm}) & (\mathrm{Nm/s}) & (\mathrm{Nm/s}) \end{bmatrix}$
$\boldsymbol{Q}_d$	$\begin{bmatrix} (\mathrm{m^2/s^2}) & (\mathrm{m^2/s^2}) & (\mathrm{m^2/s^3}) & (\mathrm{m^2/s^3}) \\ (\mathrm{m^2/s^2}) & (\mathrm{m^2/s^2}) & (\mathrm{m^2/s^3}) & (\mathrm{m^2/s^3}) \\ (\mathrm{m^2/s^3}) & (\mathrm{m^2/s^3}) & (\mathrm{m^2/s^4}) & (\mathrm{m^2/s^4}) \\ (\mathrm{m^2/s^3}) & (\mathrm{m^2/s^3}) & (\mathrm{m^2/s^4}) & (\mathrm{m^2/s^4}) \end{bmatrix}$
$\boldsymbol{R}_d$	$\begin{bmatrix} (-) & (-) & (\mathrm{m/s^2}) & (\mathrm{m/s^2}) \\ (-) & (-) & (\mathrm{m/s^2}) & (\mathrm{m/s^2}) \\ (\mathrm{m/s^2}) & (\mathrm{m/s^2}) & (\mathrm{m^2/s^4}) & (\mathrm{m^2/s^4}) \\ (\mathrm{m/s^2}) & (\mathrm{m/s^2}) & (\mathrm{m^2/s^4}) & (\mathrm{m^2/s^4}) \end{bmatrix}$
$\boldsymbol{S}_d$	$\begin{bmatrix} (\mathrm{m/s}) & (\mathrm{m/s}) & (\mathrm{m^2/s^3}) & (\mathrm{m^2/s^3}) \\ (\mathrm{m/s}) & (\mathrm{m/s}) & (\mathrm{m^2/s^3}) & (\mathrm{m^2/s^3}) \\ (\mathrm{m/s^2}) & (\mathrm{m/s^2}) & (\mathrm{m^2/s^4}) & (\mathrm{m^2/s^4}) \\ (\mathrm{m/s^2}) & (\mathrm{m/s^2}) & (\mathrm{m^2/s^4}) & (\mathrm{m^2/s^4}) \end{bmatrix}$

In section 4.3.4, a steady-state form of the G-KF-UI has been presented. With the steady-state form of the G-KF-UI, the steady-state form of the KF-UI can be obtained by setting the covariance matrix $\boldsymbol{S}_d$ to be a zero matrix. In this test, the steady-states of the KF-UI and the G-KF-UI are calculated in advance, and then are applied for online force reconstruction. Table 5.22 lists the parameter settings which are applied in the test, and table 5.23 provides the units of those parameters. The stability of the KF-UI and the G-KF-UI is achieved by the convergence of the covariance matrix of the state estimate error and the convergence of the covariance matrix of the force estimate error. The reconstruction results are plotted in figure 5.40 through figure 5.42. The values of the RMSE between the reconstructed forces and the measured (or true) forces are calculated and are plotted in form of bar plot in figure 5.43 through figure 5.45. The reconstruction results show that both the KF-UI and the G-KF-UI are suitable for the reconstruction of the quasi-static force, the impact force, and the wind load. Furthermore, the difference between the reconstruction results from using the KF-UI and from using the G-KF-UI is not obvious.

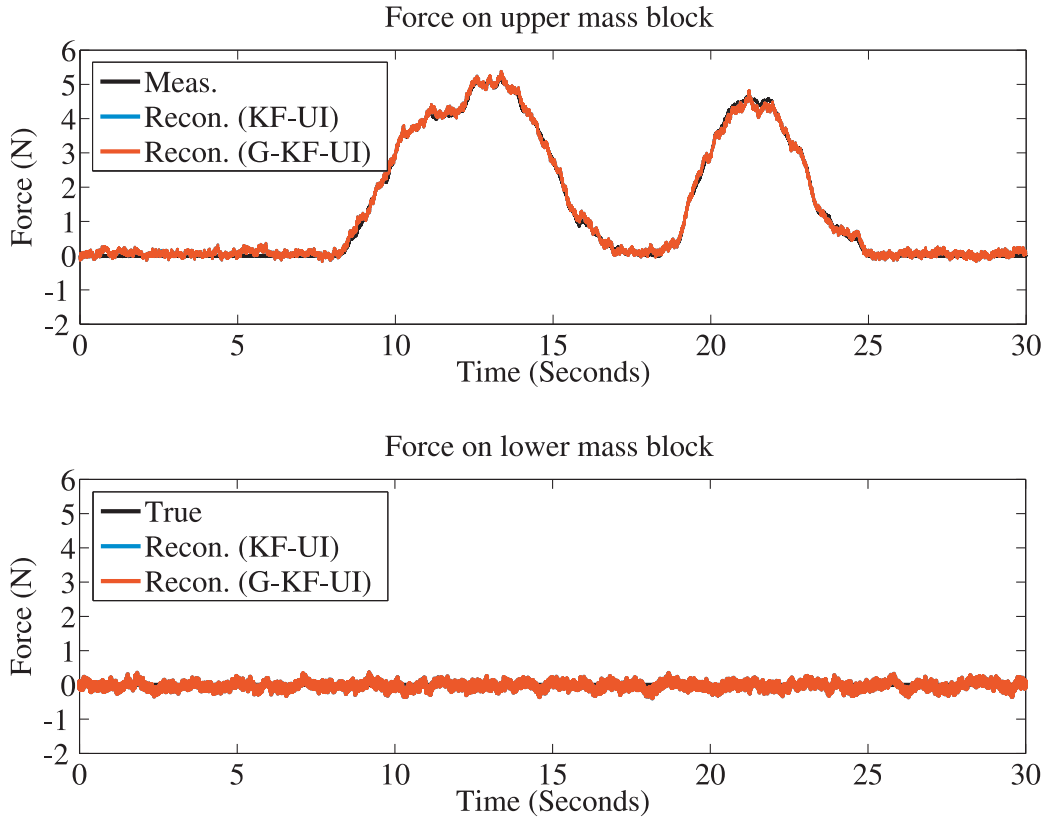

Figure 5.40. *Reconstruction results for the quasi-static force in test using KF-UI and G-KF-UI (with two strain gauges and two accelerometers)*

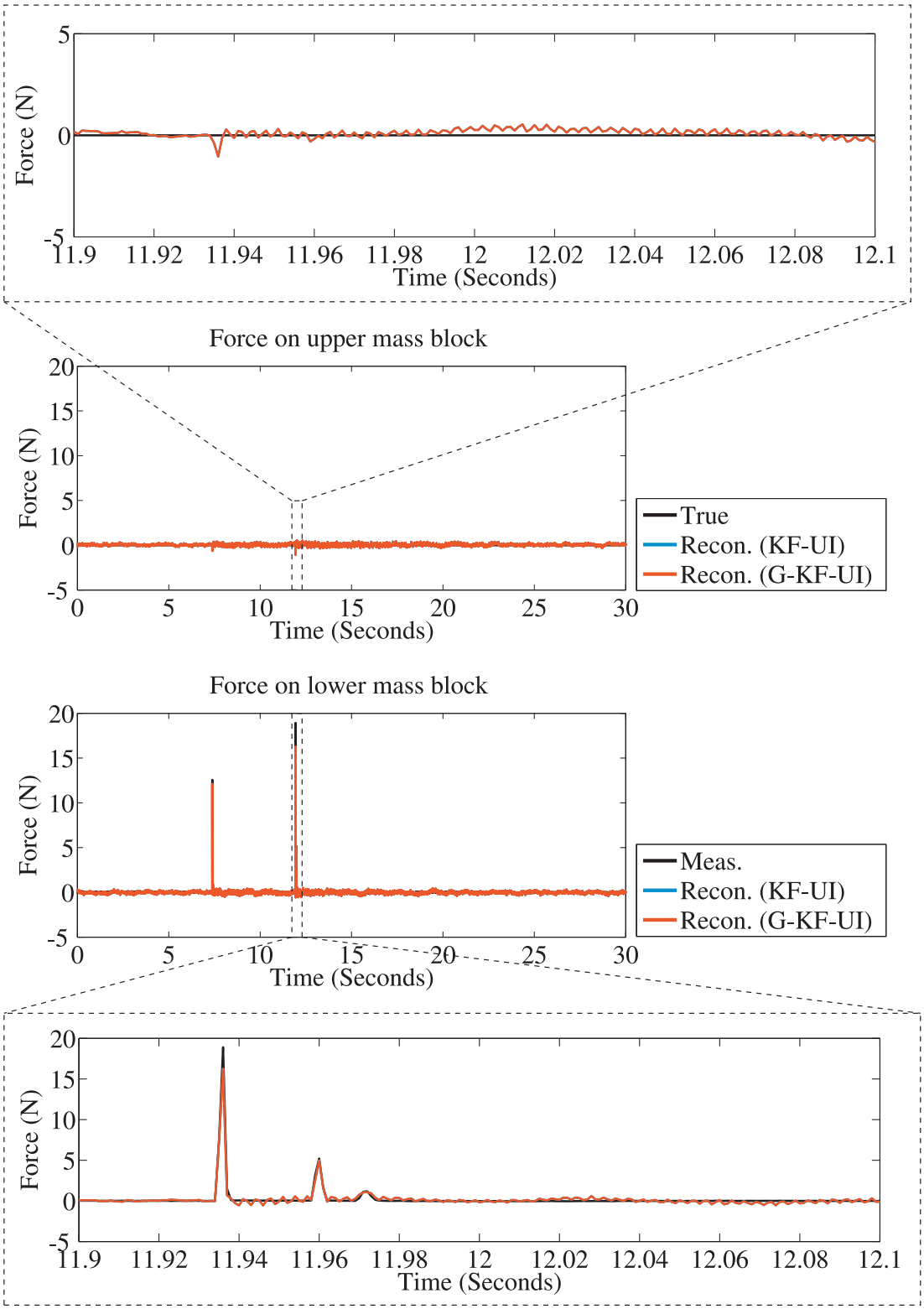

Figure 5.41. *Reconstruction results for the impact force in test using KF-UI and G-KF-UI (with two strain gauges and two accelerometers)*

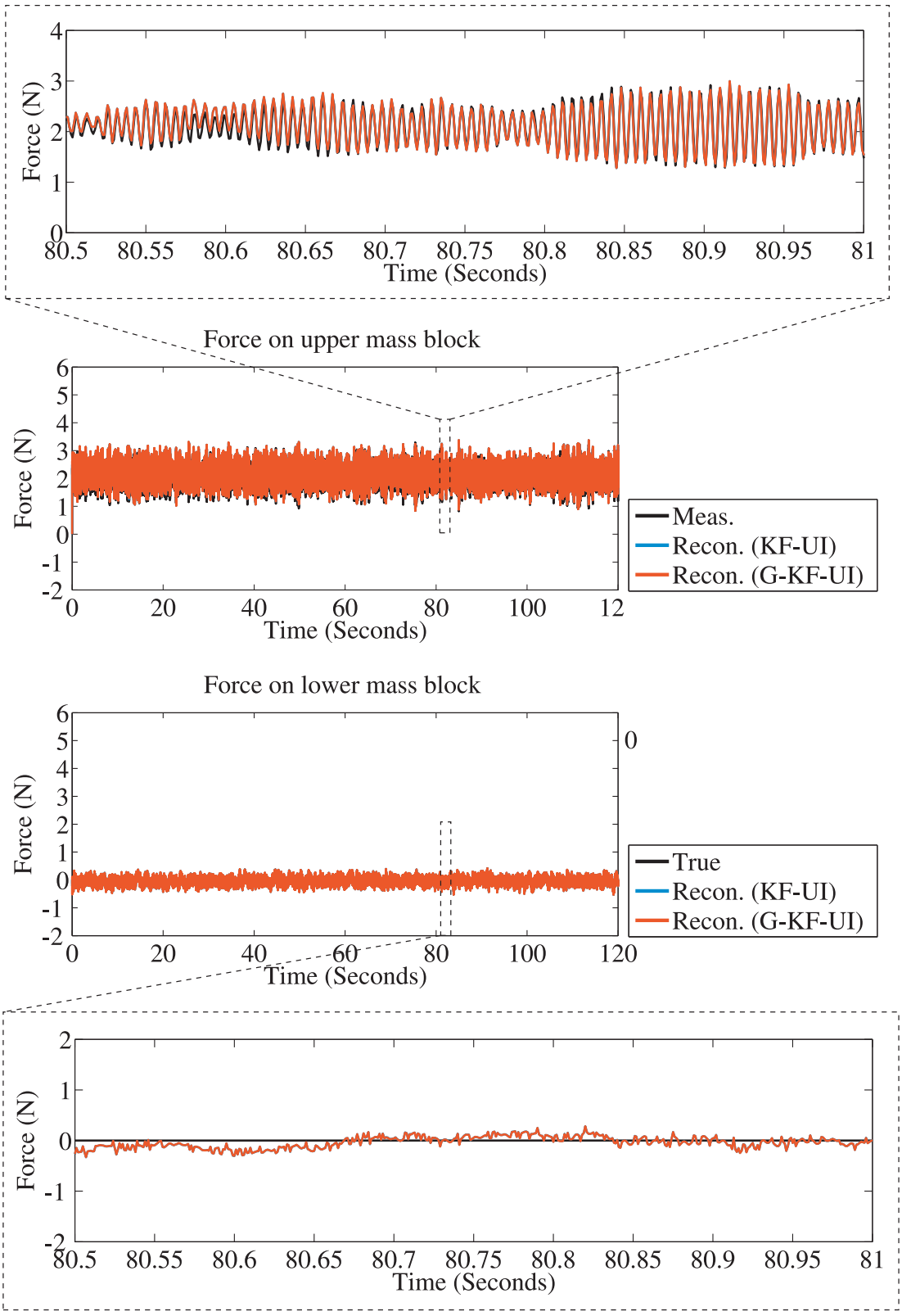

Figure 5.42. *Reconstruction results for the wind load in test using KF-UI and G-KF-UI (with two strain gauges and two accelerometers)*

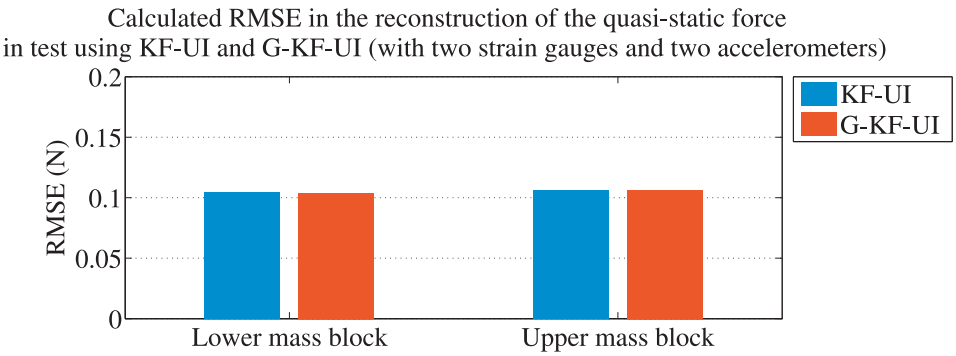

Figure 5.43. *Calculated RMSE in the reconstruction of the quasi-static force in test using KF-UI and G-KF-UI (with two strain gauges and two accelerometers)*

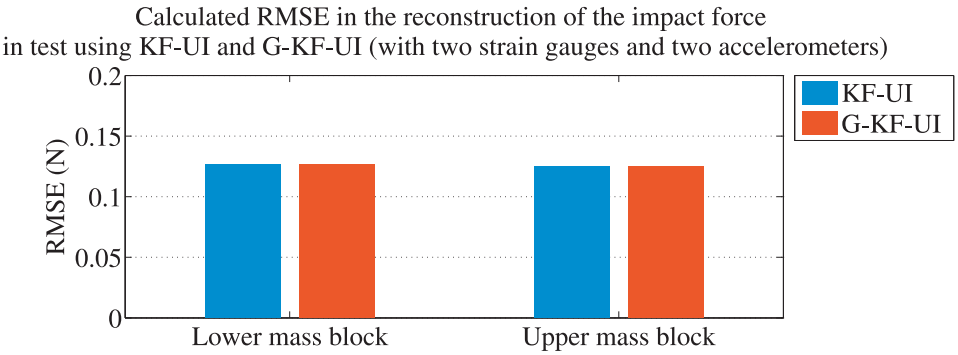

Figure 5.44. *Calculated RMSE in the reconstruction of the impact force in test using KF-UI and G-KF-UI (with two strain gauges and two accelerometers)*

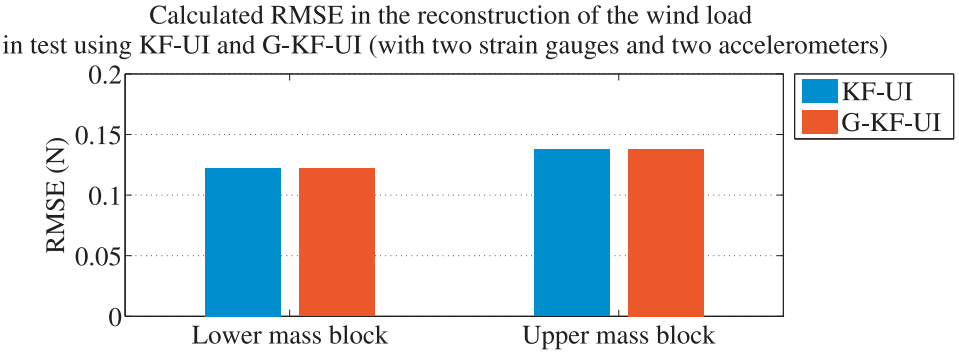

Figure 5.45. *Calculated RMSE in the reconstruction of the wind load in test using KF-UI and G-KF-UI (with two strain gauges and two accelerometers)*

5.2.9. Test using SSKF+LSE and MSSKF+LSE

Hwang et al. (2009a) presented an analytical procedure for the estimation of modal loads. The same method was applied in a study for modal wind load identification using the wind tunnel test data (Hwang et al., 2011). This method adopts the steady-state of a continuous-time Kalman filter for state estimation. This principle is similar to the Kalman-Bucy filter which has been reviewed in section 2.5. The difference is that this method considers direct feed-through in the system model. The input is estimated with the help of a least-squares estimator. In this thesis, this method is named as Steady-State Kalman Filter with a Least-Squares Estimator (SSKF+LSE). A brief review of the SSKF+LSE has been given in section 2.6.7.

The SSKF+LSE assumes the input covariance matrix $\boldsymbol{Q}_{input}$ and the measurement noise covariance matrix $\boldsymbol{Q}_{meas}$ as unknown, and sets $\boldsymbol{Q}_{input}$ as an identity matrix $\boldsymbol{I}_m$ and $\boldsymbol{Q}_{meas}$ as $\gamma \boldsymbol{I}_p$, where γ is a tuning parameter. If the input covariance matrix $\boldsymbol{Q}_{input}$ is set as an identity matrix, it actually assumes that the input forces all have the same variance and are uncorrelated. In practice, it might not always be the case. Considering this, the author has proposed a modification to the SSKF+LSE in section (4.4), where it is suggested to use the estimate of $\boldsymbol{Q}_{input}$ and the estimate of $\boldsymbol{Q}_{meas}$. To differentiate with the SSKF+LSE, the proposed modification is noted as MSSKF+LSE in which the covariance matrix $\boldsymbol{Q}_{input}$ is set to include at least the information on the intensity difference and the correlation of different input forces, and the covariance matrix $\boldsymbol{Q}_{meas}$ is set to reflect the intensity difference in the measurement noise covariance of different types of sensors.

In this benchmark study, both the SSKF+LSE and the MSSKF+LSE are applied for reconstructing the three different types of forces which have been introduced in section 5.2.3. Both the SSKF+LSE and the MSSKF+LSE assume the input forces to be stationary and white. In the SSKF+LSE, the covariance matrix of the input forces is assumed to be unknown and is set as an identity matrix. In the MSSKF+LSE, it is suggested to consider an estimate of the covariance matrix of the input forces. As least, the information on the intensity difference and the correlation of different input forces should be considered. The SSKF+LSE and the MSSKF+LSE do not require that the initial conditions have to be known *a priori*. Both methods consider the direct feed-through in the system model. However, these two methods do not require that the direct feed-through has to have full column rank. The test results with different sensor options are provided below.

Results from using only strain gauges

The necessary conditions for the existence of the existence of the SSKF+LSE have been provided in section 2.6.7. The same necessary conditions are applicable to the MSSKF+LSE, too. After checking the fulfillment of those necessary conditions, the sensors in table 5.24 are selected. Table 5.25 lists the dimension of the state, the input, and the output of the state-space model of the benchmark structure. Table 5.26 through table 5.28 provide the parameter settings which are applied in the test. The units of those parameters are given in table 5.29. The stability is achieved by the convergence of the state estimate error $\tilde{\boldsymbol{x}}(t)$ and a stable $\boldsymbol{G}_c^+$. The reconstruction results are plotted in figure 5.46 through figure 5.48. The values of the RMSE between the reconstructed forces and the measured (or true) forces are calculated and are plotted in form of bar plot in figure 5.49 through figure 5.51.

The reconstruction results show that with only strain gauges both the SSKF+LSE and the MSSKF+LSE are suitable for the reconstruction of the quasi-static force, but not suitable for the reconstruction of the impact force; and are suitable for the reconstruction of the static part of the wind load, but not the dynamics part. Furthermore, by considering reasonable values for the matrices $\boldsymbol{Q}_{input}$ and $\boldsymbol{Q}_{meas}$, the MSSKF+LSE provides better reconstruction results for the mass block where no force is applied in the x direction, especially for the cases of impact force and wind load.

Table 5.24. *Selected sensors in test using SSKF+LSE and MSSKF+LSE with only strain gauges*

Sensor type	Selected sensors
Only strain gauge	Strain gauge 1
	Strain gauge 2

Table 5.25. *Dimension of the state, the input, and the output of the state-space model of the benchmark structure in test using SSKF+LSE and MSSKF+LSE (with two strain gauges)*

Name	Symbol	Dimension
State	$\boldsymbol{x}(t)$	4×1
Input	$\boldsymbol{d}(t)$	2×1
Output	$\boldsymbol{y}(t)$	2×1

Table 5.26. *Parameter settings in the reconstruction of the quasi-static force in test using SSKF+LSE and MSSKF+LSE (with two strain gauges)*

Parameter	SSKF+LSE	MSSKF+LSE
$\boldsymbol{Q}_{input}$	$\boldsymbol{I}_2$	$\begin{bmatrix} 0 & 0 \\ 0 & 3.2171 \times 10^{0} \end{bmatrix}$
$\boldsymbol{Q}_{meas}$	$\boldsymbol{I}_2$	$\begin{bmatrix} 1.5 \times 10^{-13} & 0 \\ 0 & 1.5 \times 10^{-13} \end{bmatrix}$
γ	5×10^{1}	5×10^{1}

Table 5.27. *Parameter settings in the reconstruction of the impact force in test using SSKF+LSE and MSSKF+LSE (with two strain gauges)*

Parameter	SSKF+LSE	MSSKF+LSE
$\boldsymbol{Q}_{input}$	$\boldsymbol{I}_2$	$\begin{bmatrix} 2.54 \times 10^{-2} & 0 \\ 0 & 0 \end{bmatrix}$
$\boldsymbol{Q}_{meas}$	$\boldsymbol{I}_2$	$\begin{bmatrix} 1.5 \times 10^{-13} & 0 \\ 0 & 1.5 \times 10^{-13} \end{bmatrix}$
γ	5×10^{1}	1×10^{0}

Table 5.28. *Parameter settings in the reconstruction of the wind load in test using SSKF+LSE and MSSKF+LSE (with two strain gauges)*

Parameter	SSKF+LSE	MSSKF+LSE
$\boldsymbol{Q}_{input}$	$\boldsymbol{I}_2$	$\begin{bmatrix} 0 & 0 \\ 0 & 9.96 \times 10^{-2} \end{bmatrix}$
$\boldsymbol{Q}_{meas}$	$\boldsymbol{I}_2$	$\begin{bmatrix} 1.5 \times 10^{-13} & 0 \\ 0 & 1.5 \times 10^{-13} \end{bmatrix}$
γ	5×10^{1}	1×10^{0}

Table 5.29. *Parameter units in test using SSKF+LSE and MSSKF+LSE (with two strain gauges)*

Parameter	Unit
$\boldsymbol{Q}_{input}$	$\begin{bmatrix} (\mathrm{N}^2) & (\mathrm{N}^2) \\ (\mathrm{N}^2) & (\mathrm{N}^2) \end{bmatrix}$
$\boldsymbol{Q}_{meas}$	$\begin{bmatrix} (-) & (-) \\ (-) & (-) \end{bmatrix}$
γ	$(-)$

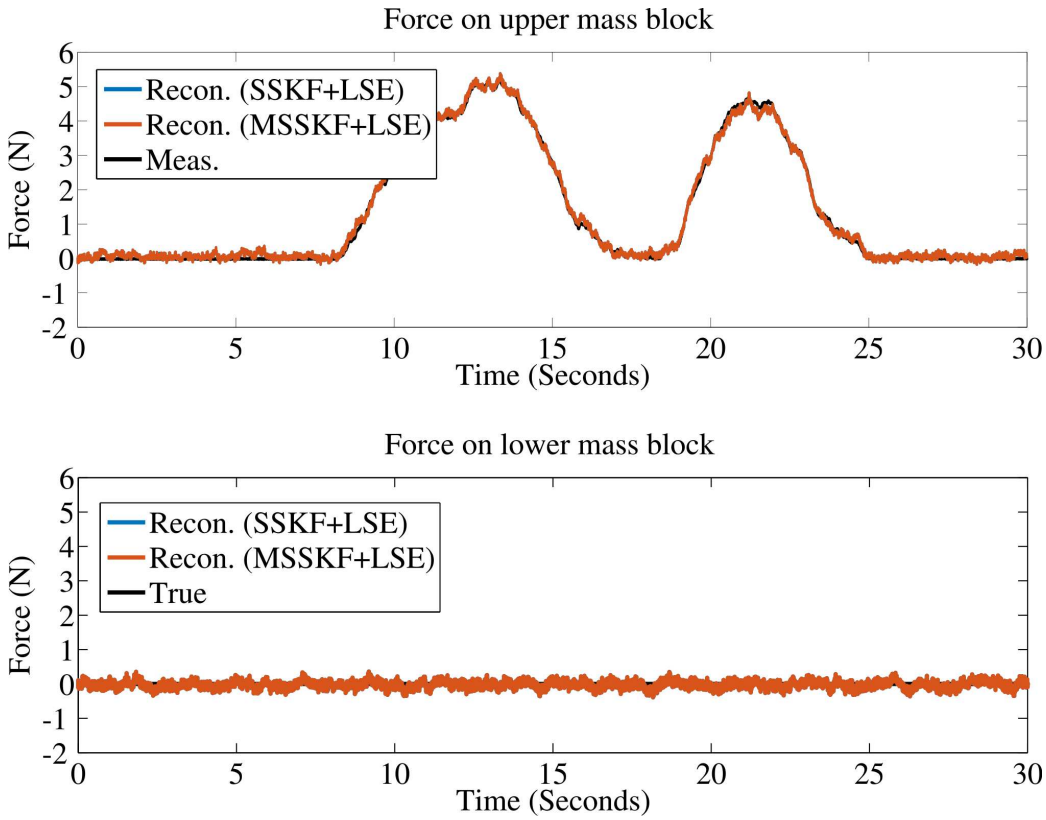

Figure 5.46. *Reconstruction results for the quasi-static force in test using SSKF+LSE and MSSKF+LSE (with two strain gauges)*

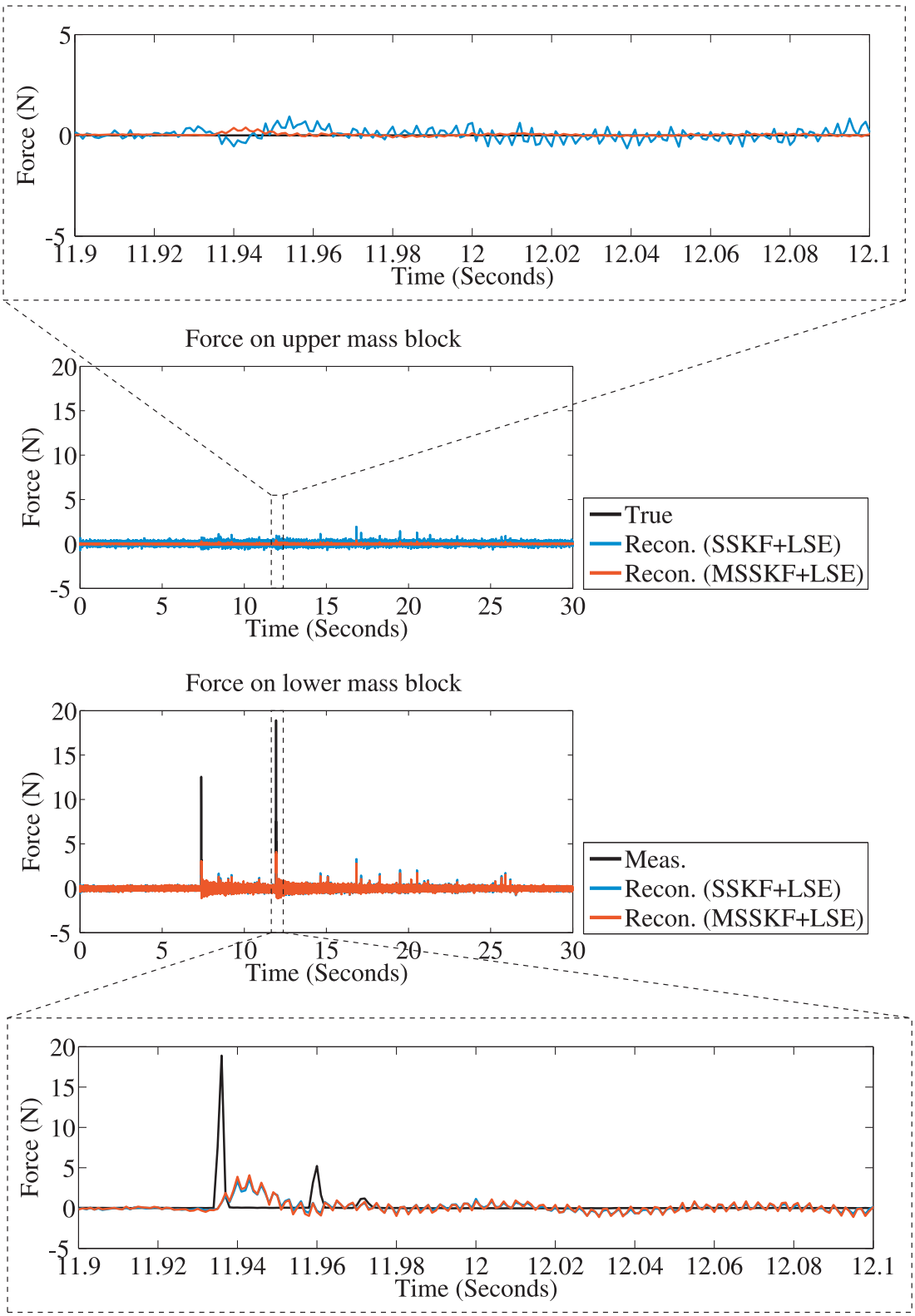

Figure 5.47. *Reconstruction results for the impact force in test using SSKF+LSE and MSSKF+LSE (with two strain gauges)*

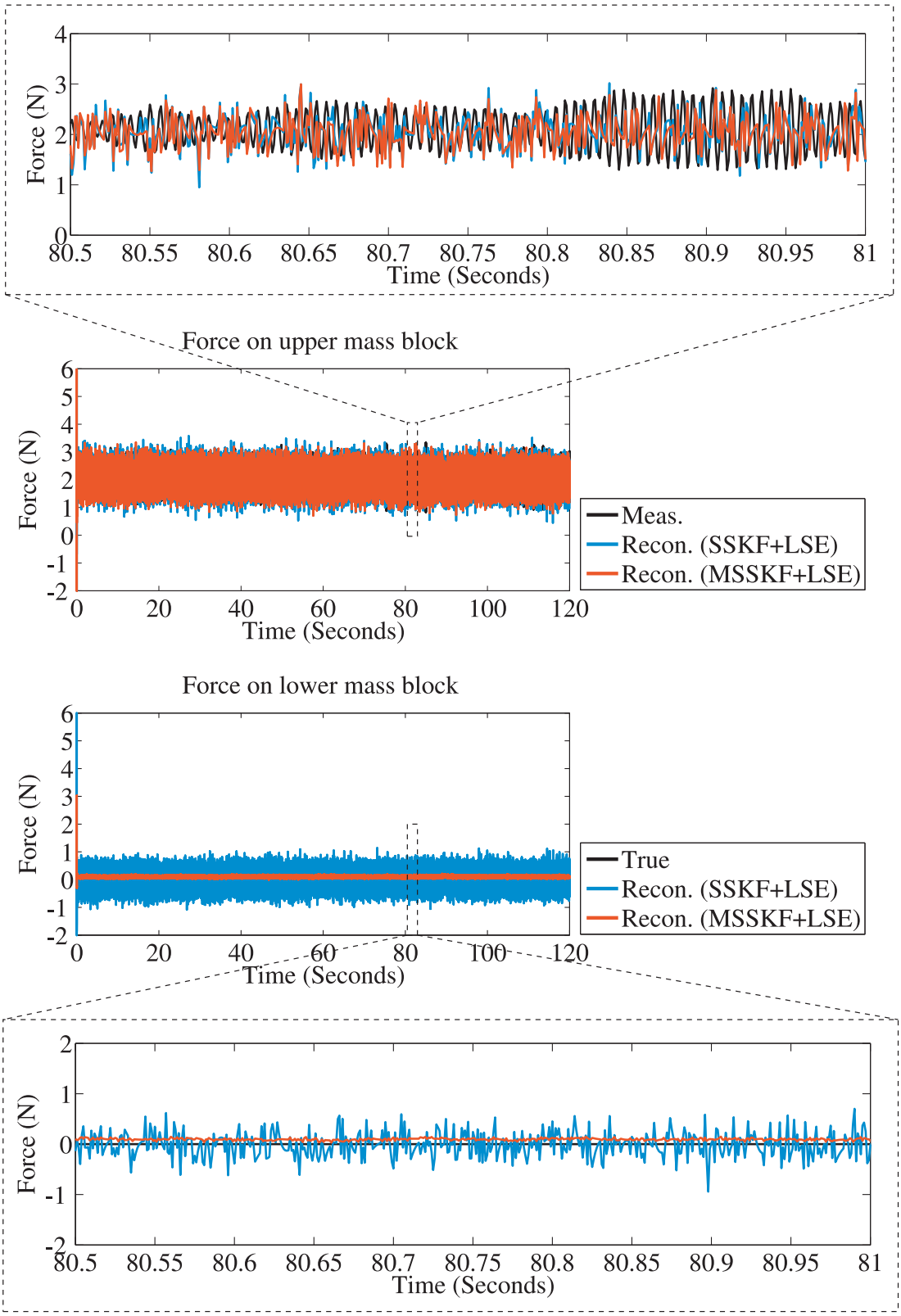

Figure 5.48. *Reconstruction results for the wind load in test using SSKF+LSE and MSSKF+LSE (with two strain gauges)*

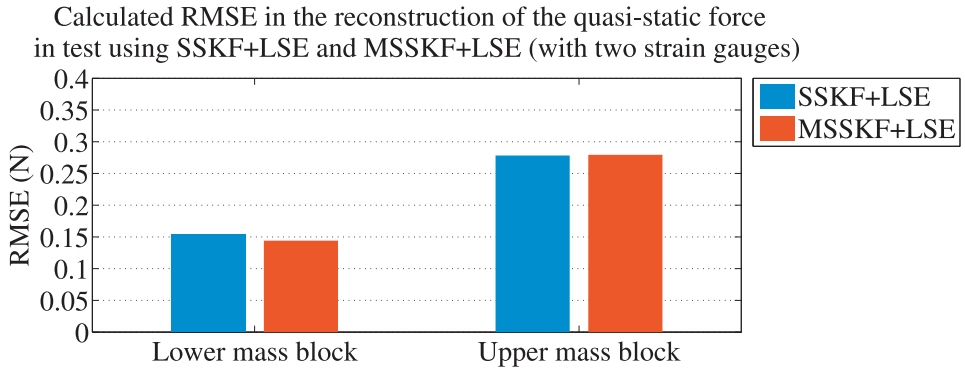

Figure 5.49. *Calculated RMSE in the reconstruction of the quasi-static force in test using SSKF+LSE and MSSKF+LSE (with two strain gauges)*

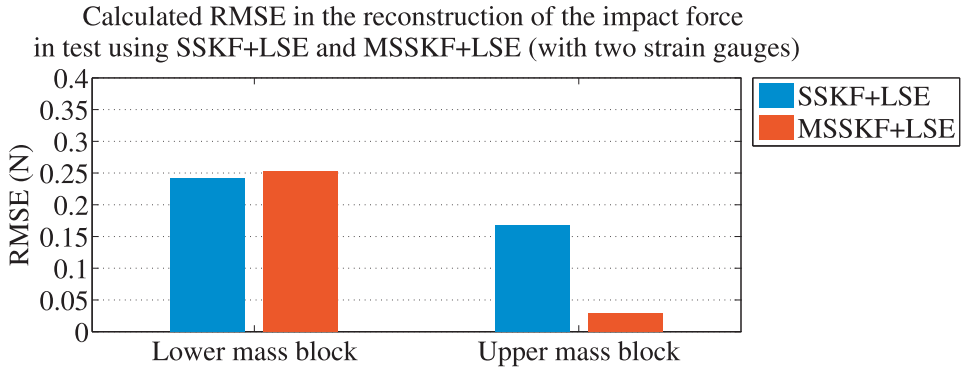

Figure 5.50. *Calculated RMSE in the reconstruction of the impact force in test using SSKF+LSE and MSSKF+LSE (with two strain gauges)*

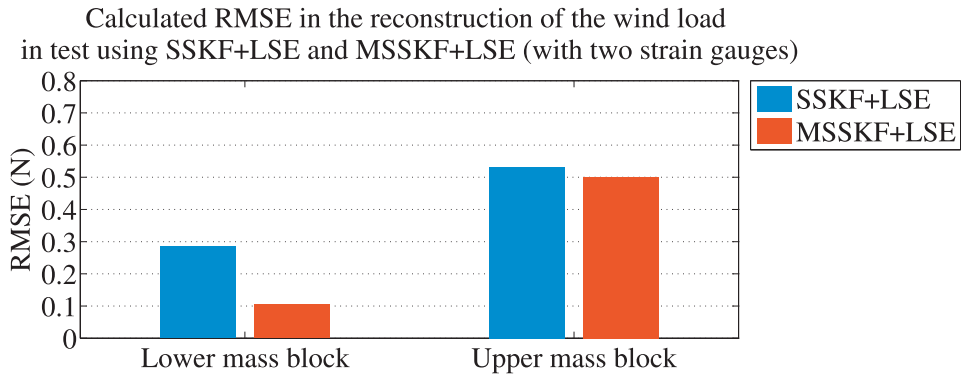

Figure 5.51. *Calculated RMSE in the reconstruction of the wind load in test using SSKF+LSE and MSSKF+LSE (with two strain gauges)*

Results from using both strain gauges and accelerometers

The necessary conditions for the existence of the existence of the SSKF+LSE have been provided in section 2.6.7. The same necessary conditions are applicable to the MSSKF+LSE, too. After checking the fulfillment of those necessary conditions, the sensors in table 5.30 are selected. Table 5.31 lists the dimension of the state, the input, and the output of the state-space model of the benchmark structure. To filter out the low frequency drift in the acceleration measurements, a second-order Butterworth filter is applied, with the cutoff frequency being set at 0.5 Hz. Table 5.32 through table 5.34 provide the parameter settings which are applied in the test. The units of those parameters are given in table 5.36. The stability is achieved by the convergence of the state estimate error $\tilde{\boldsymbol{x}}(t)$ and a stable $\boldsymbol{G}_c^+$. The reconstruction results are plotted in figure 5.52 through figure 5.53. The values of the RMSE between the reconstructed forces and the measured (or true) forces are calculated and are plotted in form of bar plot in figure 5.55 through figure 5.57.

The reconstruction results show that with both strain gauges and accelerometers the MSSKF+LSE are suitable for the reconstruction of the quasi-static force, the impact force, and the wind load, while the SSKF+LSE is suitable only for the reconstruction of the impact force and the dynamic part of the wind load. Furthermore, by considering reasonable values for the matrices $\boldsymbol{Q}_{input}$ and $\boldsymbol{Q}_{meas}$, the MSSKF+LSE provides better reconstruction results for the mass block where no force is applied in the x direction.

Table 5.30. *Selected sensors in test using SSKF+LSE and MSSKF+LSE with both strain gauges and accelerometers*

Sensor type	Selected sensors
Strain gauge & accelerometer	Strain gauge 1
	Strain gauge 2
	Accelerometer 1
	Accelerometer 2

Table 5.31. *Dimension of the state, the input, and the output of the state-space model of the benchmark structure in test using SSKF+LSE and MSSKF+LSE (with two strain gauges and two accelerometers)*

Name	Symbol	Dimension
State	$\boldsymbol{x}(t)$	4×1
Input	$\boldsymbol{d}(t)$	2×1
Output	$\boldsymbol{y}(t)$	4×1

Table 5.32. *Settings for $\boldsymbol{Q}_{input}$ and γ in the reconstruction of the quasi-static force in test using SSKF+LSE and MSSKF+LSE (with two strain gauges and two accelerometers)*

Parameter	SSKF+LSE	MSSKF+LSE
$\boldsymbol{Q}_{input}$	$\boldsymbol{I}_2$	$\begin{bmatrix} 0 & 0 \\ 0 & 3.2171 \times 10^{0} \end{bmatrix}$
γ	1×10^{-2}	1×10^{0}

Table 5.33. *Settings for $\boldsymbol{Q}_{input}$ and γ in the reconstruction of the impact force in test using SSKF+LSE and MSSKF+LSE (with two strain gauges and two accelerometers)*

Parameter	SSKF+LSE	MSSKF+LSE
$\boldsymbol{Q}_{input}$	$\boldsymbol{I}_2$	$\begin{bmatrix} 2.54 \times 10^{-2} & 0 \\ 0 & 0 \end{bmatrix}$
γ	1×10^{-2}	1×10^{0}

Table 5.34. *Settings for $\boldsymbol{Q}_{input}$ and γ in the reconstruction of the wind load in test using SSKF+LSE and MSSKF+LSE (with two strain gauges and two accelerometers)*

Parameter	SSKF+LSE	MSSKF+LSE
$\boldsymbol{Q}_{input}$	$\boldsymbol{I}_2$	$\begin{bmatrix} 0 & 0 \\ 0 & 9.96 \times 10^{-2} \end{bmatrix}$
γ	1×10^{-2}	1×10^{0}

Table 5.35. *Settings for $\boldsymbol{Q}_{meas}$ in test using SSKF+LSE and MSSKF+LSE (with two strain gauges and two accelerometers)*

Parameter	SSKF+LSE	MSSKF+LSE
$\boldsymbol{Q}_{meas}$	$\boldsymbol{I}_4$	$\begin{bmatrix} 1.5 \times 10^{-13} & 0 & 0 & 0 \\ 0 & 1.5 \times 10^{-13} & 0 & 0 \\ 0 & 0 & 3 \times 10^{-3} & 0 \\ 0 & 0 & 0 & 3 \times 10^{-3} \end{bmatrix}$

Table 5.36. *Parameter units in test using SSKF+LSE and MSSKF+LSE (with two strain gauges and two accelerometers)*

Parameter	Unit
$\boldsymbol{Q}_{input}$	$\begin{bmatrix} (\mathrm{N}^2) & (\mathrm{N}^2) \\ (\mathrm{N}^2) & (\mathrm{N}^2) \end{bmatrix}$
$\boldsymbol{Q}_{meas}$	$\begin{bmatrix} (-) & (-) & (\mathrm{m/s^2}) & (\mathrm{m/s^2}) \\ (-) & (-) & (\mathrm{m/s^2}) & (\mathrm{m/s^2}) \\ (\mathrm{m/s^2}) & (\mathrm{m/s^2}) & (\mathrm{m^2/s^4}) & (\mathrm{m^2/s^4}) \\ (\mathrm{m/s^2}) & (\mathrm{m/s^2}) & (\mathrm{m^2/s^4}) & (\mathrm{m^2/s^4}) \end{bmatrix}$
γ	$(-)$

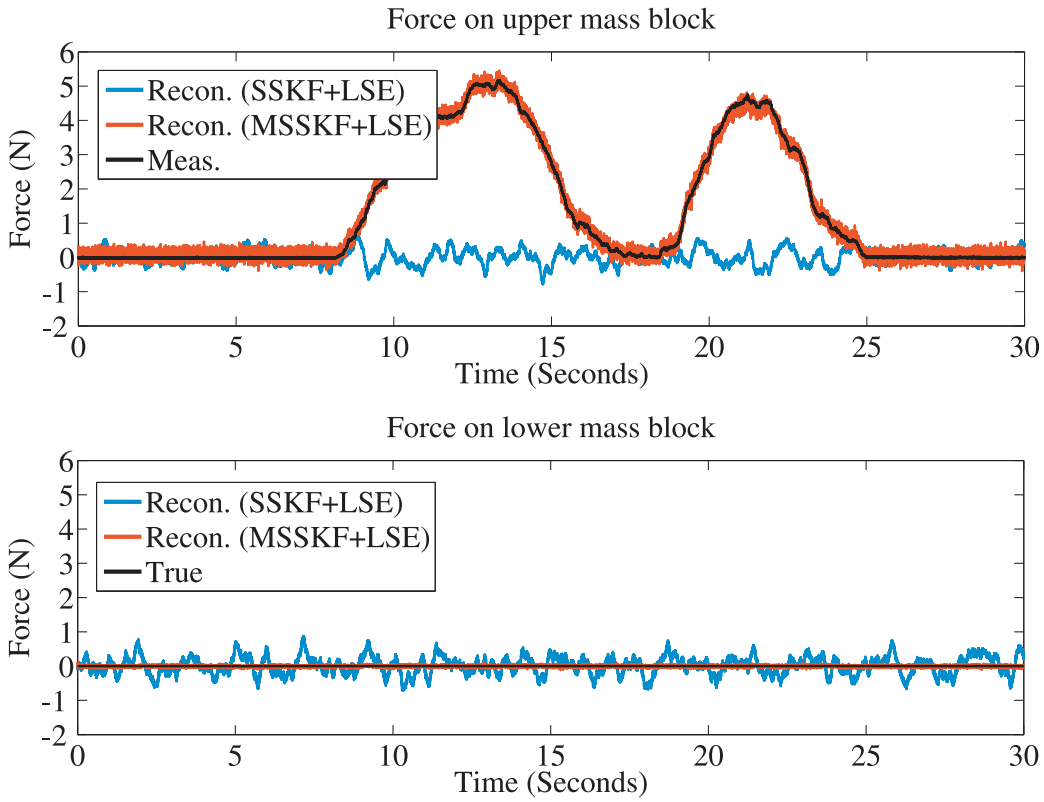

Figure 5.52. *Reconstruction results for the quasi-static force in test using SSKF+LSE and MSSKF+LSE (with two strain gauges and two accelerometers)*

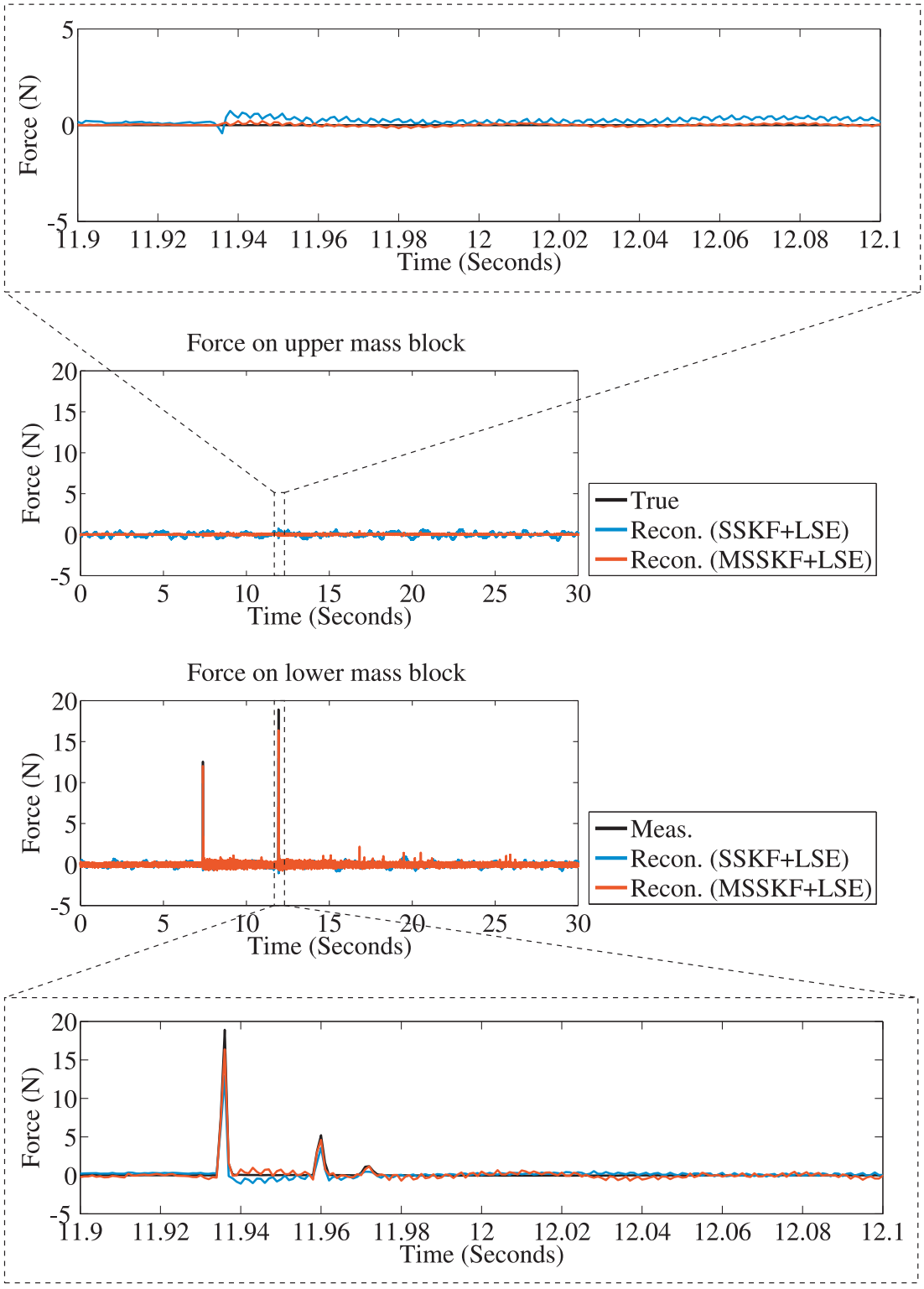

Figure 5.53. *Reconstruction results for the impact force in test using SSKF+LSE and MSSKF+LSE (with two strain gauges and two accelerometers)*

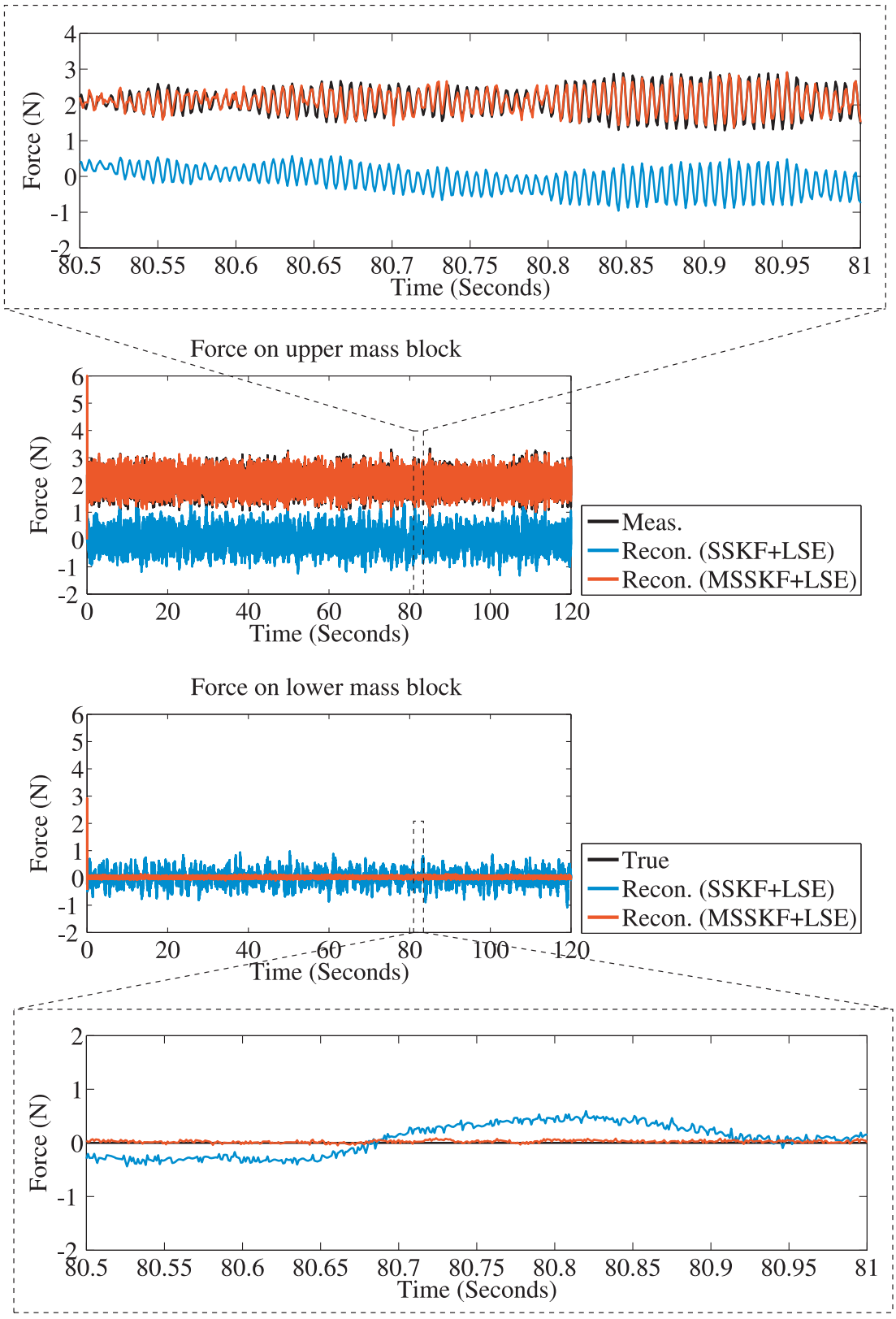

Figure 5.54. *Reconstruction results for the wind load in test using SSKF+LSE and MSSKF+LSE (with two strain gauges and two accelerometers)*

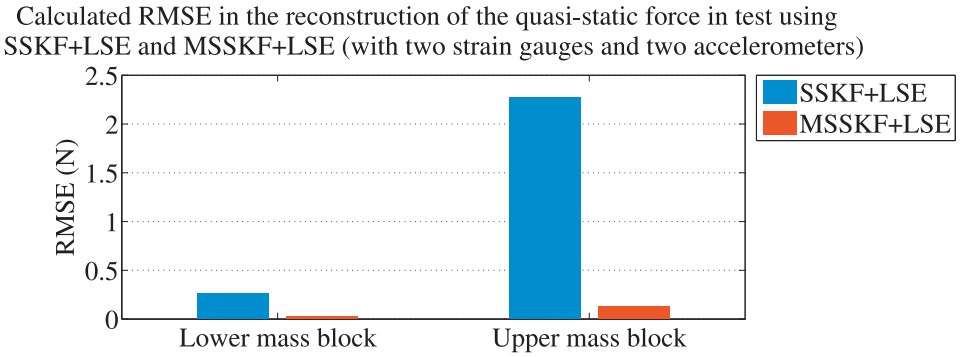

Figure 5.55. *Calculated RMSE in the reconstruction of the quasi-static force in test using SSKF+LSE and MSSKF+LSE (with two strain gauges and two accelerometers)*

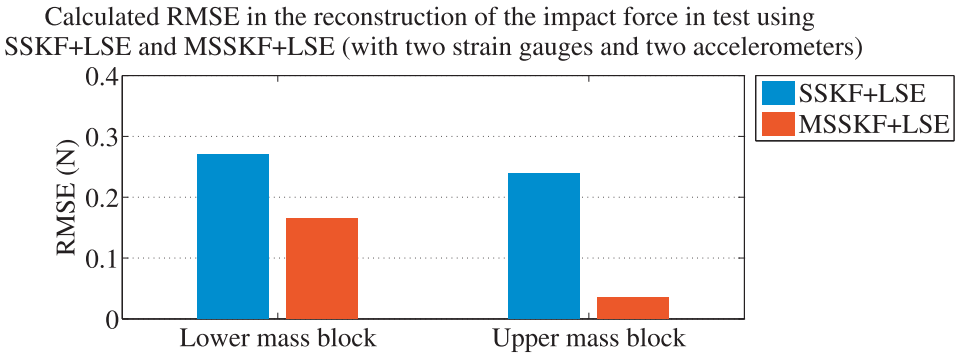

Figure 5.56. *Calculated RMSE in the reconstruction of the impact force in test using SSKF+LSE and MSSKF+LSE (with two strain gauges and two accelerometers)*

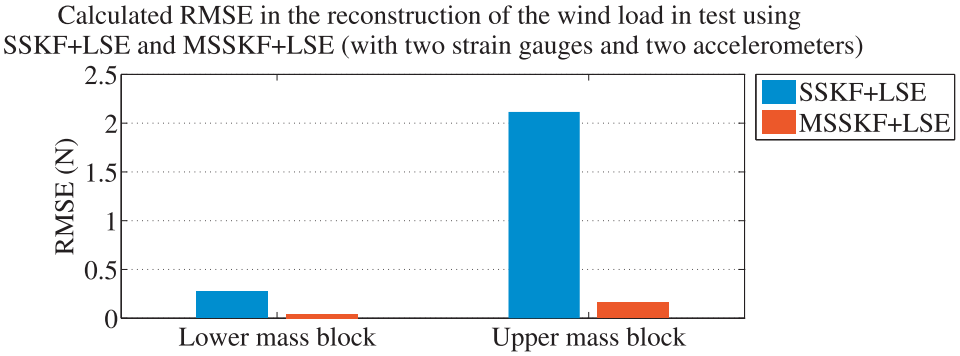

Figure 5.57. *Calculated RMSE in the reconstruction of the wind load in test using SSKF+LSE and MSSKF+LSE (with two strain gauges and two accelerometers)*

Results from using only accelerometers

The necessary conditions for the existence of the existence of the SSKF+LSE have been provided in section 2.6.7. The same necessary conditions are applicable to the MSSKF+LSE, too. After checking the fulfillment of those necessary conditions, the sensors in table 5.37 are selected. Table 5.38 lists the dimension of the state, the input, and the output of the state-space model of the benchmark structure. To filter out the low frequency drift

in the acceleration measurements, a second-order Butterworth filter is applied, with the cutoff frequency being set at 0.5 Hz. Table 5.39 through table 5.41 provide the parameter settings which are applied in the test. The units of those parameters are given in table 5.42. The stability is achieved by the convergence of the state estimate error $\tilde{\boldsymbol{x}}(t)$ and a stable $\boldsymbol{G}_c^+$. The reconstruction results are plotted in figure 5.58 through figure 5.60. The values of the RMSE between the reconstructed forces and the measured (or true) forces are calculated and are plotted in form of bar plot in figure 5.61 through figure 5.63.

The reconstruction results show that with only accelerometers the SSKF+LSE and the MSSKF+LSE are suitable for the reconstruction of the impact force and the dynamic part of the wind load, but not suitable for the reconstruction of the quasi-static force and the static part of the wind load. Furthermore, by considering reasonable values for the matrices $\boldsymbol{Q}_{input}$ and $\boldsymbol{Q}_{meas}$, the MSSKF+LSE provides better reconstruction results for the mass block where no force is applied in the x direction, especially for the cases of impact force and wind load.

In figure 5.60, a bias exists between the mean of the reconstructed wind load and the mean of the measured wind load. If an estimate of the mean of the wind load is available, then it can added to the reconstructed wind load to compensate the bias. After applying this idea, figure 5.64 shows the reconstructed wind load, and figure 5.65 provides the calculated RMSE. Based on the results in figure 5.64 and figure 5.65, it can be concluded that the MSSKF+LSE can be used for reconstructing the wind load with only accelerometers, if an estimate of the mean of the wind load is available.

Table 5.37. *Selected sensors in test using SSKF+LSE and MSSKF+LSE (with two accelerometers)*

Sensor type	Selected sensors
Accelerometer	Accelerometer 1
	Accelerometer 2

Table 5.38. *Dimension of the state, the input, and the output of the state-space model of the benchmark structure in test using SSKF+LSE and MSSKF+LSE (with two accelerometers)*

Name	Symbol	Dimension
State	$\boldsymbol{x}(t)$	4×1
Input	$\boldsymbol{d}(t)$	2×1
Output	$\boldsymbol{y}(t)$	2×1

Table 5.39. *Parameter settings in the reconstruction of the quasi-static force in test using SSKF+LSE and MSSKF+LSE (with two accelerometers)*

Parameter	SSKF+LSE	MSSKF+LSE
$\boldsymbol{Q}_1$	$\boldsymbol{I}_2$	$\begin{bmatrix} 0 & 0 \\ 0 & 3.2171 \times 10^{0} \end{bmatrix}$
$\boldsymbol{Q}_2$	$\boldsymbol{I}_2$	$\begin{bmatrix} 3 \times 10^{-3} & 0 \\ 0 & 3 \times 10^{-3} \end{bmatrix}$
γ	5×10^{1}	2×10^{2}

Table 5.40. *Parameter settings in the reconstruction of the impact force in test using SSKF+LSE and MSSKF+LSE (with two accelerometers)*

Parameter	SSKF+LSE	MSSKF+LSE
$\boldsymbol{Q}_1$	$\boldsymbol{I}_2$	$\begin{bmatrix} 2.54 \times 10^{-2} & 0 \\ 0 & 0 \end{bmatrix}$
$\boldsymbol{Q}_2$	$\boldsymbol{I}_2$	$\begin{bmatrix} 3 \times 10^{-3} & 0 \\ 0 & 3 \times 10^{-3} \end{bmatrix}$
γ	1×10^{0}	2×10^{-2}

Table 5.41. *Parameter settings in the reconstruction of the wind load in test using SSKF+LSE and MSSKF+LSE (with two accelerometers)*

Parameter	SSKF+LSE	MSSKF+LSE
$\boldsymbol{Q}_1$	$\boldsymbol{I}_2$	$\begin{bmatrix} 0 & 0 \\ 0 & 9.96 \times 10^{-2} \end{bmatrix}$
$\boldsymbol{Q}_2$	$\boldsymbol{I}_2$	$\begin{bmatrix} 3 \times 10^{-3} & 0 \\ 0 & 3 \times 10^{-3} \end{bmatrix}$
γ	1×10^{1}	1×10^{0}

Table 5.42. *Parameter units in test using SSKF+LSE and MSSKF+LSE (with two accelerometers)*

Parameter	Unit
$\boldsymbol{Q}_1$	$\begin{bmatrix} (\mathrm{N}^2) & (\mathrm{N}^2) \\ (\mathrm{N}^2) & (\mathrm{N}^2) \end{bmatrix}$
$\boldsymbol{Q}_2$	$\begin{bmatrix} (\mathrm{m}^2/\mathrm{s}^4) & (\mathrm{m}^2/\mathrm{s}^4) \\ (\mathrm{m}^2/\mathrm{s}^4) & (\mathrm{m}^2/\mathrm{s}^4) \end{bmatrix}$
γ	$(-)$

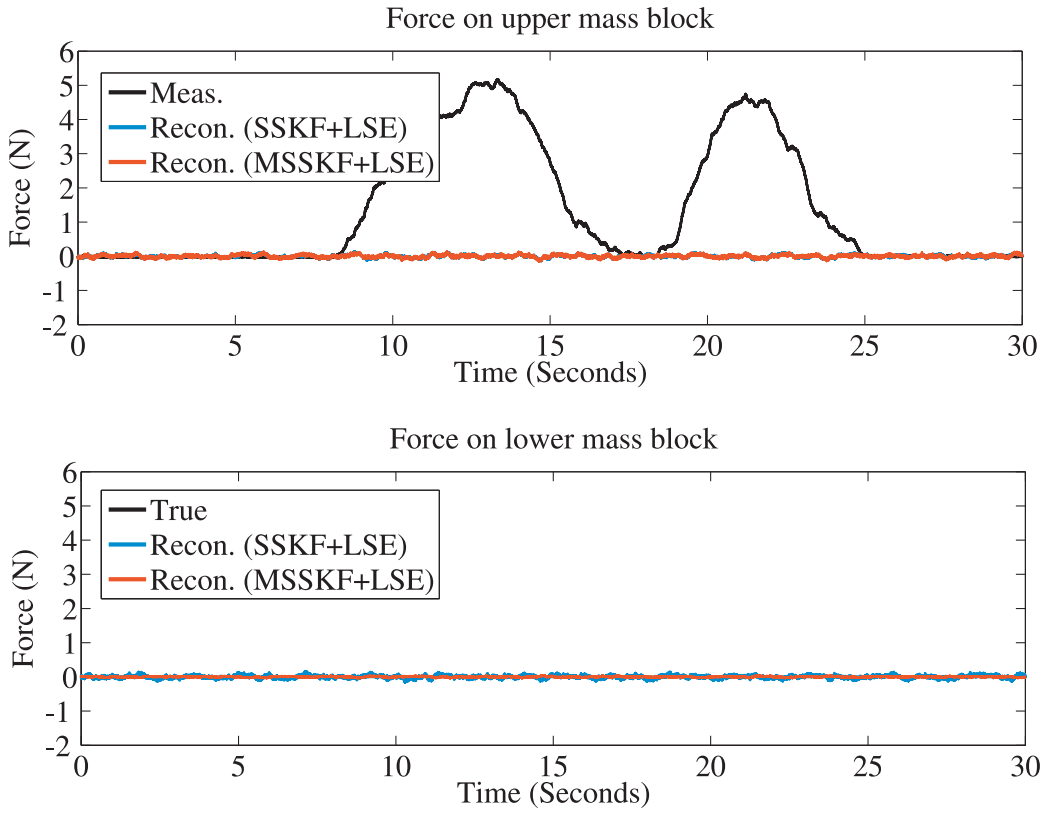

Figure 5.58. *Reconstruction results for the quasi-static force in test using SSKF+LSE and MSSKF+LSE (with two accelerometers)*

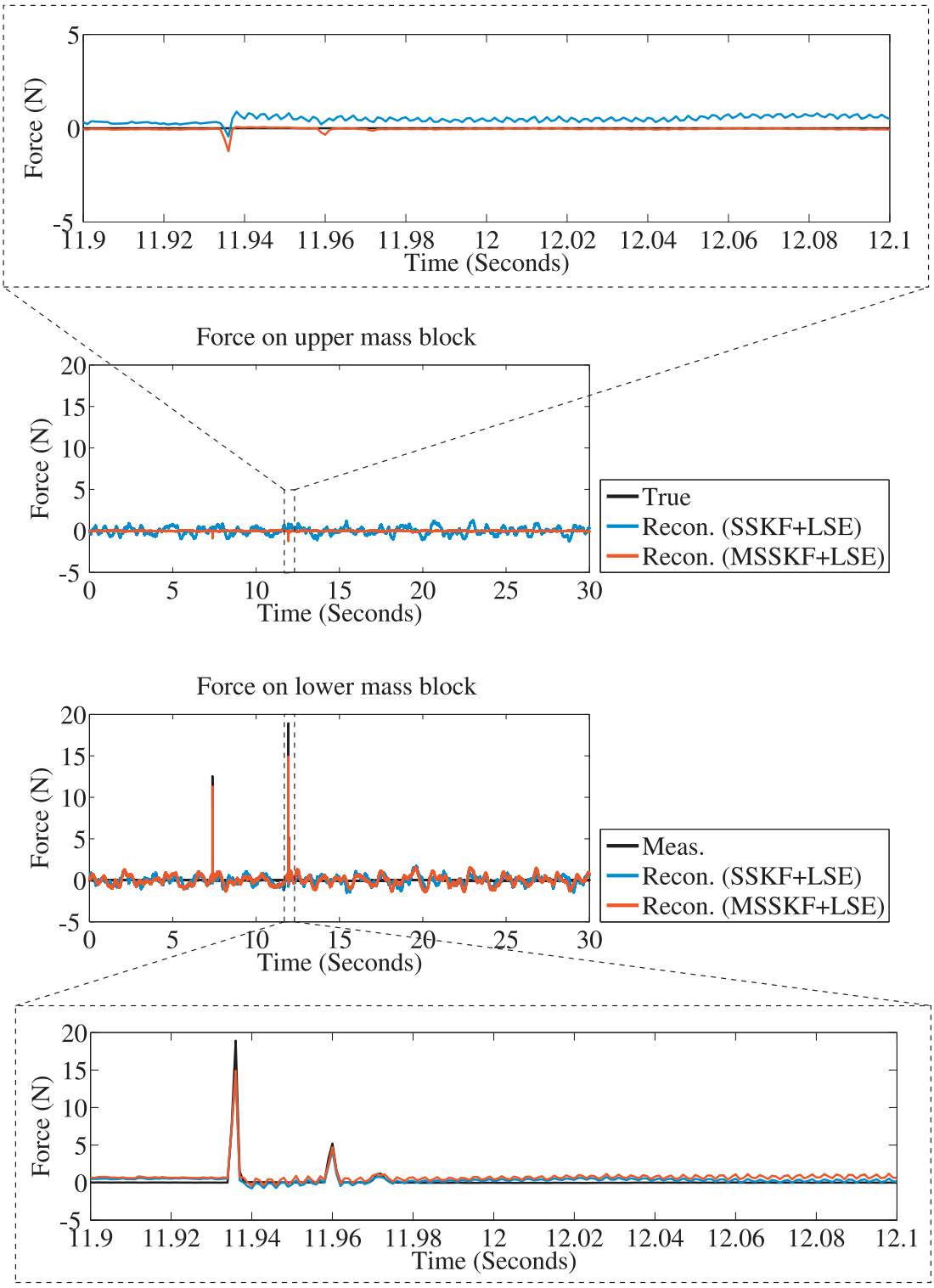

Figure 5.59. *Reconstruction results for the impact force in test using SSKF+LSE and MSSKF+LSE (with two accelerometers)*

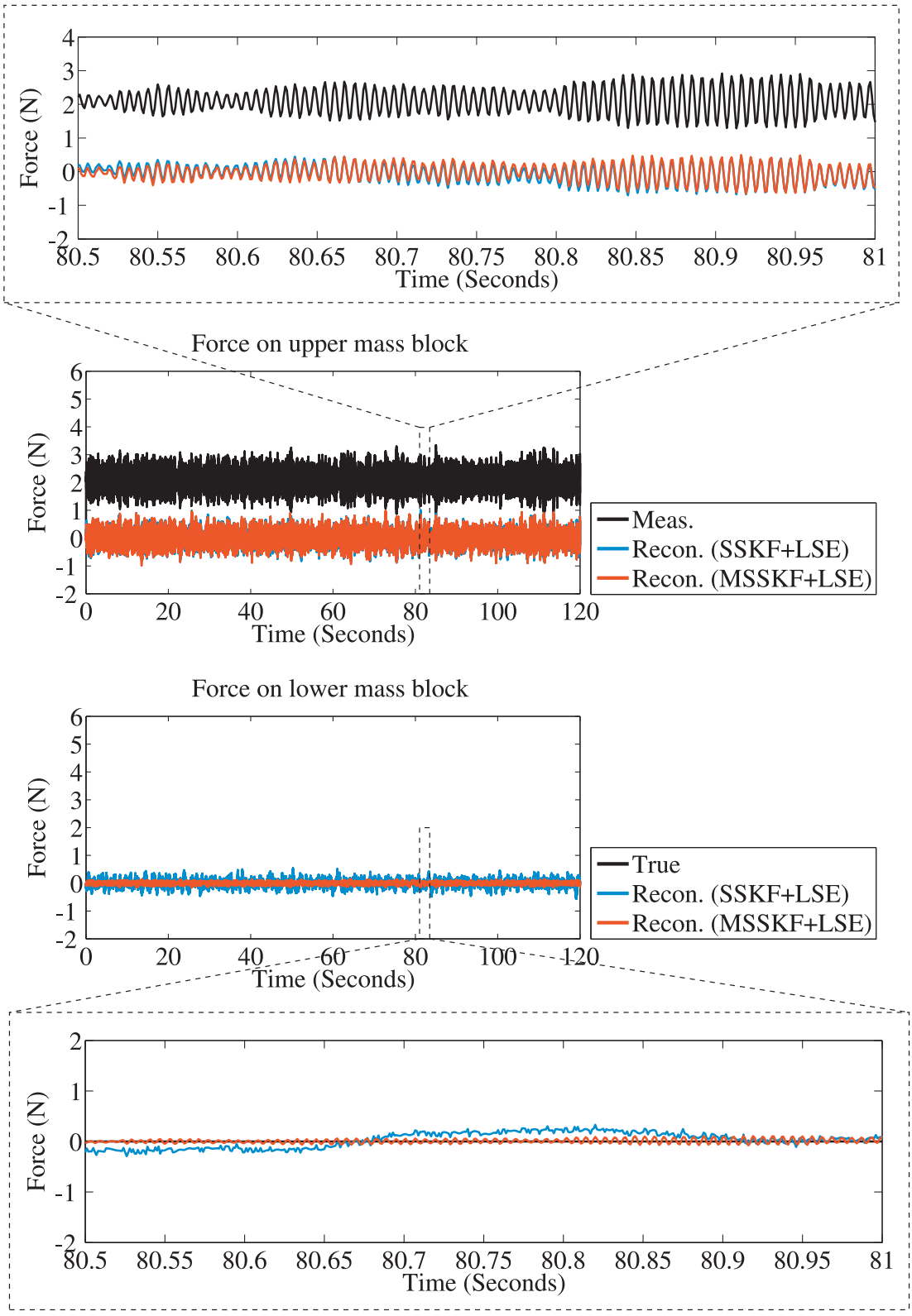

Figure 5.60. *Reconstruction results for the wind load in test using SSKF+LSE and MSSKF+LSE (with two accelerometers)*

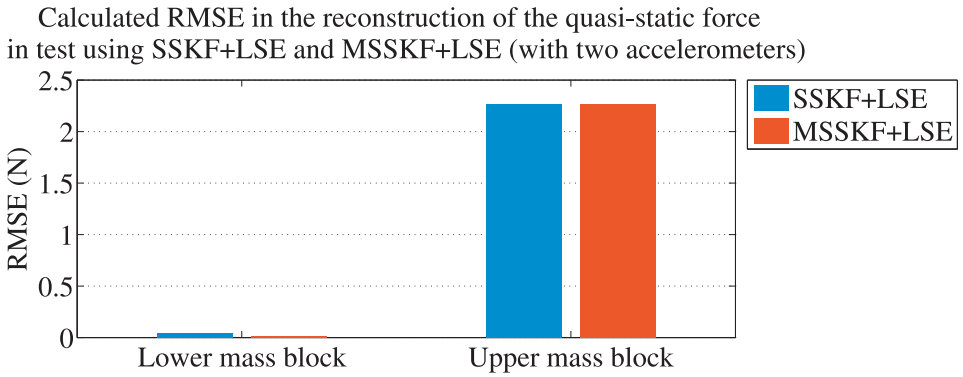

Figure 5.61. *Calculated RMSE in the reconstruction of the quasi-static force in test using SSKF+LSE and MSSKF+LSE (with two accelerometers)*

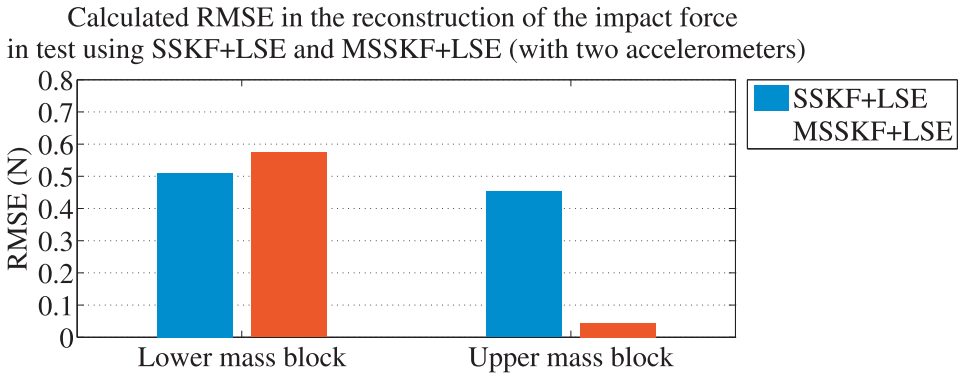

Figure 5.62. *Calculated RMSE in the reconstruction of the impact force in test using SSKF+LSE and MSSKF+LSE (with two accelerometers)*

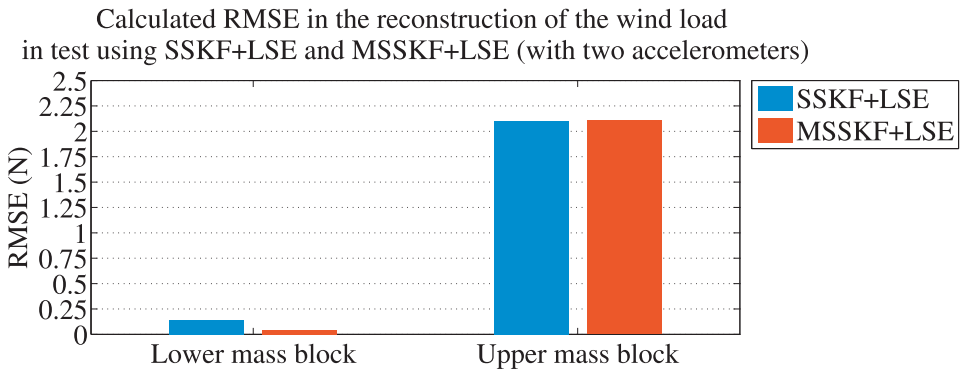

Figure 5.63. *Calculated RMSE in the reconstruction of the wind load in test using SSKF+LSE and MSSKF+LSE (with two accelerometers)*

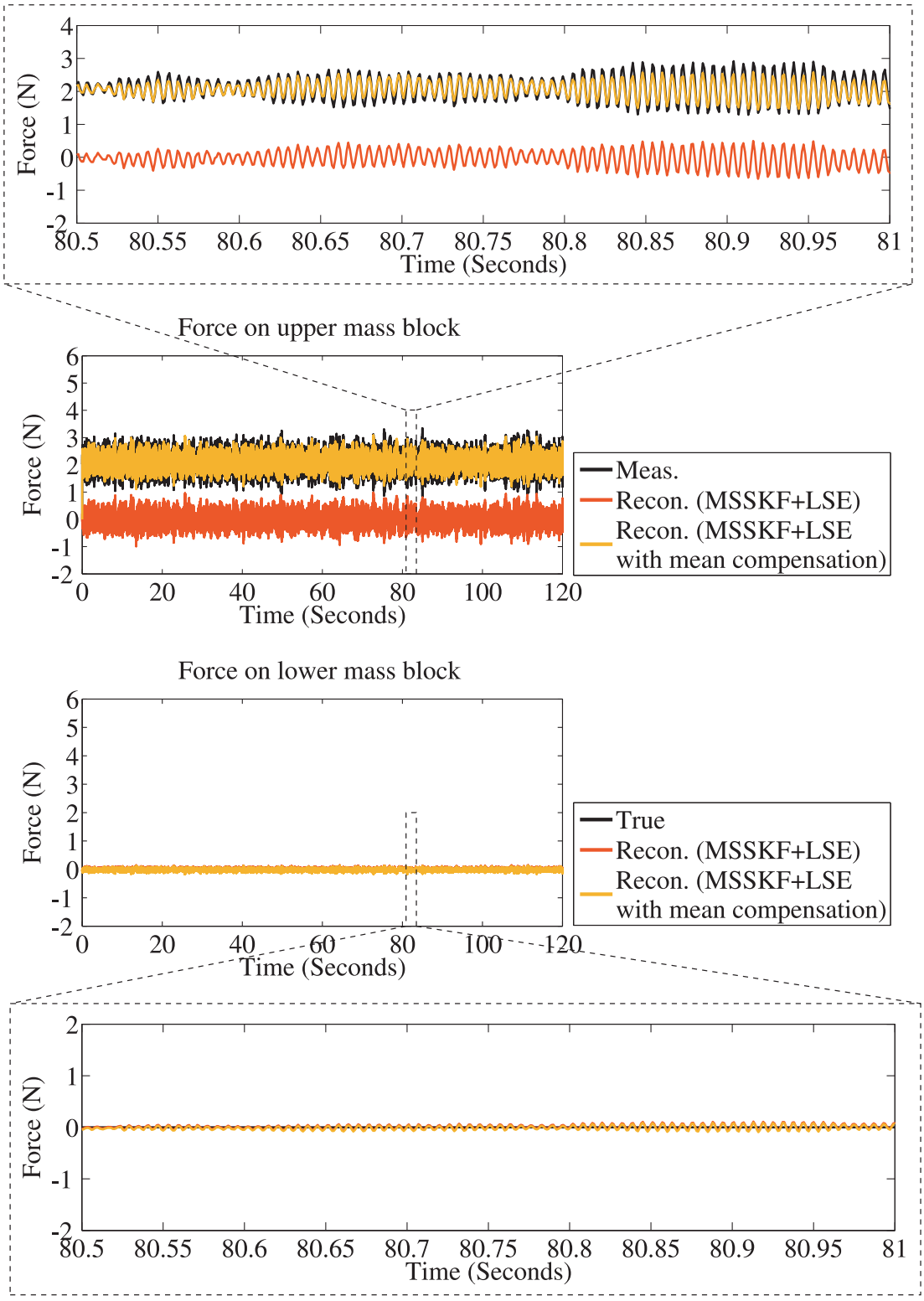

Figure 5.64. *Reconstruction results for the wind load in test using MSSKF+LSE (with only accelerometers and mean compensation)*

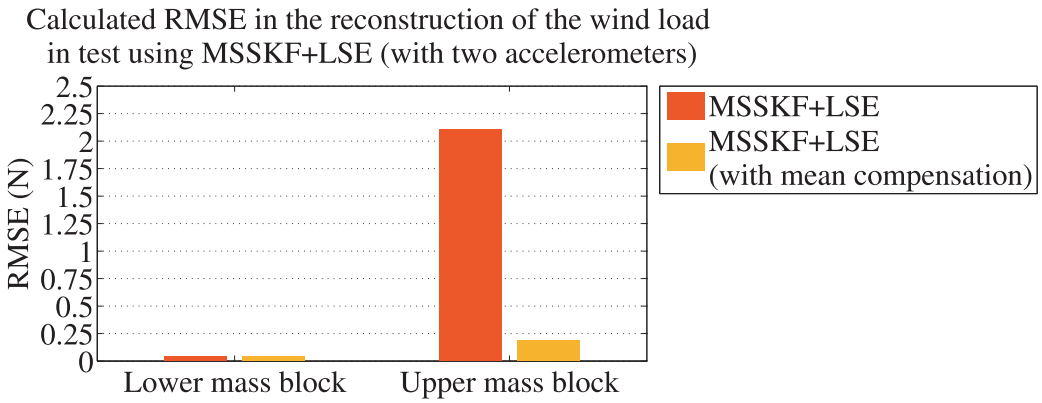

Figure 5.65. *Calculated RMSE in the reconstruction of the wind load in test using MSSKF+LSE (with two accelerometers and mean compensation)*

Table 5.43. *Summary of the suitability of the tested algorithms for the reconstruction of the quasi-static force*

Algorithm	For the reconstruction of the quasi-static force with		
	two strain gauges	*two strain gauges and two accelerometers*	*two accelerometers*
PI observer	Suitable.	N/A.	N/A.
KF+RLSE	Suitable.	N/A.	N/A.
SS&IE_L	N/A.	Suitable.	N/A.
AKF	Suitable, if an estimate of the covariance matrix of the increment of the forces is available.	Suitable, if an estimate of the covariance matrix of the increment of the forces is available.	N/A.
KF-UI	N/A.	Suitable.	N/A.
G-KF-UI	N/A.	Suitable.	N/A.
SSKF+LSE	Suitable.	Not suitable.	Not suitable.
MSSKF+LSE	Suitable, if an estimate of the covariance of the forces is available.	Suitable, if an estimate of the covariance of the forces is available.	Not suitable.

5.2.10. Summary

In this benchmark study, a laboratory two-story structure is taken as the benchmark structure. Two types of widely used sensors, strain gauge and accelerometer, are instrumented on this structure for measuring the structural response. Three different types of forces are considered, including a quasi-static force, impact forces, and a wind load which is generated by an electric fan. With the measured structural response data, in total eight different algorithms are tested. The goal is to study the suitability and the potential of these algorithms for the reconstruction of the considered three types of forces. The reconstruction results from the benchmark study are summarized in table 5.43 through table 5.45. These results actually answer the questions which are raised in the beginning of section 5.2.

Table 5.44. *Summary of the suitability of the tested algorithms for the reconstruction of the impact force*

Algorithm	For the reconstruction of the impact force with		
	two strain gauges	*two strain gauges and two accelerometers*	*two accelerometers*
PI observer	Not suitable.	N/A.	N/A.
KF+RLSE	Not suitable.	N/A.	N/A.
SS&IE_L	N/A.	Suitable.	N/A.
AKF	Not suitable.	Suitable, if an estimate of the covariance matrix of the increment of the forces is available.	N/A.
KF-UI	N/A.	Suitable.	N/A.
G-KF-UI	N/A.	Suitable.	N/A.
SSKF+LSE	Not suitable.	Suitable.	Suitable.
MSSKF+LSE	Not suitable.	Suitable, if an estimate of the covariance of the forces is available.	Suitable, if an estimate of the covariance of the forces is available.

Table 5.45. *Summary of the suitability of the tested algorithms for the reconstruction of the wind load*

Algorithm	For the reconstruction of the wind load with		
	two strain gauges	*two strain gauges and two accelerometers*	*two accelerometers*
PI observer	Suitable only for reconstructing the static part of the wind load.	N/A.	N/A.
KF+RLSE	Suitable only for reconstructing the static part of the wind load.	N/A.	N/A.
SS&IE_L	N/A.	Suitable.	N/A.
AKF	Suitable only for reconstructing the static part of the wind load, if an estimate of the covariance matrix of the increment of the forces is available.	Suitable, if an estimate of the covariance matrix of the increment of the forces is available.	N/A.
KF-UI	N/A.	Suitable.	N/A.
G-KF-UI	N/A.	Suitable.	N/A.
SSKF+LSE	Suitable only for reconstructing the static part of the wind load.	Suitable only for reconstructing the dynamic part of the wind load.	Suitable only for reconstructing the dynamic part of the wind load.
MSSKF+LSE	Suitable only for reconstructing the static part of the wind load, if an estimate of the covariance of the forces is available.	Suitable, if an estimate of the covariance of the forces is available.	Suitable only for reconstructing the dynamic part of the wind load, if an estimate of the covariance of the forces is available.

5.3. Proposed guidance for algorithm selection

In case there is a need for online force reconstruction, it can be one of the following cases.

(1) The type of the force which needs to be reconstructed is known. Which algorithm can reconstruct the force with less sensors?

(2) There are already some sensors on the structure, e.g. strain gauges or accelerometers. Which type of force can be reconstructed with the available sensors?

(3) The type of the force which needs to be reconstructed is known, and there are already some sensors on the structure, e.g. strain gauges or accelerometers. Which algorithm can reconstruct the force with the available sensors?

Based on the results from the benchmark study in section 5.2.10, an algorithm selection guidance is extracted and provided in table 5.46 through table 5.48. This guidance can be used as an assistant for algorithm selection in the cases which are listed above.

Table 5.46. *Suggested algorithms for the reconstruction of impact force*

Suggested algorithms for the reconstruction of impact force	
with only strain gauge	No suitable algorithm.
with strain gauge and accelerometer	The following algorithms can be considered. • SS&IE_L. • If an estimate of the covariance matrix of the increment of the forces is available, the AKF is suitable, too. • Both the KF-UI and the G-KF-UI are suitable, and provide similar results. • Both the SSKF+LSE and the MSSKF+LSE are suitable. If an estimate of the covariance matrix of the forces is available, the MSSKF+LSE provides better results than the SSKF+LSE.
with only accelerometer	The following algorithms can be considered. • Both the SSKF+LSE and the MSSKF+LSE are suitable. If an estimate of the covariance matrix of the forces is available, the MSSKF+LSE provides better results than the SSKF+LSE.

Table 5.47. *Suggested algorithms for the reconstruction of wind load*

Suggested algorithms for the reconstruction of wind load	
with only strain gauge	The following algorithms can be considered, but provide only an estimate of the static part of the wind load. • PI observer. • KF+RLSE. • If an estimate of the covariance matrix of the increment of the forces is available, the AKF is suitable. • Both the SSKF+LSE and the MSSKF+LSE are suitable. If an estimate of the covariance matrix of the forces is available, the MSSKF+LSE provides better results than the SSKF+LSE.
with strain gauge and accelerometer	The following algorithms can be considered. • SS&IE_L. • If an estimate of the covariance matrix of the increment of the forces is available, the AKF is suitable, too. • Both the KF-UI and the G-KF-UI are suitable, and provide similar results. • Both the SSKF+LSE and the MSSKF+LSE are suitable. If an estimate of the covariance matrix of the forces is available, the MSSKF+LSE provides better results than the SSKF+LSE.
with only accelerometer	The following algorithms can be considered, but provide only an estimate of the dynamic part of the wind load. • Both the SSKF+LSE and the MSSKF+LSE are suitable. If an estimate of the covariance matrix of the forces is available, the MSSKF+LSE provides better results than the SSKF+LSE.

Table 5.48. *Suggested algorithms for the reconstruction of quasi-static force*

Suggested algorithms for the reconstruction of quasi-static force	
with only strain gauge	The following algorithms can be considered. • PI observer. • KF+RLSE. • If an estimate of the covariance matrix of the increment of the forces is available, the AKF is suitable. • Both the SSKF+LSE and the MSSKF+LSE are suitable. If an estimate of the covariance matrix of the forces is available, the MSSKF+LSE provides better results than the SSKF+LSE.
with strain gauge and accelerometer	The following algorithms can be considered. • SS&IE_L. • If an estimate of the covariance matrix of the increment of the forces is available, the AKF is suitable, too. • Both the KF-UI and the G-KF-UI are suitable, and provide similar results. • If an estimate of the covariance matrix of the forces is available, the MSSKF+LSE is suitable, too.
with only accelerometer	No suitable algorithm.

6. Practical application to the Canton Tower

6.1. Introduction

The Canton Tower has a height with 600 meters, and is located in a typhoon active area. A long-term SHM system has been designed and integrated onto this tower (Ni et al., 2009). These factors make the Canton Tower an ideal test-bed for wind load reconstruction study. In this chapter, the online force reconstruction methodology in figure 3.5 is adopted and applied to the Canton Tower. The field measurements which were recorded during the Typhoon Nanmadol in 2011 and during the Typhoon Kai-tak in 2012 are analyzed, and the reconstruction results are presented. This study is partly sponsored by a grant from the Germany/Hong Kong Joint Research Scheme which is sponsored by the German Academic Exchange Service (DAAD) and the Research Grant Council (RGC) of Hong Kong (Reference No. G_HK035/11).

6.1.1. Canton Tower

The Canton Tower, which was formerly known as Guangzhou New Television Tower (GNTVT), is a 600 meter tall multi-purpose observation tower. It serves for the functions of TV and radio transmission, sightseeing, cultural entertainment and offers an orbital Ferris wheel, a ceremony hall, observatory decks, 4D cinemas, revolving restaurants, sky-walk, etc. In November 2010, the Canton Tower was responsible for broadcasting the 16th Asian Games which was hosted in the same city, Guangzhou, China. Currently, the Canton Tower is considered as the landmark of Guangzhou. Figure 6.1 provides a bird's eye view of the Canton Tower.

The Canton Tower comprises a 454 meter tall main tower and a 146 meter tall antenna mast. The whole structure has a tube-in-tube geometry, including a reinforced concrete inner structure and a steel lattice outer structure. Figure 6.2 describes the tube-in-tube geometry of the Canton Tower. The reinforced concrete inner structure has an oval shape and a constant dimension of 14 m x 17 m in plan. The steel lattice outer structure consists of 24 Concrete-Filled-Tube (CFT) columns, which are uniformly spaced in an oval shape and inclined in the vertical direction. With a dimension 50 m x 80 at the ground level, the oval decreases to 20.65 m x 27.5 m at the height of 280 m, and increases to 41 m x 55 m at the top of the outer structure. All 24 CFT columns are interconnected transversely by steel ring beams and bracings.

The height of the Canton Tower was originally designed and constructed with a height of 618 meters. For aviation safety reasons, the height of the Canton Tower was reduced to 600 meters in July in 2010 by adjusting the length of the antenna mast. The comparison in figure 6.3 shows the change of the antenna mast before and after the height adjustment. After this height adjustment, an orbital Ferris wheel was installed on top of the main tower.

Figure 6.1. *A bird's eye view of the Canton Tower (source: http://www.cantontower.com/en/)*

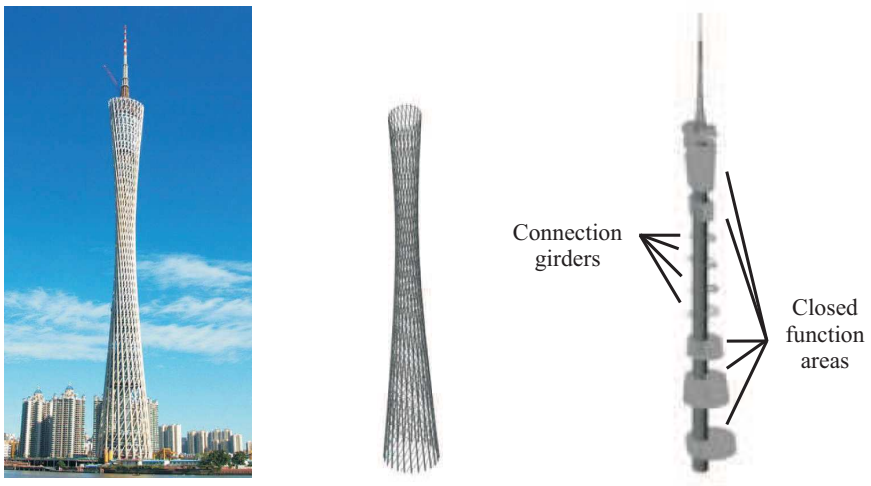

Figure 6.2. *Tube-in-tube geometry of the Canton Tower: Canton Tower (left); steel lattice outer structure (middle); reinforced concrete inner structure (right) (Ni et al., 2009)*

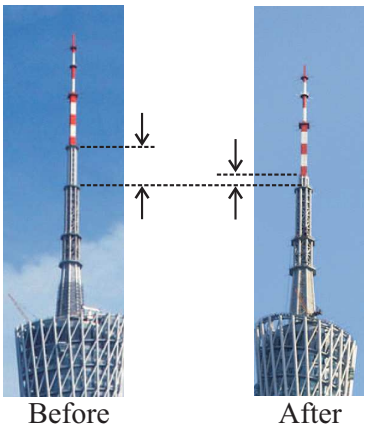

Figure 6.3. *Change of the antenna mast before and after the height adjustment*

6.1.2. SHM system for the Canton Tower

Together with the attractive design of the Canton Tower, come not only nicknames e.g. "Slim Waist" but also complex and challenging mechanics. To facilitate the life-cycle monitoring and the assessment of this high-rise slender structure, a long-term SHM system has been designed and instrumented by The Hong Kong Polytechnic University to the Canton Tower for both in-construction and in-service real-time monitoring (Ni et al., 2009). Figure 6.4 describes the modules of the SHM system for the Canton Tower. Figure 6.5 illustrates the deployment of the sensors and the sub-stations for the in-construction monitoring. Figure 6.6 illustrates the depolyment of the sensors and the sub-stations for the in-service monitoring. In figure 6.5 and figure 6.6, each sub-station represents one Data Acquisition Unit (DAU), and the number inside the paranthesis after the name of each sensor type indicate the total number of that type of sensors at the corresponding height level.

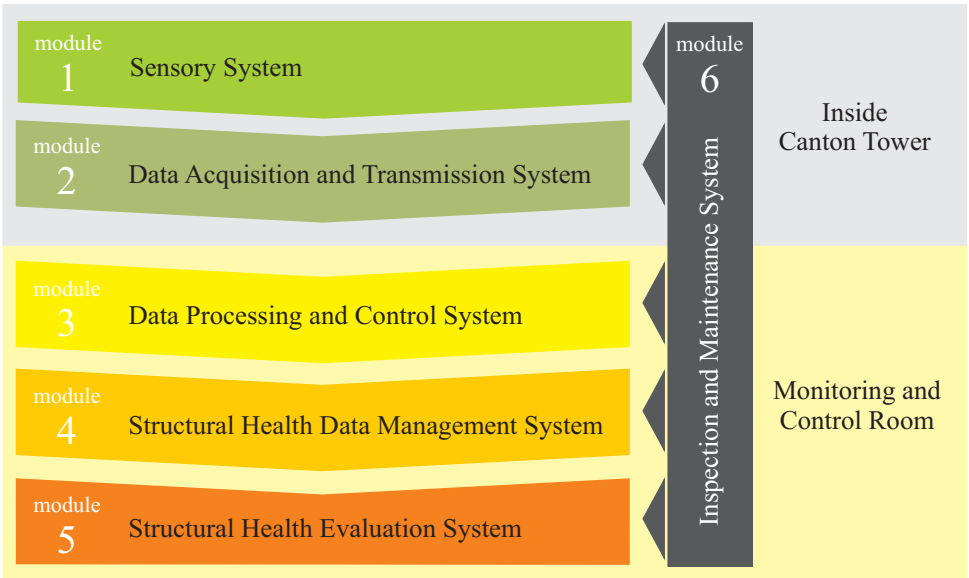

Figure 6.4. *Modules of the SHM system for the Canton Tower (Ni et al., 2009)*

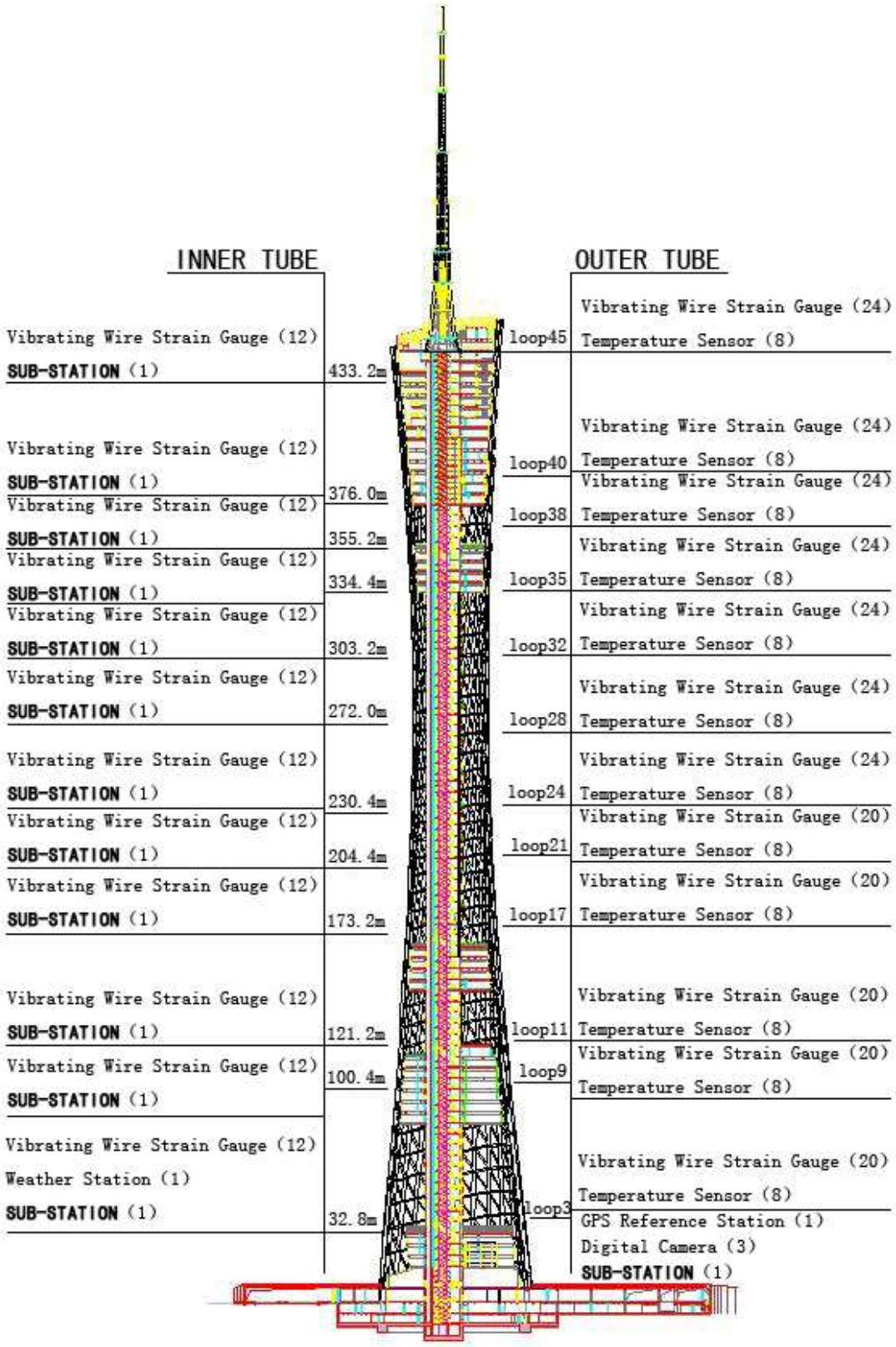

Figure 6.5. *Deployment of sensors and sub-stations for in-construction monitoring (Ni et al., 2009)*

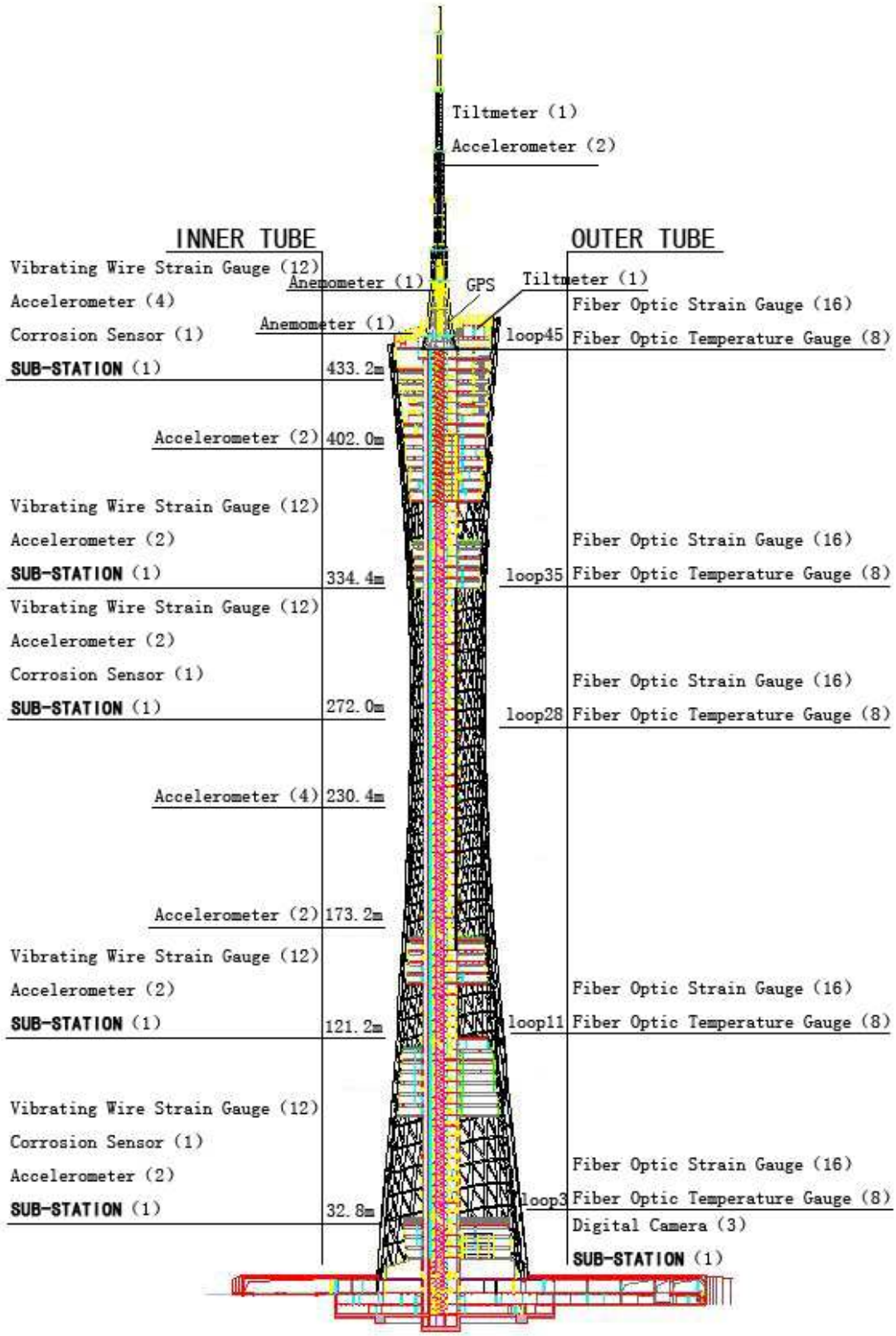

Figure 6.6. *Deployment of sensors and sub-stations for in-service monitoring (Ni et al., 2009)*

6.1.3. SHM benchmark study for the Canton Tower

Under the auspices of the Asian-Pacific Network of Centers for Research in Smart Structure Technology (ANCRiSST), an SHM benchmark problem for high-rise structures is developed by taking the instrumented Canton Tower as a host structure. This SHM benchmark study aims to provide an open platform to the researchers and practitioners in the field of SHM for examining the applicability and reliability of their methods to a real high-rise structure with the use of field monitoring data. To facilitate the benchmark study, a benchmark website (http://www.cse.polyu.edu.hk/benchmark) has been constructed, providing information for different research topics, including modal parameter identification, model updating, force identification, SHM-oriented optimal sensor placement and damage detection (Ni et al., 2012).

6.1.4. Organization of this chapter

This chapter is organized as follows. The methodology which applied in the wind load reconstruction study for the Canton Tower is presented in section 6.2. In section 6.3, an Operational Modal Analysis (OMA) is performed using the field measurement data which were recorded during the Typhoon Nanmadol, and the identified modal parameters are presented. By taking these identified modal parameters as the reference, an available reduced-order FE model of the Canton Tower is updated. The model updating results are presented in section 6.4. In section 6.5, an suitable real-time executable state and input estimation algorithm is selected. With the selected algorithm and the field measurement data which were recorded during the Typhoon Kai-tak, the wind load on the Canton Tower is reconstructed. The reconstruction results are provided in section 6.6. Finally, a summary of this chapter is given in section 6.7.

6.2. Methodology for wind load reconstruction for the Canton Tower

The methodology which is applied for the reconstruction of the wind load on the Canton Tower is described in figure 6.7 . This methodology is a practical application of the one in figure 3.5 to the Canton Tower.

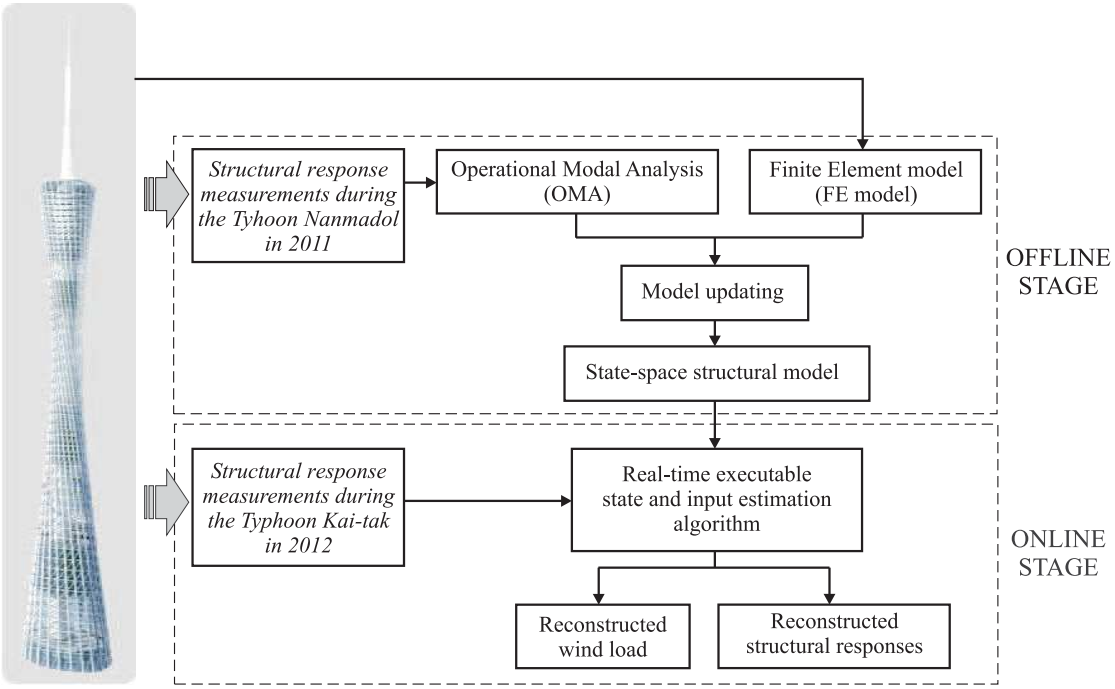

Figure 6.7. *Methodology for the reconstruction of the wind load on the Canton Tower*

6.3. Operational modal analysis for the Canton Tower

For the Canton Tower, a 600 meter tall high-rise structure, it is not feasible to apply an a artificial excitation as in Experimental Modal Analysis (EMA). Operational Modal Analysis (OMA) is capable of extracting the modal parameters of a structure under operational conditions with only structural response measurements. In this study, the OMA is considered to be more suitable for the modal parameter identification for the Canton Tower. The field measurement data which were recorded during the Typhoon Nanmadol are used in the OMA. The applied OMA algorithm is the Vector AutoRegressive models (ARV) method. The principle of the OMA and the ARV method has been briefly reviewed in section 2.1.5.

6.3.1. Sensor deployment and field measurements

The field measurement data which are used in the OMA are

- twenty-four one-hour field measurement datasets which were recorded during the Typhoon Nanmadol on 31 August 2011.

These field measurement datasets include information on acceleration, wind speed, and wind direction. The acceleration were measured by twenty Tokyo Sokushin AS-2000C uni-axial accelerometers which are installed on the reinforced concrete inner structure of the Canton Tower. Figure 6.8 and figure 6.9 describe the positions and the measurement

directions of these accelerometers. In figure 6.8, only the data from the accelerometers whose channel number is in black are applied in the OMA. Figure 6.10 provides an example of two of the twenty accelerometers. The wind speed and the wind direction were measured by one RM Young 05103L anemometer which is installed at a height of 461 meters on the Canton Tower. Figure 6.11 shows the position of this anemometer. The accelerometers and the anemometer are sampled at 50 Hz. The 10-minute mean of the measured wind speed and the measured wind direction are plotted in Figure 6.12. To represent the distribution of the measured wind speed and the measured wind direction, a rose diagram is generated and is provided in figure 6.13.

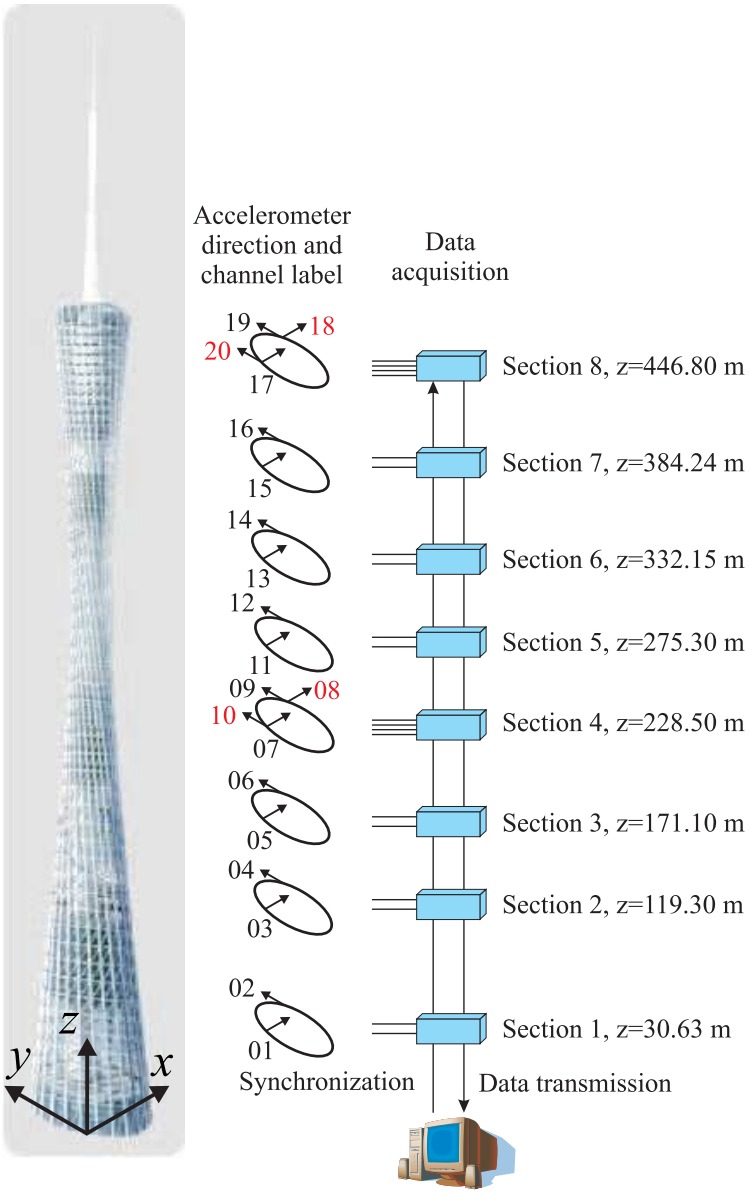

Figure 6.8. *Data acquisition system for the accelerometers on the Canton Tower (http://www.cse.polyu.edu.hk/benchmark)*

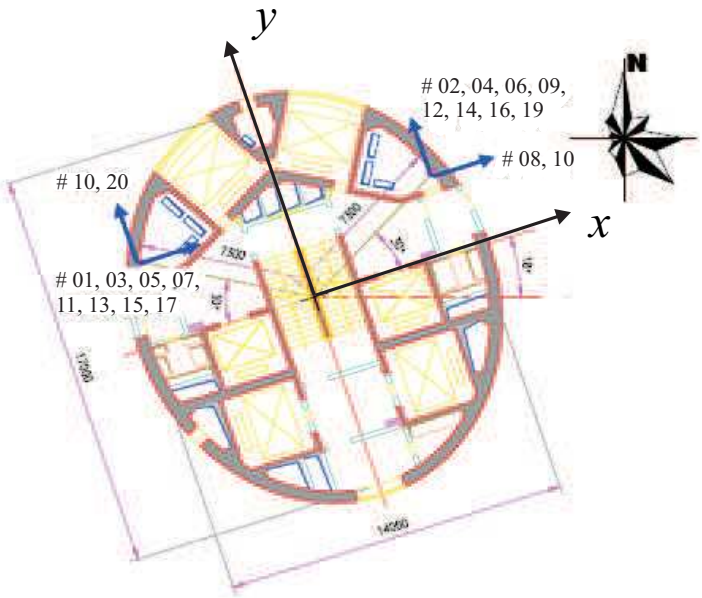

Figure 6.9. *Positions and measurement directions of the accelerometers on the Canton Tower (http://www.cse.polyu.edu.hk/benchmark)*

Figure 6.10. *An example of 2 accelerometers installed on the Canton Tower (http://www.cse.polyu.edu.hk/benchmark)*

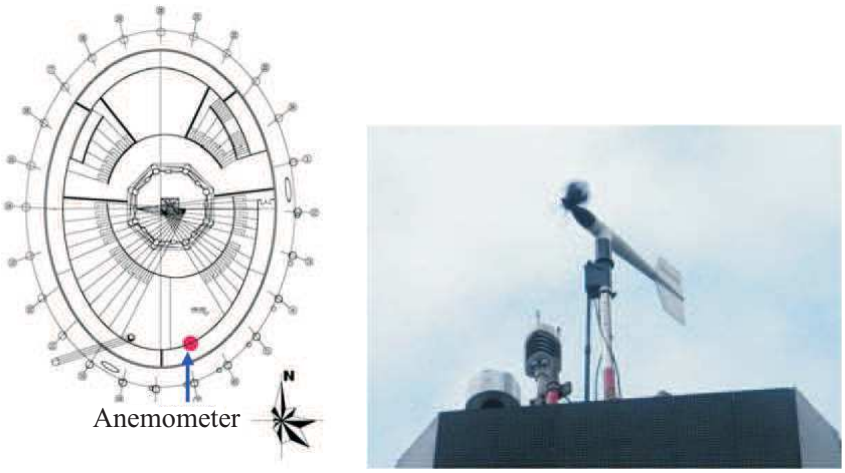

(a) *Position of anemometer* **(b)** *Anemometer*

Figure 6.11. *Anemometer on the Canton Tower (http://www.cse.polyu.edu.hk/benchmark/)*

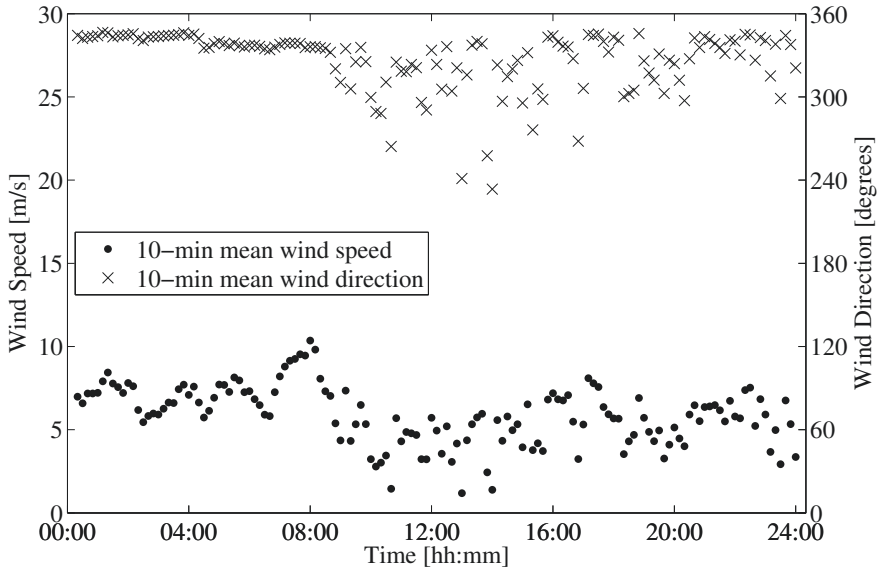

Figure 6.12. *10-minute mean wind speed and wind direction recorded from 00:07:45 on 31 August 2011 to 00:07:45 on 1 September 2011*

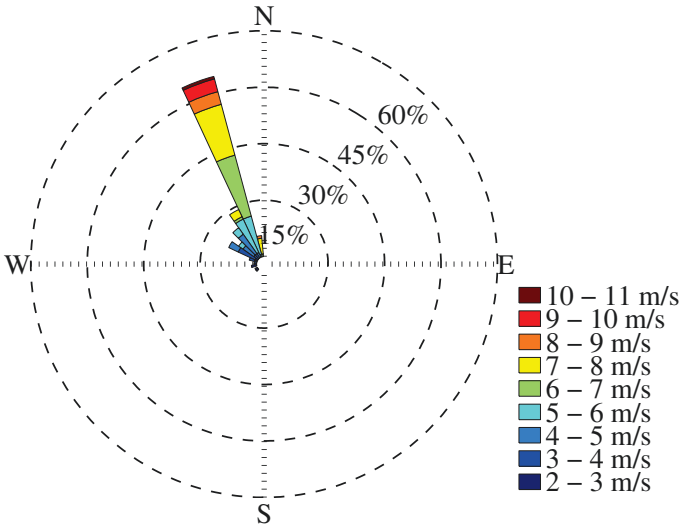

Figure 6.13. *Rose diagram of the wind measurements from 00:07:45 on 31 August 2011 to 00:07:45 on 1 September 2011*

6.3.2. Stationarity test

To identify the modal parameters of the Canton Tower, the ARV method is applied. A brief review of the ARV method has been provided in section 2.1.5. This method assumes that the field measurements are stationary. So before applying the ARV method, a stationarity test is performed on the twenty-four one-hour acceleration datasets. This stationarity test applies a multivariate outlier detection technique based on the Mahalanobis-distance with the threshold provided by the F-distribution (Rencher, 2002). Only the datasets which pass the stationarity test are processed by the ARV method.

6.3.3. OMA results

In this study, the ARV method is applied to identify the modal parameters of the Canton Tower. The ARV method is a parametric method. An advantage of the parametric method is that a stabilization diagram can be constructed, with which the physical modes of the Canton Tower can be objectively separated from the spurious modes which are caused by measurement noise or numerical errors. To construct the stabilization diagram, three criteria are applied, including the percentage frequency difference f_{diff}, the percentage damping ratio difference ζ_{diff}, and the Modal Assurance Criterion (MAC). The definition of these three criteria have been provided in section 2.1.5. In this study, the settings for these three criteria are listed in table 6.1. With these three criteria, a stabilization diagram is constructed for each of the one-hour acceleration datasets which have passed the stationarity test in section 6.3.2. As an example, figure 6.14 provides the constructed stabilization diagram for the one-hour dataset which was recorded from 02:07:45 to 03:07:45 on 31 August 2011. Table 6.2 lists the identified natural frequencies and the identified damping ratios of the first twelve modes. The identified bending mode shapes of the main tower of the Canton Tower are plotted in figure 6.15 through figure 6.20, where the black dash line with square represents the reference, and the red solid line with star describes the scaled mode shape.

Table 6.1. *Settings of the criteria in the construction of the stabilization diagram*

Criteria	Setting	Unit
f_{diff}	1%	(-)
ζ_{diff}	10%	(-)
MAC	97%	(-)

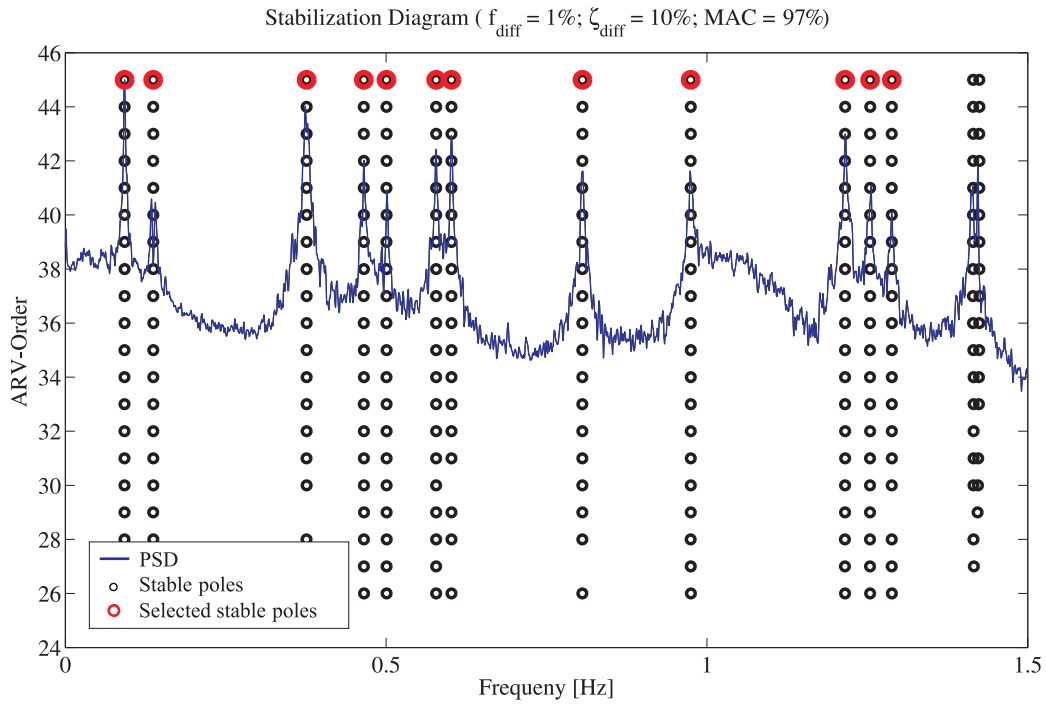

Figure 6.14. *Stabilization diagram for the dataset from 02:07:45 to 03:07:45 on 31 August 2011*

Table 6.2. *Identified natural frequencies and identified damping ratios of the first 12 modes of the Canton Tower under Typhoon Nanmadol from 00:07:45 on 31 August 2011 to 00:07:45 on 1 September 2011*

Mode	Natural frequency f (Hz)	Damping ratio ζ (%)	Mode decription
1	0.0919	0.4114	1st short-axis bending of main tower
2	0.1356	1.2857	1st long-axis bending of main tower
3	0.3735	0.3791	-
4	0.4640	0.3466	-
5	0.4989	0.4560	1st torsion of main tower
6	0.5780	0.1568	2nd short-axis bending of main tower
7	0.6017	0.1731	2nd long-axis bending of main tower
8	0.8031	0.2827	3rd short-axis bending of main tower
9	0.9722	0.2648	3rd long-axis bending of main tower
10	1.2132	0.2271	-
11	1.2522	0.2256	2nd torsion of main tower
12	1.2881	0.1310	-

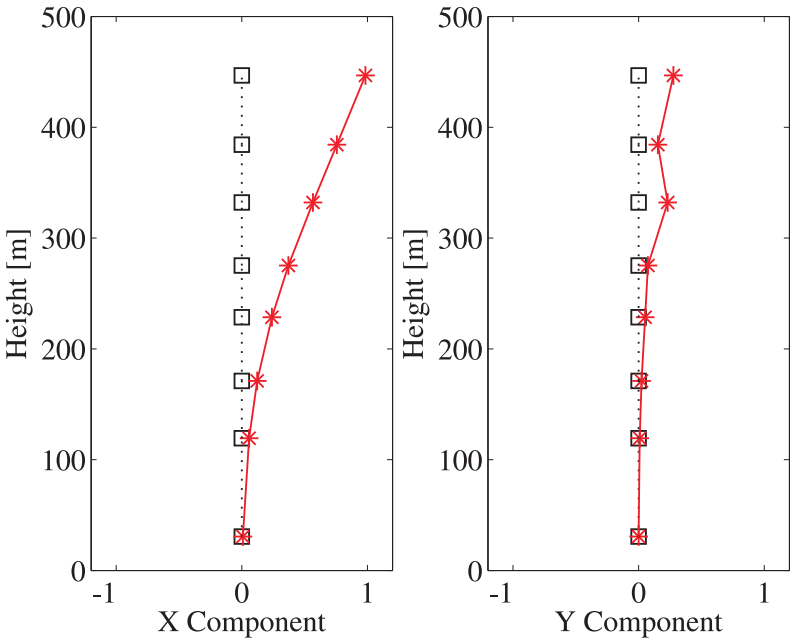

Figure 6.15. *Mode 1: the 1st short-axis bending mode*

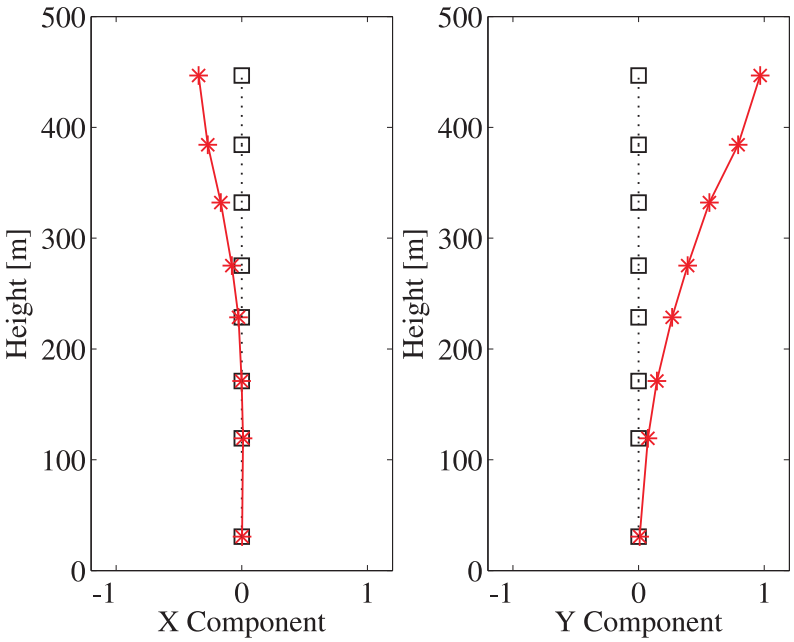

Figure 6.16. *Mode 2: the 1st long-axis bending mode*

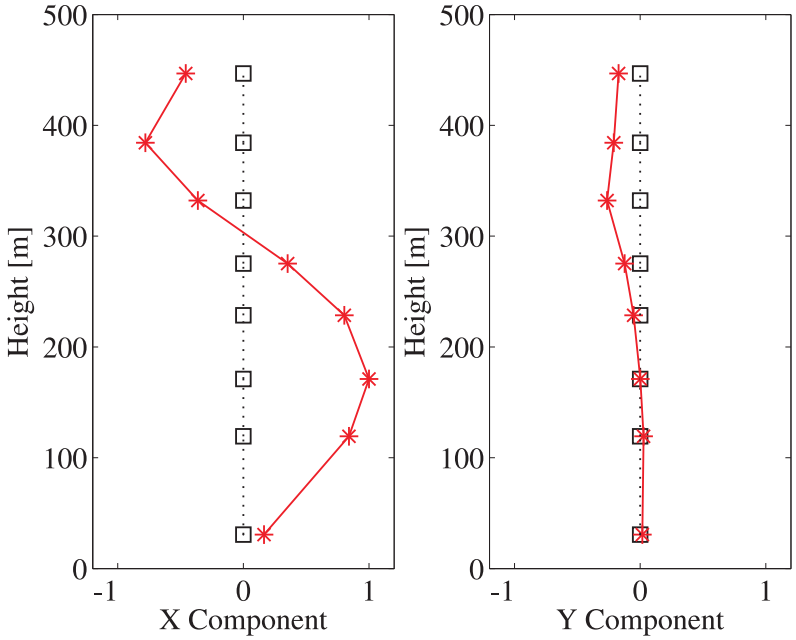

Figure 6.17. *Mode 6: the 2nd short-axis bending mode*

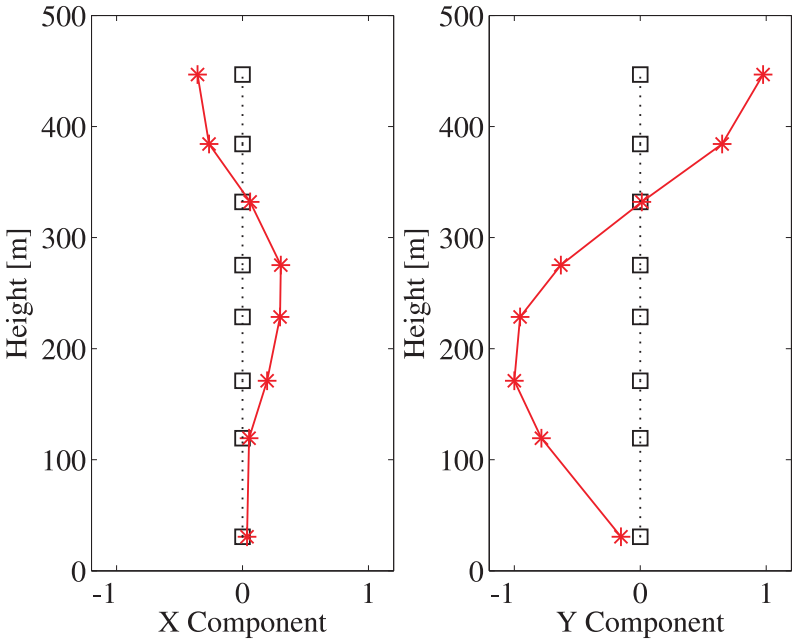

Figure 6.18. *Mode 7: the 2nd long-axis bending mode*

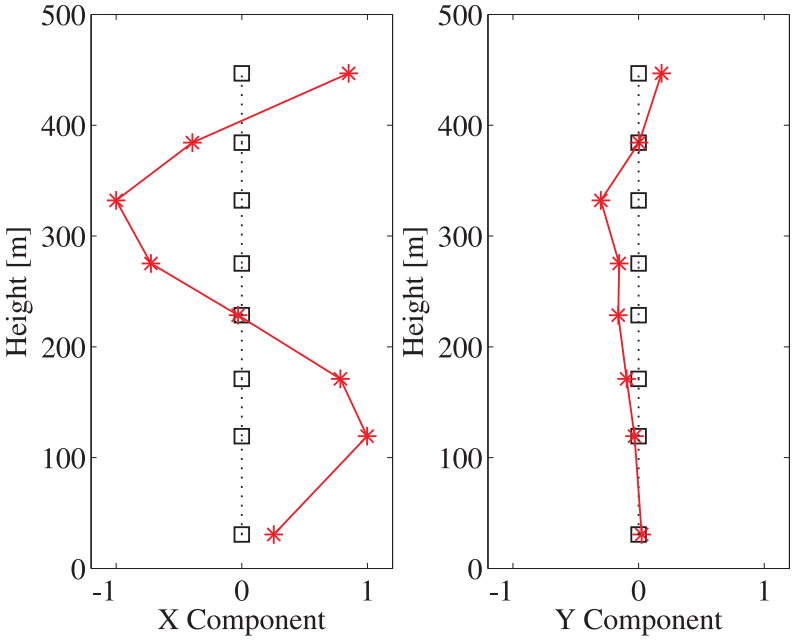

Figure 6.19. *Mode 8: the 3rd short-axis bending mode*

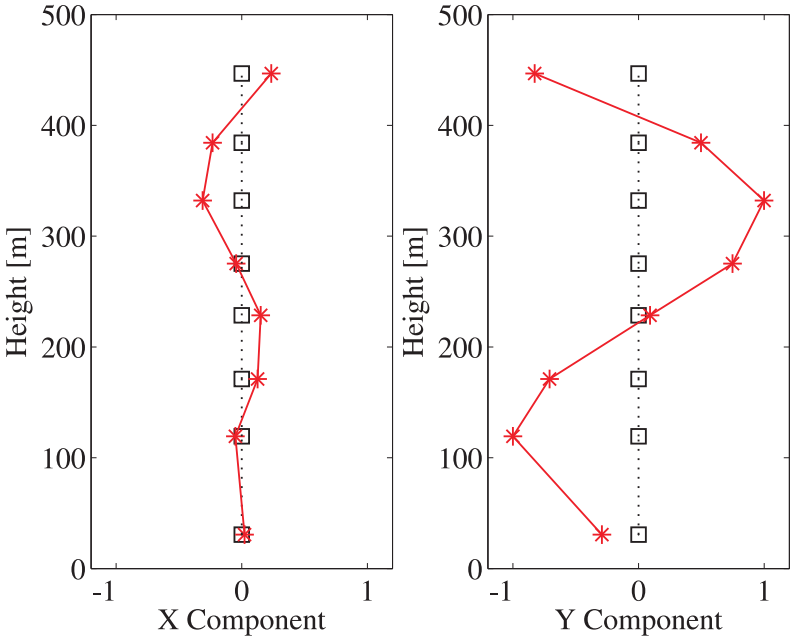

Figure 6.20. *Mode 9: the 3rd long-axis bending mode*

6.3.4. Discussion

The benchmark website of the SHM study for the Canton Tower provides the following data.

- A reduced-order FE model of the Canton Tower;
- Twenty-four one-hour field measurement datasets which were recorded under normal ambient excitation from 18:00 on 19 January 2010 to 18:00 on 20 January 2010.

With the mass matrix and the stiffness matrix from the reduced-order FE model of the Canton Tower, the natural frequencies are calculated. Table 6.3 lists the calculated natural frequencies of the first twelve modes and their corresponding mode descriptions. Niu et al. (2012) performed an OMA for the Canton Tower using the ARV method and the field measurement datasets which are listed above. The identified natural frequencies and the identified damping ratios of the first twelve modes of the Canton Tower are provided in table 6.4. With the results in table 6.2 through table 6.4, the following differences are noticed.

(1) Differences in natural frequencies. Figure 6.21 plots the natural frequencies which are calculated with the reduced-order FE model and the natural frequencies which are identified using field measurement data. It is noticed that the identified natural frequency for a certain modes show some obvious difference from the natural frequency which is calculated from the FE model. For example, the identified natural frequencies are larger than the calculated natural frequencies for the fourth mode through the twelfth mode.

(2) Differences in damping ratios. Figure 6.22 plots the identified damping ratios using the field measurement data which were recorded under two different excitation conditions. For a specific mode, some differences in damping ratios are noticed. For the second mode, which is the first long-axis bending mode of the main tower, the damping ratio that is identified with data from the Typhoon Nanmadol is much larger than the damping ratio that is identified with data from the normal ambient excitation. Such a damping ratio increase in the along-wind direction is also noticed in Guo et al. (2012). According to the cross-sectional view of the main tower in figure 6.9 and the rose diagram in figure 6.13, the dominant wind direction is in parallel with the long axis (or y axis) of the main tower. A possible contribution to this relatively larger damping ratio of the second mode could be the aerodynamic damping.

(3) Differences in mode sequence. The sequence of the identified modes in table 6.4 is in accordance with that in table 6.3, but not with that in table 6.2. In table 6.2, the first torsion mode of the main tower appears as the fifth mode, the second short-axis bending mode of the main tower appears as the sixth mode, and the second torsion

mode of the main tower appears as the twelfth mode. The sequential positions of these modes are not in accordance with those in table 6.3.

According to the methodology in figure 6.7, a state-space structural model of the Canton Tower is needed. This structural model should be capable of representing the dynamics of the Canton Tower. The differences which are listed above indicate that the available reduced-order FE model of the Canton Tower should be updated before it is applied to represent the Canton Tower under similar excitation conditions.

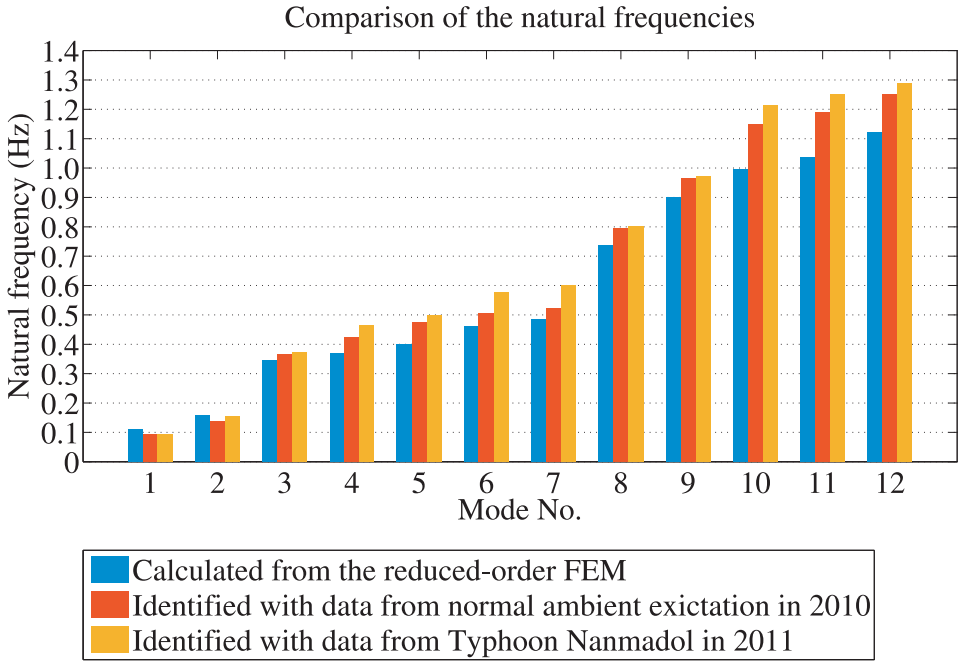

Figure 6.21. *Comparison of the natural frequencies*

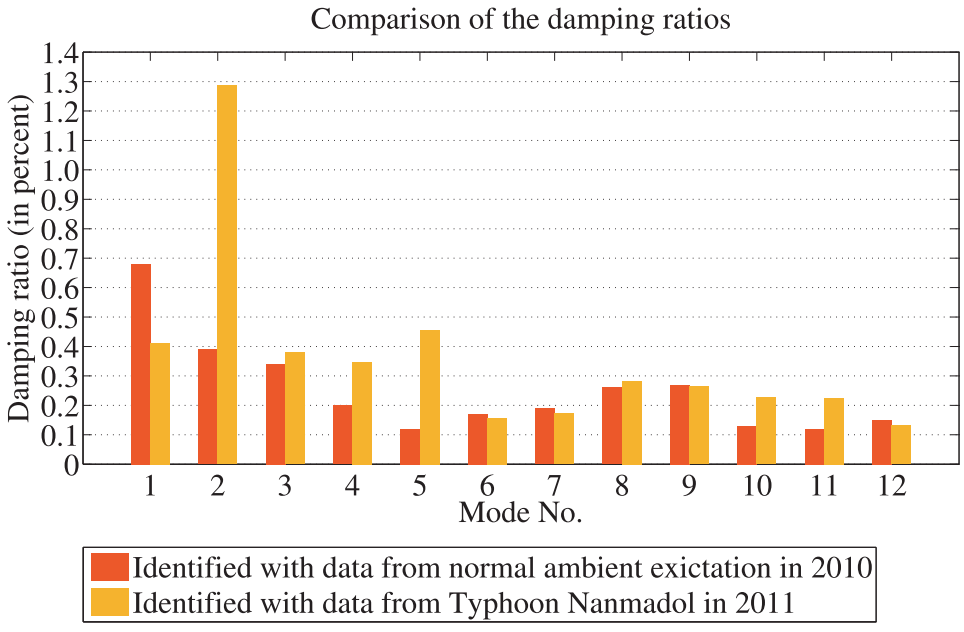

Figure 6.22. *Comparision of the damping ratios*

Table 6.3. *Calculated natural frequencies of the first 12 modes from the reduced-order FEM*

Mode	Natural frequency f (Hz)	Mode description
1	0.110	1st short-axis bending of main tower
2	0.159	1st long-axis bending of main tower
3	0.347	1st short-axis bending of mast
4	0.368	1st long-axis bending of mast
5	0.399	2nd short-axis bending of main tower
6	0.460	1st torsion of main tower
7	0.485	2nd long-axis bending of main tower
8	0.738	3rd short-axis bending of main tower
9	0.902	3rd long-axis bending of main tower
10	0.997	2nd short-axis bending of mast
11	1.038	2nd long-axis bending of mast
12	1.122	2nd torsion of main tower

Table 6.4. *Identified natural frequencies and Identified damping ratios of the 12 modes of the Canton Tower under normal ambient excitation*

Mode	Natural frequency f (Hz)	Damping ratio ζ (%)	Mode description
1	0.0936	0.68	1st short-axis bending of main tower
2	0.1384	0.39	1st long-axis bending of main tower
3	0.3659	0.34	-
4	0.4238	0.20	-
5	0.4747	0.12	2nd short-axis bending of main tower
6	0.5055	0.17	1st torsion of main tower
7	0.5224	0.19	2nd long-axis bending of main tower
8	0.7953	0.26	3rd short-axis bending of main tower
9	0.9648	0.27	3rd long-axis bending of main tower
10	1.1505	0.13	-
11	1.1909	0.12	-
12	1.2507	0.15	2nd torsion of main tower

6.4. Model updating for the Canton Tower

The reduced-order FE model, which is available on the benchmark website for the Canton Tower, was developed when the Canton Tower was with the height of 618 meters. Table 6.5 lists the vertical coordinates of the nodes in the reduced-order FE model. For aviation safety reasons, the height of the Canton Tower was reduced to 600 meters in July 2010 by adjusting the length of the antenna mast. After this height adjustment, an orbital Ferris wheel was installed on top of the main tower. Such changes on the structure may cause the modal parameters change, and the available reduced-order FE model will not be able to represent the dynamics of the Canton Tower.

In this section, the available reduced-order FEM is first modified to better represent the positions of the accelerometers and the current height of the Canton Tower. Then the modified reduced-order FEM is updated according to the OMA results in table 6.2.

Table 6.5. *Vertical coordinates of the nodes in the reduced-order FEM*

Node No.	z (m)	Node No.	z (m)	Node No.	z (m)	Node No.	z (m)
1	-10.00	13	168.00	25	417.45	37	598.00
2	0.00	14	204.25	26	427.85	38	618.00
3	12.00	15	225.20	27	438.25		
4	22.25	16	272.00	28	443.60		
5	27.60	17	308.25	29	480.00		
6	58.65	18	329.20	30	497.60		
7	84.65	19	344.65	31	505.20		
8	95.05	20	355.05	32	520.70		
9	105.45	21	375.85	33	531.20		
10	116.20	22	381.20	34	545.20		
11	147.05	23	396.65	35	565.20		
12	157.45	24	407.05	36	580.70		

6.4.1. Modified reduced-order FE model of the Canton Tower

The available reduced-order FE model of the Canton Tower is modified as below.

(1) The nodes for the main tower in the reduced-order FEM are adjusted to coincide with the vertical coordinates of the accelerometers.

(2) The nodes for the antenna mast in the reduced-order FEM are adjusted to reflect the length adjustment.

After the modifications above, the number of the nodes is reduced from 38 to 36. Table 6.6 lists the vertical coordinates of the nodes of the modified reduced-order FE model. In figure 6.23 the nodes of the modified reduced-order FE model are plotted. This modified reduced-order FEM has in total 36 nodes and 35 beam elements, with 27 elements for the main tower and 8 elements for the antenna mast. Each node has two horizontally translated DOFs and three rotational DOFs. With the node 1 being constrained, the modified reduced-order FEM has in total 175 unconstrained DOFs.

Table 6.6. *Vertical coordinates of the nodes in the modified reduced-order FEM*

Node No.	z (m)	Node No.	z (m)	Node No.	z (m)
1	-10.00	13	171.10	25	417.45
2	0.00	14	204.25	26	427.85
3	12.00	15	228.50	27	438.25
4	22.25	16	275.30	28	446.80
5	30.63	17	308.25	29	480.00
6	58.65	18	332.15	30	497.60
7	84.65	19	344.65	31	502.00
8	95.05	20	355.05	32	520.70
9	105.45	21	375.85	33	547.20
10	119.30	22	384.24	34	562.70
11	147.05	23	395.65	35	580.00
12	157.45	24	407.05	36	600.00

6.4.2. Model updating method

The method which is applied in this study for updating the modified reduced-order FE model is inspired by the work in Chung et al. (2012). Two updating parameters α_x and α_y are assigned to each element stiffness matrix to represent the bending stiffness changes in the x direction and in the y direction, respectively. The mass matrix are all kept constant. For the modified reduced-order FE model of the Canton Tower, in total 35 pairs of α_x and α_y need to be updated. Figure 6.24 shows a typical updated element stiffness matrix, where $\boldsymbol{K}_U^e$ represents the updated element stiffness matrix, and $K_{i,j}$ denotes the ij-th element of the initial element stiffness matrix $\boldsymbol{K}^e$, with $1 \leq i \leq 10$ and $1 \leq j \leq 10$.

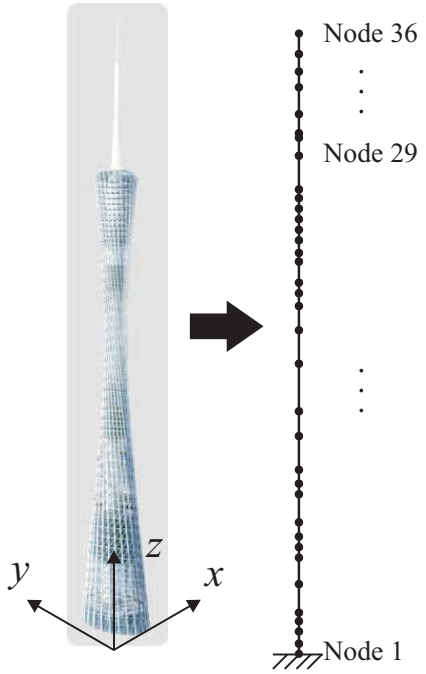

Figure 6.23. *Modified reduced-order FEM of the Canton Tower*

$$\boldsymbol{K}_U^e = \begin{bmatrix}
\alpha_x K^e_{1,1} & \alpha_x\alpha_y K^e_{1,2} & \alpha_x K^e_{1,3} & \alpha_x K^e_{1,4} & \alpha_x K^e_{1,5} & \alpha_x K^e_{1,6} & \alpha_x\alpha_y K^e_{1,7} & \alpha_x K^e_{1,8} & \alpha_x K^e_{1,9} & \alpha_x K^e_{1,10} \\
\alpha_x\alpha_y K^e_{2,1} & \alpha_y K^e_{2,2} & \alpha_y K^e_{2,3} & \alpha_y K^e_{2,4} & \alpha_y K^e_{2,5} & \alpha_x\alpha_y K^e_{2,6} & \alpha_y K^e_{2,7} & \alpha_y K^e_{2,8} & \alpha_y K^e_{2,9} & \alpha_y K^e_{2,10} \\
\alpha_x K^e_{3,1} & \alpha_y K^e_{3,2} & K^e_{3,3} & K^e_{3,4} & K^e_{3,5} & \alpha_x K^e_{3,6} & \alpha_y K^e_{3,7} & K^e_{3,8} & K^e_{3,9} & K^e_{3,10} \\
\alpha_x K^e_{4,1} & \alpha_y K^e_{4,2} & K^e_{4,3} & K^e_{4,4} & K^e_{4,5} & \alpha_x K^e_{4,6} & \alpha_y K^e_{4,7} & K^e_{4,8} & K^e_{4,9} & K^e_{4,10} \\
\alpha_x K^e_{5,1} & \alpha_y K^e_{5,2} & K^e_{5,3} & K^e_{5,4} & K^e_{5,5} & \alpha_x K^e_{5,6} & \alpha_y K^e_{5,7} & K^e_{5,8} & K^e_{5,9} & K^e_{5,10} \\
\alpha_x K^e_{6,1} & \alpha_x\alpha_y K^e_{6,2} & \alpha_x K^e_{6,3} & \alpha_x K^e_{6,4} & \alpha_x K^e_{6,5} & \alpha_x K^e_{6,6} & \alpha_x\alpha_y K^e_{6,7} & \alpha_x K^e_{6,8} & \alpha_x K^e_{6,9} & \alpha_x K^e_{6,10} \\
\alpha_x\alpha_y K^e_{7,1} & \alpha_y K^e_{7,2} & \alpha_y K^e_{7,3} & \alpha_y K^e_{7,4} & \alpha_y K^e_{7,5} & \alpha_x\alpha_y K^e_{7,6} & \alpha_y K^e_{7,7} & \alpha_y K^e_{7,8} & \alpha_y K^e_{7,9} & \alpha_y K^e_{7,10} \\
\alpha_x K^e_{8,1} & \alpha_y K^e_{8,2} & K^e_{8,3} & K^e_{8,4} & K^e_{8,5} & \alpha_x K^e_{8,6} & \alpha_y K^e_{8,7} & K^e_{8,8} & K^e_{8,9} & K^e_{8,10} \\
\alpha_x K^e_{9,1} & \alpha_y K^e_{9,2} & K^e_{9,3} & K^e_{9,4} & K^e_{9,5} & \alpha_x K^e_{9,6} & \alpha_y K^e_{9,7} & K^e_{9,8} & K^e_{9,9} & K^e_{9,10} \\
\alpha_x K^e_{10,1} & \alpha_y K^e_{10,2} & K^e_{10,3} & K^e_{10,4} & K^e_{10,5} & \alpha_x K^e_{10,6} & \alpha_y K^e_{10,7} & K^e_{10,8} & K^e_{10,9} & K^e_{10,10}
\end{bmatrix}$$

Figure 6.24. *An updated element stiffness matrix with updating parameters*

The OMA results in section 6.3.3 are taken as the reference, and the model updating procedure in section 2.1.6 is adopted. The weighting matrix $\boldsymbol{W}_r$ is set as $1 \times 10^2 \boldsymbol{I}_{12}$ and the regularization parameter λ is set as 1×10^{-1} . The MATLAB function *fmincon* is applied to minimize the objective function.

6.4.3. Model updating results

Table 6.7 lists the natural frequencies and the calculated MAC values before and after the model updating. The natural frequencies which are identified in section 6.3 are taken as the reference. The values in the parentheses are the absolute values of the differences from the OMA results in percent. Based on the model updating results in table 6.7, the following conclusions can be obtained.

(1) After the model updating process, the differences in the natural frequencies for a specific mode become smaller.

(2) After the model updating process, the calculated MAC values are closer to 100%. This indicates that the mode shape vectors which are calculated from the modified reduced-order FE model are more consistent with the mode shape vectors which are identified using the field measurement data from the Typhoon Nanmadol. In such a way, the differences in mode sequence are corrected.

The above conclusions indicate that the modified reduced-order FE model after the model updating process can better represent the dynamics of the first twelve modes of the Canton Tower under typhoon events which are similar to the Typhoon Nanmadol.

Table 6.7. *Model updating results*

Mode	Natural frequency f (Hz)			MAC value (%)	
	Reference	Before updating	After updating	Before updating	After updating
1	0.0919	0.1129 (22.83)	0.0918 (0.09)	91.11	96.96
2	0.1356	0.1610 (18.73)	0.1355 (0.08)	90.62	99.12
3	0.3735	0.3670 (1.73)	0.3727 (0.21)	88.92	97.76
4	0.4640	0.4539 (2.18)	0.4647 (0.16)	90.43	97.07
5	0.4989	0.4777 (4.24)	0.4977 (0.23)	8.16	98.39
6	0.5780	0.5822 (0.73)	0.5817 (0.64)	87.38	96.63
7	0.6017	0.5875 (2.37)	0.5985 (0.53)	85.15	97.82
8	0.8031	0.7449 (7.25)	0.8036 (0.06)	82.22	94.01
9	0.9722	0.9220 (5.16)	0.9729 (0.07)	74.14	96.16
10	1.2132	1.0983 (9.47)	1.2096 (0.30)	18.17	95.98
11	1.2522	1.1628 (7.14)	1.2523 (0.01)	1.52	91.82
12	1.2881	1.2481 (3.10)	1.2921 (0.31)	53.60	95.10
Average		(7.08)	(0.2232)	64.29	96.40

6.5. Algorithm selection

In this practical application, the type of the force which needs to be reconstructed is wind load. For the reconstruction of wind load, table 5.47 suggests different algorithms for different cases with different sensor types. The Canton Tower has been instrumented with an SHM system for in-service monitoring. Table 6.8 lists the sensors which are deployed on the Canton Tower for in-service monitoring. In this section, the algorithm,

which is considered to be suitable for the reconstruction of the wind load, is selected with the help of the sensor information in table 6.8 and the algorithm selection guidance in table 5.47.

In table 6.8, the sensor types which are considered as potential candidates to be used for wind load reconstruction are categorized into the following three groups.

- Displacement sensors: GPS and digital video camera.
- Strain sensors: vibrating wire gauge and fiber optic sensor.
- Acceleration sensors: accelerometer.

In this study, only the accelerometers are selected for the reconstruction of the wind load. The arguments are given below.

In the algorithm selection guidance in table 5.47, the suggested algorithms all require that the total number of strain gauges should be larger than or equal to the total number of modes which are considered in the structural model. This requirement applies not only to strain sensors but also to displacement sensors. In table 6.8, there are in total 4 displacement sensors, including 2 GPS sensors and 2 digital video cameras. The modified reduced-order FE model is updated by taking the identified modal parameters of the first 12 modes of the Canton Tower as the reference. The constructed structural model in the modal domain includes the first 12 modes. It can be seen that the total number of the modes which is considered in the structural model is larger than the total number of the displacement sensors.

For measuring the strain responses of the Canton Tower, vibrating wire gauges and fiber optic sensors are applied. The sampling frequency for the vibrating wire gauge is 0.1 Hz. The Nyquist frequency of such a sampling frequency is 0.05 Hz. This is even lower than the identified natural frequency of the 1st mode of the Canton Tower. The sampling frequency of the fiber optic sensor is 50 Hz. The Nyquist frequency of such a sampling frequency is 25 Hz. This is higher than the identified natural frequency of the 12th mode. However, all the fiber optic sensors are installed on the steel lattice outer structure of the Canton Tower. Figure 6.25 provides an example of the installed fiber optic sensors. It is very challenging to identify the relationship between the strain responses at such positions and the modified reduced-order FE model with acceptable accuracy.

The accelerometers are sampled at 50 Hz, the Nyquist frequency of which is much higher than the natural frequency of the 12th mode. The positions of the accelerometers coincide with the nodes in the modified reduced-order FE model. Thus the acceleration responses at the same positions as the accelerometers can be represented by the acceleration of the nodes in the modified reduced-order FE model.

Based on the discussion above, only the accelerometers are selected for this wind load reconstruction study. According to the algorithm selection guidance in table 5.47, both

the SSKF+LSE and the MSSKF+LSE are suitable for the case with only accelerometers, and in this case both algorithms are only capable of reconstructing the dynamic part of the wind load . In this study, the MSSKF+LSE is selected. The covariance matrix of the wind load is estimated with the help of a simulated wind field.

Table 6.8. *Sensors on the Canton Tower for in-service monitoring (Ni et al., 2009)*

No.	Sensor type	No. of sensors	Sampling frequency (Hz)	Monitoring items
1	Weather station	1	1	Temperature
				Humidity
				Air pressure
				Rain
2	Anemometer	2	50	Wind speed
				Wind direction
3	Tiltmeter	2	50	Inclination of tower
4	GPS	2	10	Displacement
5	Vibrating wire gauge	60	1/10	Strain
6	Thermometer	60	1/60	Temperature
7	Digital video camera	2	59	Displacement
8	Seismograph	1	100	Earthquake motion
9	Corrosion sensor	3	once per year	Corrosion
10	Accelerometer	22	50	Acceleration
11	Fiber optic sensor	120	50	Strain
				Temperature

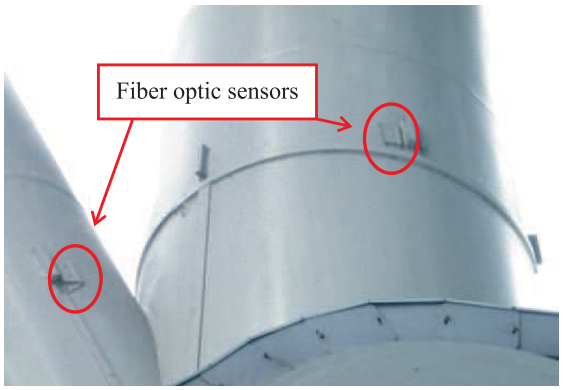

Figure 6.25. *An example of the fiber optic sensors on the steel lattice outer structure*

6.6. Wind load reconstruction for the Canton Tower

In this study, the wind load during the Typhoon Kai-tak is reconstructed. The field measurement data which are applied in the study are

- eight one-hour field measurement datasets which were recorded during the Typhoon Kai-tak from 05:00:00 to 13:00:00 on 17 August 2012.

These field measurement datasets include information on acceleration, wind speed, and wind direction. The wind speed and the wind direction were measured by one RM Young 05103L anemometer which is installed at a height of 461 meters on the Canton Tower. Figure 6.26 provides the 10-minute mean of the measured wind speed and the measured wind direction. The distribution of the measured wind speed and the measured wind direction is presented in the form of a rose diagram in figure 6.27. By comparing figure 6.27 and figure 6.13, it is noticed that the dominant wind direction during the Typhoon Kai-tak is roughly in parallel with the dominant wind direction during the Typhoon Nanmadol. Thus the Typhoon Kai-tak is considered as a similar typhoon event to the Typhoon Nanmadol, and the modified reduced-order FE model which is updated in section 6.4 is used to represent the dynamics of the Canton Tower during the Typhoon Kai-tak.

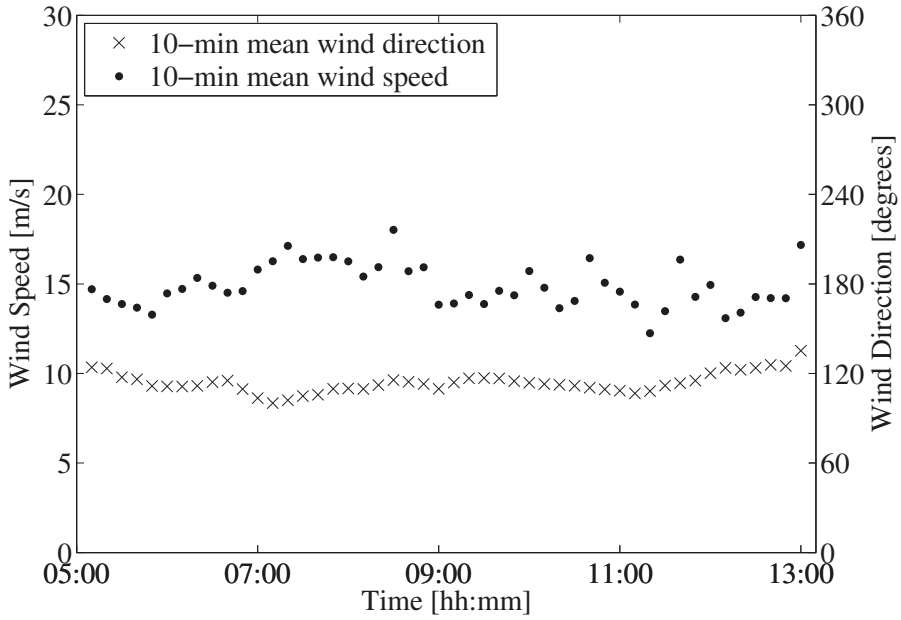

Figure 6.26. *10-minute mean of the measured wind speed and the measured wind direction from 05:00:00 to 13:00:00 on 17 August 2012*

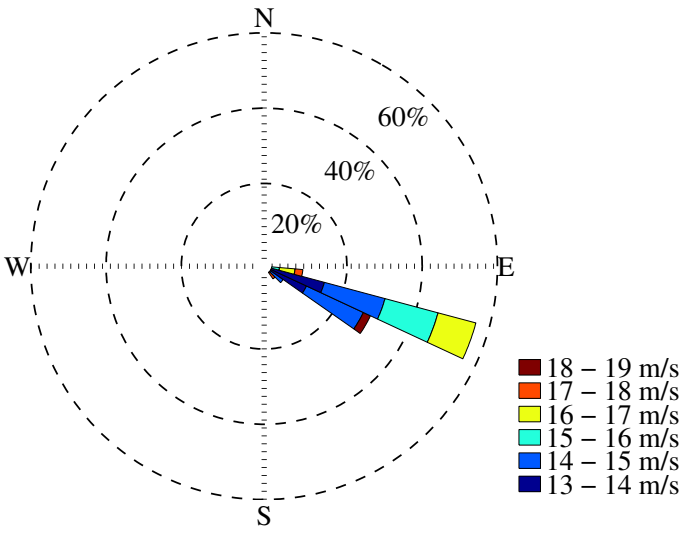

Figure 6.27. *Rose diagram of the wind measurements from 05:00:00 to 13:00:00 on 17 August 2012*

6.6.1. Reconstruction of the wind load

At the height of z meters, the time-varying wind speed $u(z,t)$ can be represented by

$$u(z,t) = \bar{u}(t) + \tilde{u}(z,t), \tag{6.1}$$

where $\bar{u}(z)$ denotes the mean wind speed and $\tilde{u}(z,t)$ represents the fluctuating wind speed. According to Simiu and Scanlan (1996), the time-varying wind load $f(z,t)$ at the height of z meters can be calculated with

$$f(z,t) = \frac{1}{2}\rho\mu a_w u^2(z,t), \tag{6.2}$$

where ρ, μ and a_w denote the air density, the aerodynamic force coefficient, and the orthogonal exposed wind area for the considered section, respectively. By substituting equation (6.1) into equation (6.2), the time-varying wind load $f(z,t)$ can be expressed by

$$f(z,t) = \bar{f}(z) + \tilde{f}(z,t), \tag{6.3}$$

where $\bar{f}(z)$ can be calculated with

$$\bar{f}(z) = \frac{1}{2}\rho\mu a_w(z)\left\{\bar{u}^2(z) + E\left[\tilde{u}^2(z,t)\right]\right\} \tag{6.4}$$

and $\tilde{f}(z,t)$is represented as

$$\tilde{f}(z,t) = \rho\mu a_w(z)\,\bar{u}(z)\,\tilde{u}(z,t) + \frac{1}{2}\rho\mu a_w(z)\left\{\tilde{u}^2(z,t) - E\left[\tilde{u}^2(z,t)\right]\right\}. \tag{6.5}$$

Table 6.9. *Parameter settings for the calculation of the mean wind speeds at different heights*

Terrain category	Gradient height z_g (m)	Exponent α	Air density ρ (kg/m^3)
C	400	0.22	1.225

According to equation (6.3) through equation (6.5), the wind load $f(z,t)$ is composed of two components, the mean wind load $\bar{f}(z)$ and the fluctuating wind load $\tilde{f}(z,t)$.

In this study, the mean wind load is calculated with the help of the wind speed measurements and the aerodynamic force coefficients which are identified from a wind tunnel test. The fluctuating wind load is reconstructed by using the methodology in figure 6.7.

6.6.1.1. Reconstruction of mean wind load

In addition to equation (6.4), the mean wind load can also be calculated with

$$\bar{f}(z,t) = \frac{1}{2}\rho\bar{\mu}_{WT}a_w(z)\,\bar{u}^2(z)\,, \tag{6.6}$$

where $\bar{\mu}_{WT}$ denotes the mean aerodynamic force coefficient. In this study, the mean aerodynamic force coefficients are identified through the wind tunnel test which is described in Gu et al. (2006) and Zhou et al. (2010).

According to Simiu and Scanlan (1996), the mean wind speed at a given height follows the power law

$$\bar{u}(z) = \bar{u}_g\left(\frac{z}{z_g}\right)^{\alpha}, \tag{6.7}$$

where z_g denotes the gradient height and $\bar{u}_g$ represents the mean wind speed at the height of z_g meters. In this study, the mean wind speed at the height of 461 meters is calculated with the wind speed measurements. Then the wind speeds at other heights can be calculated with equation (6.7) and the parameters in table 6.9 where the terrain catgory, the gradient height z_g, and the exponent α are set according to the Building Structure Design Code of China (GB50009-2001, 2006).

According to table 6.6, the vertical coordinates of the nodes 3 to 36 all have positive values. This means nodes 3 to 36 are all above the ground, and are under the effect of the wind load. The orthogonal exposed area a_w in equation (6.6) is calculated according to the dimension of the Canton Tower. With equation (6.6), the mean wind load in x direction, the mean wind load in y direction, and the mean moment around z direction are calculated for each element of the updated modified reduced-order FE model. For each element, the calculated mean wind load is evenly divided and concentrated to the connecting nodes of the element. Figure 6.28 through figure 6.30 present the reconstructed mean wind load at the nodes of the modified reduced-order FEM. In table 6.6, the tower section between 200

meters and 350 meters has sparse nodes. This leads to relative larger orthogonal exposed area values and in turn causes relative larger mean wind load (moment) in figure 6.28, figure 6.29, and figure 6.30.

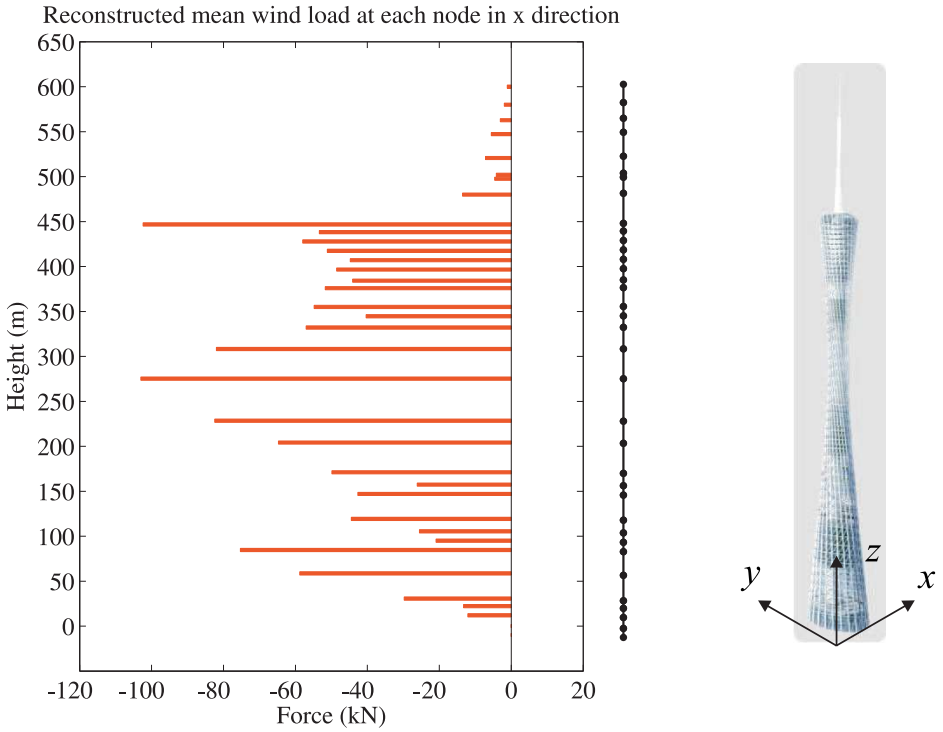

Figure 6.28. *Reconstructed mean wind load at each node in x direction*

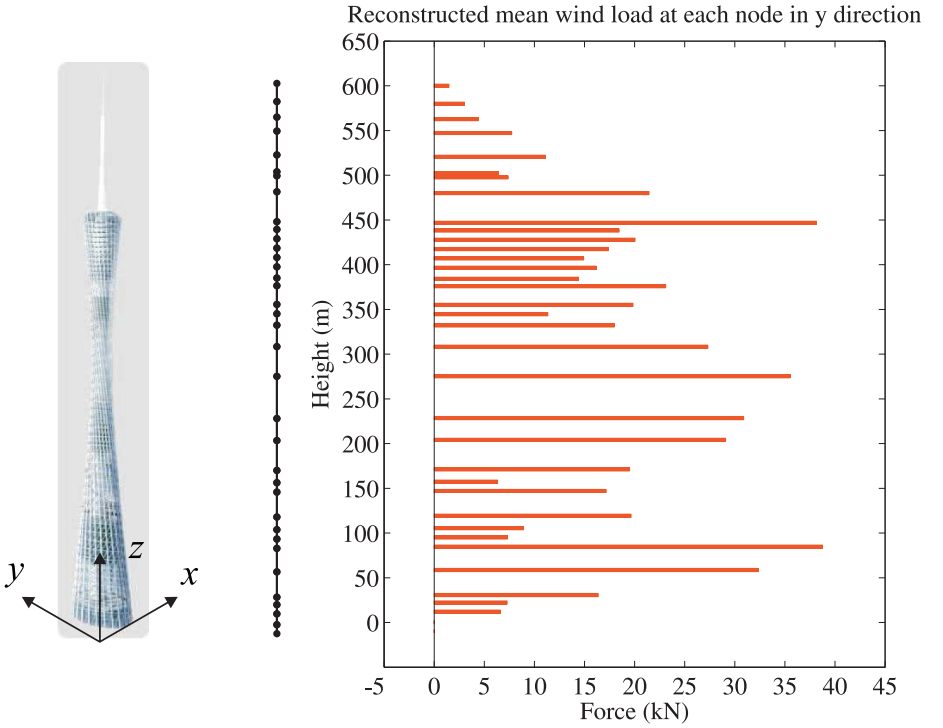

Figure 6.29. *Reconstructed mean wind load at each node in y direction*

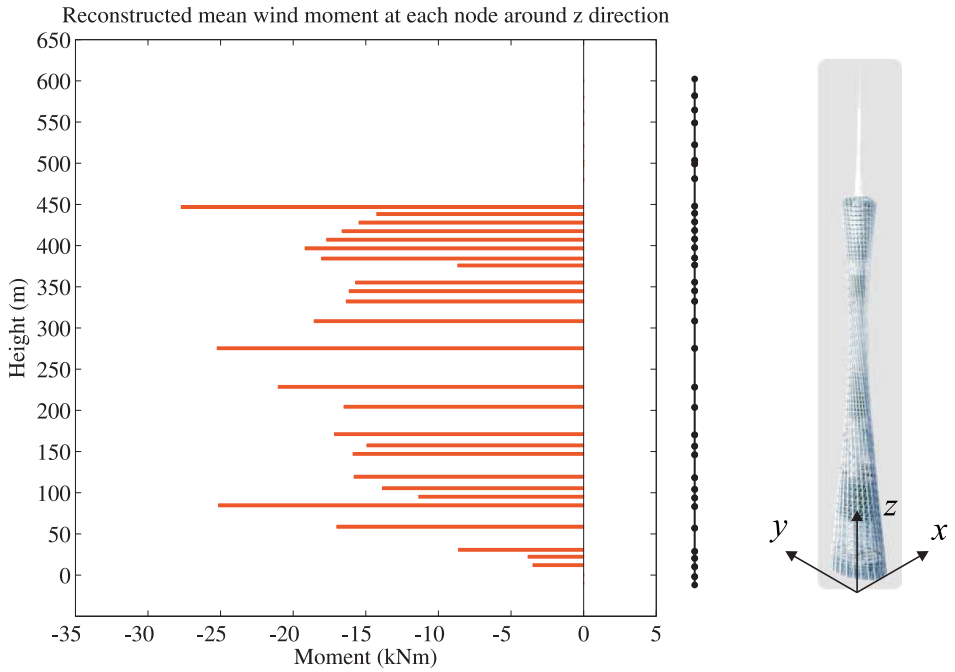

Figure 6.30. *Reconstructed mean wind moment at each node around z direction*

6.6.1.2. Reconstruction of the fluctuating wind load

The fluctuating wind load is reconstructed by applying the methodology in figure 6.7. The modified reduced-order FE model is updated by taking the modal properties, which have been identified in section 6.3, as the reference. Following the steps in section 2.1.1, a second-order structural model in the modal domain is constructed, where the first 12 modes of the Canton Tower are included. The matrix $\boldsymbol{B}_o$, which describes the spatial distribution of the input forces, are set according the methodology in section 3.6. According to the discussion in section 6.5, the MSSKF+LSE is selected for the reconstruction of the fluctuating wind load. This algorithm requires that the total number of the accelerometers should be larger than or equal to the total number of the modes which are included in the structural model. In this study, in total 12 accelerometers are selected for the reconstruction of the fluctuating wind load. In figure 6.31 the accelerometers whose channel numbers are in green are selected for the wind load reconstruction. The accelerometers whose channel numbers are in red are not used for the reconstruction of the fluctuating wind load but only for the validation purpose. With the sensors being selected, a state-space structural model of the Canton Tower is constructed. Table 6.10 lists the dimension of this state-space structural model.

With the wind speed measurements which were recorded by an anemometer at the height of 461 meters on the Canton Tower, a wind velocity field is simulated by using the algorithm in Ding et al. (2006). With the simulated wind velocity, an estimate of the matrix $\boldsymbol{Q}_{input}$ is obtained. The matrix $\boldsymbol{Q}_{input}$ is the covariance matrix of the fluctuating wind load at different nodes of the updated modified reduced-order FE model. The matrix

$\boldsymbol{Q}_{meas}$, which is the covariance matrix of the measurement noise, is set as $10^{-8}I_{12}$.

Wind load is a type of distributed force, and the spatial distribution of the fluctuating wind load is unknown. In this study, the columns of the force input matrix $\boldsymbol{B}_o$ include the mode shape vectors of the first 12 modes of the Canton Tower. After applying the MSSKF+LSE, the fluctuating wind load at node 3 through node 36 are reconstructed. The boxplots in figure 6.32 through figure 6.34 show the distribution of the reconstructed fluctuating wind load. For each node, the black dot inside the white circle represents the median, the left and right edges of the narrow filled blue box indicate the 25th and the 75th percentiles, and the blue circles denote outliers which are either less than 1.5 interquartile range of the 25th percentile or larger than 1.5 interquartile range of the 75th percentile.

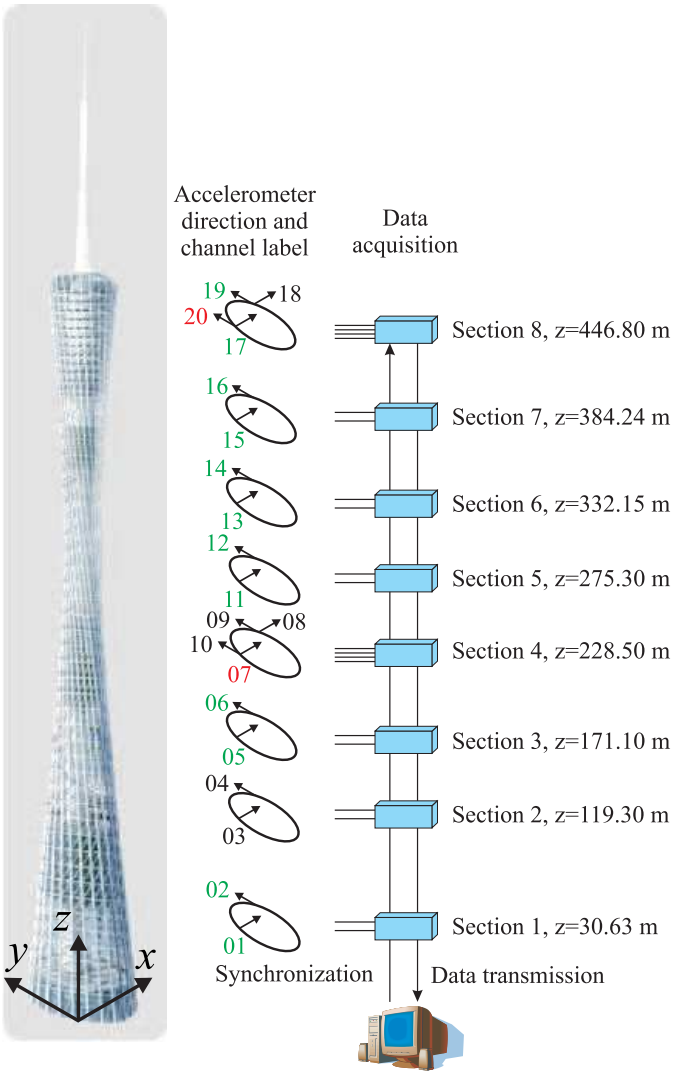

Figure 6.31. *Positions of accelerometers for the reconstruction of the fluctuating wind load (with green channel number) and positions of accelerometers for the validation of the reconstruction results (with red channel number)*

Table 6.10. *Dimension of the state, the input, and the output of the state-space model of the Canton Tower*

Name	Symbol	Dimension
State	$\boldsymbol{x}(t)$	24×1
Input	$\boldsymbol{d}(t)$	12×1
Output	$\boldsymbol{y}(t)$	12×1

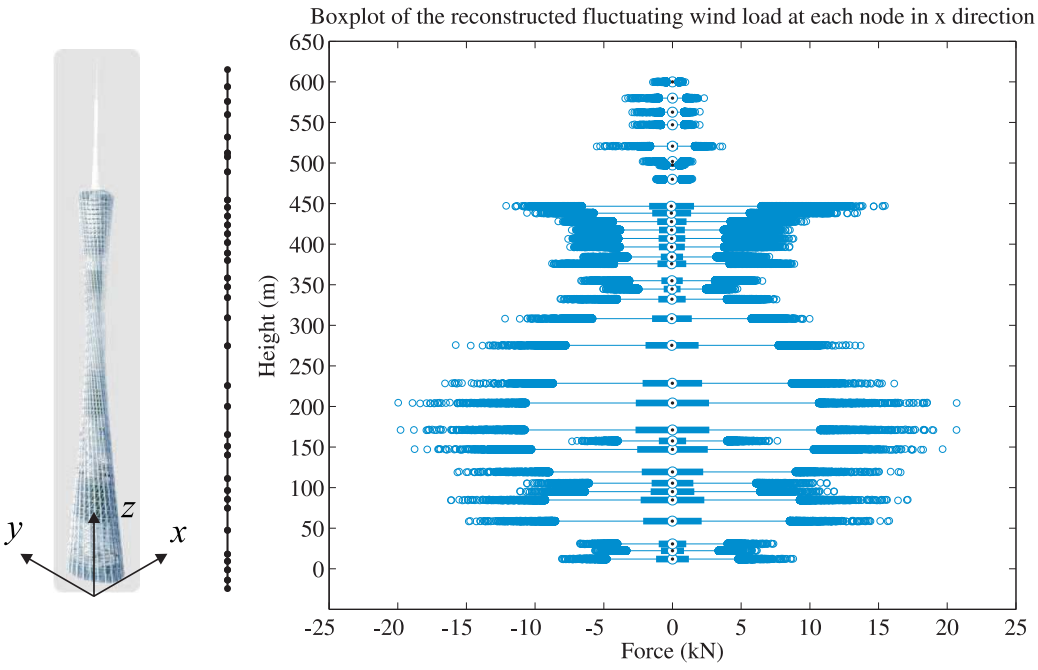

Figure 6.32. *Boxplot of the reconstructed fluctuating wind load at each node in x direction*

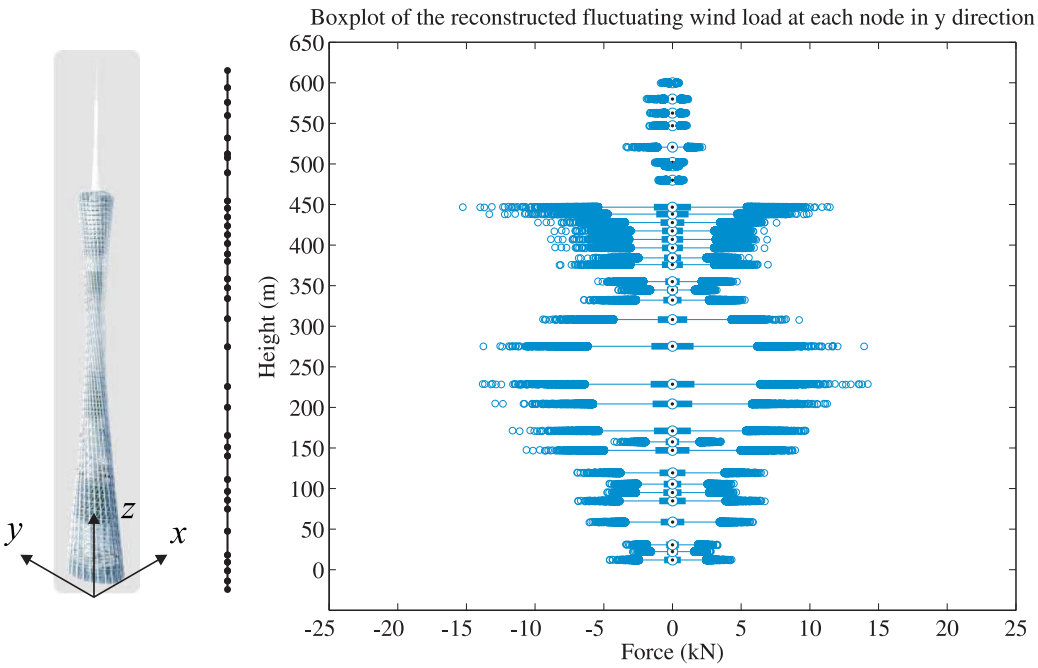

Figure 6.33. *Boxplot of the reconstructed fluctuating wind load at each node in y direction*

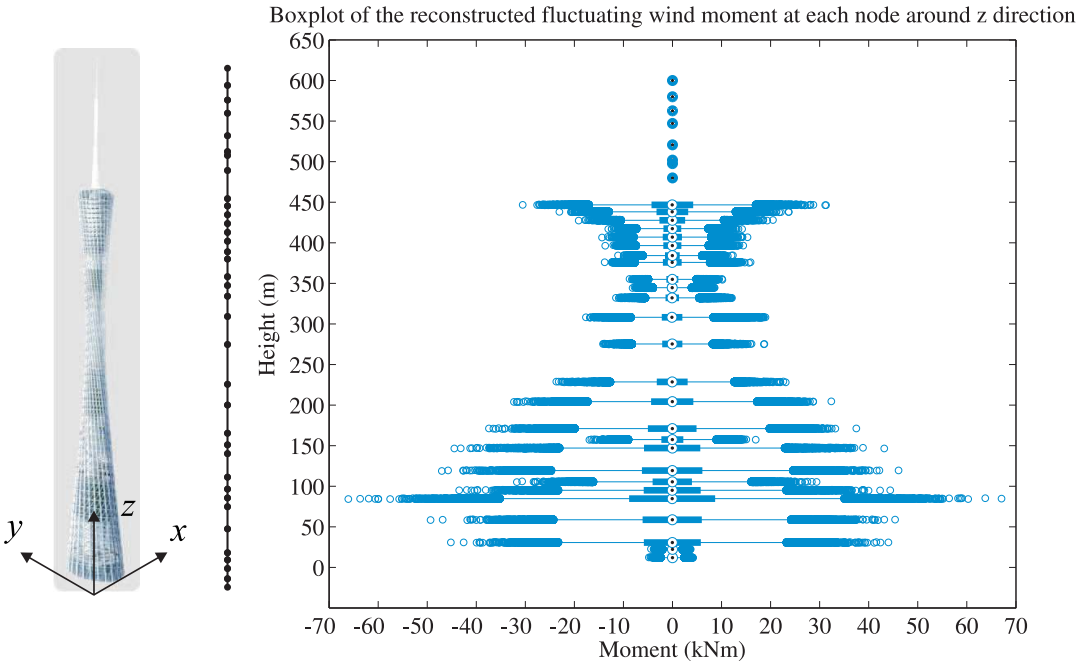

Figure 6.34. *Boxplot of the reconstructed fluctuating wind moment at each node around z direction*

6.6.2. Validation of the reconstructed fluctuating wind load

For the laboratory structure in section 5.2, the reconstructed force can be validated by the force measurements. However, it is not the case for the Canton Tower. There is no direct measurements of the fluctuating wind load. In this study, the following procedure is adopted for the validation of the reconstructed fluctuating wind load.

(1) Apply the reconstructed fluctuating wind load to the structural model to reconstruct the acceleration response of the Canton Tower at the accelerometer channel 7 and the accelerometer channel 20. The data from these two accelerometer channels are not applied for the reconstruction of the fluctuating wind load but only for the validation purpose.

(2) For the accelerometer channel 7 and the accelerometer channel 20, compare the reconstructed acceleration with the real measurements. If the reconstructed acceleration fit the real measurements, the reconstructed fluctuating wind load can be considered as acceptable.

Figure 6.35 provides a comparison of the reconstructed acceleration and the real measurements for the accelerometer channel 7. Figure 6.36 provides a comparison of the reconstructed acceleration and the real measurements for the accelerometer channel 20. In figure 6.35 and figure 6.36, the reconstructed acceleration fit the measured acceleration in both the time domain and the frequency domain. This actually indirectly demonstrates that the reconstructed fluctuating wind load is acceptable.

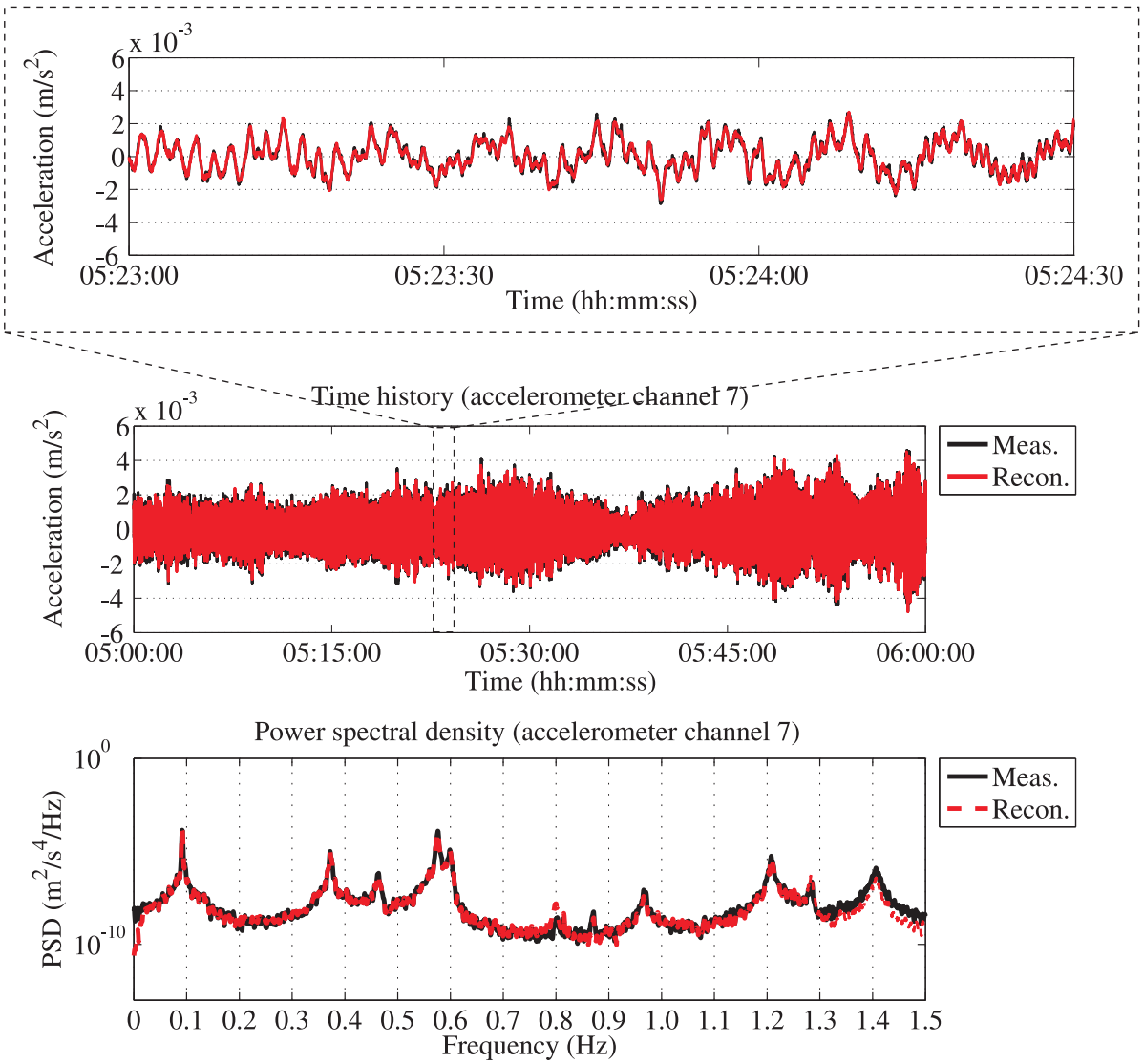

Figure 6.35. *Measured and reconstructed acceleration in accelerometer channel 7*

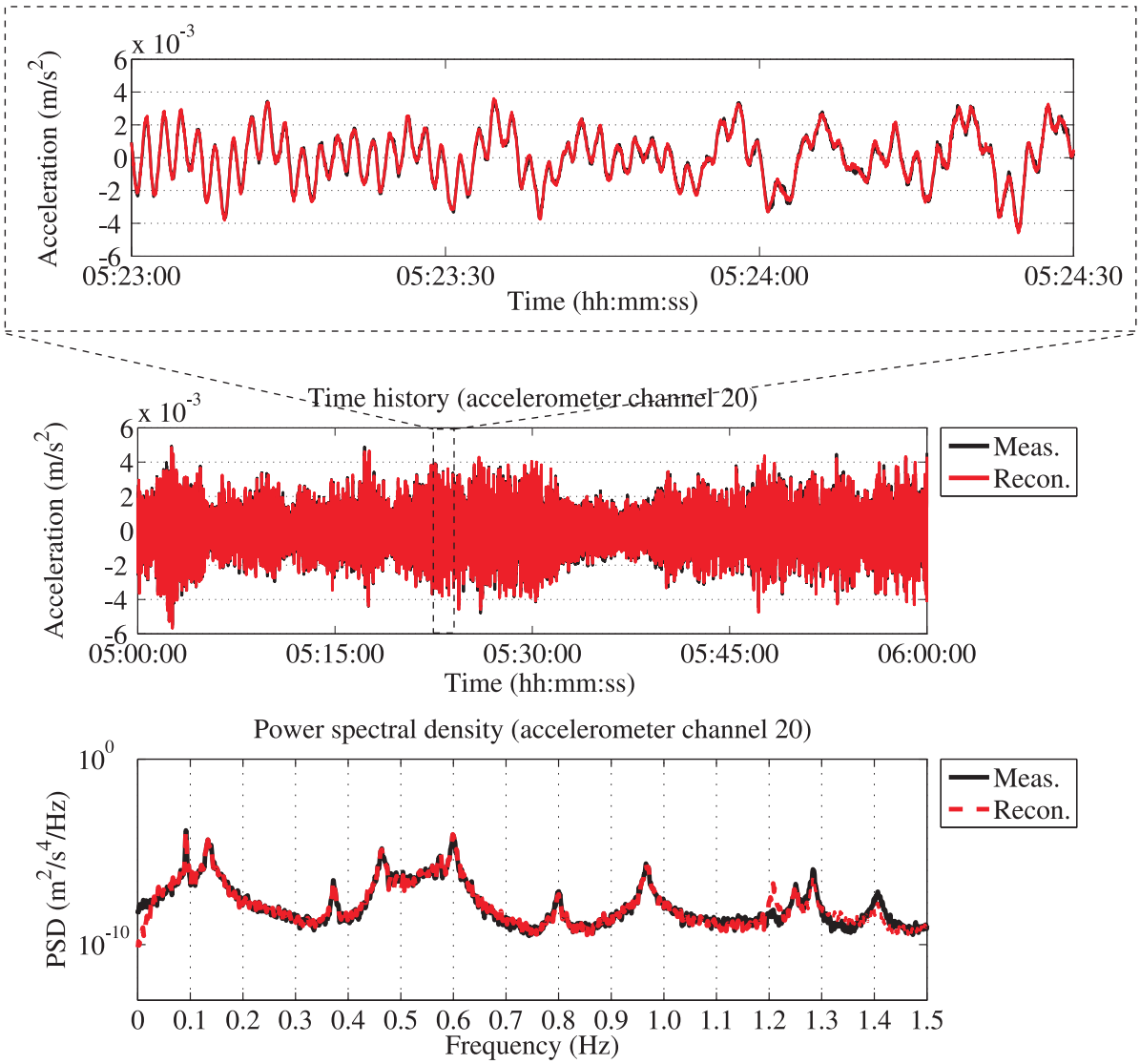

Figure 6.36. *Measured and reconstructed acceleration in accelerometer channel 20*

6.7. Summary

The 600 meter tall Canton Tower is located in a typhoon active area, and has been instrumented with a long-term SHM system for in-service monitoring. These factors make this high-rise structure an ideal test bed for the study of online wind load reconstruction. In this chapter, the online force reconstruction methodology in figure 3.5 is applied to the Canton Tower for the reconstruction of the wind load. The field measurements from the following two typhoon events are analyzed in this study.

- Typhoon Nanmadol in 2011.
- Typhoon Kai-tak in 2012.

The two typhoon events above both happened in August and both have the dominant wind direction in parallel with each other.

With the field measurements from the Typhoon Nanmadol in 2011, an Operational Modal Analysis (OMA) is performed and the modal properties of the first 12 modes of the Canton Tower are identified using the ARV method. These modal properties, including natural frequencies, damping ratios, and mode shapes, are used to construct the second-order structural model which can represent represent the dynamics of the Canton Tower under the excitation of the Typhoon Nanmadol.

On the benchmark website for the Canton Tower, a reduced-order FE model of the Canton Tower is provided. In this study, this reduced-order FEM is first modified to reflect the height adjustment of the Canton Tower, and then is updated by taking the identified modal properties as the reference.

The SHM system for the Canton Tower includes different types of sensors. Considering different factors, including sensor type, sensor number, sensor position, sampling frequency, only the accelerometers on the main tower are selected to be used in the wind load reconstruction study. According to the algorithm selection guidance in table 5.47, both the SSKF+LSE and the MSSKF+LSE are potential condidates to be used for the reconstruction of the wind load. In this study, a wind velocity field is simulated with the available wind speed measurements. With the simulated wind velocity at different heights, an estimate of the covariance matrix of the wind load is obtained. According to the results from the benchmark study, the MSSKF+LSE, with an estimate of the covariance matrix of the force, can provide better reconstruction results than the SSKF+LSE. Thus, the MSSKF+LSE is selected for this wind load reconstruction study.

The wind load is composed of two components, the mean wind load and the fluctuating wind load. According to the results in section 5.2.9, the MSSKF+LSE is only capable of reconstructing the fluctuating wind load, if only accelerometers are used. In this study, the wind load during the Typhoon Kai-tak is reconstructed and the reconstruction results are presented. The mean wind load is calculated with the mean wind speeds and the mean

aerodynamic force coefficients which are identified from a wind tunnel test. The fluctuating wind load is reconstructed with the MSSKF+LSE algorithm and the acceleration measurements which were recorded during the Typhoon Kai-tak.

To validate the reconstruction results, the reconstructed fluctuating wind load is applied back onto the structural model, and the acceleration responses of the Canton Tower are reconstructed. The validation strategy is to compare the reconstructed acceleration responses with the real acceleration measurements which are not applied for the wind load reconstruction. In this study, two accelerometer channels, i.e. channel 7 and channel 20, are selected for the validation purpose. The acceleration measurements from these two accelerometers are not applied in the reconstruction of the fluctuating wind load. The reconstructed acceleration responses for these two accelerometer channels are compared with the real acceleration measurements in the form of time history and power spectral density. The comparison results show the reconstructed acceleration data fit the real acceleration measurements with acceptable accuracy. Based on this comparison results, it can be concluded that the reconstruction results for the fluctuating wind load is acceptable.

7. Summary and outlook

The knowledge of the external load acting on a structure plays a very important role in Structural Heath Monitoring (SHM) and in Damage Prognosis (DP). In some practical cases, a direct measurement of the external load is physically or economically not feasible. For such practical cases, a possible solution is to get the information of the external load by reconstructing it from the measured structural responses, e.g. displacement, strain, velocity, acceleration, etc. This process is defined as force reconstruction, and it is a type of inverse problem which tends to be ill-posed in the sense that the measurement noise and the modelling error can be amplified and in turn cause large deviations in the reconstructed force. Online force reconstruction is the research topic which studies the methods which can relax the ill-posedness in the force reconstruction process and can realize the force reconstruction in real-time. This thesis focuses on the online force reconstruction. A summary of the work in this thesis is provided in section 7.1. In section 7.2, some open topics are described. From the author's point of view, these open topics can be considered as the extension of the work in this thesis.

7.1. Summary

Online force reconstruction needs to solve the following two problems.

(1) How to relax the ill-posedness in the process of force reconstruction?

(2) How to realize force reconstruction in real-time?

To solve the two problems above, this thesis applies a methodology which needs a real-time executable state and input estimation algorithm. This algorithm fulfills the following three requirements.

(a) The system input (i.e. the excitation force) and the system states (i.e. displacement vector in the modal coordinates and its first derivative) should be able to be inferred from the system output (i.e. structural response measurements).

(b) The state estimator and input estimator should be stable.

(c) The estimation error of the excitation force should converge ideally to zero.

By fulfilling the three requirements above, the ill-posedness in the process of force reconstruction can be relaxed. Meanwhile, the "real-time executable" ability of the algorithm makes the force reconstruction "online".

The methodology for online force reconstruction is composed of two stages, an offline stage and an online stage. In the offline stage, a state-space model of the structure is

constructed. If it is possible to apply an artificial excitation force on the structure, the modal properties (i.e. natural frequencies, damping ratios, and mode shapes) of the structure are identified using the Experimental Modal Analysis (EMA) technique. In case it is difficult or not possible to apply an artificial excitation force on the structure, the modal properties of the structure can be identified with the help of the Operational Modal Analysis (OMA) technique. In this case, a Finite Element Model (FEM) of the structure is needed to correctly scale the identified mode shapes. Once the modal properties of the structure are available, a state-space structural model in the modal domain can be constructed. In the online stage, a real-time executable state and input estimation algorithm is applied to provide an estimate of the force. The ill-posedness in the process of force reconstruction is relaxed through the convergence of the force estimate error. Together with the reconstructed force, this methodology is also capable of reconstructing the structural response.

Besides the algorithms which have been proposed or applied in earlier online force reconstruction studies, there are also some real-time executable state and input estimation algorithms which were proposed for applications in other fields, e.g. inverse heat conduction, fault detection, robot control, etc. All these available algorithms are potential candidates to be the algorithm for online force reconstruction. As theoretical foundations for the discussion in this thesis, a brief review of these available algorithms is given in the beginning of this thesis.

To be sure that the applied algorithm is theoretically suitable for online force reconstruction, the following modifications to some of the available algorithms are proposed in this thesis.

- The structural models are often linear. Considering this, the Simultaneous State and Input Estimation for a class of Nonlinear systems (SS&IE_N), which was proposed in Ha and Trinh (2004), is modified to be suitable for linear systems. To differentiate with the SS&IE_N, this modified algorithm is named as SS&IE_L , short for Simultaneous State and Input Estimation for Linear systems.
- The filter equations in the KF-UI, which was proposed in Pan et al. (2011), have been proven to be equivalent with the filter equations of the RTSF, which was proposed in Gillijns and De Moor (2007). The necessary and sufficient conditions of the KF-UI algorithm is updated. The KF-UI algorithm assumes that the process noise and the measurement noise are uncorrelated, and requires that acceleration response has to be considered in the output equation of the state-space structural model. However, it is proved that the consideration of acceleration response indicates that the process noise and the measurement noise are correlated. This contradicts with the assumption of the KF-UI. In this thesis, the KF-UI is generalized so that it is compatible with the correlation of the process noise and the measurement noise. This generalized KF-UI is named as G-KF-UI.

- Hwang et al. (2009a) proposed a Steady-State Kalman Filter with a Least-Squares Estimator (SSKF+LSE) for the estimation of modal loads. In the SSKF+LSE, the covariance matrix of the forces is assumed to be an identity matrix. Such a setting means the forces all have the same variance and are uncorrelated. In some practical case, e.g. wind load, it is not the case. In this thesis, it is suggested, if possible, to consider an estimate of the covariance of the forces. To differentiate with the SSKF+LSE, this proposed modification is named as MSSKF+LSE, short for modified SSKF+LSE.

In case there is a practical need for online force reconstruction, it is reasonable to raise the following questions.

(i) Which algorithms are suitable for the reconstruction of the force?

(ii) If the structure under investigation has already been instrumented with some sensors for some other monitoring purposes, can the force be reconstructed with the available sensors?

To answer the questions above, a benchmark study is performed. A two-story laboratory structure is taken as the benchmark structure, on which two types of widely used sensors are installed, including strain gauge and accelerometer. Three different types of input forces are considered, including quasi-static force, impact force, and wind load generated by an electric fan. The above illustrated methodology is applied. In the offline stage, the structural model of the benchmark structure is identified with the help of the EMA technique. In the online stage, in total eight different algorithms are tested. The force reconstruction results are validated by real force measurements. Based on the results from the benchmark study, a guidance for algorithm selection is extracted and presented.

As an example of practical application, the above illustrated online force reconstruction methodology is applied to the 600 meter tall Canton Tower for the reconstruction of wind load. The Canton Tower is located in a typhoon active area, and has been instrumented with a long-term SHM system for in-service monitoring. These two factors make this high-rise structure an ideal test bed. The field measurements from the following two typhoon events are analyzed.

- Typhoon Nanmadol in 2011.
- Typhoon Kai-tak in 2012.

In the offline stage, the structural model of the Canton Tower is constructed with the help of the OMA technique and the available reduced-order FEM of the Canton Tower. The Typhoon Nanmadol and the Typhoon Kai-tak happened both in August and have the dominant wind direction in parallel with each other. Thus it is assumed that the modal properties which are identified using field measurements from the Typhoon Nanmadol can also be used to represent the dynamics of the Canton Tower under the excitation of the Typhoon Kai-tak. With the field measurements from the Typhoon Nanmadol in 2011,

the modal properties of the Canton Tower are identified using the ARV method. The reduced-order FEM of the Canton Tower is first modified to reflect the height adjustment of the Canton Tower, and then is updated by taking the identified modal properties as the reference. In the SHM system for the Canton Tower, different types of sensors have been applied. Through an evaluation of these available sensors from different aspects, e.g. sensor type, sensor number, sensor position, sampling frequency, etc., only the accelerometers on the main tower are selected for the reconstruction of the wind load. With the help of the proposed guidance for algorithm selection, the MSSKF+LSE is selected for the use in the online stage. In this study, the covariance matrix of the wind load is estimated with the help of a simulated wind velocity field. The wind load is composed of two components, the mean wind load and the fluctuating wind load. In this study, the field measurement which were recorded during the Typhoon Kai-kai are applied, and the wind load reconstruction results are presented. The mean wind load is calculated with the mean wind speeds and the mean aerodynamic force coefficients which are identified from a wind tunnel test. The fluctuating wind load is reconstructed with the MSSKF+LSE algorithm and the acceleration measurements which were recorded during the Typhoon Kai-tak. Different from the case in the benchmark study, there is no direct measurement of the wind load. So it is not possible to compare the reconstructed wind load with real wind load measurements. To validate the reconstruction results, the reconstructed fluctuating wind load is applied back to the structural model, and the acceleration responses of the Canton Tower are reconstructed. The validation strategy is to select some acceleration channels which are not applied for the wind load reconstruction, and compare the reconstructed acceleration responses with the real acceleration measurements. The comparison results show that the reconstructed acceleration data fit the real acceleration measurements with acceptable accuracy. Based on this comparison results, it can be concluded that the reconstruction results for the fluctuating wind load is acceptable.

7.2. Outlook

It is already known that the modal properties of a structure is affected by environmental conditions, e.g. Niu et al. (2012) noticed that the natural frequencies of the Canton Tower changes as the temperature changes. Furthremore, the geometry of some structures is not fixed but changes with time, e.g. wind turbines. To make the methodology for online force reconstruction more robust, a model bank can be constructed instead of a single model in the offline stage of the methodology. Each structural model in the model bank corresponds to a specific Environmental and Operational Condition (EOC). According to the real measurements of the EOC in the online stage, the suitable structural model can be selected for online force reconstruction. Figure 7.1 provides the block diagram of this extended methodology. This methodology has been applied in a simulation study for the

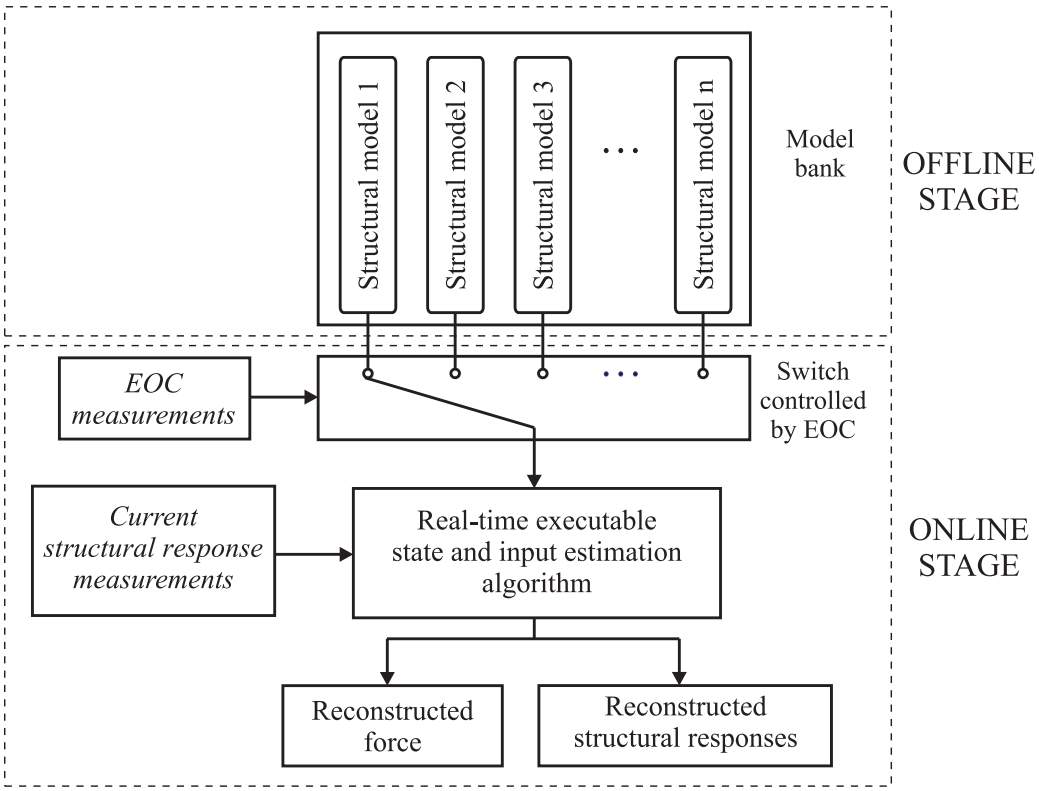

Figure 7.1. *Block diagram of the methodology for online force reconstruction with EOC consideration*

reconstruction of wind load on a rotating wind turbine (Ginsberg et al., 2013).

The knowledge of the history of external load on a structure allows the update of earlier lifetime prediction of the structure (Fritzen et al., 2013). So another interesting topic is to combine online force reconstruction with the prediction of the remaining service life of the structure. This is also in accordance with the block diagram in figure 1.1

Bibliography

Arnold, W. F. and Laub, A. J. (1984). Generalized eigenproblem algorithms and software for algebraic Riccati equations. In *Proceedings of the IEEE*, volume 72, pages 1746–1754.

Avitabile, P. (2001). Experimental modal analysis a simple non-mathematical presentation. *Journal of Sound and Vibration*, 35(1):25–31.

Balageas, D. (2006). Introduction to structural health monitoring. In Balageas, D., Fritzen, C.-P., and Güemes, A., editors, *Structural Health Monitoring*. ISTE Ltd.

Berg, J. and Miller, K. (2010). Force estimation via Kalman filtering for wind turbine blade control. In *Proceedings of the IMAC-XXVIII*.

Brown, R. G. and Hwang, P. Y. (1997). *Introduction to Random Signals and Applied Kalman Filtering: with MATLAB Exercises and Solutions*. John Wiley & Sons, Inc.

Chen, T.-C. and Lee, M.-H. (2008). Research on moving force estimation of the bridge structure using the adaptive input estimation method. *Electronic Journal of Structural Engineering*, 8:20–28.

Chung, T. T., Cho, S., Yun, C. B., and Sohn, H. (2012). Finite element model updating of Canton tower using regularization technique. *Smart Structures and Systems*, 10(4-5):459–470.

Clough, R. W. and Penzien, J. (2003). *Dynamics of Structures*. Computers & Structures, Inc.

Darouach, M. (2009). Complements to full order observer design for linear systems with unknown inputs. *Applied Mathematics Letters*, 22(7):1107–1111.

Darouach, M., Zasadzinski, M., and Xu, S. (1994). Full-order observers for linear systems with unknown inputs. *IEEE Transactions on Automat*, 39:606–609.

Dascotte, E. (2007). Model updating for structural dynamics: past, present and future outlook. In *Proceedings of International Conference on Engineering Dynamics (ICED)*.

De Silva, C. W. (2007). *Vibration: Fundamentals and Practice*. CRC, Taylor & Francis, Boca Raton.

Deng, S. and Heh, T.-Y. (2006). The study of structural system dynamic problems by recursive estimation method. *The International Journal of Advanced Manufacturing Technology*, 30:195–202.

Dettmann, K.-U. and Söffker, D. (2011). Adaptive modeling of reliability properties for control and supervision purposes. *International Journal of Applied Mathematics and Computer Science*, 21(3):479–486.

Ding, Q., Zhu, L., and Xiang, H. (2006). Simulation of stationary gaussian stochastic wind velocity field. *Wind and Structures*, 9(3):231–243.

Engl, H. W., Hanke, M., and Neubauer, A. (1996). *Regularization of Inverse Problems*. Mathematics and Its Applications. Kluwer Academic Publishers.

Farrar, C., Sohn, H., Hemez, F., Anderson, M., Bement, M., Corwell, P., Doebling, S., Schultze, J., Lieven, N., and Robertson, A. (2003). Damage prognosis: Current status and future needs. Technical report, Los Alamos National Laboratory, Los Alamos, NM, USA.

Farrar, C. R. and Lieven, N. A. (2007). Damage prognosis: The future of structural health monitoring. *Philosophical Transactions of The Royal Society A*, 365:623–632.

Farrar, C. R., Lieven, N. A., and Bement, M. T. (2005). An introduction to damage prognosis. In Inman, D. J., Farrar, C., Junior, V., and Junior, V., editors, *Damage Prognosis for Aerospace, Civil and Mechanical Systems*, pages 1–12. John Wiley & Sons Ltd.

Farrar, C. R. and Worden, K. (2007). An introduction to structural health monitoring. *Philosophical Transactions of The Royal Society A*, 356:303–315.

Franklin, G. F., Powell, J. D., and Emami-Naeini, A. (2006). *Feedback Control of Dynamic Systems*. Pearson Prentice Hall, Upper Saddle River, New Jersey.

Fritzen, C.-P. (2006). Vibration-based techniques for structural health monitoring. In Balageas, D., Fritzen, C.-P., and Güemes, A., editors, *Structural Health Monitoring*. ISTE Ltd.

Fritzen, C.-P., Klinkov, M., and Krämer, P. (2013). Vibration-based damage diagnosis and monitoring of external loads. In Ostachowicz, W. and Güemes, A., editors, *New Trends in Structural Health Monitoring*, pages 149–208. Springer.

Gawronski, W. K. (2004). *Advanced Structural Dynamics and Active Control of Structures*. Mechanical Engineering Series. Springer-Verlag, New York.

GB50009-2001 (2006). *Load Code for the Design of Building Structures*. National Standard of the People's Republic of China.

Gillijns, S. and De Moor, B. (2007). Unbiased minimum-variance input and state estimation for linear discrete-time systems with direct feedthrough. *Automatica*, 43:934–937.

Ginsberg, D., Niu, Y., and Fritzen, C.-P. (2013). Online wind load reconstruction for a wind energy plant using simulated structural responses. In *The 6th International Conference on Structural Health Monitoring of Intelligent Infrastructure*, Hong Kong, China.

Gu, M., Huang, P., Zhou, X., and Zhu, L. (2006). Wind tunnel test on sectional models and analysis of wind induced vibration of the guangzhou new tv tower. Research report, Tongji University.

Guillaume, P., Verboven, P., Vanlanduit, S., Auweraer, H. V. d., and Peeters, B. (2003). A poly-reference implementation of the least-squares complex frequency-domain estimator. In *The International Modal Analysis Conference (IMAC 21)*, Kissimmee, FL., USA.

Guo, Y., Kareem, A., Ni, Y., and Liao, W. (2012). Performance evaluation of Canton tower under winds based on full-scale data. *Journal of Wind Engineering and Industrial Aerodynamics*, 104-106:116–128.

Ha, Q. and Trinh, H. (2004). State and input simultaneous estimation for a class of nonlinear systems. *Automatica*, 40:1779–1785.

Hadamard, J. (1902). Sur les problemes aux dérivées partielles et leur signification physique. *Princeton University Bulletin*, 13:49–52.

Hadamard, J. (1923). *Lectures on Cauchy's Problem in Linear Partial Differential Equations*. Yale University Press.

Hansen, P. (1998). *Rank-deficient and discrete ill-posed problems: numerical aspects of linear inversion*. Society for Industrial and Applied Mathematics.

Hansen, P. C. (1988). Computation of the singular value expansion. *Computing*, 40:185–199.

Hsieh, C.-S. (2009). Extension of unbiased minimum-variance input and state estimation for systems with unknown inputs. *Automatica*, 45:2149 – 2153. Printed.

Hsieh, C.-S. (2010). On the optimality of unbiased minimum-variance state estimation for systems with unknown inputs. *Automatica*, 46:708 – 715. Printed.

Hwang, J.-S., Kareem, A., and Kim, H. (2011). Wind load identification using wind tunnel test data by inverse analysis. *Journal of Wind Engineering and Industrial Aerodynamics*, 99:18–26.

Hwang, J.-s., Kareem, A., and Kim, W.-j. (2009a). Estimation of modal loads using structural response. *Journal of Sound and Vibration*, 326(3-5):522–539.

Hwang, J.-S., Lee, S.-G., Ji-hoon, P., and Eun-Jong, Y. (2009b). Force identification from structural responses using kalman filter. *Materials Volume*, 33:257–266.

Inman, D. J., Farrar, C. R., Junior, V. L., and Junior, V. S., editors (2005). *Damage Prognosis: For Aerospace, Civil and Mechanical Systems*. John Wiley & Sons Ltd, Chichester, UK.

Ji, C.-C. and Liang, C. (2000). A study on an estimation method for applied force on the rod. *Computer Methods in Applied Mechanics and Engineering*, 190:1209–1220.

Kalman, R. (1959). On the general theory of control systems. *IRE Transactions on Automatic Control*, 4(3):110–110.

Kalman, R. (1960). A new approach to linear filtering and prediction problems. *Transaction of the ASME - Journal of Basic Engineering,*, 82:35–45.

Kalman, R. and Bucy, R. (1961). New results in linear filtering and prediction theory. *Transactions of ASME - Jounal of Basic Engineering*, 83(1):95–108.

Keller, J. B. (1976). Inverse problems. *American Mathematical Monthly*, 83:107–118.

Klinkov, M. and Fritzen, C.-P. (2006). Online estimation of external loads from dynamic measurements. In *Proceedings of International Conference on Noise and Vibration Engineering (ISMA)*, pages 3957–3968, Leuven, Belgium.

Klinkov, M. and Fritzen, C.-P. (2009). On field wind load reconstruction for a 5mw onshore wind energy plant. In *Proceedings of 7th International Workshop on Structural Health Monitoring*, pages 1613–1620.

Kraemer, P. and Fritzen, C.-P. (2010). Aspects of operational modal analysis for structures of offshore wind energy plants. In *Proceedings of The 28th International Modal Analysis Conference (IMAC XXIX)*, Jacksonville, Florida, USA.

Krajcin, I. and Söffker, D. (2003). Model-based estimation of conctact forces in rotating machines. In *Proceedings of the 4th IMACS Symposium on Mathematical Modeling*.

Krajcin, I. and Söffker, D. (2005). Diagnosis and control of 3D elastic mechanical structures. In *Proceedings of the 12th SPIE Symposium on Smart Structures and Materials*, pages 335–347.

Kress, R. (1989). *Linear Integral Equations*. Applied Mathematical Sciences. Springer Verlag.

Lourens, E.-M., Papadimitriou, C., Gillijns, S., Reynders, E., De Roeck, G., and Lombaert, G. (2012a). Joint input-response estimation for structural systems based on reduced-order models and vibration data from a limited number of sensors. *Mechanical Systems and Signal Processing*, 29:310–327.

Lourens, E.-M., Reynders, E., Roeck, G. D., Degrande, G., and Lombaert, G. (2012b). An augmented Kalman filter for force identification in structural dynamics. *Mechanical Systems and Signal Processing*, 27:446–460.

Luenberger, D. (1964). Observing the state of a linear system. *IEEE Transactions on Military Electronics*, 8(2):74–80.

Luenberger, D. (1971). An introduction to observers. *IEEE Transactions on Automatic Control*, 16(6):596–602.

Ma, C.-K., Chang, J.-M., and Lin, D. (2003). Input forces estimation of beam structures by an inverse method. *Journal of Sound and Vibration*, 259(2):387 – 407.

Ma, C.-K. and Ho, C.-C. (2004). An inverse method for the estimation of input forces acting on non-linear structural systems. *Journal of Sound and Vibration*, 275:953–971.

Maybeck, P. (1979). *Stochastic Models, Estimation, and Control*. Academic Press, Inc.

Müller, I., Vonnieda, K., Das, S., and Chang, F.-K. (2011). A robust impact force determination technique for complex structures. In *International Workshop on Structural Health Monitoring (IWSHM)*, pages 343–353, Stanford, CA, USA.

Mottershead, J., Link, M., and Friswell, M. (2011). The sensitivity method in finite element model updating: A tutorial. *Mechanical Systems and Signal Processing*, 25:2275–2296.

Neumaier, A. and Schneider, T. (2001). Estimation of parameters and eigenmodes of multivariate autoregressive models. *ACM Transactions on Mathematical Software*, 27(1):27–57.

Ni, Y., Xia, Y., Liao, W., and Ko, J. (2009). Technology innovation in developing the structural health monitoring system for Guangzhou new TV tower. *Structural Control and Health Monitoring*, 16:73–98.

Ni, Y., Xia, Y., Lin, W., Chen, W., and Ko, J. (2012). SHM benchmark for high-rise structures: a reduced-order finite element model and field measurement data. *Smart Structures and Systems*, 10(4-5):411–426.

Niu, Y. and Fritzen, C.-P. (2012). Comparison and practical aspects of two approaches for online load reconstruction. In *Proceedings of the 6th European Workshop on Structural Health Monitoring*, pages 651–658, Dresden, Germany.

Niu, Y., Klinkov, M., and Fritzen, C.-P. (2010). Online reconstruction of concentrated and continuously distributed force using a robust observer technique. In Casciati, F. and Giordano, M., editors, *The Fifth European Workshop on Structural Health Monitoring*, pages 994–999, Sorrento, Naples, Italy.

Niu, Y., Klinkov, M., and Fritzen, C.-P. (2011). Online force reconstruction using an Unknown-Input Kalman filter approach. In *The 8th International Conference on Structural Dynamics (EURODYN 2011)*, pages 2569–2576, Leuven, Belgium.

Niu, Y., Kraemer, P., and Fritzen, C.-P. (2012). Operational modal analysis for Canton Tower. *Smart Structures and Systems*, 10(4-5):393–410.

O'Reilly, J. (1983). *Observers for linear systems*. Academic Press.

Pan, S., Su, H., Wang, H., and Chu, J. (2011). The study of joint input and state estimation with Kalman filtering. *Transactions of the Institute of Measurement and Control*, 33(8):901–918.

Pan, S., Su, H., Wang, H., Chu, J., and Lu, R. (2009). Input and state estimation for linear systems: A least squares estimation approach. In *Proceedings of the 7th Asian Control Conference*, pages 378–383, Hong Kong, China.

Peeters, B., Guillaume, P., Auweraer, H. V. d., Cauberghe, B., Verboven, P., and Leuridan, J. (2004). Automotive and aerospace applications of the polymax modal parameter estimation method. In *The International Modal Analysis Conference (IMAC 22)*, Dearborn, MI, USA.

Peeters, B., Leurs, W., Van der Auweraer, H., and Deblauwe, F. (2006). 10 years of industrial operational modal analysis: Evolution in technology and applications. In *Proceedings of the IOMAC Workshop 2006*.

Perisic, N., Pedersen, B., and Kirkegaard, P. (2012). Gearbox fatigue load estimation for condition monitoring of wind turbines. In *Proceedings of International Conference on Noise and Vibration Engineering ISMA2012 : International Conference on Uncertainty in Structural Dynamics*.

Rencher, A. (2002). *Methods of Multivariate Analysis*. John Wiley & Sons, Inc., Canada.

Reynders, E. (2012). System identification methods for (operational) modal analysis: Review and comparison. *Archives of Computational Methods in Engineering*, 19:51–124.

Rocklin, G., Crowley, J., and Vold, H. (1985). A comparation of H1, H2 and Hv frequency response functions. In *Proceedings of the 3rd International Modal Analysis Conference*.

Rytter, A. (1993). *Vibrational Based Inspection of Civil Engineering Structures*. Ph.D. thesis, Aalborg University, Denmark.

Schneider, T. and Neumaier, A. (2001). Algorithm 808: ARfit | a Matlab package for the estimation of parameters and eigenmodes of multivariate autoregressive models. *ACM Transactions on Mathematical Software*, 27(1):58–65.

Schwarz, B. J. and Richardson, M. H. (1999). Experimental modal analysis.

Söffker, D. (1999). Observer-based measurement of contact forces of the nonlinear rail-wheel contact as a base for advanced traction control. *Mechatronics and Advanced Motion Control*, 49:305–320.

Söffker, D., Yu, T.-J., and Müller, P. (1995). State estimation of dynamical systems with nonlinearities by using Proportional-Integral observer. *International Journal of System Science*, 26:1571–1582.

Simiu, E. and Scanlan, R. H. (1996). *Wind effects on structures*. Wiley, New York.

Sohn, H., Farrar, C., Hemez, F., Shunk, D., Stinemates, D., Nadler, B., and Czarnecki, J. (2004). A review of structural health monitoring literature: 1996-2001. Report LA-13976-MS, Los Alamos National Laboratory, Los Alamos, NM, USA.

Stevens, K. (1987). Force identification problems - an overview. In *Spring Meeting of SEM*, pages 838 – 844, Houston, USA.

Torres-Arredondo, M., Yang, C., and Fritzen, C.-P. (2011). On the application of Bayesian analysis and advanced signal processing techniques for the impact monitoring of smart structures. In *Proceedings of The 8th International Workshop on Structural Heath Monitoring (IWSHM 2011)*.

Tuan, P.-C., Ji, C.-C., Fong, L.-W., and Huang, W.-T. (1996). An input estimation approach to on-line two dimentional inverse heat conduction problems. *Numerical Heat Transfer, Part B: Fundamentals*, 29(3):345–363.

Welch, G. and Bishop, G. (2006). An introduction to the Kalman filter.

Worden, K. and Dulieu-Barton, J. (2004). An overview of intelligent fault detection in systems and structures. *Structural Health Monitoring*, 3(1):85–98.

Wu, A.-L., Loh, C.-H., Yang, J. N., Weng, J.-H., Chen, C.-H., and Ueng, T.-S. (2009). Input force identification: Application to soil-pile interaction. *Structural Control and Health Monitoring*, 16:223–240.

Yang, F. and Wilde, R. (1988). Observers for linear systems with unknown inputs. *IEEE Transactions on Automatic Control*, 33(7):677–681.

Zhang, L., Brincker, R., and Andersen, P. (2005). An overview of operational modal analysis: major development and issues. In *The 1st International Operational Modal Analysis Conference*, pages 179–190, Copenhagen, Denmark.

Zhou, X., Huang, P., Gu, M., Zhu, L., and Pan, H. (2010). Wind loads and wind-induced responses of guangzhou new tv tower. *Advances in Structural Engineering*, 13(4):707–726.

A. Derivation of the SS&IE_L

The proposed SS&IE_L method is based on an UIO and can realize simultaneous state and input estimation for linear systems. The derivation of the SS&IE_L is based on the work in Ha and Trinh (2004).

Consider the system which is described by

$$\dot{\boldsymbol{x}}(t) = \boldsymbol{A}_c\boldsymbol{x}(t) + \boldsymbol{G}_c\boldsymbol{d}(t) \tag{A.1}$$

and

$$\boldsymbol{y}(t) = \boldsymbol{C}_c\boldsymbol{x}(t) + \boldsymbol{H}_c\boldsymbol{d}(t), \tag{A.2}$$

where $\boldsymbol{x}(t) \in \mathbb{R}^n$ represents the state; $\boldsymbol{d}(t) \in \mathbb{R}^m$ denotes the unknown input; $\boldsymbol{y}(t) \in \mathbb{R}^p$ is the output; and $\boldsymbol{A}_c$, $\boldsymbol{G}_c$, $\boldsymbol{C}_c$ and $\boldsymbol{H}_c$ are system matrices with appropriate dimensions.

Introduce an augmented state $\boldsymbol{x}_{aug}(t)$ as

$$\boldsymbol{x}_{aug}(t) = \begin{bmatrix} \boldsymbol{x}(t) \\ \\ \boldsymbol{d}(t) \end{bmatrix}. \tag{A.3}$$

The system in equations (A.1) and (A.2) can be transformed to

$$\boldsymbol{E}_{ssie}\dot{\boldsymbol{x}}_{aug}(t) = \boldsymbol{M}_{ssie}\boldsymbol{x}_{aug}(t) \tag{A.4}$$

and

$$\boldsymbol{y}(t) = \boldsymbol{H}_{ssie}\boldsymbol{x}_{aug}(t), \tag{A.5}$$

where matrices $\boldsymbol{E}_{ssie}$, $\boldsymbol{M}_{ssie}$ and $\boldsymbol{H}_{ssie}$ are defined as

$$\boldsymbol{E}_{ssie} = \begin{bmatrix} \boldsymbol{I}_n & \boldsymbol{0}_{n\times m} \end{bmatrix}, \tag{A.6}$$

$$\boldsymbol{M}_{ssie} = \begin{bmatrix} \boldsymbol{A}_c & \boldsymbol{G}_c \end{bmatrix}, \tag{A.7}$$

and

$$\boldsymbol{H}_{ssie} = \begin{bmatrix} \boldsymbol{C}_c & \boldsymbol{H}_c \end{bmatrix}. \tag{A.8}$$

The SS&IE_L has the form

$$\dot{\boldsymbol{\xi}}_{aug}(t) = \boldsymbol{N}_{ssieL}\boldsymbol{\xi}_{aug}(t) + \boldsymbol{L}_{ssieL}\boldsymbol{y}(t) \tag{A.9}$$

and

$$\hat{\boldsymbol{x}}_{aug}(t) = \boldsymbol{\xi}_{aug}(t) + \boldsymbol{Q}_{ssieL}\boldsymbol{y}(t), \tag{A.10}$$

where $\hat{\boldsymbol{x}}_{aug}(t)$ represents the estimate of $\boldsymbol{x}_{aug}(t)$, and $\boldsymbol{N}_{ssieL}$, $\boldsymbol{L}_{ssieL}$ and $\boldsymbol{Q}_{ssieL}$ are the matrices which need to be determined.

Introduce the notations

$$\boldsymbol{S}_{ssieL} = \begin{bmatrix} \boldsymbol{E}_{ssie} \\ \boldsymbol{H}_{ssie} \end{bmatrix}, \tag{A.11}$$

$$\boldsymbol{J}_{ssieL} = \boldsymbol{I}_{n+m}\boldsymbol{S}^{+}_{ssieL}\begin{bmatrix} \boldsymbol{I}_{n} \\ \boldsymbol{0} \end{bmatrix}, \tag{A.12}$$

$$\boldsymbol{\Phi}_{ssieL} = \boldsymbol{J}_{ssieL}\boldsymbol{M}_{ssie}, \tag{A.13}$$

$$\boldsymbol{G}_{ssieL} = \left(\boldsymbol{I}_{n+p} - \boldsymbol{S}_{ssieL}\boldsymbol{S}^{+}_{ssieL}\right)\begin{bmatrix} \boldsymbol{I}_{n} \\ \boldsymbol{0} \end{bmatrix}, \tag{A.14}$$

$$\boldsymbol{\Psi}_{ssieL} = \boldsymbol{G}_{ssieL}\boldsymbol{M}_{ssie}, \tag{A.15}$$

$$\boldsymbol{V}_{ssieL} = \boldsymbol{I}_{n+m}\boldsymbol{S}^{+}_{ssieL}\begin{bmatrix} \boldsymbol{0} \\ \boldsymbol{I}_{m} \end{bmatrix}, \tag{A.16}$$

and

$$\boldsymbol{K}_{ssieL} = \left(\boldsymbol{I}_{n+p} - \boldsymbol{S}_{ssieL}\boldsymbol{S}^{+}_{ssieL}\right)\begin{bmatrix} \boldsymbol{0} \\ \boldsymbol{I}_{p} \end{bmatrix}, \tag{A.17}$$

where $\boldsymbol{S}^{+}_{ssieL}$ represents the left inverse of $\boldsymbol{S}_{ssieL}$.

Theorem. Define $\tilde{\boldsymbol{x}}_{aug}(t)$ as

$$\tilde{\boldsymbol{x}}_{aug}(t) = \boldsymbol{x}_{aug}(t) - \hat{\boldsymbol{x}}_{aug}(t). \tag{A.18}$$

The dynamics of $\tilde{\boldsymbol{x}}_{aug}(t)$can be described by

$$\dot{\tilde{\boldsymbol{x}}}_{aug}(t) = \boldsymbol{N}_{ssieL}\tilde{\boldsymbol{x}}_{aug}(t), \tag{A.19}$$

where $\boldsymbol{N}_{ssieL}$ is determined by

$$\boldsymbol{N}_{ssieL} = \boldsymbol{\Phi}_{ssieL} - \begin{bmatrix} \boldsymbol{Z}_{ssieL} & \boldsymbol{F}_{ssieL} \end{bmatrix}\begin{bmatrix} -\boldsymbol{\Psi}_{ssieL} \\ \boldsymbol{H}_{ssie} \end{bmatrix}. \tag{A.20}$$

The eigenvalues of $\boldsymbol{N}_{ssieL}$ can be arbitrarily set, if the following sufficient conditions are fulfilled.

(1) Matrix $\boldsymbol{H}_{ssie}$ has full column rank.

(2) Matrix pair $(\boldsymbol{\Phi}_{ssieL}, \begin{bmatrix} -\boldsymbol{\Psi}_{ssieL} \\ \boldsymbol{H}_{ssie} \end{bmatrix})$ is observable.

Proof of the Theorem

Introduce the following lemma.

Lemma 1. The dynamics of $\tilde{\boldsymbol{x}}_{aug}(t)$can be described by equation (A.19), if the following conditions hold.

Condition 1: $\boldsymbol{T}_{ssieL}\boldsymbol{E}_{ssie} + \boldsymbol{Q}_{ssieL}\boldsymbol{H}_{ssie} = \boldsymbol{I}$.

Condition 2: $\begin{cases} \boldsymbol{N}_{ssieL} = \boldsymbol{T}_{ssieL}\boldsymbol{M}_{ssie} - \boldsymbol{F}_{ssieL}\boldsymbol{H}_{ssie} \\ \boldsymbol{F}_{ssieL} = \boldsymbol{L}_{ssieL} - \boldsymbol{N}_{ssieL}\boldsymbol{Q}_{ssieL} \end{cases}$.

Proof of Lemma 1

Substituting equations (A.5) and (A.10) into equation (A.18) leads to

$$\tilde{\boldsymbol{x}}_{aug}(t) = (\boldsymbol{I} - \boldsymbol{Q}_{ssieL}\boldsymbol{H}_{ssie})\,\boldsymbol{x}_{aug}(t) - \boldsymbol{\xi}_{aug}(t). \tag{A.21}$$

With *Condition 1*, equation (A.21) can be transformed to

$$\tilde{\boldsymbol{x}}_{aug}(t) = \boldsymbol{T}_{ssieL}\boldsymbol{E}_{ssie}\boldsymbol{x}_{aug}(t) - \boldsymbol{\xi}_{aug}(t). \tag{A.22}$$

Taking the first derivative on both sides of equation (A.22) leads to

$$\dot{\tilde{\boldsymbol{x}}}_{aug}(t) = \boldsymbol{T}_{ssieL}\boldsymbol{E}_{ssie}\dot{\boldsymbol{x}}_{aug}(t) - \dot{\boldsymbol{\xi}}_{aug}(t). \tag{A.23}$$

Substituting equations (A.4), (A.9) and (A.5) into equation (A.23) leads to

$$\dot{\tilde{\boldsymbol{x}}}_{aug}(t) = \boldsymbol{T}_{ssieL}\boldsymbol{M}_{ssie}\boldsymbol{x}_{aug}(t) - \boldsymbol{N}_{ssieL}\hat{\boldsymbol{x}}_{aug}(t) - (\boldsymbol{L}_{ssieL} - \boldsymbol{N}_{ssieL}\boldsymbol{Q}_{ssieL})\,\boldsymbol{H}_{ssie}\boldsymbol{x}_{aug}(t). \tag{A.24}$$

With *Condition 2*, equation (A.24) can be transformed to equation (A.19). This finishes the proof of Lemma 1.

Lemma 2. If matrix $\boldsymbol{H}_c$ has full column rank, *Condition 1* of **Lemma 1** is always satisfied, and matrices $\boldsymbol{T}_{ssieL}$ and $\boldsymbol{Q}_{ssieL}$ are given by

$$\boldsymbol{T}_{ssieL} = \boldsymbol{J}_{ssieL} + \boldsymbol{Z}_{ssieL}\boldsymbol{G}_{ssieL} \tag{A.25}$$

and

$$\boldsymbol{Q}_{ssieL} = \boldsymbol{V}_{ssieL} + \boldsymbol{Z}_{ssieL}\boldsymbol{K}_{ssieL}, \tag{A.26}$$

where $\boldsymbol{Z}_{ssieL}$ is an arbitrary matrix.

Proof of Lemma 2

With equation (A.11), *Condition 1* of **Lemma 1** can transformed to

$$\left[\begin{array}{cc} \boldsymbol{T}_{ssieL} & \boldsymbol{Q}_{ssieL} \end{array}\right] \boldsymbol{S}_{ssieL} = \boldsymbol{I}. \tag{A.27}$$

The necessary and sufficient condition for equation (A.27) to have a solution to matrices $\boldsymbol{T}_{ssieL}$ and $\boldsymbol{Q}_{ssieL}$ is that $\boldsymbol{S}_{ssieL}$ has full column rank.

Substituting equations (A.6) and (A.8) into equation (A.11) leads to

$$\boldsymbol{S}_{ssieL} = \left[\begin{array}{cc} \boldsymbol{I}_n & \boldsymbol{0} \\ \boldsymbol{C}_c & \boldsymbol{H}_c \end{array}\right], \tag{A.28}$$

which indicates that the condition

$$rank\left(\boldsymbol{S}_{ssieL}\right) = n + rank\left(\boldsymbol{H}_c\right) \tag{A.29}$$

holds.

If $\boldsymbol{H}_c$ has full colum rank, $\boldsymbol{S}_{ssieL}$ will have full column rank. The solution to $\boldsymbol{T}_{ssieL}$ and $\boldsymbol{Q}_{ssieL}$ are given by

$$\boldsymbol{T}_{ssieL} = \left(\boldsymbol{S}^{+}_{ssieL} + \boldsymbol{Z}_{ssieL}\left(\boldsymbol{I} - \boldsymbol{S}_{ssieL}\boldsymbol{S}^{+}_{ssieL}\right)\right) \left[\begin{array}{c} \boldsymbol{I}_n \\ \boldsymbol{0} \end{array}\right] \tag{A.30}$$

and

$$\boldsymbol{Q}_{ssieL} = \left(\boldsymbol{S}^{+}_{ssieL} + \boldsymbol{Z}_{ssieL}\left(\boldsymbol{I} - \boldsymbol{S}_{ssieL}\boldsymbol{S}^{+}_{ssieL}\right)\right) \left[\begin{array}{c} \boldsymbol{0} \\ \boldsymbol{I}_m \end{array}\right]. \tag{A.31}$$

Substituting equations (A.12), (A.14), (A.16) and (A.17) into equations (A.30) and (A.31) leads to equations (A.25) and (A.26). This finishes the proof of **Lemma 2**.

Lemma 3. If Matrix pair $(\boldsymbol{\Phi}_{ssieL}, \left[\begin{array}{c} -\boldsymbol{\Psi}_{ssieL} \\ \boldsymbol{H}_{ssie} \end{array}\right])$ is observable, the first equation in *Conditon 2* of **Lemma 1** holds and the eigenvalues of $\boldsymbol{N}_{ssieL}$ can be arbitrarily set.

Proof of Lemma 3

Substituting equation (A.25) into the first equation of *Conditon 2* of **Lemma 1** leads to

$$\boldsymbol{N}_{ssieL} = \boldsymbol{J}_{ssieL}\boldsymbol{M}_{ssie} + \boldsymbol{Z}_{ssieL}\boldsymbol{G}_{ssieL}\boldsymbol{M}_{ssieL} - \boldsymbol{F}_{ssieL}\boldsymbol{H}_{ssie}. \tag{A.32}$$

Substituting equations (A.13) and (A.15) into equaiton (A.32) leads to the first equation in *Conditon 2* of **Lemma 1**. This finishes the proof of **Lemma 3**.

This finishes the proof of **Theorem**.

B. Proof of the equivalence of filter equations of the KF-UI and the RTSF

Within this section, the matrix inversion formula

$$(\boldsymbol{A}_1 + \boldsymbol{A}_2\boldsymbol{A}_3\boldsymbol{A}_4)^{-1} = \boldsymbol{A}_1^{-1} - \boldsymbol{A}_1^{-1}\boldsymbol{A}_2\left(\boldsymbol{A}_3^{-1} + \boldsymbol{A}_4\boldsymbol{A}_1^{-1}\boldsymbol{A}_2\right)^{-1}\boldsymbol{A}_4\boldsymbol{A}_1^{-1} \tag{B.1}$$

is used, where $\boldsymbol{A}_1$, $\boldsymbol{A}_2$, $\boldsymbol{A}_3$, and $\boldsymbol{A}_4$ are matrices.

By comparing the filter equations of the KF-UI in section 2.6.5 and the filter equations in the RTSF in section 2.6.4, it can be concluded that the equivalence of the filter equations of the KF-UI and the RTSF can be proved with the following 3 theorems.

Theorem 1. Introduce

$$\tilde{\boldsymbol{R}}_{kfui,k} \equiv \boldsymbol{R}_k^{-1}(\boldsymbol{I} - \boldsymbol{C}_k\boldsymbol{K}_{kfui,k}) \tag{B.2}$$

and

$$\tilde{\boldsymbol{R}}_{rtsf,k} \equiv \boldsymbol{C}_k\boldsymbol{P}_{k|k-1}^x\boldsymbol{C}_k^T + \boldsymbol{R}_k. \tag{B.3}$$

Then the condition $\tilde{\boldsymbol{R}}_{kfui,k} = \tilde{\boldsymbol{R}}_{rtsf,k}$ holds.

Proof of Theorem 1.

Define $\boldsymbol{K}_k$ which corresponds to $\boldsymbol{K}_{kfui,k}$ in KF-UI or $\boldsymbol{K}_{rtsf,k}$ in RTSF. For both the KF-UI and the RTSF, $\boldsymbol{K}_k$ is determined by an equation with the form

$$\boldsymbol{K}_k = \boldsymbol{P}_{k|k-1}\boldsymbol{C}_k^T\left(\boldsymbol{C}_k\boldsymbol{P}_{k|k-1}^x\boldsymbol{C}_k^T + \boldsymbol{R}_k\right)^{-1}. \tag{B.4}$$

Substituting equation (B.4) into the right side of equation (B.2) leads to

$$\tilde{\boldsymbol{R}}_{kfui,k} = \boldsymbol{R}_k^{-1} - \boldsymbol{R}_k^{-1}\boldsymbol{C}_k\boldsymbol{P}_{k|k-1}^x\boldsymbol{C}_k^T\left(\boldsymbol{C}_k\boldsymbol{P}_{k|k-1}^x\boldsymbol{C}_k^T + \boldsymbol{R}_k\right)^{-1}. \tag{B.5}$$

By applying the matrix inversion formula in equation (B.1), equation (B.3) can be transformed to

$$\tilde{\boldsymbol{R}}_{rtsf,k} = \boldsymbol{R}_k^{-1} - \boldsymbol{R}_k^{-1}\boldsymbol{C}_k\boldsymbol{P}_{k|k-1}\boldsymbol{C}_k^T\left[\boldsymbol{R}_k^{-1} - \left(\boldsymbol{C}_k\boldsymbol{P}_{k|k-1}^x\boldsymbol{C}_k^T + \boldsymbol{R}_k\right)^{-1}\boldsymbol{C}_k\boldsymbol{P}_{k|k-1}^x\boldsymbol{C}_k^T\boldsymbol{R}_k^{-1}\right]. \tag{B.6}$$

Lemma 1. If $\boldsymbol{B}_1$ and $\boldsymbol{B}_2$ are non-singular square matrices, then the condition

$$\left(\boldsymbol{B}_1^{-1} + \boldsymbol{B}_2\right)^{-1} = \boldsymbol{B}_1 - \left(\boldsymbol{B}_1^{-1} + \boldsymbol{B}_2\right)^{-1}\boldsymbol{B}_2\boldsymbol{B}_1. \tag{B.7}$$

holds.

Proof of Lemma 1.

By applying the matrix inversion formula in equation (B.1), the left side of equation (B.7) can be transformed to

$$\left(\boldsymbol{B}_1^{-1}+\boldsymbol{B}_2\right)^{-1}=\left[\boldsymbol{I}-\boldsymbol{B}_1\left(\boldsymbol{B}_2^{-1}+\boldsymbol{B}_1\right)^{-1}\right]\boldsymbol{B}_1. \tag{B.8}$$

If $\boldsymbol{B}_1$ and $\boldsymbol{B}_2$ are non-singular square matrices, the equation

$$\left(\boldsymbol{B}_2^{-1}\boldsymbol{B}_1^{-1}+\boldsymbol{B}_1\boldsymbol{B}_1^{-1}\right)^{-1}=\left(\boldsymbol{B}_2^{-1}\boldsymbol{B}_1^{-1}+\boldsymbol{B}_2^{-1}\boldsymbol{B}_2\right)^{-1} \tag{B.9}$$

can be obtained.

With the property of matrix inverse, equation (B.9) can be transformed to

$$\boldsymbol{B}_1\left(\boldsymbol{B}_2^{-1}+\boldsymbol{B}_1\right)^{-1}=\left(\boldsymbol{B}_1^{-1}+\boldsymbol{B}_2\right)^{-1}\boldsymbol{B}_2. \tag{B.10}$$

Substituting equation (B.10) into equation (B.8), the right side of equation (B.7) can be obtained. This finishes the proof of Lemma 1.

By applying equation (B.7) to the right side of equation (B.5) and the right side of equation B.6, the equation $\tilde{\boldsymbol{R}}_{kfui,k}=\tilde{\boldsymbol{R}}_{rtsf,k}$ can be obtained. This finishes the proof of Theorem 1.

Theorem 2. Introduce

$$\boldsymbol{P}^x_{kfui,k|k}=(\boldsymbol{I}+\boldsymbol{K}_{kfui,k}\boldsymbol{H}_k\boldsymbol{S}_k\boldsymbol{H}_k^T\boldsymbol{R}_k^{-1}\boldsymbol{C}_k)(\boldsymbol{I}-\boldsymbol{K}_{kfui,k}\boldsymbol{C}_k)\boldsymbol{P}^x_{k|k-1} \tag{B.11}$$

and

$$\boldsymbol{P}^x_{rtsf,k|k}=\boldsymbol{P}^x_{k|k-1}-\boldsymbol{K}_{rtsf,k}\left(\tilde{\boldsymbol{R}}_k-\boldsymbol{H}_k\boldsymbol{P}^d_k\boldsymbol{H}_k^T\right)\boldsymbol{K}^T_{rtsf,k}. \tag{B.12}$$

Then the equation $\boldsymbol{P}^x_{kfui,k|k}=\boldsymbol{P}^x_{rtsf,k|k}$ holds.

Proof of Theorem 2.

With equation (2.187) and equation (B.2), the right side of equation (B.11) can be transformed to

$$\boldsymbol{P}^x_{kfui,k|k}=\boldsymbol{P}^x_{k|k-1}-\boldsymbol{K}_{kfui,k}\left[\boldsymbol{C}_k-\boldsymbol{H}_k\left[\boldsymbol{H}_k^T\tilde{\boldsymbol{R}}_{kfui,k}\boldsymbol{H}_k\right]^{-1}\boldsymbol{H}_k^T\tilde{\boldsymbol{R}}_{kfui,k}\boldsymbol{C}_k\right]\boldsymbol{P}^x_{k|k-1}. \tag{B.13}$$

With equation (2.179) and equation (B.3), the right side of equation B.12 can be transformed to

$$\boldsymbol{P}^x_{rtsf,k|k}=\boldsymbol{P}^x_{k|k-1}-\boldsymbol{K}_{rtsf,k}\left[\boldsymbol{C}_k-\boldsymbol{H}_k\left[\boldsymbol{H}_k^T\tilde{\boldsymbol{R}}_{rtsf,k}\boldsymbol{H}_k\right]^{-1}\boldsymbol{H}_k^T\tilde{\boldsymbol{R}}_{rtsf,k}\boldsymbol{C}_k\right]\boldsymbol{P}^x_{k|k-1}. \tag{B.14}$$

With Theorem 1, the equivalence of $\boldsymbol{P}^x_{kfui,k|k}$ and $\boldsymbol{P}^x_{rtsf,k|k}$ can be proved. This finishes

the proof of Theorem 2.

Theorem 3. In KF-UI, the cross-covariance of $\tilde{\boldsymbol{x}}_{k|k}$ and $\tilde{\boldsymbol{d}}$ is determined by

$$\boldsymbol{P}^{xd}_{kfui,k} = -\boldsymbol{P}^{x}_{k|k-1}\boldsymbol{C}_k^T \left(\boldsymbol{C}_k \boldsymbol{P}^{x}_{k|k-1}\boldsymbol{C}_k^T + \boldsymbol{R}_k\right)^{-1} \boldsymbol{H}_k \boldsymbol{S}_k. \tag{B.15}$$

Proof of Theorem 3.

Following the derivation steps 15, 25, A15 and A17 in Pan et al. (2009), equation (B.15) can be obtained. This finishes the proof of Theorem 3.